UNIVERSITY OF SOUTHAMPTON

FACULTY OF NATURAL AND ENVIRONMENTAL SCIENCES

Chemistry

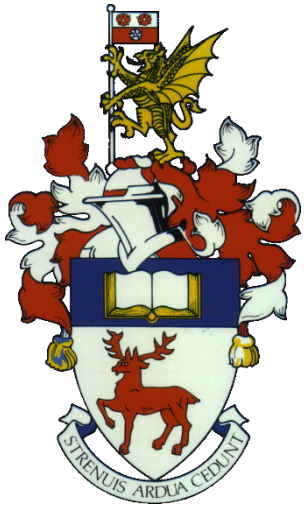

The Extrusion of Noble Metal Nanoparticle Catalysts for Sustainable Oxidation Reactions

by

Arran Michael Gill

Thesis for the degree of Doctor of Philosophy

November 2017

UNIVERSITY OF SOUTHAMPTON

ABSTRACT

FACULTY OF NATURAL AND ENVIRONMENTAL SCIENCES

Chemistry

Thesis for the degree of Doctor of Philosophy

THE EXTRUSION OF NOBLE METAL NANOPARTICLE CATALYSTS FOR SUSTAINABLE OXIDATION REACTIONS

Arran Michael Gill

Through employing a combination of complimentary structural, spectroscopic and high-resolution microscopy techniques, the superior properties of a $[PtCl_4]^{2-}$ precursor to yield well-defined, isolated nanoparticles (predominantly 2-3 nm) upon microporous framework architectures, have been established. These are prepared via a one-step, in situ methodology, within three-dimensional porous molecular architectures, to afford robust heterogeneous catalysts. The catalytic activity of these materials can be intrinsically linked to the degree of nanoparticle formation. The $[PtCl_4]^{2-}$ precursor bestows a greater propensity for nanoparticle formation across a range of activation conditions by comparison to $[PdCl_4]^{2-}$ and $[AuCl_4]^{-}$ precursors. This, in concert with the surrounding microporous architecture, donates superior catalytic performance for the aerobic oxidation of KA oil to cyclohexanone (precursor for adipic acid and ε-caprolactam), under continuous flow conditions. It is able to approach unrivalled yields of >90% by adapting a 'closed-loop' system.

Detailed spectroscopic investigations into the nature of the active sites at the molecular level, coupled with high-resolution electron microscopy, reveal that the intricacies of the synthetic methodology and associated activation procedures play a vital role in regulating the locality, morphology and size of the metal nanoparticles produced. These

investigations also offer insights into the potential consequences of prolonged catalytic exposure.

All three (Au, Pt & Pd) nanoparticle systems demonstrate a profound influence on the activation of molecular oxygen and alkyl peroxides for a plethora of selective catalytic oxidations. Furthermore, this design strategy offers adequate scope for the creation of multi-metallic (e.g. Pd-Cu, Au-Cu & Au-Pt), multifunctional heterogeneous catalysts, in the continued quest for the activation of molecular oxygen in sustainable catalytic processes.

Table of Contents

List of Tables

List of Schemes

List of Equations

List of Figures

DECLARATION OF AUTHORSHIP

I, Arran Michael Gill

declare that this thesis and the work presented in it are my own and has been generated by me as the result of my own original research.

The Extrusion of Noble Metal Nanoparticle Catalysts for Sustainable Oxidation Reactions

I confirm that:

1. This work was done wholly or mainly while in candidature for a research degree at this University;
2. Where any part of this thesis has previously been submitted for a degree or any other qualification at this University or any other institution, this has been clearly stated;
3. Where I have consulted the published work of others, this is always clearly attributed;
4. Where I have quoted from the work of others, the source is always given. With the exception of such quotations, this thesis is entirely my own work;
5. I have acknowledged all main sources of help;
6. Where the thesis is based on work done by myself jointly with others, I have made clear exactly what was done by others and what I have contributed myself;
7. Parts of this work have been published as:
    - Utilizing Benign Oxidants for Selective Aerobic Oxidations Using Heterogenized Platinum Nanoparticle Catalysts – C. S. Hinde, A. M. Gill, P. P. Wells, T. S. A. Hor and R. Raja, *ChemPlusChem,* **2015**, *80,* 1226 – 1230.

- Design of Highly Selective Platinum Nanoparticle Catalysts for the Aerobic Oxidation of KA-Oil using Continuous-Flow Chemistry – A. M. Gill, C. S. Hinde, R. K. Leary, M. E. Potter, A. Jouve, P. P. Wells, P. A. Midgley, J. M. Thomas and R. Raja, *ChemSusChem,* **2016**, *9,* 423 – 427.

- Nanoparticle Catalysts for Conversion of Cyclohexanol to Cyclohexanone – A. B. Levy, S. R. Keenan, R. Raja, A. M. Gill, M. E. Potter and S. A. Van Aswegen, *United States Patent Office (Application),* US 15/279,837, **2016**.

Signed: .....

Date: .....

Definitions and Abbreviations

Abs Sc	Absorbing Atom-Scattering Atom
AC	Aberration Corrected
ADF	Annular Dark Field
BDE	Bond Dissociation Energy
BE	Binding energy
CN	Coordination Number
CTAB	Cetyltrimethyl Ammonium Bromide
CuCIP	Copper Chloropyrophosphate
DI	De-ionised
EDTA	Ethylenediaminetetraacetic Acid
EDXS	Energy Dispersive X-Ray Spectroscopy
EXAFS	Extended X-Ray Absorption Fine Structure
FCC	Face Centred Cubic
FID	Flame Ionisation Detector
FT	Fourier Transform
FWHM	Full Width Half Maximum
GC	Gas Chromatography
GHG	Greenhouse Gas
HAADF	High Angle Annular Dark Field
HMF	5-Hydroxymethyl-2-Furfural
HOMO	Highest Occupied Molecular Orbital
ICP – OES	Inductively-Coupled Plasma – Optical Emission Spectroscopy
IR	Infrared

KE	Kinetic Energy
LbL	Layer-by-Layer
LSPR	Localised Surface Plasmon Resonance
LUMO	Lowest Unoccupied Molecular Orbital
MOF	Metal-Organic Framework
MS	Mass Spectroscopy
PVA	Polyvinyl Alcohol
PVP	Poly-Vinylpyrrolidone
PXRD	Powder X-Ray Diffraction
RBF	Round Bottomed Flask
R_f	Response Factor
RT	Room Temperature
SDS	Dodecyl Sulphate
SMSI	Strong Metal-Support Interaction
SPR	Surface Plasmon Resonance
STEM	Scanning Transmission Electron Microscopy
TBHP	Tertiary Butyl Hydrogen Peroxide
TEM	Transmission Electron Microscopy
TON	Turnover Number
TOF	Turnover Frequency
UV-vis	Ultra-Violet Visible
WGS	Water Gas Shift
WHSV	Weight Hourly Space Velocity
XAS	X-Ray Absorption Spectroscopy
XANES	X-Ray Absorption Near Edge Spectroscopy

XPS X-Ray Photoelectron Spectroscopy

XRD X-Ray Diffraction

XRF-CT X-Ray Fluorescence Computed Tomography

Chapter 1: Introduction

1.1 Catalysis

1.1.1 Catalysis – "The Heart of a Chemical Process"

The terms catalysis and catalyst were first documented in Jöns Jacob Berzelius' 1835 appraisal of the researches of Sir Humphry (1815) and Edmond Davy (1820), among others.[1–3] Indeed, it was the pioneering discoveries made by Sir H. Davy and his cousin in the early 19th century while working with platinum that led to both the Davy lamp[4,5] and what is now established as the first '*observed*' catalytic oxidation: the oxidation of ethanol to acetic acid in the presence of platinum (scheme 1-a).[6] Despite doing no research on the subject himself, Berzelius critically described the phenomena observed by others as *"catalytic powers"* of particular materials that *"awaken affinities, which are asleep at a particular temperature, by their mere presence and not by their own affinity"*.[2]

$$CH_3CH_2OH + O_2 \xrightarrow{[Pt]} CH_3CO_2H + H_2O$$

Scheme 1-a: The catalytic oxidation of ethanol.

Throughout this period many other observations of '*catalytic action'* were made by other scientists across the globe although true scientific appreciation of their mode of action would have to wait for the true study of reaction rates. F. W. Ostwald would then describe catalysts as *"substances which change the velocity of a reaction without modification of the energy factors of the reaction", "a substance that increases the rate at which a chemical system approaches equilibrium, without being consumed in the process".* Indeed it was through the kinetic and thermodynamic principles laid down in the early 1900s by Ostwald and others that truly refined our understanding of what a catalyst is.[7] Over half a century later J. M. Thomas would utilize three adopted principles of catalysis in order to explicitly define what a single-site catalyst is:[1]

> *"(i) A catalyst can increase the rate of only those processes that are thermodynamically favourable: it cannot initiate reactions that are not thermodynamically feasible.*
>
> *(ii) Any increase that a catalyst brings about in the velocity constant of the forward reaction is accompanied by a corresponding increase in the velocity constant of the reverse reaction. A catalyst facilitates the approach to equilibrium of a given chemical change.*

(iii) For a reactant or group of reactants there may be several reaction paths, and by the appropriate choice of catalyst any one of these paths may be 'selected'."

Now, almost half a century later, over 85% of all chemical manufacturing processes involve catalysts in at least one stage.[8,9] The sales of the catalysts themselves sum to approximately one hundred billion dollars (U.S.) and this figure is less than 1% of the revenue generated by the commodities they produce.[10] Therefore, it is little wonder that catalysis remains an increasingly evolving and rapidly progressing field of research. This is due in part to the vast array of global funding provided, feeding its exceptionally lucrative development.

1.1.2 Theory & Methods for Measuring Catalytic Activity

The catalytic principles laid down by F. W. Ostwald and others encapsulate the true essence of the catalytic effect and have thus stood the test of time. One important implication of these principles is the position of equilibrium, upon which a catalyst can have no effect. This is because the equilibrium constant *K* is determined by the thermodynamics of the process, the Gibbs free energy change (Equation 1), which is defined by the enthalpy and entropy changes (Equation 2).

$$K = e^{\left(\frac{-\Delta G}{RT}\right)}$$

Equation 1: Arrhenius equation where K is the equilibrium constant, ΔG is the Gibbs free energy change, R is the universal gas constant and T is the temperature.

$$\Delta G = \Delta H - T\Delta S$$

Equation 2: Gibbs free energy definition where H is the enthalpy, T is the temperature and S is the entropy.

The change in Gibbs free energy of a chemical transformation defines whether it will be spontaneous or not i.e. if ΔG is negative (the free energy of the products is less than the free energy of the reactants) then the thermodynamics will determine that the process is spontaneous, at a given temperature and pressure. This then determines the impact of J. M. Thomas' first principle, a catalyst can only impact a *"thermodynamically feasible"* or *'spontaneous'* process, therefore one with a negative ΔG.

So what does a catalyst influence if not the thermodynamics of a process? The obvious answer is the kinetics of said process, but what specifically? This was first portrayed by S. Arrhenius who described the effect of temperature on a non-catalysed, homogeneous gas-phase reaction. His work on quantifying the dependence of the reaction rate on the fraction of colliding molecules, that between them possess enough energy to carry out the

chemical transformation, which he called the '*activation energy',* was later extended to establish the now widely recognised Arrhenius equation (Equation 3).[11]

$$k = Ae^{\left(\frac{-E_a}{RT}\right)}$$

Equation 3: Arrhenius equation where k is the reaction rate constant, A is the pre-exponential factor, E_a is the activation energy, R is the universal gas constant and T is the temperature.

Through this work it was determined that a catalyst acts by altering this '*activation energy*' and thus impacting the reaction rate constant. As a reaction rate constant is equal for both the forward and backward reactions of the chemical transformation and it is this kinetic parameter that a catalyst influences, then J. M Thomas' second principle is advocated. A catalyst can influence the activation energy in a number of ways such as: holding reagents in close proximity or in a particular configuration, donating or accepting electrons, stretching and weakening bonds or simply stabilizing reaction transition states. These influences often result in a more energetically favourable or lower overall activation energy pathway and therefore an increased rate of reaction as per Figure 1-a. It is the purpose of the catalyst to offer these alternative, lower energy pathways and one can envisage different catalysts will offer different pathways through the differing influences listed above.

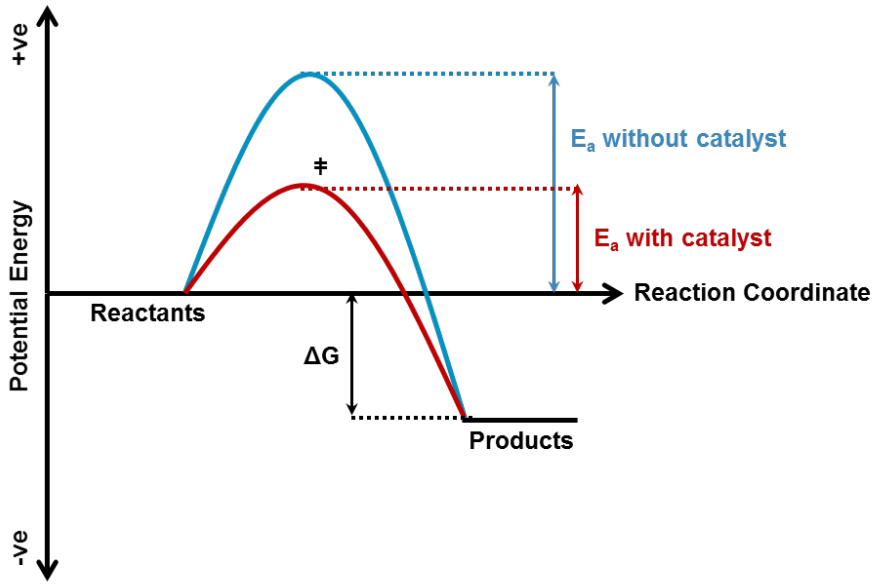

Figure 1-a: Potential energy profiles for a non-catalysed (blue) and catalysed (via a transition state, ‡) (red) reaction.

When it comes to analysing a catalytic reaction or any chemical transformation, determining the overall order of the reaction or order with respect to a particular

component can offer invaluable information on the reaction mechanism or kinetic processes in play. The order of the reaction defines how the concentration of a species or multiple species will affect the rate and visa versa. It is understood that the reaction rate depends on both the component concentration, raised to a power, known as the order and temperature through Equation 3. For a simple first order process of substrate *A* to product *P*, as shown in Equation 4, the rate is equal to the rate constant, as determined by the Arrhenius equation and the concentration of *A*. Note that this process is first order with respect to *[A]* as the power *[A]* is raised to is 1. Similarly, the rates displayed in Equation 5 are both second order. Equation 5a is second order with respect to *[A]* and Equation 5b is first order with respect to both *[A]* and *[B]* and therefore second order overall, meaning other species may be present but their concentrations have no influence over the rate of the reaction or rate of consumption of *A* and *B*.

$$rate = k[A]$$

Equation 4: Rate equation for a first order reaction where k is the rate constant and [A] is the concentration of species A within the system.

$$a) \quad rate = k[A]^2 \qquad 2A \rightarrow P$$
$$b) \quad rate = k[A][B] \qquad A + B \rightarrow P$$

Equation 5: Rate equations (left) for potential second order reactions (right) where k is the rate constant and [A]/[B] is the concentration of species A or B within the system.

Experimentally, the rate constant *k* is determined through tracking the component concentration as a function of time and depending on the component order, a straight line plot of *f([A])* vs *t* can be generated where the gradient is equal to the rate constant. These plots are deduced from the integrated rate laws as shown in Equation 6 where the integrated rate laws are represented in the linear *y = mx + c* form used to generate the plots needed to ascertain a value for '*k*'. Consequently plots of *[A]* vs *t* and *ln[A]* vs *t* would yield a gradient of *–k* for zero and first order reactions respectively.

$$a) \quad rate = -\frac{d[A]}{dt} = k \qquad [A]_t = [A]_0 - kt$$
$$b) \quad rate = -\frac{d[A]}{dt} = k[A] \qquad [A]_t = [A]_0 e^{-kt}$$

Equation 6: Rate laws (left) and their respective forms when integrated between $[A]_t$ and $[A]_0$, the concentration at time t and initial concentration (right). a) zero order and b) first order.

Once *k* has been determined for a specific reaction and set of conditions, then the rate can be generated for any concentration. Manipulation of the Arrhenius equation in the

form of Equation 7 allows the determination of E_a. According to Equation 7, a plot of *ln k* vs *1/T* gives a gradient equal to the activation energy over the gas constant. These kinetic laws therefore allow catalytic chemists to directly evaluate the ability of different catalysts for the same process through activation energy comparisons.

$$\ln k = \ln A - \frac{E_a}{RT}$$

Equation 7: Arrhenius equation where k is the reaction rate constant, A is the pre-exponential factor, E_a is the activation energy, R is the universal gas constant and T is the temperature.

Equation 7 also highlights another important aspect of catalysis; it not only demonstrates that through lowering the activation energy catalysts increase the rate of the reaction but also that they reduce the temperatures at which these more useful rates are achieved. In practice, this is a highly significant attribute as lower temperatures result in much lower energy requirements and hence a significant reduction in process cost.[7]

Despite the observable parameters discussed above, much of the catalytic literature relies on the comparison of reaction conversions (Equation 8), product selectivity (Equation 9) and yields (Equation 10) in order to measure the impact of a catalyst on a given process. While the reliance on these concepts can make direct comparisons challenging due to their lack of contained information, manipulation of these terms allows the investigating chemist to evaluate a catalytic system on a much more reliable measure of activity; turn over number (TON) (Equation 11) and turn over frequency (TOF) (Equation 12), taking into account the amount of catalyst used.

$$Conversion\ (mol\%) = 100 \times \frac{[Substrate_{initial}] - [Substrate_{final}]}{[Substrate_{initial}]}$$

Equation 8: Equation to calculate reaction conversion.

$$Selectivity\ (mol\%) = 100 \times \frac{[Product_{desired}]}{\sum[All\ Products]}$$

Equation 9: Equation to calculate product selectivity.

$$Yield\ (mol\%) = 100 \times \frac{[Product_{desired}]}{[Substrate_{initial}]}$$

Equation 10:Equation to calculate product yield.

Use of the activation energy to measure catalytic activity, while valid, is limited by its assumptions: that the precise nature of the catalyst remains the same across varying temperatures; that the reactant concentration at the catalysts surface is constant and

independent of temperature. While the former is not often the case, the latter is a particular limitation to this order of measure as clearly the reactant concentration would vary greatly with temperature.[12] For this reason it is much more common to find reference to a catalysts TON or TOF for a given process as opposed to its activation energy.

$$TON = \left[\frac{\frac{Conversion}{100} \times [Substrate_{initial}]}{[active\ site]}\right] = \frac{mol\ of\ substrate\ converted}{mol\ of\ active\ site}$$

Equation 11:Equation to calculate TON.

$$TOF\ (hr^{-1}) = \frac{TON}{time\ (hr)}$$

Equation 12:Equation to calculate TOF.

TON is simply the number of catalytic turnovers or cycles per catalytic site, analogous to enzymatic catalysis. TOF is this value per unit time.[13] Figure 1-b depicts an example of one full catalytic cycle whereby two gas or liquid phase molecules chemisorb onto the catalyst's surface, or active site, carry out a transformation to a new species which then desorbs, regenerating the catalyst's active site. This final step completes the catalytic cycle, or turnover and would represent one turnover (TON = 1).

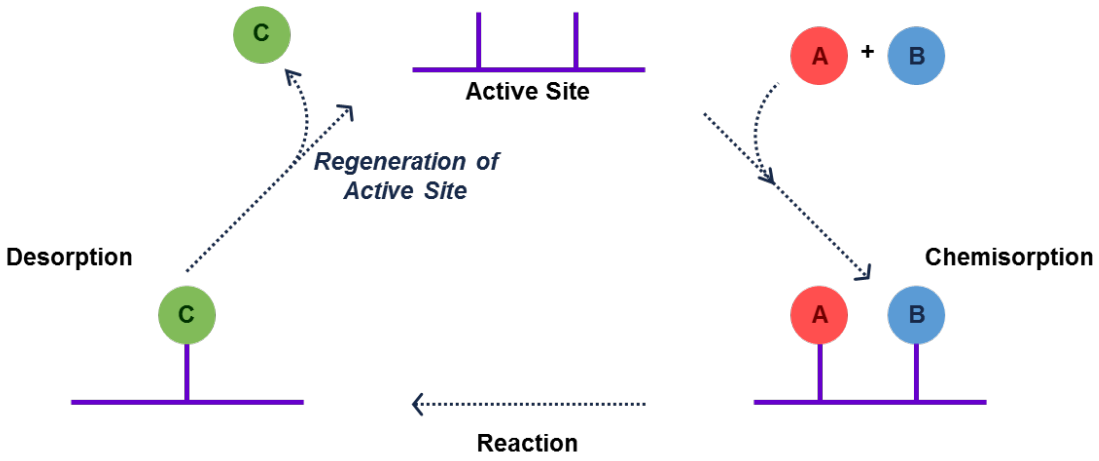

Figure 1-b: Depiction of a simple A + B → C catalytic cycle.[7]

1.1.3 Heterogeneous vs. Homogeneous Catalysis

The two predominant forms of catalysis are homogeneous and heterogeneous, with all other forms falling into subcategories of the two. The terms homogeneous and heterogeneous are dictated by the phase of the catalyst with respect to the reactants. For homogeneous catalysts they are within the same phase as the substrate; liquid-liquid or less commonly solid-solid or gas-gas. For heterogeneous they are different, most commonly solid-liquid or solid-gas systems. Homogeneous catalysts are generally liquids

or solutions such as acids/bases, dissolved ionic or alkyl species, nanoparticles or alternatively coordinated metal complexes, macromolecules or enzymes and as a result they act uniformly throughout a same phase system. Heterogeneous catalysts are more commonly solid materials such as: bulk metals or metal oxides, supported nanoparticle systems or solid acid/base materials causing catalytic processes to occur on their surface within liquid or gas phase systems.

Each system possesses certain advantages and disadvantages, detailed in Table 1-a and Table 1-b,[6,14–19] but despite the often far superior product selectivity bestowed by homogeneous systems, they are rarely adopted into industry due to the challenging separation of the catalyst from its same phase system. This industrial reluctance stems from the cost associated with the recovery which often requires large quantities of solvents and multistep processes for separation, purification and overall retrieval of the catalyst.[6,20] Heterogeneous catalysts are not limited by such strenuous separation as often, simple filtration is sufficient to recover the active material. Indeed, for most gas phase systems no separation is required at all. The economic costs associated with this simple process, on an industrial scale, appear to outweigh the added selectivity of homogeneous systems and this has facilitated the development of heterogeneous and heterogenized catalysts.

However certain materials within catalysis fall into both categories, such as nanoparticles. These materials as an example can be both homogeneous (acting in solution) or heterogeneous (immobilized upon a solid support). Therefore possessing the ability, in principle, to couple the clear benefits of homogeneous systems (high levels of activity and product selectivity) with the industrially significant benefits of facile catalyst recovery. These goals have led to a rapidly increasing level of importance to find ways of taking traditionally homogeneous catalysts and heterogenizing them, such as nanoparticles, in order to create catalytic species able to combine the benefits of both fields.[14–18]

Advantages	Disadvantages
Very high levels of selectivity, including chemo/regio/enantiomeric	Poor thermal stability (<150 °C)
All active sites accessible	Challenging catalyst recovery due to same-phase system
Excellent diffusion due to same-phase system	Expensive manufacturing costs due to catalysts complexity
Good mechanistic understanding	Expensive treatment often required to regenerate catalysts
Well defined active sites	Cannot be used within a continuous flow system

Table 1-a: Advantages and disadvantages of homogeneous catalysts when compared against heterogeneous systems.

Advantages	Disadvantages
Facile catalyst recovery due to phase separation	Poor comparative selectivity
Inexpensive to manufacture due to (often) simple catalyst structure	Often exhibits inaccessible active sites within bulk material
Excellent thermal stability	Poor diffusion due to laboured catalyst mobility
Often simple to regenerate & recycle catalysts	Active site is often ill-defined
Easily utilized within a continuous flow system	Limited mechanistic understanding

Table 1-b: Advantages and disadvantages of heterogeneous catalysts when compared against homogeneous systems.

1.1.4 The Quest for Sustainability: Green Chemistry & Sustainable Oxidants in the Chemical Industry

In order to achieve high production efficiency, low production cost, energy consumption and to meet increasingly stringent environmental regulations, approx. 90% of chemical processes employ catalysts. Nevertheless, the chemical industry consumes 30% of the global industrial energy use, which is 10% of the total worldwide energy demand. Just 18 products (of which ε-caprolactam is one) account for 80% of that energy consumption and produce 75% of the total greenhouse gas (GHG) emissions from the chemical industries.[21,22] Therefore, approx. 8% of the global energy demand is spent on the production of just 18 chemical products. Clearly improvements within the production of these significant products could have immensely powerful impacts on a global scale. Thus improvements in catalysts are vital in order to sustainably utilize the global energy supply. Furthermore, a recent global chemical industry technology roadmap describes the potential impact of continuous advances in catalytic processes, within which partial oxidation reactions were highlighted as a key area of interest. This roadmap suggested that advances in the design and application of catalysts and their related processes could yield global energy savings approaching 13×10^{15} kJ by 2050 – equivalent to the current annual primary energy usage of Germany (2013).[22]

Amongst the growing concern over global energy resources, the consumption of fossil fuels and the generation of GHGs, the 21st century has seen vast improvements in both legislation and infrastructure towards a more sustainable chemical industry. This is exemplified by the industry's desire to move away from a pure economical focus and towards a more open minded, environmentally friendly approach to chemical production. The implementation of 'green chemistry' is one such development. Green chemistry is the design of chemical products and processes that generate and use less or no hazardous

substances. Implementing green chemistry has been facilitated through its embodiment within 12 key principles:[20,23]

1. Prevent waste instead of treating it.
2. Design atom-efficient synthetic methods.
3. Choose synthetic routes using nontoxic compounds where possible.
4. Design new products that preserve functionality while reducing toxicity.
5. Minimize the use of auxiliary reagents and solvents.
6. Design processes with minimal energy requirements.
7. Use preferably renewable raw materials.
8. Avoid unnecessary derivatization.
9. Replace stoichiometric reagents with catalytic cycles.
10. Design new products with biodegradable capabilities.
11. Develop real-time and online process analysis and monitoring methods.
12. Choose feedstocks and design processes that minimize the chance of accidents.

Despite the convenience of these outlining principles quantification of a process' environmental impact is still required. Conversion, selectivity and yield are all measures of a reaction's efficiency, i.e. high selectivities produce less waste and high conversions over lower times facilitate smaller/safer reactors. However the true measure of a processes efficiency is most commonly observed through E-factors (Equation 13) and atom economies (Equation 14).

$$E\text{-}Factor = \frac{waste\ (kg)}{product\ (kg)}$$

Equation 13:E-Factor.

$$Atom\ Economy = \frac{MW\ of\ desired\ product}{\sum MW\ of\ all\ reactants} \times 100\%$$

Equation 14:Atom economy.

Atom economy is based on a chemical yield of 100% and assumes that reactants are used stoichiometrically. It disregards solvent and species utilized in the work-up which do not appear in the stoichiometric equation. However it is generally a good measure of a '*reaction's'* efficiency, highlighting wasteful reactants and massive by-products. The E-factor, in contrast, is a much better measure of a '*process''* efficiency. Defined as the mass ratio of waste against the desired product, it takes into account the chemical yield, all reagents, solvents losses and all process aids. A higher E-factor means more waste and consequently, a greater negative environmental impact. Table 1-c displays E-factors

for the various chemical industrial sectors. Clearly there is a trend from low E-factor for bulk chemical production to very high E-factors for specialist chemicals. This stems from the higher degrees of molecular complexity within these sectors requiring more widespread use of stoichiometric reagents. Contrastingly, due to the large production volumes within bulk chemical manufacturing, the use of stoichiometric reagents is not economically viable resulting in the considerably lower E-factors.[20]

Industrial sector	Production / tonyr^{-1}	E-factor
Petrochemicals	$10^6 – 10^8$	<0.1
Bulk chemicals	$10^4 – 10^6$	1 – 5
Fine chemicals	$10^2 – 10^4$	5 – 50
Pharmaceuticals	$10 – 10^3$	20 – 100

Table 1-c: Annual production and E-factors in the chemical industries.[23]

Evidently, replacement of these stoichiometric reagents, often oxidants such as permanganate, manganese dioxide or chromium (VI) species with green catalytic alternatives is one key area of interest within green chemistry (point 9). Another is to minimize both the use of solvents as they are a major contributor towards high E-factors (point 1) but also the nature of necessary solvents towards more environmentally friendly alternatives (point 3).[20]

One way in which the chemical industry is currently managing its waste chemical production is to consider the recycling of process by-products. This is especially important when potentially harmful chemicals are used and produced because reducing the quantity of the chemicals that are required to leave the site reduces exposure risks and carries economic advantages. One such example is the recently implemented recycling of dinitrogen monoxide, a significant GHG, by Solutia. The dinitrogen monoxide produced from the nitric acid oxidation of cyclohexanone to adipic acid is recycled within the same process for the hydroxylation of benzene. Also, the nitrogen oxides produced are re-oxidised to reform nitric acid making the process more sustainable as the use of nitric acid is done semi-stoichiometrically, see Scheme 1-b.

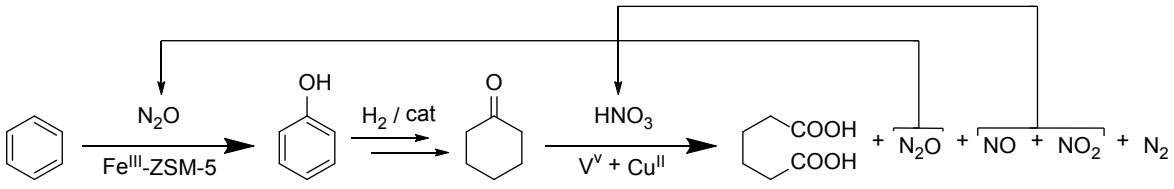

Scheme 1-b: The route adopted by Solutia to recycle dinitrogen monoxide.[24]

Implementing the aforementioned challenges, whilst working towards advancing the essential field of partial oxidation reactions would therefore be highly desirable.[22,25,26] In

order to do this, one must consider the alternative: more environmentally benign oxidants. For example, hydrogen peroxide, tertiary-butyl hydroperoxide (TBHP) and molecular oxygen are highlighted as some of the most environmentally favourable oxidants available, where the only by-product produced is generally water (or tertiary butanol in the case of TBHP).[14,15] The ready availability and minimal toxicity of molecular oxygen has it stand out as the ideal candidate. However, activation of molecular oxygen remains a challenge, due in part to its comparatively high bond dissociation energy (BDE) (TBHP approx. 185 $kJmol^{-1}$, hydrogen peroxide approx. 210 $kJmol^{-1}$ and molecular oxygen >480 $kJmol^{-1}$)[27] and is consequently, a vastly studied area of catalysis research.[14,15,28,29] To say the more readily active hydrogen peroxide and TBHP are environmentally benign may be true but they also carry significant limitation themselves.

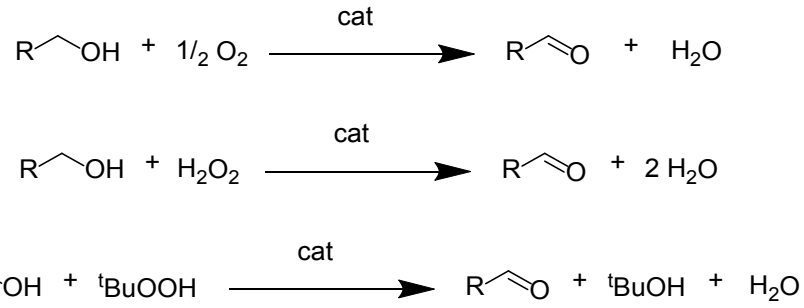

Scheme 1-c: Reaction schemes demonstrating the waste production from environmentally benign oxidants: molecular oxygen (top), hydrogen peroxide (middle) and TBHP (bottom).

While alkyl hydroperoxides produce more waste by contrast with hydrogen peroxide (Scheme 1-c), they are considerably easier to work with. TBHP, for example, has superior thermal stability over hydrogen peroxide and is considerably less corrosive and therefore possesses fewer handling risks. It is highly soluble in non-polar solvents making it more versatile, often yields selective products when employed with an appropriate catalyst and the alcohol by-product is easily recoverable via distillation while being a value added product in itself. Tertiary-butanol is used in the production of methyl tertiary-butyl ether.[24] Contrastingly, while hydrogen peroxide appears the more sustainable alternative due to its high active oxygen content (47 wt. % vs. 18 wt. % for TBHP) and production of water as its sole by-product, its use in industry has been limited. This stems from safety concerns over both the pure species, which is highly corrosive but mainly the fact that hydrogen peroxide oxidations progress through extremely hazardous peracid intermediates.[24]

As mentioned, triplet ground state molecular oxygen will not readily react with organic molecules and therefore the use of a catalyst is imperative in order to utilize this ideal oxidant. Two pathways exist towards the catalytic oxidation of an organic molecule by molecular oxygen and these are conveniently termed: type I and type II oxidations, see Scheme 1-d. For type I reactions the molecular oxygen is not itself incorporated into the

product, its role is to regenerate the catalyst's active site and achieve turnover. The dehydrogenation of alcohols to aldehydes and ketones makes up the largest class of this reaction. Type II reactions involve the incorporation of one or both oxygen atoms into the product with the oxidation of C-H bonds being a key example. These reactions proceed through a free radical mechanism.[26] Typically it is undesirable to carry out aerobic oxidations as batch processes due to both the large reactor head space and high pressures required to solubilize the oxygen but also due to the generation of aerated organic solvents posing significant flammability/explosion risks. As a result of these draw backs it is highly desirable from an industrial perspective to utilize continuous flow processes for aerobic oxidations.

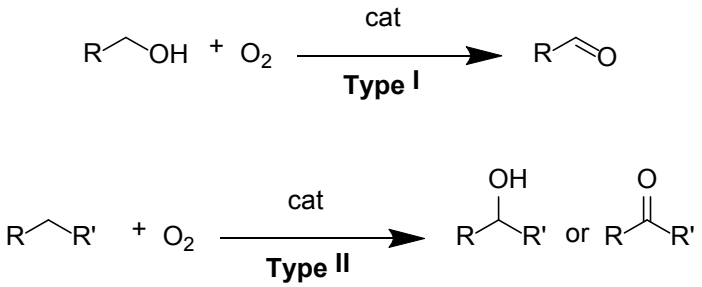

Scheme 1-d: Different types of aerobic oxidation reactions.[26]

Not only do batch based systems pose complications for aerobic oxidations on an industrial scale but continuous flow operations carry significant benefits over batch systems. For example, aerobic oxidations are generally highly exothermic and thus a continuous flow process is advantageous due to the significant reduction in internal reactor volume, resulting in increased heat dissipation and improved control over mass transfer, reducing the risk of hot spot formation and allowing for safer operations. Similarly, continuous flow operations facilitate the precise control over residence times through manipulation of the flow rates, reducing the risk of thermal run-aways. These capabilities coupled with the removal of flammable aerated organic solvents, significant ease of catalyst recovery/separation and level of control offered by continuous flow processes makes them ideal candidates for a range of industrial chemical productions but specifically aerobic oxidations.[26]

1.2 Nanoparticle Catalysis

1.2.1 Metal Nanoparticles & Quantum Size Effects

The rapid progression of characterisation technologies in recent decades has facilitated the study and understanding of increasingly small, sub-micron sized materials. Nanoparticles are defined by having at least one dimension on the nanometre length scale (1-100 nm) and their research interest has been growing at a rapidly increasing rate since the early 1990s.[8,30] This boom in interest does not simply stem from the ability to study these systems but that nanoparticle materials have found pivotal uses in a vast array of fields from chemical, pharmaceutical and catalysis,[19,31–33] to biology, medicinal and biomimicry[30,34–37] as well as energy, optics, sensing and water purification.[19,35–39]

A number of nano-sized phenomena can contribute to the activity of small metallic or metal oxide nanoparticles (Table 1-d) but those discussed here will be from a catalytic perspective. Small metallic nanoparticles often behave differently to their analogous bulk species for example, gold. By virtue of its nobility it was not considered that gold would exhibit any form of catalytic activity, despite surrounding elements in the periodic table being regarded as effective catalysts: Pt/Pd (car exhaust treatment), Cu (methanol synthesis), Ag (ethane epoxidation) and Hg (acetylene hydrochlorination).[40] It wasn't until pioneering work by Haruta *et al.*[41] and later, Hutchings and co-workers[42] that displayed gold having significant catalytic potential as a redox catalyst, provided the gold particles were within the nanometre size regime.

Phenomenon	Typical length scale
Size quantization	tens of nanometres
Crystal phase	tens of nanometres
Doping/defects	tens of nanometres
Single-charge effects	approx. 50 nm
Charge depletion (screening length)	approx. 100 nm
Scattering/interference of light	hundreds of nanometres
Ballistic electron transport	hundreds of nanometres

Table 1-d: Different size-related phenomena. The length scales are a rough estimation of the size below which the phenomenon can be observed (for the last three phenomena, typical values of the sizes—screening lengths and ballistic transport in particular—can vary over orders of magnitude).[39]

Size quantization is an effect observed in the energy-level structures of materials as the material-unit size drops below a certain threshold. This results in a lower density of the

electronic states, due to fewer atoms, increasing the bandgap and separation of the energy levels. In other words, the energy continuum of the bulk metal changes as a function of crystallite size to produce increasingly discrete energy levels as displayed in (Figure 1-c).[30] For semiconductor materials this is usually between 2-10 nm but for metallic species it can be much smaller, for Au nanoparticles it is approx. 1 nm.[39]

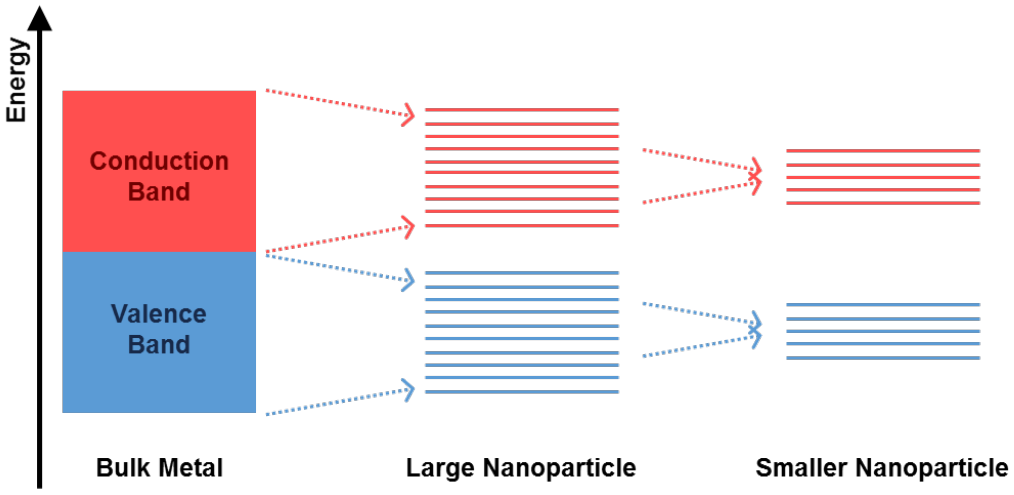

Figure 1-c: Schematic layout demonstrating the size quantization phenomenon i.e. the progression from metallic band structure to quantized electronic structure as nanoparticle dimensions decrease.

Metallic nanoparticles also demonstrate an interactive relationship with light due to the size of the particles and the wave length of the light being on similar size scales. Surface plasmon resonance (SPR) is the coherent oscillation of a metals surface conduction electrons due to their excitation by electromagnetic radiation.[43] The electric field component of the incident light induces these oscillations, which are termed plasmons and they can propagate across a metals surface for tens to hundreds of microns but typically decay away from the surface on the order of 200 nm. This effect has further implications within nanoparticle systems as the induced plasmon oscillates locally across the particles entire electron cloud with a frequency known as the localised surface plasmon resonance (LSPR).[43] The displacement of the electron cloud by the electric field leads to the creation of opposing surface charges on either side of the particle, as shown in Figure 1-d.[35] Whilst LSPR is not intrinsically related to catalytic activity, the optical phenomenon is related to the electronic properties of the nanoparticle which do contribute to the chemical reactivity and thus can be utilized as a tool to probe changes in electronic character of the system. Many things can impact these electronics and thus the frequency of the LSPR such as: nanoparticle size and shape as these will impact the electron cloud density, any changes in the dielectric constant of the metal due to polarization or metal nuclei charge as well as

the surface absorption or binding of additional species. These contributions have aided in the application of these systems in many sensory devices, as eluded to earlier.[35–37]

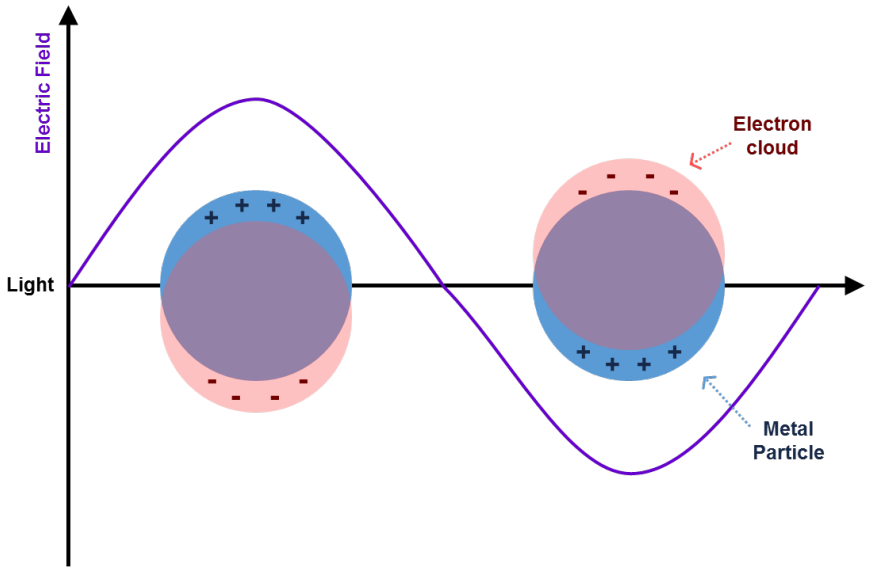

Figure 1-d: Oscillation of a metal nanoparticle's (blue) electron cloud (red) in response to an electromagnetic field – localised surface plasmon resonance.[30]

Another key property from a catalytic perspective is the surface area to volume ratio of nanoparticles. Considering many nanoparticle catalysts are comprised of expensive, often noble metals this feature bears a significant economic advantage but it also carries important energetic advantages as well. As the size of a particle decreases it is clear that the percentage of surface atoms will increase inversely with the radius and this is significant at very small particle sizes, approx. <10000 atoms. For example, for Pd nanoparticles of 1.2 nm (55 atom) 76% of the atoms are located on the nanoparticle surface. This drops significantly for nanoparticles of 2.5 nm (561 atoms) where only 46% are located on the surface and further still where 3.4 nm (1415 atoms) particles exhibit only 35% surface atoms.[44] The lack of neighbouring atoms at the particles surface facilitates a greater degree of vibrational freedom and it is hypothesised that this is the key to the catalytic enhancements observed at smaller particle sizes. It is known that corner, edge and kinked surface sites of catalytic materials are often the more reactive (or 'hyper' active) centres. This is due to their improved accessibility and lower absorption energies (Figure 1-e), due to the vibrational freedom mentioned. As you reduce the particle size and the percentage of surface sites increases then, by extension, so does the quantity of kinks, edges and corner sites, yielding a higher proportion of under coodinated, highly active catalytic sites per unit weight. As described, it is the increase in the density of these low energy binding sites that facilitates improved catalytic conversions and turn overs and it is now believed, due to significant research that optimum levels of catalytic activity are generally found <10 nm. For example, Tsunoyama *et al.*[45,46] observed decreasing rate

constants with increasing Au nanoparticle size (1-5 nm) for the aerobic oxidation of *p*-hydroxylbenzyl alcohol, many other works can be found that display analogous trends.[19,47,48]

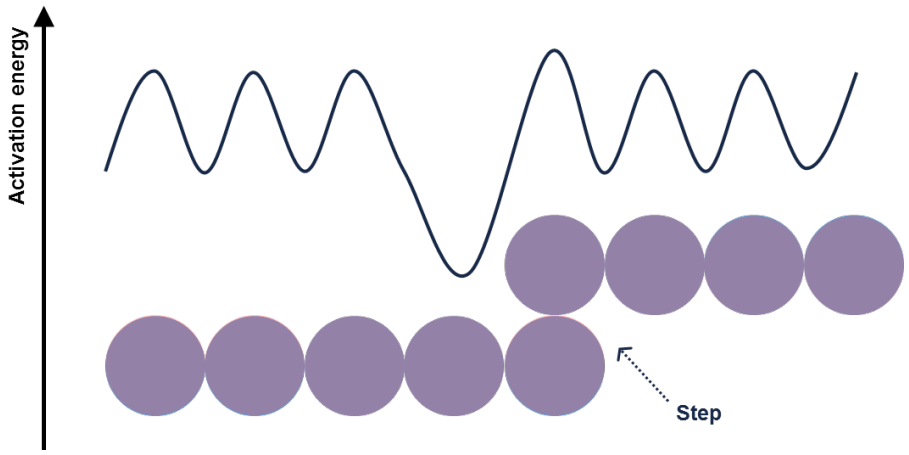

Figure 1-e: Approx. 1D plot of the activation barrier to adsorption as a function of distance across a surface with a step. Highlighting the more favourable adsorption at step and edge sites on a surface.[5]

1.2.2 Reactions at Surfaces

As discussed, when one considers catalysis on a nanoparticle's surface there exists a metal surface upon which the catalysis is carried out. Therefore adsorption must always precede the catalysis. Both physical adsorption and chemisorption of the gas or liquid molecules upon the particle surface play vital roles in catalysis. Physical adsorption or Van der Waals adsorption consists of dipole, induced dipole and quadrupole attraction and typically produces small enthalpy changes of the order of: 10 – -40 $kJmol^{-1}$. Chemisorption on the other hand involves the rearrangement of electrons and the formation and breaking of chemical bonds. Chemisorption occurs at closer distances to the solid surface and generally produces enthalpy changes >100 $kJmol^{-1}$.[12]

When considering the adsorption (or collision) of a molecule on nanoparticle surface there are a number of pathways that the molecule might take:

1. The molecule can be elastically scattered back into the gas or solution phase.
2. The molecule can lose sufficient energy to become physically adsorbed on the surface.
3. If the molecule has sufficient energy and an appropriate site is available, the molecule can pass directly to the chemisorbed state.

4. Once a molecule is in the physisorbed state it may; be inelastically scattered, become chemisorbed or migrate to neighbouring sites where it could then become chemisorbed or inelastically scattered and so on.

These pathways are dictated by the substrate-surface interactions. For catalysis it is imperative that the adsorbed states are not too favourable as to irreversibly bind the substrate. This leads to blocking of the active site and catalyst poisoning, ideally these interactions are favourable enough to bind the substrate and '*activate'* or destabilise the species to facilitate the desired chemical transformation. For heterogeneous catalysis there are two pathways in which these transformations progress once the chemisorbed state has been achieved; the Langmuir-Hinshelwood mechanism (Figure 1-f) and the Eley-Rideal mechanism (Figure 1-g). For reactions of '*A + B → C'*, either both '*A*' and '*B*' can be adsorbed, migrate towards a position that allows them to react, react and then desorb as '*C*', this is described as the Langmuir-Hinshelwood mechanism. Alternatively for the same reaction, one of '*A*' or '*B*' can absorb, the other can then react with the adsorbed species from the gas or liquid phase and the product '*C*' can then desorb, this is described as the Eley-Rideal mechanism.

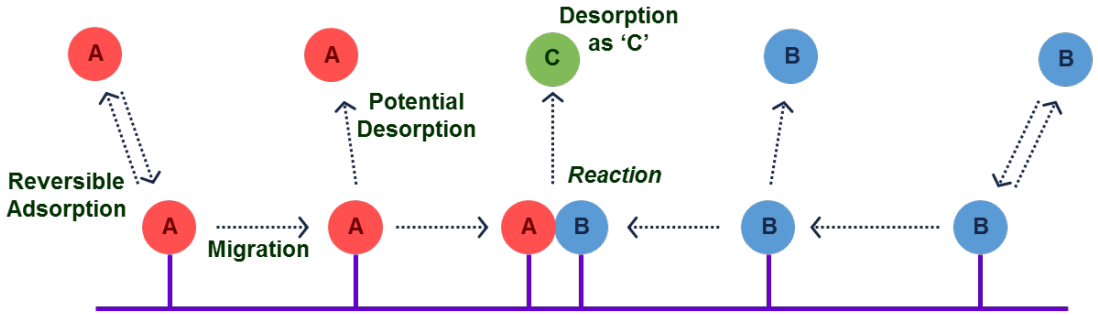

Figure 1-f: Depiction of the Langmuir-Hinshelwood mechanism.

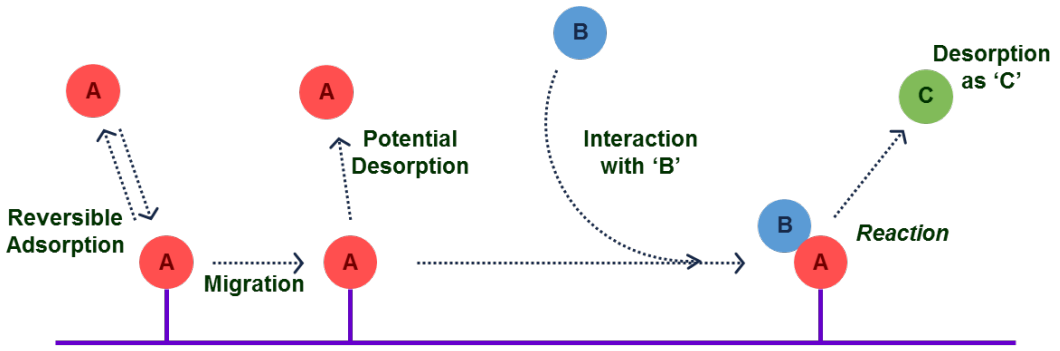

Figure 1-g: Depiction of the Eley-Rideal mechanism.

Contrary to the depictions of these mechanisms in Figure 1-f and Figure 1-g, the migration of the adsorbed species and the precise adsorption site are dramatically important when considering the precise nature of the active site. As described in Figure 1-e there exist energetically favourable binding sites upon a particle surface and as discussed, it is

believed that these step, edge and kink sites with their larger degrees of vibrational freedom are able to sufficiently destabilise the substrate whilst stabilising the necessary transition states required to carry the catalytic transformation. With the importance of specific binding sites being highlighted, it would be logical to expect the nature of the exposed crystallite face to also be important. Indeed this is the case, the different atomic arrangements offered by different lattice planes of the same metal can have great impacts on the catalytic outcome.[3] With this in mind, many studies have been carried out investigating the effect of both nanoparticle size as eluded to, but also the exposed crystallite face on various catalytic processes.[8,9,47,49–53] For example, this phenomenon has been observed extensively in platinum nanoparticle catalysed reactions. Bratlie *et al.*[54] demonstrated that for the hydrogenation of benzene exposure to either the Pt (100) or a combination of the (100) and (111) planes produced drastically different product selectivity profiles. The Pt (100) produced exclusively cyclohexane as opposed to cyclohexane and cyclohexene mixtures. Similarly Komanicky and co-workers suggested that different Pt planes demonstrate contrasting affinities towards oxygen with the Pt (111) able to reduce the oxygen but not adsorb it initially. Therefore they concluded that the oxygen molecule would adsorb on the Pt (100) plane and then migrate to the Pt (111) where the molecule would become activated and react.[52] These studies would therefore suggest that by uniquely controlling the size, shape and exposed lattice plane of a nanoparticle species, it is possible to control the catalytic outcome of various processes. Therefore this highly desired level of atomic control will have to come from the synthetic methodology employed.

1.2.3 Synthesis of Nanoparticle Catalysts

There is now a broad array of synthetic protocols adopted for the synthesis of metallic nanoparticles, the most common of which are generally divided into two categories, chemical and physical methods. Traditional chemical methods proceed through nucleation of the metal atoms and growth into the nanoparticles, a so called bottom-up methodology. Physical methods occur through the mechanical subdivision of metallic aggregates, top-down, see Figure 1-h.[31] Further to these more common approaches two other widely used techniques that are often utilized are electrochemical and electroless deposition.[33]

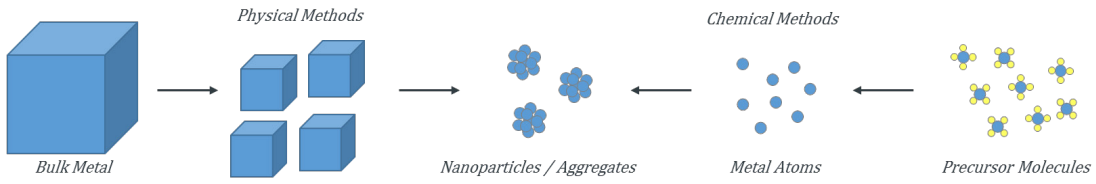

Figure 1-h: Illustration of preparative methods of metal nanoparticles.

Typical physical approaches to nanoparticle synthesis include; sputtering, ion/electron beam deposition, laser ablation and irradiation, amongst others. Historically physical methods suffered severely from poor size and shape control over the final particles with many systems producing both large (>10 nm) particles and broad size distributions resulting in irreproducible catalysis work. This has more recently, with technological advancements, been overcome in many cases with methods offering analogous or better control over many chemical methods. While this may be the case, the production of nanoparticles with analogous precision through physical means requires significantly elevated hardware and equipment costs, thus for many catalytic chemists, chemical synthesis methodologies are preferred. That is not to say that high levels of morphological control cannot be achieved through chemical means, because they can, at a fraction of the cost.[30,31,33]

1.2.3.1 Impregnation

Impregnation is considered the simplest of all the methodologies available for generating heterogeneous nanoparticle catalysts. Impregnation is divided into two categories: wet and dry impregnation methodologies. These differ by the volume of solvent employed, typically dry impregnation exploits a minimum quantity of solvent as opposed to wet impregnation methods which employ an excess of solvent. Due to its wide use wet impregnation methods are explored within these works and consists of 'wetting' the support surface with a solvent followed by the addition of the metal precursor, or wetting in the form of a solution with the metal precursor, often a chloride salt. This is then followed by removal of the solvent through rotary evaporation and/or oven drying and subsequent calcination or reduction of the final solid, as depicted in Figure 1-i.

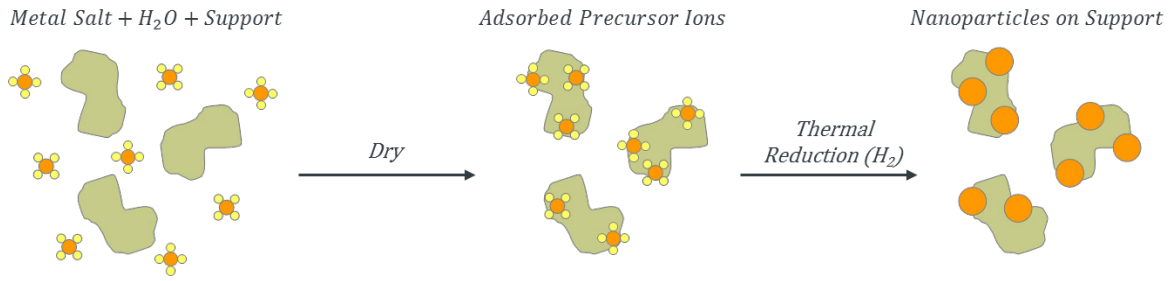

Figure 1-i: Illustration of a typical impregnation synthesis protocol.

Impregnation is commonly used due to its versatility and simplicity. In fact, impregnation can be employed, to varying degrees of success, to any support one might desire. This facet in particular has led to its widespread use for the formation of metallic nanoparticles in catalysis. Impregnation also offers excellent control over the metal loading as the conversion of precursor to nanoparticle is often close to 100%.[7,30] However the final particle size is strongly correlated to the metal loading employed, this coupled with the

frequent use of metal chloride salts as precursors hinders the controlled formation of small particles with narrow size distributions. Small particles possess high surface energies and are therefore unstable and susceptible to agglomeration for thermodynamic reasons. Further, the presence of chloride ions facilitates the mobility of the nanoparticles and therefore these systems are prone to a significant degree of agglomeration. As a result impregnation methodologies almost always suffer from large particle production and broad particle size distributions.[9,53] One way to circumvent this problem is to carry out the thermal activation in the presence of hydrogen gas as this liberates the chloride ions as hydrogen chloride gas.[7]

1.2.3.2 Colloidal Deposition

Colloidal deposition consists of an aqueous solution of metal ions and an organic stabilizing agent, often alcohol or amine based. Upon reduction of the metal precursor a nanoparticle sol is generated (hence the method alternatively named sol-immobilisation) whereby the nanoparticles are coated by the organic stabilizing agent. Following the generation of the nanoparticle suspension the support is added and stirred before collection and drying, as in Figure 1-j.[7] A range of organic stabilizers have been utilized within this protocol; common examples include: dodecyl sulphate (SDS), cetyltrimethyl ammonium bromide (CTAB), poly-vinylpyrrolidone (PVP), polyethylene glycol and polyvinyl alcohol (PVA).[38]

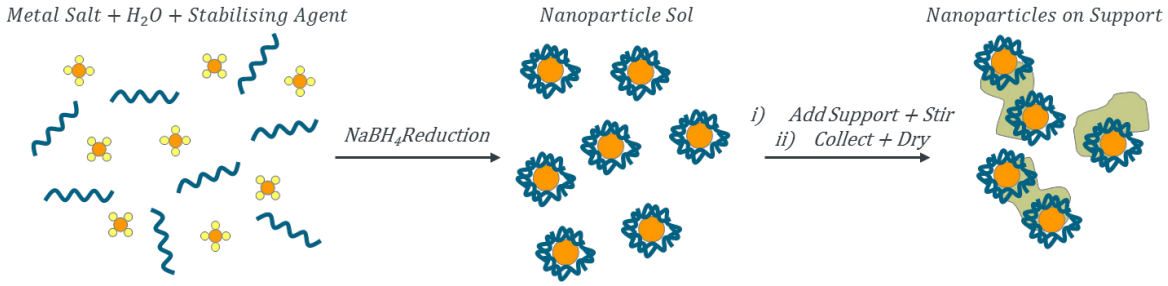

Figure 1-j: Illustration of a typical colloidal deposition protocol.

The key purpose and benefit of employing these stabilizing agents is the protection against agglomeration. Over short nanoparticle separations (therefore this becomes increasingly important as the metal loading is increased) Van der Waals forces cause agglomeration and thus the colloidal shell prevents this, either sterically or electrostatically. For example, ionic compounds form a charged double-layer around the nanoparticle and therefore coulombic repulsion prevents agglomeration. For these particular systems high temperatures induce significant thermal motion which is often detrimental to this stabilizing effect. Alternatively, steric stabilization restricts the motion in the inter-particle distance therefore lowering the entropy and increasing the free energy, making the interaction less favourable. Further, osmotic repulsion also comes into effect in

these inter-particle regions as the concentrations of the ligands increases as the particles come together.[31,53]

This procedure allows the user to define the nanoparticle size, precisely, by tuning the characteristics of the sol through control over the nature of the stabilizer and rate of reduction. The reduction is frequently carried out through chemical means such as $NaBH_4$ as these systems are not stable to high temperature environments due to the stability of the organic stabilizer. Many other chemical reductants have also been employed such as; hydroquinone, potassium borohydride, lithium hydride, ascorbic acid, hydrazine, glucose and dimethylamine borane.[53] Additionally, the same compounds can act as both a stabilizing and reducing agent such as; ethylenediaminetetraacetic acid (EDTA) and citrate.[38,53] Further, through the careful selection of the organic stabilizer one can not only control the size but often the surface facets of the nanoparticles generated and through manipulation of the organic-nanoparticle-support interactions a vast array of supports can be utilized through this methodology.[7,30,33,47]

The advantages of employing stabilizing agents for the generation of nanoparticles has been widely reported[7,30,31,33,38,47] but these organic compounds can offer much more when one considers the substrate interactions. Tuning of this nanoparticle shell can allow the user to impact the electronics of the nanoparticle metal and control the substrate orientation, transition state orientation and even employ a particular stabiliser that might chemically interact or take part in the reaction.[47] These ‘capped’ nanoparticles are effective catalysts within liquid phase systems, where the system mobility is facilitated and the substrate access to the particle surface is less restricted. For gas phase applications, however, these capping agents cause significant problems by blocking the nanoparticle surface. Typical surface coverages are upwards of 60%, severely hampering the substrate access to the nanoparticle active sites.[9,38] Further, attempts to remove these capping agents by thermal means, post-synthesis can cause nanoparticle oxidation and sintering or in a non-oxidising environment agglomeration/sintering can still occur due to the elevated temperatures.[7,9] Another key consideration for the use of colloidal deposition is the compatibility of the stabilizing agent with the support. The capping agent dramatically influences the binding of the nanoparticle to the support surface, which can allow control over the distribution and leaching of the nanoparticles but if the support and stabilizer were to repel each other, the supported nanoparticle systems would not be generated.[7,9] Therefore, while these organic stabilizers have the possibility to offer significant benefits for both the direct nanoparticle formation and potential catalytic impacts, they are a burden when applied in many catalytic applications through capping of the nanoparticle surface. This has been well demonstrated in a recent review by Liu and

co-workers where they detail the negative impacts of SDS, PVP and CTAB stabilizers in an array of silver and gold nanoparticle catalysed reductions.[38]

1.2.3.3 Deposition-Precipitation

Deposition-precipitation relies on the adjustment of pH (i.e. 5-10) to achieve precipitation (or deposition onto the support) of the metal hydroxide which is subsequently calcined and/or reduced to the elemental species.[7] The adjustment of pH removes the problems caused by the presence of chloride species referred to in Section 1.2.3.1 through the deposition of metal hydroxide species. While one can accurately control the nanoparticle size generated through tailoring the system pH, this use of pH does limit the options available. For this protocol to be effective the removal of chloride ions from the metal and replacement with hydroxide must occur but the resulting species must also be able to bind to the support surface through electrostatic attraction. Therefore, the pH at which the support becomes positively or negatively charged is of great importance to maximise the interactions towards successfully binding the (generally) negatively charged precursor to the surface. This 'point of zero charge', either side of which the support surface carries charge, is a key point and generally limits this synthetic methodology to materials that are compatible in this regard to the pH characteristics of the metal precursor.[55,56] For many noble metal systems, the point of zero charge would lie between 5 and 8 and this corresponds to many metal oxides such as TiO_2, Al_2O_3, CeO_2, ZrO_2 and Fe_2O_3.[7,30,53] While this technique is very effective at generating controlled, uncapped, nanoparticle species in absence of chloride within its limitations, it does suffer from poor yields (60%) in terms of conversion of salt to nanoparticle, especially when operating at high metal loadings, >1 wt. %, further limiting its applications.[7]

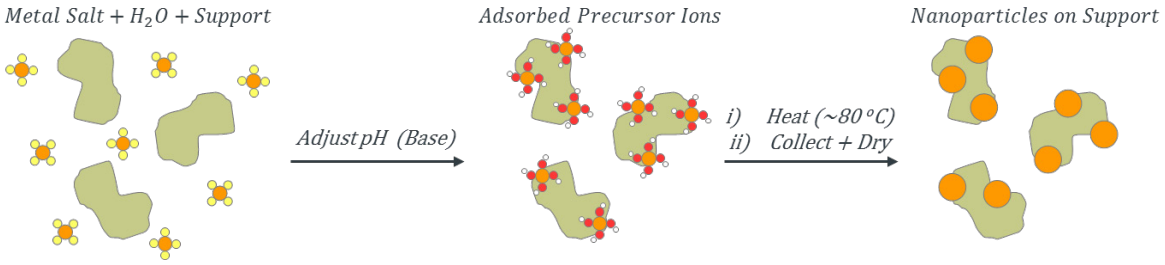

Figure 1-k: Illustration of a typical deposition-precipitation methodology.

1.2.3.4 Co-Precipitation

Co-precipitation shares many similarities with the deposition-precipitation method but with one key difference. Co-precipitation involves the simultaneous precipitation of the metallic species and the support. The initial solution of metal and support precursors is influenced either by pH adjustment or the addition of precipitating agent, such as; sodium hydroxide, urea, sodium carbonate or ammonium hydroxyl, to allow both the support and metallic

nanoparticles to form together.[53] In some examples the support can be precipitated independently after which the metal precursors, now adsorbed onto the support surface, would be reduced either thermally or chemically.[7] This methodology benefits primarily from excellent distribution of the nanoparticle species throughout the support material, often resulting in more reliable size distributions by comparison with impregnation methods.[30] While this technique is limited, similarly to deposition-precipitation, to a subset of supports due to the precipitation requirements it does offer an excellent means of generating well dispersed nanoparticle species within many porous support networks in a facile, single-step protocol. Aside from the limited number of supports available, this technique is regularly restricted by its high losses of metal precursor to the bulk of the support material, often imparting defects within the support. This poor economy towards the metal precursor becomes increasingly significant for noble metal systems due to the elevated cost of the species.[7]

1.2.3.5 Modern Developments in Nanoparticle Catalyst Synthesis & the Predominant Role of Nanoparticle Supports

While the natural development of the aforementioned traditional nanoparticle synthesis methods is on-going, alternative synthetic protocols are simultaneously being developed and in light of the above discussions (Sections 1.1.3, 1.1.4 and 1.2.3) some key considerations need to be realised:[38]

1. Without a carrier system or support, recovery of nanoparticle catalysts is difficult and costly to the extent that it almost entirely prevents their industrial application.
2. Recycling of the catalyst is key not only from an economical perspective but also from an environmental one as the toxicity of many nanoparticle materials is not well understood.[30]
3. Without protection or immobilization onto the support surface, metal nanoparticles are highly susceptible to aggregation due to their high surface energies and strong Van der Waals interactions.
4. Development of materials that are both highly active and durable is of paramount interest and improvement of one property has often been at the expense of the other i.e. strong organic stabilizing agents will improve the systems stability but are detrimental to the catalytic activity due to capping of the particle surface.
5. Thus, single component stabilized systems are not likely to achieve sufficient efficiency and durability for practical applications and it is therefore necessary to explore the fabrication of integrated heterogeneous systems possessing multiple functional components.

It is therefore clear that in order to produce catalytic materials with these desired properties, one must consider the nature of the nanoparticle support and the nanoparticle-support synergies that can be utilized. This is perhaps one criticism of the early research into nanoparticle catalysis; the nature of the support was less important than the nanoparticles themselves as they bestow no significant catalytic properties. Traditionally these systems employ single metal oxide supports as they are easy to use, non-toxic, economically cheap, readily available, chemically and thermally stable and provide the desired nanoparticle-support relationship – they are able to easily support a range of nanoparticle catalysts.[30]

It is now understood that the nanoparticle host, or support can have a significant impact over the catalytic behaviour. Therefore although good particle adhesion is imperative for stability of the catalyst one must also consider the nanoparticle-support synergies in play for a given system in order to maximise catalytic performance. Such nanoparticle-support interactions can impact the electronic structure of the nanoparticles through charge transfer, the crystalline and electronic structure of the nanoparticles due to induced strain at the nanoparticle-support interface as well as the properties of the interfacial sites, as graphically represented in Figure 1-I.[48]

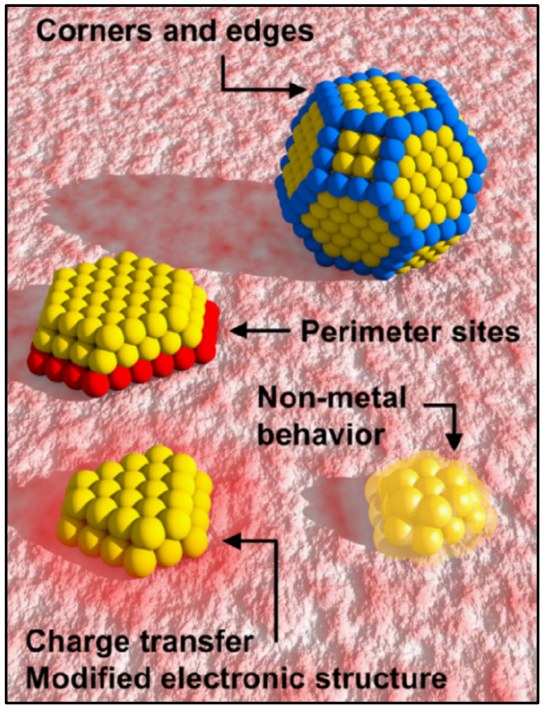

*Figure 1-I: Different phenomena involved in the unusual reactivity of supported metal nanoparticle catalysts. Reprinted with permission from B. Roldan Cuenya and F. Behafarid, Surf. Sci. Rep., 2015, **70**, 135–187. Copyright 2015 American Chemical Society.*[48]

Away from the more niche developments in the synthesis of catalytic nanoparticles and their hosts, four main categories can be considered: typical inorganic hosts, microporous inorganic materials and fundamentally organic supports (metal-organic frameworks (MOFs) and polymer assemblies). Among these support systems, special attention should be paid to the nanoparticle perimeter sites, the atoms at the particle-support interface. While the majority of such sites are typically buried beneath the nanoparticles themselves they are also subject to the greatest nanoparticle-support influences and thus, in many cases are hypothesised to carry out the majority of the catalysis. They possess superior reactivity as a result of these effects.[48] One well studied system would be Au/TiO_2 where the critical role of perimeter sites has been shown both experimentally and theoretically for a range of oxidation reactions: CO oxidation,[57] H_2 oxidation[58] and methanol oxidation.[59] Other examples include the water gas shift (WGS) reaction over Pt/Mo_2C[60] and propylene epoxidation to propylene oxide over Ag/Al_2O_3 catalysts.[61] The authors showed that the reaction energy profiles for two of the O_2 dissociation pathways differed significantly at two distinct sites. Namely the energy barrier for O_2 dissociation at the nanoparticle-support interface was significantly lower (0.16 eV) as compared to that for O_2 dissociation at the top most face of the nanoparticle (0.46 eV).[62]

In many cases perimeter sites display enhanced reactivity due to charge transfer that can facilitate particular reaction steps with high activation energies. Alternatively they can simply provide sites at which reactants can form bonds with both atoms within the nanoparticle and the support. Another possibility, one particularly prominent in metal oxide supports, is the use of lattice oxygen (present within the support) directly within the reaction itself. This is observed in a range of metal oxide supported Au, Pt, Pd and Ni nanoparticles for the oxidation of CO.[48,57]

Another relevant nanoparticle-support interaction that particularly applies to metal oxide supports is the spillover phenomenon as depicted in Figure 1-m. This effect generally leads to compromised catalytic activity due to the strong metal-support interactions (SMSIs) resulting in the support spillover (often under reducing environments) leading to the encapsulation of the nanoparticle by a thin film of the support species (or similar), blocking the catalytically active sites of the nanoparticle.[48] These damaging support spillover effects have been observed for a number of systems: Rh/TiO_2,[63] Pd/TiO_2,[64,65] Pt/Fe_3O_4[66] and Pt/TiO_2.[67,68] While the detrimental impact of support spillover and SMSIs is well documented it has also been employed to overcome the often poor nanoparticle stability upon traditional metal oxide supports. Establishing SMSIs helps prevent agglomeration and sintering at high reaction temperatures for many metal oxide supports as the overgrowth of a thin layer of the metal oxide around the nanoparticle leads to a decrease in the surface energy. This has been seen to have catalytic advantages while

also aiding the system stability as observed by Freund and Lewandowski *et al*.[69–74] It is shown that through the provision of alternative, lower energy reaction pathways the thin layer of FeO surrounding the Pt nanoparticles can impart significant catalytic advantages.

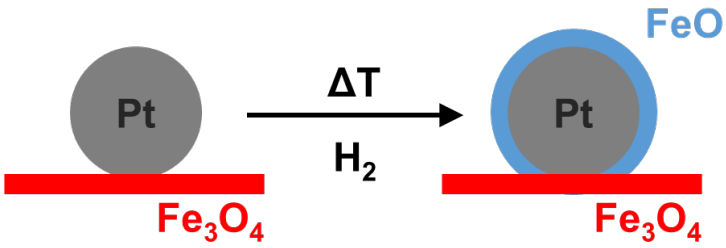

Figure 1-m: Strong metal – support interactions can lead to the encapsulation of the nanoparticle species.

Many alternative methods of achieving higher levels of nanoparticle stability upon metal oxide supports involve the addition of other species, either organic[38] or inorganic.[75] Three strategies have been adopted depending on the sequence of introducing the metal and the modifier/additive. A support can be pre-modified where-by the catalyst support is first treated by a modifier, and the metal is subsequently deposited upon the pre-modified support. Or it can be post-modified where the metal is loaded onto the support and a modifier is subsequently introduced. Alternatively the metal and an inorganic component are simultaneously deposited onto the support. Therefore, metal-support, metal-modifier, and modifier-support interfaces are all constructed. As a result, new active sites may be created, and the metallic nanoparticles may be stabilized at these relatively complex interfaces.[75] These additives are often other metal oxides due in part to their large compatibility with each other and their high levels of stability but also their ability to greatly influence catalytic activity on various applications.[76–79] For example, Dai and co-workers were able to deposit manganese oxide at the interface of gold nanoparticles and the silica support resulting in a catalytic enhancement towards the oxidation of CO.[80] While the addition of modifiers/additives frequently leads to catalytic enhancements, reports of stability improvements through these methods are much more limited, implying that this may in fact not be a viable route towards developing highly active and stable supported catalytic nanoparticle materials.

While the developments towards typical metal oxide systems are on-going much research is also underway exploring comparatively more complex support systems. One pivotal example is the use of organic polymers as a support medium. This enables the user to tailor the adhesion of the nanoparticles through electrostatics much more readily without the polymer having to completely cover the nanoparticle. These polymer assemblies can be fabricated through a variety of methods such as; template-assisted or pressure-

induced synthesis and layer-by-layer or evaporation-induced deposition.[34] For example layer-by-layer deposition involves the adsorption of a charged (often polymer) species onto a substrate, followed by washing and the adsorption of an oppositely charged species on top of the initial substituent. This constitutes a bilayer which will normally display a thickness in the nanometre range. This process of depositing oppositely charged species on top of each other is then continued in a cyclic fashion until the desired film thickness is achieved. At any point whether it be cyclically or just within the final few bilayers, one can deposit a solution of the ionic metal precursor which electrostatically binds to the polymer assembly and can then be chemically reduced to form accessible but anchored nanoparticles, Figure 1-n.[81,82]

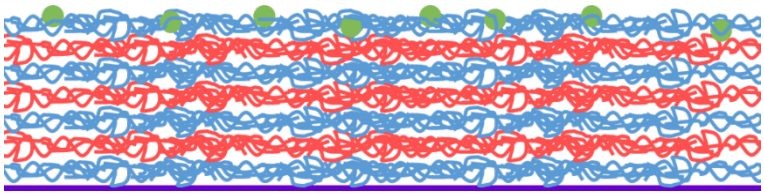

Figure 1-n: Depiction of a layer-by-layer assembly. Support surface shown in purple with anionic (blue) and cationic (red) polymer constituents built upon it forming the layered structure with a single nanoparticle (green) containing layer at the material surface.

Many polymer species are available to this method (see Figure 1-o) and as a result a high degree of control is available. For example the user can influence the stability, particle size, distribution, inter-particle distance and surrounding environment through the addition of other organic and inorganic components, providing tremendous catalytic potential for these systems.[34] The first incorporation of noble metallic nanoparticles within these assemblies was by Decher *et al*.[83] and now after just 20 years, they are widely studied for numerous applications, including catalysis.[30,34,38,82]

A recent review by Liu *et al.*[38] highlights the use of these polymer supported systems towards the catalytic reduction of a number of dyes and waste water pollutants such as 4-nitro phenol and methylene blue. While they present detailed discussions on these systems, the catalytic comparisons highlight one key aspect with regards to the use of such supports: low operating temperatures. None of the catalytic applications are carried out above 60 °C and due to the organic nature of these systems they suffer from poor thermal stability, a significant issue if one desires to generate feasible oxidation catalysts for industrial applications.

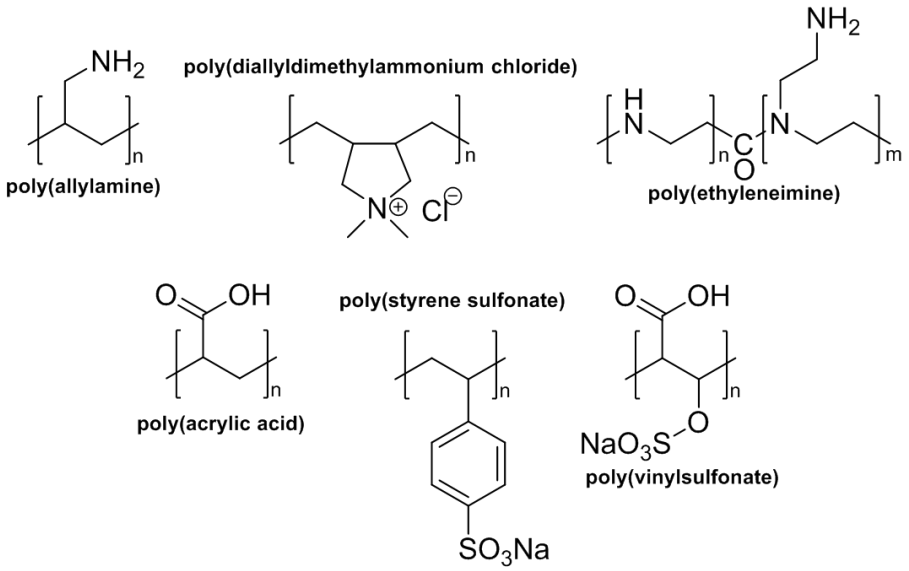

Figure 1-o: Some common polyelectrolytes used with polyelectrolyte multilayer assemblies: cationic; poly(allylamine), poly(diallyldimethylammonium chloride), poly(ethyleneimine) and anionic; poly(acrylic acid) poly(styrene sulfonate) and poly(vinyl sulfonate).

Utilizing microporous framework materials is another way to improve on the catalytic selectivity and the stability of the nanoparticles. The benefits of utilizing micro and mesoporous materials for catalytic applications has been well document by Raja and Thomas *et al.* [12,84–86] describing the intuitive use of the porous network to influence substrate access to the active site and the confinement of reactions within framework materials imparting particular desired transition state and product selectivities. These attributes coupled with the confinement or 'encapsulation' of the nanoparticles within a porous network, limiting migration, leaching and preventing aggregation while also limiting the access of potential catalyst poisons could lead to a highly active and robust catalytic nanoparticle material.[87]

Encapsulation can be achieved via two methods, either the growth of nanoparticles within a preformed porous material or the formation of the porous material around the preformed nanoparticles.[88] One common example of this is the use of MOFs in heterogeneous catalysis. A MOF is a porous crystalline material in which the lattice contains metal ions or metal clusters held by rigid, normally aromatic, bi- or multipodal organic linkers.[89] The use of MOFs within heterogeneous catalysis is a rapidly expanding area of research where many hope to be able to couple the catalytic activity of a range of active species including nanoparticles with the inherent tunability of the MOF systems. An illustration of a gold nanoparticle encapsulated within a ZIF-8 framework is depicted in Figure 1-p. MOFs possess a range of potentially catalytic species within themselves as both the organic linkers and metallic nodes have demonstrated catalytic activities, hence the significant

interest.[47,89,90] These attributes stem from the inherent ability to incorporate multiple active sites within the same material in order to achieve true support-catalyst synergies. For example if you were to encapsulate a metallic nanoparticle within a MOF structure and employ basic linkers then you would remove the need to add a base separately which is a common issue for many C-C coupling reactions.[17] Similarly acidic sites can be generated as well as other more complex active centres and these easily tunable properties have led to MOFs becoming widely used for many multi-step processes, often as tandem catalysts, a catalyst capable of catalysing two separate reactions within the same system. While this is true their organic nature again, often results in poor thermal stability by comparison with truly inorganic framework materials.

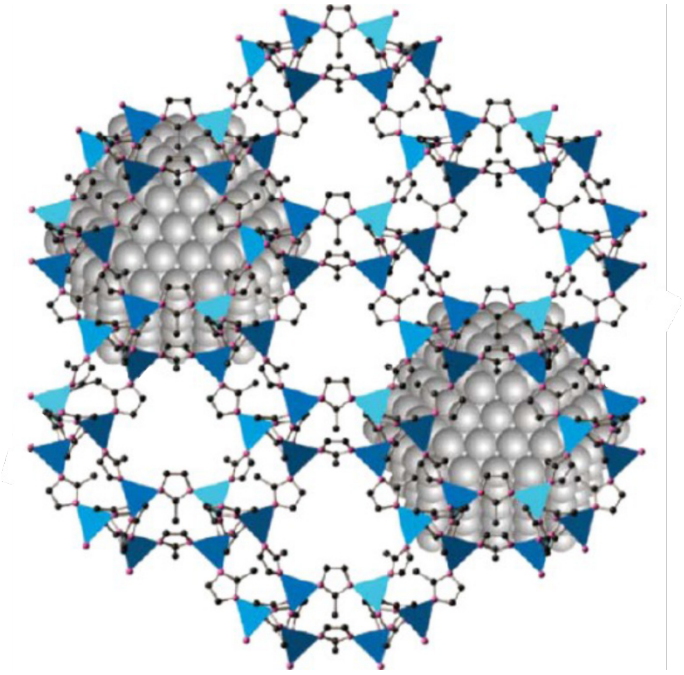

*Figure 1-p: Illustration of a gold nanoparticle encapsulated within a ZIF-8 framework.[91] Reprinted with permission from D. Esken, S. Turner, O. I. Lebedev, G. Van Tendeloo and R. A. Fischer, Chem. Mater., 2010, **22**, 6393–6401 Copyright 2010 American Chemical Society.*

Evidently thermal stability is a significant issue for many systems. The enhanced tunability offered by the incorporation of organic moieties into catalytic nanoparticle materials appears to inevitably lead to poor thermal stability. One way to circumvent this is to employ a purely inorganic support system. One such example would be the use of zeolites and zeotype materials as nanoparticle hosts. Their industrial applicability has already been demonstrated as zeolites are widely used within the petrochemical industry frequently for high temperature applications.[92] The wide range of zeolite structures available allow the user to select the appropriate porous structure for the desired encapsulated species and reactants. With many porous inorganic materials able to

demonstrate a degree of tunability, including zeolites, the unison of microporous inorganic framework materials as nanoparticle hosts could in fact be a viable system for high temperature oxidation catalysis. Although the incorporation of multiple active centres within these host materials is less common, the generation of bifunctional materials is readily available. For example, the use of zeolites as solid acid or basic supports coupled with an encapsulated active species. This has facilitated their use in many reactions as host materials[93–96] as well as nanoparticle hosts.[17,97,98] The ion exchange capabilities of zeolites which facilitates their tuneable acidity/basicity makes them viable candidates for the generation of metal nanoparticles *in situ*, within their porous architectures. The ion exchange allows the facile incorporation of precursor metal ions which can be easily reduced to produce active, isolated nanoparticle species. This has been successfully demonstrated by Talebi and co-workers who generated silver nanoparticles within zeolite-Y using this method.[99]

Further to zeolites, other porous inorganic structures are frequently used. Porous silica is a common nanoparticle support in a variety of forms. Examples can be found of a whole host of nanoparticle systems supported on porous silica for oxidation reactions including iron and gold nanoparticles supported on MCM-41[100] and faujasite[101] as well as platinum[102] and palladium[103] on mesoporous silica. Another common example and one which can offer facile ion exchange properties, is the use of layered-double-hydroxide structures such as hydrotalcite.[104,105] The use of such structures with notable properties such as ion exchange capabilities is of significant catalytic interest as it is these material properties that can facilitate the fabrication of hybrid catalytic materials. Therefore allowing the exploitation of true support-nanoparticle synergies without the stability burden of incorporating organic moieties within the catalysts structure.

1.2.4 The Significance & Control over Nanoparticle Size & Shape

Much of the discussion thus far has focused on the nanoparticle preparation techniques, support influences and overall stability of the nanoparticle-host system. One fundamental aspect of nanoparticle systems that has only been eluded to in Sections 1.2.1 and 1.2.2 is the impact and required control over the nanoparticles' morphology, its size and shape. Following the discussions in Section 1.2.1 which outline the inverse (1/r) relationship of the atomic surface to bulk ratio whereby, decreasing the nanoparticle size (given a similar shape) increases the percentage of atoms on the nanoparticles surface, this relationship is shown in more detail in Figure 1-q. This has significant impacts from a catalytic perspective, especially when dealing with noble metal species, given the added economic incentives. Increasing the percentage of the metal volume available for reaction, at a consistent loading will logically lead to an increase in TOF and this is observed in many

catalytic systems.[19,45–48] Further to this, by reducing the nanoparticle size one is also increasing the percentage of under coordinated, highly active catalytic sites due to their frequently more favourable binding energies and these two effects in conjunction are termed the 'size-effect' within nanoparticle catalysis.[48]

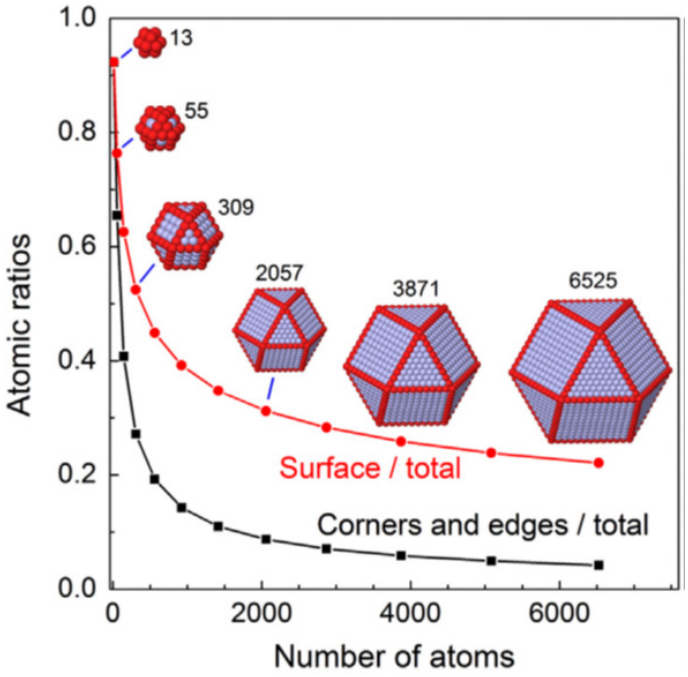

*Figure 1-q: The ratios of the surface atoms to the total number of atoms (red) and the atoms at corner and edge sites to the total number of atoms (black) for FCC cuboctahedron nanoparticles. Reprinted with permission from B. Roldan Cuenya and F. Behafarid, Surf. Sci. Rep., 2015, **70**, 135–187. Copyright 2015 American Chemical Society.*[48]

For most face centred cubic (FCC) metals such as: Cu, Ag, Au, Pd and Pt the lowest energy facets are the (111), (100) and (110) in order of increasing surface energy.[48] Thus it is most common to observe the (111) and (100) as the exposed facets upon the nanoparticle surfaces of these particular metals. While this is predominantly the case other factors do influence the energetically preferred morphology and these generally become more significant as the nanoparticle size decreases. For example the ratio of under coordinated (corner and edge) sites can greatly alter the total surface energy as can surface reconstruction and lattice strain as well as adsorbate species.[48] For FCC systems such as Au and Pt the coordination numbers (CNs) of surface atoms within (111) and (100) facets are 9 and 8 respectively as opposed to bulk atom CNs of 12. The CNs can drop as low as 4-7 at edge and corner sites of FCC nanoparticles and the dramatic increase in the volume of these under coordinated sites occurs at nanoparticle sizes approx. <700 atoms, as per Figure 1-q, corresponding to nanoparticle diameters of approx. 2-3 nm.[48,106,107]

Adsorption of species to these low coordination sites often results from their structure extending outside the metal lattice and into the surrounding environment, facilitating their contribution towards adsorbate binding.[108] This preferential adsorbate binding has been observed in CO binding to stepped Au facets as opposed to smooth Au (111) surfaces.[109,110] In fact the correlation between catalytic activity and the number of exposed low coordination sites on small nanoparticles is now particularly well established for the oxidation of CO over Au/TiO_2 nanoparticles.[111,112] This phenomena of increased activity with smaller nanoparticle sizes although well documented, is intrinsically linked to the more favourable binding of adsorbates to these low coordination atoms. For example contrasting observations with Pt nanoparticles can be explained through these means. Mostafa *et al.*[49] observed the direct relationship between the average CNs of surface atoms against the catalytic onset temperature of propan-2-ol oxidation over Pt/Al_2O_3 systems i.e. the lower the average CN the lower the catalytic onset temperature, analogous to many of the other systems discussed thus far. However, Mistry *et al.*[113] observed the opposite trend for the oxidation of butan-2-ol over Pt/Al_2O_3 catalysts and this was found to be due to oxygen poisoning that occurs more readily at the low coordination sites as a result of the higher binding energies towards oxygen of those atoms. Therefore, when considering nanoparticle size-effects, one must consider the complete picture. One whereby a line must be trodden between the increased catalytic activity on offer from encouraged adsorbate binding but whilst being aware of the potential for catalyst poisoning from the irreversible binding of such species.

When discussing nanoparticle morphology, in conjunction with size and exposed facets the specific nanoparticle shape can play a significant role in the final catalytic performance. Given the diversity within nanoparticle research the range of shapes reported is vast, ranging from typical cubic, octahedral, spherical particles to truncated polyhedra, nanoplates and flat particles as well as hollow structures.[48] Controlled fabrication of such distinct shapes would allow the catalytic chemist an even greater degree of control over the catalyst-substrate interface. Therefore, observing these complex structures and drawing the appropriate structure-property correlations will facilitate a greater understanding of their catalytic activity. In fact, it has also been shown in Section 1.2.1 that deviations in catalytic activity, namely selectivity, can be achieved through the control over the exposed facet and nanoparticle shape. Bratlie *et al.*[54] demonstrated that the nature of the exposed facet delivers control over the product distribution within the Pt catalysed hydrogenation of benzene. Also, due to the intrinsic relationship between the exposed facet and resulting nanoparticle shape, these same deviations can be shown to be a result of the contrasting cubic and cuboctahedral morphologies.

Given the rapid nature of the nucleation process within nanoparticle formation control over the final particle shape often relies on slower degrees of growth. With rapid growth being detrimental to isotopic growth patterns, it is imperative to produce systems that can grow uniformly to produce a particular facet upon the particle surface or a particular shape. Another way to do this would be to prohibit the growth of a particular facet and consequently produce a dominant exposed facet. Control over the exposed facet often leads to control over the resulting nanoparticle shape. For example, a capping agent that preferentially binds to the Pt (111) or (100) plane could produce cubic or octahedral particle morphologies depending on the preferred facet inhibited,[48,114] as per Figure 1-r. Another similar example is shown by Ahmadi and co-workers where controlled reduction of the Pt^{II} precursor was found to occur preferentially upon the Pt (111) facet producing cubic particles via the same pathway as that depicted in Figure 1-r. Alternatively if the Pt (111) facet was capped by an appropriate capping agent, sodium polyacrylate in this case, then smaller tetrahedral particles are formed.[115,116]

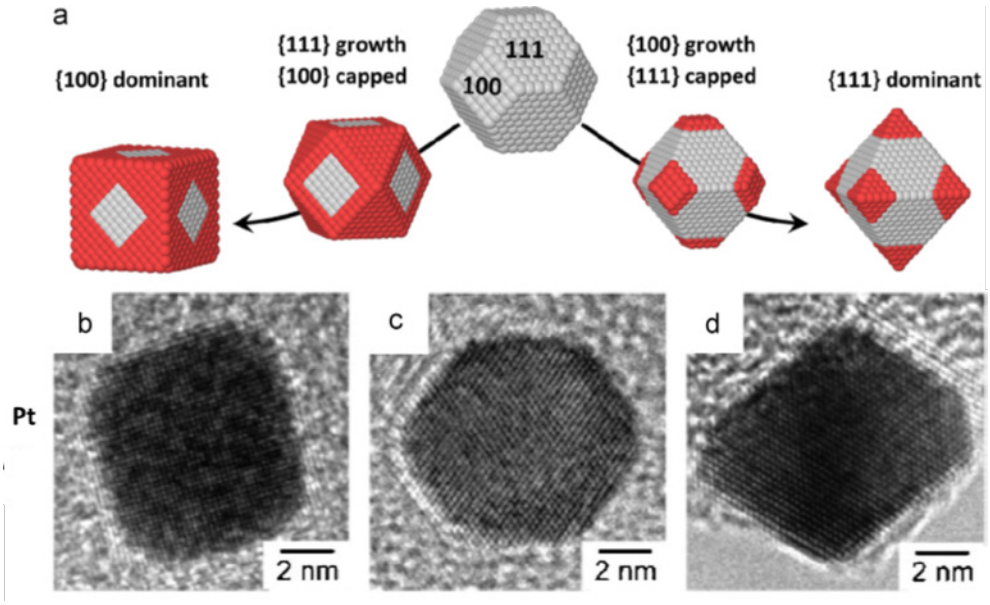

Figure 1-r: (a) Model shapes illustrating the anisotropic growth from a truncated cuboctahedron nanoparticle. Hindering the (111) facet growth leads to growth in the (100) facets until they disappear, leaving predominantly (111) facets, right. The opposite effect results in cubic nanoparticles with only (100) facets, left. Example of shape-selected Pt nanoparticles (b–d).[48,114]

In addition to controlled nanoparticle growth by the use of capping agents, the crystalline nature of the support species can be used to generate an epitaxial relationship towards the generated nanoparticles. For example, the controlled formation of Pt nanoparticles upon various strontium titanate facets, namely the (100), (111) and (110) lead to varying ratios of exposed Pt facet ((111) to (100)) and consequently different nanoparticle

shapes.[52,117] Further, nanoparticle shape can be influenced by doping of the support material. Schauermann *et al.*[118] has presented a review on the subject within which they compare the distinctly different nanoparticle shapes that can be generated through simple doping of metal oxide supports with both high and low valence transition metals.

While one might desire to form highly faceted, small nanoparticles of controlled shapes, the reality is that the stability of such species does not always facilitate the goal. This is often a problem when designing catalytic species that need to be adapted to operate at high temperatures and sometimes pressures. For example, Figure 1-s demonstrates the change in silica supported Pt nanoparticles towards a predominantly spherical shape and the loss of (111) facets and tetrahedral morphology after high temperature treatments. It is also noteworthy that this transition occurs without significant particle size deviation.[119]

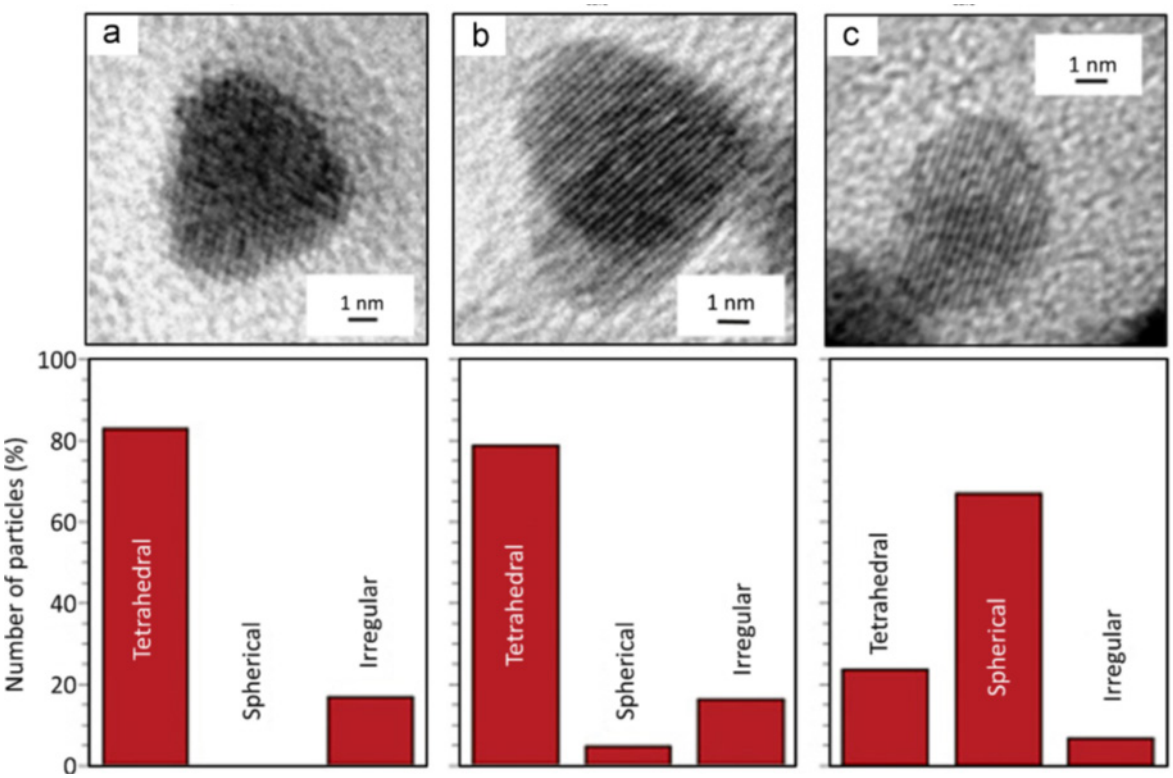

*Figure 1-s: TEM images of Pt nanoparticles immediately after growth in colloidal solutions (a), and after their dispersion on a silica xerogel support and calcination at 202 °C (b), and 302 °C (c). Reprinted with permission from B. Roldan Cuenya and F. Behafarid, Surf. Sci. Rep., 2015, **70**, 135–187. Copyright 2015 American Chemical Society.*[48,119]

Given the discussions above surrounding nanoparticle morphology, it is clear that the relationship between nanoparticle morphology and the ensuing catalytic characteristics is complicated to say the least. Therefore, it is useful to divide nanoparticle catalysed reactions into two categories: structure-sensitive and structure-insensitive.[120] The structure-sensitivity depends on both the nanoparticle material/support and the reaction itself. For example, Pt catalysed reactions such as alcohol oxidations,[49,113,120,121]

benzene[54,122] and pyrrole[123,124] hydrogenation, cyclohexene dehydrogenation[125,126] as well as other oxidations[127,128] have all been shown to be structure sensitive. Whereas, the WGS reaction[129] and hydrogenation of ethylene[130] have been shown to be structure-insensitive over similar Pt nanoparticle catalysts. The reason for some systems to appear structure-insensitive is often unknown, although some suggest that it could be due to surface poisoning, which that would alter surface compositions and obstruct binding sites. Another alternative is that the rate determining step only involves binding to one surface atom and thus is independent of the surrounding environment.[48] Nonetheless, these discussions have demonstrated that a vast number of reactions are structure-sensitive whether, it be due to positive size-effects where smaller nanoparticle produce improved catalytic performances or due to negative size-effects whereby the opposite trend is observed. Clearly control over the nanoparticle morphology is a significant aspect when designing nanoparticle catalysts.

1.2.5 Heterogeneous Noble Metal Nanoparticles for Sustainable Oxidation Reactions

As described earlier in Section 1.1.4, oxidation reactions are of significant global interest and the need to make continual developments in their sustainability: waste reduction, removal of solvents and harmful reactants/by-products as well as their overall effectiveness: activity and selectivity is of paramount importance. Clearly the ideal situation would be one where all harmful components are removed and the desired oxidation processes proceed through the use of a solid catalyst, environmentally benign oxidants and in a solvent free manner. Therefore, it is not surprising that the propensity shown by nanoparticle systems to activate the otherwise unreactive molecular oxygen as well as many peroxides, has facilitated their application within this area of research. This wide spread application of nanoparticle catalysts within many oxidation processes is demonstrated in Table 1-e and Table 1-f which display the heterogeneous nanoparticle catalysts employed for the oxidation of some common alcohol and hydrocarbon compounds. While these tables are not extensive, they do highlight the significant interest from the research community towards employing nanoparticle catalysts within these processes.

Table 1-e and Table 1-f focus solely on monometallic gold, platinum and palladium catalysts as these are the most relevant systems to the work contained within this thesis. While research into the development of bimetallic nanoparticle catalysts and the catalytic synergies that can be attained is of great interest, these materials will be covered in more detail in Chapters 4, 5 and 7. That being said, the desire to employ molecular oxygen for these applications is evident from the sheer number of examples by comparison to the

peroxide systems. This signifies the industry's desire to move away from synthetic oxidants and employ the most sustainable oxidant available – molecular oxygen. Also, the range of support-nanoparticle combinations highlight the need to fully understand the synergies between the two and in turn fully understand the mechanism of action to critically develop the most active catalytic system.

Within the broad spectrum of oxidation reactions available for the potential application of nanoparticle catalysts, two stand out in the current research literature as clear areas of desired application. One of which is the oxidation of alcohol substrates, Table 1-e. A common problem with the oxidation of alcohols is their over-oxidation to the acid product. This has in fact been a key incentive to employ nanoparticle catalysts as they have shown to be highly effective as aldehyde/ketone selective catalysts in an area where historically, catalysts have displayed poor activities and selectivities.[28] While the array of notable alcohol substrates is vast, ethanol, octanol, glycerol, 5-hydroxymethylfurfural (HMF) and glucose to name a few. The examples shown in table Table 1-e are some key compounds of interest and ones which are frequently used to test a catalysts activity towards such processes.[28,121,131]

Benzylic alcohols are important functional groups found in many pharmaceutical and fine-chemical intermediates. Many of the resulting aromatic aldehydes are used heavily in the fragrance and flavouring industries. Benzyl alcohol, being the simplest of this class, is oxidised to benzaldehyde which has a wide range of applications. These include being used as an almond flavouring and odorant, as precursors for plastic additives, photographic chemicals and dyes. It is also useful as an intermediate towards a number of other useful compounds such as: benzoin, benzylamine and mandelic acid, including pharmaceutical compounds such as; chloramphenicol, ephedrine and ampicillin.[132,133] Vanillin, the aldehyde product formed by the oxidation of vanillyl alcohol, is one of the most highly produced synthetic flavouring and fragrance chemicals in the world. Original production from natural extraction has all but stopped and now makes up only 0.1% of the total global vanillin production. Therefore, there is a clear incentive to develop new processes to produce synthetic vanillin in order to maintain production in a sustainable manor.[134,135] Not only is vanillin extensively used in as fragrance and flavouring agent but it is also employed, similarly to benzaldehyde, as a pharmaceutical intermediate, in the syntheses of L-3,4-dihydroxy-phenylalanine (L-DOPA), Methyldopa and Papaverine.[135] Similarly, cinnamaldehyde is a widely used odorant and flavouring. While cyclohexanol is not a benzylic alcohol, it's ketone product cyclohexanone is a key intermediate in the synthesis of both nylon 6 and nylon 6,6, some of the most widely produced plastics in the world. The production of these will be detailed in significantly more detail in Section 1.3.

Substrate	Structure	Oxidant	Catalyst
Benzyl Alcohol	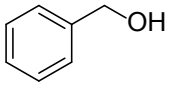	O_2	Au/C,[136–140] Au/Ca-ZSM-5,[97] Au/Hydrotalcite,[104] Au/Al_2O_3,[141] Au/BaO,[141] Au/CaO,[141] Au/CeO_2,[142] Au/Co_3O_4,[143] Au/CuO,[141] Au/Fe_2O_3,[141] Au/MgO,[143,144] Au/MnO_2,[141] Au/NiO,[141] Au/SiO_2,[137,143,145,146] Au/TiO_2,[143,147] Au/ZnO,[141,143] Pd/C,[136,138,139,148,149] Pd/Ca-ZSM-5,[97] Pd/SBA-15,[150] Pd/SBA-16,[103] Pd/Hydroxyapatite,[148] Pd/Al_2O_3,[148] Pd/CeO_2,[150] Pd/SiO_2,[148] Pd/TiO_2,[147] Pt/C,[136,139,149,151] Pt/Ca-ZSM-5,[97] Pt/Mg-ZSM-5,[97] Pd/SBA-15,[150] Pt/CaO,[97] Pt/MgO,[97]Pt/SiO_2[97,102]
		TBHP	Au/Al_2O_3,[152] Au/BaO,[152] Au/CaO[152]
		H_2O_2	Au/TiO_2[153–155]
Cyclohexanol	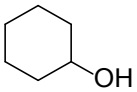	O_2	Au/Hydrotalcite,[104] Au/EP-FDU-12,[101] Pd/SBA-16,[103] Pd/CeO_2,[150] Pt/C,[156] Pt/Ca-ZSM-5,[97] Pt/Mg-ZSM-5,[97] Pt/BaO,[157] Pt/CaO,[157] Pt/SiO_2,[97,102] Pt/MgO[157]
		TBHP	-
		H_2O_2	Au/TiO_2[153]
Vanillyl Alcohol	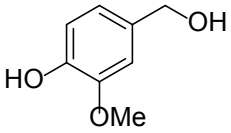	O_2	Au/CeO_2,[158] Pd/SiO_2,[159] Pd/TiO_2,[159] Pt/C,[159] Pt/MOF-5,[160] Pt/MgO,[159] Pt/SiO_2,[159] Pt/TiO_2[160]
		TBHP	-
		H_2O_2	-
Cinnamyl Alcohol	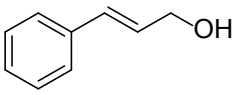	O_2	Au/Hydrotalcite,[104] Au/C,[139] Au/CeO_2,[158] Au/SiO_2,[145] Pd/C,[139,148] Pd/Hydroxyapatite,[148] Pd/Al_2O_3,[148] Pd/SiO_2,[148] Pt/C[139]
		TBHP	-
		H_2O_2	Au/TiO_2[153]

Table 1-e: Summary of heterogeneous noble metal nanoparticle catalysts for the oxidation of some common alcohol substrates utilizing molecular oxygen, TBHP and hydrogen peroxide as oxidants.

Industrial production of benzaldehyde either requires the hydrolysis of benzyl chloride or the oxidation of toluene. Use of benzyl chloride inevitably produces hazardous chlorinated waste and thus is not an environmentally friendly approach. The oxidation process is more environmentally benign. However, it has to be carried out at low conversions (10-20 %) in order to avoid over-oxidation to benzoic acid, a frequent issue with these compounds that was eluded to earlier. Thus these low conversions result high volumes of waste by-products and solvents.[132,133] The industrial production of vanillin on the other hand starts with guaiacol and although it employs nanoparticle catalysts, they require promoters such

as cadmium and bismuth which even then do not achieve high selectivities, resulting in significant volumes of waste being generated.[134,135] Similarly, the production of cinnamaldehyde is carried out by aldol condensation reactions requiring basic catalysts with basic conditions that again produce many organic by-products and large volumes of waste. Therefore, there is significant scope for development of not just these synthetic protocols but those of many other alcohol to ketone/aldehyde transformations. This is an area in which heterogeneous nanoparticle catalysts are beginning to show their significance.

Another such area is the activation of C-H bonds and the oxidation of hydrocarbon substrates. The lack of functional groups on these substrates, such as benzene, toluene or cyclohexane makes them especially difficult to oxidise selectively. These reactions require harsh conditions in order to introduce any functionality and such conditions make doing so selectivity, very difficult.[161] Activation of these compounds leads to the production of a vast array of commodity chemicals including those described above and thus there is an ever present precedence to find new, single-step, economical and sustainable ways to activate these compounds.[162]

Substrate	Structure	Oxidant	Catalyst
Benzene		O_2	Au/Al_2O_3,[163] Au/MgO,[163] Au/ZnO,[163] Pt/Al_2O_3[164]
		TBHP	-
		H_2O_2	-
Cyclohexane		O_2	Au/C,[165,166] Au/Cr-MIL-101,[167] Au/Hydroxyapatite,[166] Au/Ca-ZSM-5,[168] Au/SBA-15,[169] Au/MCM-41,[167] Au/Al_2O_3,[170] Au/CaO,[170] Au/Fe_2O_3,[167] Au/MgO,[170] Au/TiO_2,[170] Au/ZrO_2[170]
		TBHP	-
		H_2O_2	Au/C[165]
Toluene	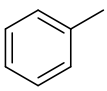	O_2	Au/C,[171] Au/Al_2O_3,[163] Au/MgO,[163] Au/ZnO,[163] Pd/C,[171] Pt/SBA-15,[172] Pt/Al_2O_3,[164,173] Pt/SiO_2[172]
		TBHP	Au/TiO_2,[174] Pd/TiO_2[174]
		H_2O_2	-

Table 1-f: Summary of heterogeneous noble metal nanoparticle catalysts for the oxidation of some common hydrocarbon substrates utilizing molecular oxygen, TBHP and hydrogen peroxide as oxidants.

1.3 The Significance & Industrial Production of KA Oil & Cyclohexanone

Since the commercial process for nylon 6,6 production was implemented in 1939, polyamide resins have become of huge interest for the plastics industry. Cyclohexanone is therefore a vital commodity chemical within the industry as it is used in the production of both adipic acid via oxidation (Scheme 1-e) and ε-caprolactam via oximation followed by the Beckmann rearrangement. Both are essential precursors in the industrial manufacture of nylon 6,6 and nylon 6 respectively.[175–178] There are three primary industrial routes towards synthesizing a cyclohexanone product (detailed below) and these have their associated advantages and disadvantages depending on the requirements of the ensuing process for which the cyclohexanone product is to supply. This is due to the optimum feedstock purity and/or alcohol to ketone ratios for either adipic acid or ε-caprolactam production. For adipic acid production a mixture of cyclohexanone and cyclohexanol (Ketone-Alcohol or KA oil) is desired as opposed to the very high purity cyclohexanone product that is required for the production of ε-caprolactam. In fact, all current industrial methods for ε-caprolactam production utilize a pure cyclohexanone feedstock.[178,179] The high quality of the cyclohexanone product required is a result of its position in the early stages of the process towards the synthesis of nylon 6. Impurities in the initial feedstock would be detrimental to the caprolactam polymerization as well as affecting the final properties of the polyamide, such as its colouration and ageing resistance.[180] As a result, it is vital to continuously develop new, increasingly environmentally begin synthetic approaches for the production of high purity cyclohexanone. A review of the existing industrial methods of producing cyclohexanone is given below. These include: phenol hydrogenation, cyclohexane oxidation, cyclohexanol dehydrogenation and the potential oxidation of cyclohexanol as an alternative to these established practices.

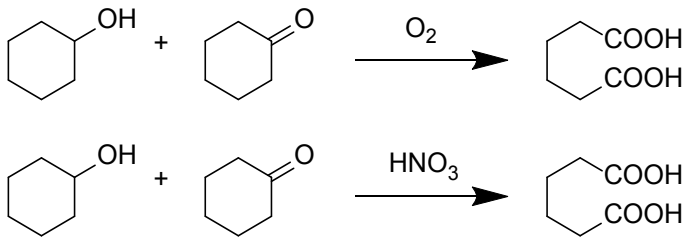

Scheme 1-e: Oxidation of KA oil to adipic acid either via molecular oxygen or nitric acid. Both reactions are generally carried out in the liquid phase, molecular oxygen oxidations utilize cobalt or manganese catalysts at 80 – 85 °C and 6 bar, while nitric acid reactions employ vanadium oxide or copper catalysts at 60 – 80 °C and > 2 bar.[27]

1.3.1 The Selective Hydrogenation of Phenol

The hydrogenation of phenol (Scheme 1-f) is a well-studied and efficient system in both the liquid and vapour phases. The reaction itself is versatile possessing the ability to produce either pure cyclohexanol or pure cyclohexanone products as well as KA oil solutions of various ratios merely by carefully selecting the appropriate catalyst. For KA oil mixtures or pure cyclohexanol supported nickel, copper, cobalt and manganese oxides are used with nickel being the most common. These catalysts are able to achieve yields of up to 98% in both the liquid and vapour phases. For the selective production of a cyclohexanone product palladium, platinum, iridium, ruthenium and osmium catalysts are utilized, with palladium proving to be the most effective.[175,176,181]

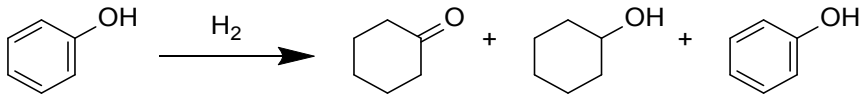

Scheme 1-f: The hydrogenation of phenol can be engineered to produce KA oil, pure cyclohexanol or pure cyclohexanone although, despite a pure product being desired this reaction often leads to small impurity mixtures of the three compounds shown. A problem of great industrial interest due to the azeotropic nature of phenol-cyclohexanol and phenol-cyclohexanone mixtures.

The hydrogenation of phenol to cyclohexanone is almost exclusively carried out with palladium nanoparticle (≤5 nm) catalysts upon either carbon or alumina supports, utilized in either a batch or continuous flow set-up. Due to the expense of metallic Pd these small nanoparticle sizes are significant but they also play a key role in maximising activity, as discussed in Section 1.2.4. The economical draw-backs of industrial batch processes are well known as catalyst recovery by filtration and subsequent distillation is not merely expensive but hazardous, due to the handling of highly combustible and potentially auto-flammable materials. In addition the catalytic lifetime within batch processes is often limited compared to continuous flow systems.[181] This reaction is carried out in both the vapour and liquid phases but despite the liquid phase process possessing certain safety benefits (carried out below the boiling point of the reaction components) and often higher selectivities, the hydrogenation of phenol is more commonly operated within the vapour phase at approx. 150 – 200 °C due to the resulting higher levels of conversion.[175,176,182,183]

Despite the hydrogenation of phenol being a well-established industrial technology, it does suffer from two significant difficulties: catalyst susceptibility towards impurities and the production of phenol-cyclohexanol and phenol-cyclohexanone mixtures. The palladium catalysts employed are known to be particularly vulnerable towards nitrogen, sulphur and mercury poisoning, as well as carbon monoxide generators such as formic or oxalic acids.

These lead to significant decreases in selectivity and catalyst lifetime and should be kept below 10 ppm in order to maintain the productivity of the catalyst.[182] Nonetheless, the palladium catalysts commonly incur 'induction' or 'run in' periods where the selectivity towards cyclohexanone is significantly lower than desired. This is due to cyclohexanone existing as an intermediate between phenol and, the final hydrogenation product, cyclohexanol.[181] Upon initial use of the catalyst, this intermediate nature causes some complications with the presence of 'hyper active' sites within the catalyst producing large quantities of undesired cyclohexanol. As eluded to in the previous paragraph, the small nature of these nanoparticles leads to a high volume of highly active, under coordinated surface sites. These sites display extremely high levels of activity which lead to over reduction to the cyclohexanol product. With Pd nanoparticle catalysts known to be responsive to a number of influential species, from subsurface carbon species, poisons or adsorbates, it is thought that in these early stages of the reaction deactivation through irreversible CO binding to these 'hyper active' sites is required in order to limit their reactivity and sufficiently increase the selectivity towards cyclohexanone.[118,182] Thus, it is clear that there is an intricate balance in play with the proportion of deactivating impurities present in order to achieve the cyclohexanone selectivity required.

One way the industry has been able to extend the lifetime of these catalysts is with the addition of small amounts of alkali or alkaline earth metal oxide additives[182–184] or basic promoters.[185] Although the current state of art has moved away from basic promoters such as sodium hydroxide or carbonate, there still exists a precedent for the inclusion of group one and two metal oxides in small quantities, typically 0.2 – 5 catalyst wt. %, in order to increase the overall activity of the catalyst.[183] The inclusion of these additives to the alumina support of the catalyst itself. However, increasing the catalytic lifetime of the material, decreases the mechanical stability of the catalyst. Hence, there must be a compromise in order to obtain the optimum catalytic system with these hybrid materials. In fact, a Japanese patent recently published by Matsuura *et al.*[183] in 2014 detailed the catalytic enhancements bestowed by adsorbing tertiary amine structures such as; trimethyl, triethyl and tri-isopropylamine (amongst others) onto the surface of the palladium nanoparticle catalyst. These catalysts are able to produce short term cyclohexanone yields of up to 95 – 96%, marking a significant development in the field.

Despite the complications with the catalysts employed and the advances made in catalyst development over the years, the most significant hurdle/undesirable expense remains the purification of cyclohexanol-phenol and cyclohexanone-phenol mixtures. It is well understood that these combinations form azeotropic mixtures leading to challenging and expensive purification methods being required. The azeotropic nature of these mixtures make separation by distillation, although still possible, much more challenging and

complex, thus, incurring additional expense. Although separation of phenol-cyclohexanone mixtures is possible by rectification, when additional homologues are present (which is often the case) this becomes even more challenging. This is because methods such as the addition of alkali metal hydroxides, which would be expected to hold the phenols back, cannot be used because the ketones are then susceptible to undergoing intermolecular condensation reactions.[186] In some cases, only a fraction of the cyclohexanone product is distilled away and the remaining mixture is either fed back into the initial phenol dehydrogenation or delivered, depending on the phenol content, to a separate assembly for the dehydrogenation of the remaining cyclohexanol, these processes are described in detail later.[182,183,186–188]

1.3.2 The Direct Oxidation of Cyclohexane

The oxidation of cyclohexane (Scheme 1-g) is not as widely employed by comparison to the hydrogenation of phenol, in part due to it being highly endothermic (ΔH = 65 kJmol^{-1}) thus requiring high temperatures to proceed.[189] That being said, it does possess the advantage of having no phenol in the reaction product, leading to easier isolation of the cyclohexanol and cyclohexanone products. The oxidation can be done with or without the use of a catalyst but both employ air as the oxidative species and generally produce KA oil mixtures. Catalytic reactions are seen to employ homogeneous organometallic cobalt and ruthenium complexes, namely 1:1 mixtures of ruthenium acetylacetonate and cobalt octylate, amongst others.[176,190] Both processes suffer from the production of unwanted by-products, primarily due to the production of the highly reactive cyclohexylhydroperoxide species that is generated upon reaction with oxygen and due to this, although the reaction can be done in both the liquid and vapour phases, the liquid phase is preferred and often operated at low conversions in order to minimize the production of unwanted by-products.[175,176] This is achieved with conversions < 10% facilitating a cyclohexanone selectivity of approx. 80%. Of the remaining 20%, 10-15% is cyclohexanol with the remainder being cyclohexylhydroperoxide and other impurities such as cyclopent-1-ene-1-carbaldehyde (Scheme 1-g).[176,180,190] In order to achieve the pure product, there have been a number of methods employed, two of the most common being either a further catalytic oxidation or a series of basic treatments. The catalytic purification is often carried out using zinc and magnesium oxide catalysts, although nickel and copper oxide are also utilized. These catalytically convert the KA oil solution, post distillation into the pure cyclohexanone product.[175,176,180] The alternative method of a basic treatment or distillation in basic media facilitates the saponification of esters and hydroperoxides to their respective alcohols and ketones, after which separation by distillation or crystallisation is easier.[175,180,190] Clearly these processes have subsequent costs associated with them, the

basic processes particularly, with the recovery of the metal hydroxides often employing effluents that then require incineration or disposal by other means.[180]

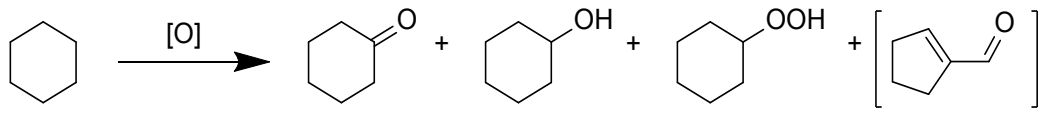

Scheme 1-g: The direct oxidation of cyclohexane generally produces KA oil mixtures and is also prone to producing additional side products. It is for this reason that it is nearly always run at very low conversions, e.g. < 10%.

Some impurities in particular can be particularly difficult to remove, cyclopent-1-ene-1-carbaldehyde, for example (see Scheme 1-g), is not only difficult to separate through distillation but also responds to a number of cyclohexanone qualification tests, particularly those commonly used for caprolactam feedstocks e.g. UV and oxidation tests.[180] Thus, for obvious reasons it is highly desirable to avoid the production of such impurities or, at the very least, only produce impurities that can be easily identified and removed.

1.3.3 Oxidative Dehydrogenation of Cyclohexanol

The dehydrogenation of cyclohexanol (Scheme 1-h) is largely considered one of the most sustainable routes to forming cyclohexanone as it can be done non-catalytically and the hydrogen produced can be easily recovered and used in other processes or sold separately. Un-catalysed methods require higher temperatures of > 400 °C, although they are able to produce cyclohexanone products that can be up to 98% pure.[176] Despite obtaining these high levels of purity, many catalysed routes are able to achieve equivalent purity levels with overall superior yields, at lower temperatures such as 100-350 °C, through employing nickel, copper and/or zinc catalysts.[176,186,191–193] The most effective of which, copper-chromium-barium mixed metal oxide catalysts, achieve impressive cyclohexanone yields of 94% at 325 °C.[191] Zinc-copper (9:1) alloy catalysts achieve yields of >90% at 300 °C.[186]

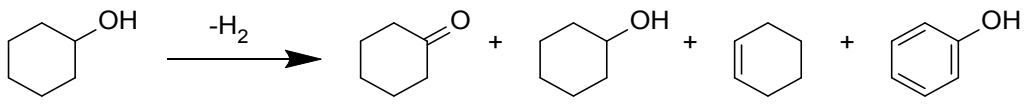

Scheme 1-h: The dehydrogenation of cyclohexanol is capable of producing cyclohexanone in very high yields of approx. 98% but still suffers from the presence of unwanted by-products such as cyclohexene and phenol.

In spite of the high yielding and sustainable dehydrogenation process, common impurities still persist and none are more significant than phenol. As discussed previously, phenol-cyclohexanone and phenol-cyclohexanol mixtures can be highly expensive to purify.

Although catalysed routes generally produce less phenol, catalytic dehydrogenations commonly suffer from the production of solid impurities which deposit onto the catalyst surface, decreasing the reaction yield, blocking catalytically active sites and deactivating the catalyst over time, leading towards the requirement to regenerate or replace the catalyst.[193] Therefore, it is a choice the industrial chemist must make, whether to opt for the more energy intensive process that produces a cyclohexanone product lased with phenol or to select the catalytic process within which the catalyst lifetime could pose a significant challenge.

1.3.4 The Aerobic Oxidation of Cyclohexanol

Despite the above mentioned disadvantages, it might be considered that the dehydrogenation of cyclohexanol would be the most appealing process for the production of cyclohexanone due to its ability to produce high yields via a highly atom economic process. However, although the aerobic oxidation of cyclohexanol (Scheme 1-i) can also be prone to producing some high boiling side products it does not produce phenol and can be employed to achieve very high yields. The oxidation of cyclohexanol also possesses a number of energetic advantages over dehydrogenation pathways. For example, as eluded to previously, unless the temperature is significantly elevated cyclohexanol conversion is limited. This is due to the thermodynamic equilibrium as the Gibbs free energy for the process is approx. zero at 227 °C. On top of this, the reaction is highly endothermic (H = 66.1 kJmol^{-1} at 227 °C) resulting in high operation costs and expensive shell and tube reactors being required.[177] This is in contrast to the oxidation of cyclohexanol where the Gibbs free energy much lower (G = -217.6 kJmol^{-1} at 227 °C) meaning the equilibrium conversion is increased and also the oxidation reaction is exothermic by contrast (H = -117.8 kJmol^{-1} at 227 °C) therefore, there is no need to supply large amounts of heat during the reaction saving on capital investment in the reactor.[177]

Despite there being a need to utilize low temperatures within the oxidation reaction, often due to catalyst stability, restricting conversions to below 70%, cyclohexanone selectivities of over 98% can still be achieved. This is done through the use of copper and zinc oxide catalysts, at modest temperatures of 180-270 °C, allowing a significant reduction in purification costs.[177] Also the lack of phenol within the reactor off stream allows the simple extraction of cyclohexanone through distillation and the remaining cyclohexanol can be simply re-supplied to the reactor inlet. Cobalt carbonate catalysts have also been employed in batch processes achieving cyclohexanone selectivities of approx. 92% with a 3 hr time period.[184]

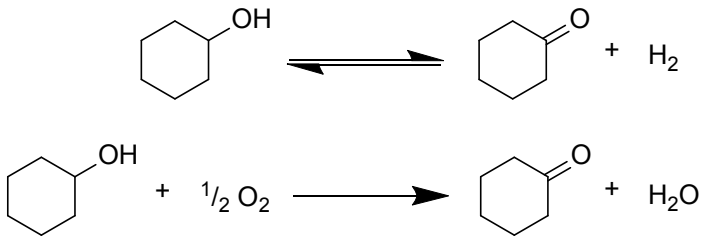

Scheme 1-i: The dehydrogenation of cyclohexanol and the aerobic oxidation of cyclohexanol to cyclohexanone.

Clearly the higher selectivities available to the industrial chemist through the oxidation process and the fact that the only significant by-product is water, are exceptionally appealing and largely out-weigh the drawbacks of the process. However, if these near 100% cyclohexanone selectivities can be coupled with higher cyclohexanol conversions, this would begin to further highlight the appeal of this process over more conventional hydrogenation and dehydrogenation protocols.

1.3.5 KA Oil as a Feedstock

With the chemical industry continually in transition in response to changing feedstock availability, the potential use of new feedstocks or better still, existing feedstocks for new processes is a welcome concept to increase the flexibility within the industry.[21] Hence the aerobic oxidation of the existing KA oil feedstock could be a viable alternative to the above processes. Coupling the advantages of the aerobic oxidation of cyclohexanol (high atom economy (85%); lack of co-catalysts/additives and high selectivities which result in a high purity of product with reduced purification processes) with the utilization of an existing large volume feedstock, lead to huge reductions in the specific investment needed for its potential implementation. In fact, the use of KA oil as a feedstock with molecular oxygen has already been highlighted as an ideal alternative for the production of adipic acid as opposed to the existing nitric acid intensive pathway.[24] Therefore, there is huge incentive to develop catalytic systems that are more diverse and able to utilize KA oil and air directly as much more sustainable feedstocks, consequently diversifying the options available within the chemical industry for a number of large volume products.

1.4 Targets & Scope

Following the findings of the literature discussed, there are a number of key points to address within the works discussed in the coming chapters:

- The development of environmentally sustainable processes is imperative for the continued advance of industrially significant processes,
- Diversifying existing feedstocks and synthetic pathways is an important challenge to tackle in order to facilitate the continual development of the chemical industry,
- One must be willing to explore new and pioneering methods of producing nanoparticle catalysts in order to widen our existing understanding of such materials,
- Not only must a catalytic material be highly active, selective towards the desired species and efficient in its doing so but it must also be robust in nature, demonstrating extended catalytic lifetimes if it is to be a viable candidate for employment in an industrial process,
- One should observe closely the nanoparticle support system upon which the nanoparticle-host synergies are produced in order to fully determine its impact and functionality,
- The resulting nanoparticle morphology generated is of paramount importance when designing catalytically active nanoparticle materials,
- Thus, above all else through the drawing of structure-property correlations a thorough understanding of the catalytic system, its characteristics, mode of action and the precise nature of the active site needs to be established.

With these objectives defined the following chapters aim to realise each point in order to draw meaningful and significant conclusions from the works within.

Chapter 3 outlines the characteristics and merits of a new nanoparticle host material: an inorganic microporous copper chloropyrophosphate framework system. Through the use of this material it is shown that surface supported Pt nanoparticles can be generated in a controlled manor from within the microporous framework via a new ‘extrusion’ methodology. The challenges of this nanoparticle production method are observed with limitations imposed by the host framework and the activation conditions. The catalytic merits of the materials generated are then established and their versatility to exploit multiple sustainable oxidants (TBHP and O_2) for a given benzyl alcohol substrate is demonstrated.

Chapter 4 probes these materials further, demonstrating their ability to produce a range of Au, Pt and Pd metallic nanoparticle species. Continued development of the extrusion

protocol is reflected in the resulting improved level of control over the final nanoparticle morphology. This enhancement is further realised through their exceptional catalytic performance for producing cyclohexanone from KA oil within a continuous flow system while employing molecular oxygen as the active oxygen species.

Chapter 5 presents the potential diversity of these systems to generate bimetallic species through pushing the physical limits of the extrusion process, enhancing our understanding in the process. Catalytic enhancements, resulting from the newly introduced bimetallic species are realised for both primary alcohol (benzyl alcohol) and lactam (valerolactam) selective oxidations, further widening the substrate pool for these oxidation catalysts.

Finally, Chapter 6 demonstrates the improvements possible through meticulous process refinement for the Pt catalysed oxidation of KA oil and through these refinements the full potential of the Pt system is realised. Further, in order to expand our understanding of this highly active species the full catalytic lifetime and deactivation pathway is probed in detail.

For the readers' clarity: the works discussed in the following chapters are presented chronologically and thus the understanding of the materials and processes discussed is developed accordingly through the chapters.

Chapter 2: Experimental Methods

2.1 Catalyst Synthesis

All chemicals for synthesis and catalysis were purchased from Sigma Aldrich or Fisher Scientific and used without further purification. Gases were sourced from BOC Industrial Gases and used as supplied.

2.1.1 Hydrothermal Synthesis of Metal Doped Copper Chloropyrophosphate Frameworks

Hydrothermal synthesis of metal doped copper chloropyrophosphate (CuClP) materials was carried out in a custom built hydrothermal autoclave/bomb and adapted from that reported by Weller *et al*.[194] A graphical illustration of the autoclaves used is provided in Figure 2-a, typical gel compositions are presented in Table 2-a and a general experimental procedure is as follows:

Copper(II) fluoride (0.1168 g, 1.150 mmol), 85 wt.% orthophosphoric acid (0.2 mL, 2.922 mmol), 50 wt. % rubidium hydroxide (0.24 mL, 2.037 mmol), rubidium chloride (0.28 g, 2.316 mmol) and a source of MCl_y: gold(III) chloride hydrate (0.0422 g, 0.124 mmol), potassium tetrachloroplatinate (0.0598 g, 0.144 mmol) or potassium tetrachloropalladate (0.0470 g, 0.144 mmol) were mixed in the Teflon® liner of a custom-made 23 mL hydrothermal vessel, Figure 2-a. The vessel was sealed and heated within a fan assisted oven to 175 °C for 48 hr. After which the materials were filtered and washed with 250 mL of DI water and dried before activation. Products formed as brilliant green cuboid crystals for both the Au and Pt material, and as light brown crystals for the Pd material.

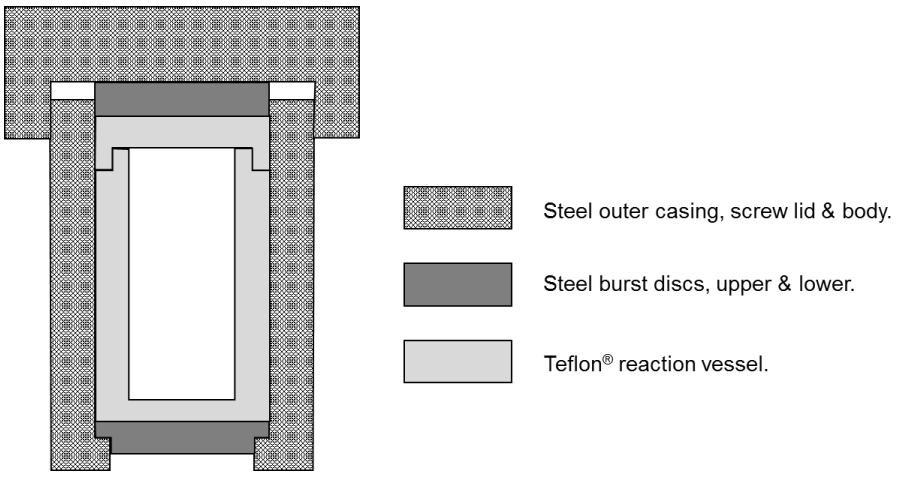

Figure 2-a: Graphical representation of the custom built hydrothermal vessels employed for the synthesis of the CuClP materials. This representation is not to scale.

Sample	Theoretical wt. %					
	M	Rb	Cu	P	O	Cl
Au/CuClP	6.8	35.4	17.6	11.4	20.6	8.2
Pd/CuClP	3.7	35.6	17.6	11.5	20.7	8.2
Pt/CuClP	1.0	39.3	19.5	12.7	22.9	4.3
Pt/CuClP	2.9	37.6	18.7	12.1	21.9	5.6
Pt/CuClP	4.7	36.0	17.9	11.6	21.0	6.8
Pt/CuClP	6.6	34.5	17.1	11.1	20.1	8.0
AuPt/CuClP	3.4 / 3.3	35.0	17.3	11.3	20.4	6.7

Table 2-a: Typical gel compositions for the synthesis of M/CuClP catalysts (M: Pt, Au or Pd). NOTE: 100% incorporation of the 'M' species is assumed for theoretical calculations.

2.1.2 Thermal Activation Procedures

All CuClP materials were activated under calcination conditions: a flow of air for 2 hr at the specified temperature, typically 500 but also 200, 400 or 600 °C (unless otherwise stated), or by reduction under a flow of 5 % H_2/N_2 at approx. 150 $mLmin^{-1}$, for 2 hr at the specified temperature, typically 200 but also 150, 175, 250, 300 or 350 °C (unless otherwise stated). Colours for all materials remain unchanged under calcination conditions. After reduction, the Au material appears unchanged in colour up to 280 °C and then progressively red with temperature, the Pd material appears a progressively darker brown up to 175 °C after which it appears black and the Pt catalyst a darker khaki-green above 150 °C. Typical chemical compositions for the materials made are given in Table 2-b.

Sample	Theoretical wt. %						wt. %*
	M	Rb	Cu	P	O	Cl	M
Au/CuClP	7.2	37.2	18.5	12.0	21.7	3.4	7.1
Pd/CuClP	4.0	38.5	19.0	12.4	22.4	3.6	3.7
Pt/CuClP	1.0	39.7	19.7	12.8	23.1	3.7	0.6
Pt/CuClP	3.0	38.9	19.2	12.5	22.7	3.6	4.0
Pt/CuClP	5.0	38.1	18.9	12.3	22.2	3.5	5.5
Pt/CuClP	7.1	37.3	18.5	12.0	21.7	7.1	6.9
AuPt/CuClP	3.6 / 3.5	37.3	18.5	12.0	21.7	3.4	3.9 / 4.0

*Table 2-b: Typical chemical compositions after activation for the synthesis of M/CuClP catalysts (M: Pt, Au or Pd). * - average wt. % as determined by ICP analysis. NOTE: 100% extrusion of the 'M' species is assumed for theoretical calculations.*

2.1.3 Synthesis of Titania Supported Nanoparticle Catalysts

A standard colloidal deposition approach was adopted. Aqueous stock solutions of the metal precursors were prepared. Gold chloride hydrate (9.92 $mgmL^{-1}$, 1.72 mL); potassium tetrachloroplatinate (12.45 $mgmL^{-1}$, 1.72 mL); potassium tetrachloropalladate (19.58 $mgmL^{-1}$, 1.56 mL) were diluted with DI water (390 mL) and stirred. An aqueous solution of PVP (6.50 $mgmL^{-1}$, 1.00 mL) was added to the stirred solution of metal precursor. After which an aqueous solution of sodium borohydride (0.1 M, 2.50 mL) was added drop-wise to the stirred solution. The solution was left to stir for 30 min to allow for complete reduction.

Titania (P25 Degussa; 0.5 g) was added to the aqueous colloidal solution of gold, platinum or palladium nanoparticles (400 mL) under vigorous stirring. Concentrated sulphuric acid (4 drops) was then added to acidify the surface of the Titania particles, reducing the pH below the point of zero charge. After 1 hr the solution was filtered and washed with 1 L of DI water and dried yielding a lilac colour for the gold materials and a grey colour for the platinum and palladium.

2.2 Catalytic Techniques

2.2.1 Batch Reactor: Reactions at Elevated Pressures

Heterogeneous oxidation catalysis was carried out in a 75 mL Teflon® lined Parr batch reactor sourced from Cambridge Reactor Designs. The reactor was fitted with a pressure gauge, gas inlets and outlets, a sampling port and a digital feedback thermocouple connected to a heater/magnetic stirrer plate.

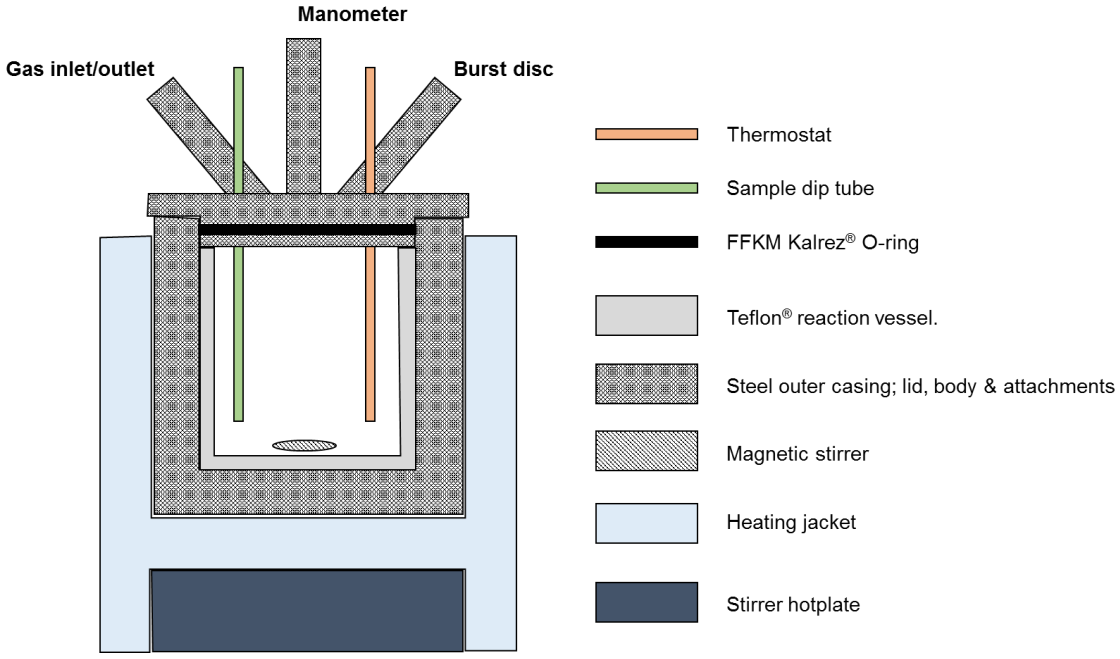

Figure 2-b: Illustration of the Parr batch reactor employed. This representation is not to scale.

For a typical catalytic reaction the substrate (1.00 g), diethylene glycol dimethyl ether (0.85 g, 6.3 mmol) and the solvent (35 mL) were added to the 75 mL Teflon® liner. Lastly, the catalyst (50 mg) and magnetic stirrer bar were added to the mixture.

The liner was then sealed within the assembled reactor and pressurised with dry air, typically 20 bar (unless otherwise stated). The reactor was then set up under stirring to be heated to the specified temperature using the thermocouple and digital temperature regulator. Samples (1 mL) were taken throughout the reaction via the sample port or directly from the solution once the reactor is depressurised at RT. Samples were centrifuged in order to remove any suspended catalyst and were subjected to GC analysis without dilution.

2.2.2 "Bench Top Reactions": Reactions at Ambient Temperatures & Pressures

A standard reflux set-up was employed. A 10 mL RBF was charged with benzyl alcohol (1.5 g, 13.3 mmol) and the catalyst (50 mg) followed by tertiary-butyl hydroperoxide in decane (5.5 M, 1.73 mL, 9.5 mmol) providing an oxidant to substrate ratio of 1:1.5. Reactions were carried out under heating at 60 °C for 6 hr unless stated otherwise.

After completion the reaction mixture was worked up by addition of tertiary butanol (2 mL) followed by the external standard, diethylene glycol dimethyl ether (0.85 g, 6.3 mmol). Samples were then taken and centrifuged in order to remove any suspended catalyst and were subjected to GC analysis without further dilution.

2.2.3 Fixed-Bed Flow Reactor: Continuous Flow Systems

Catalytic reactions were carried out in a custom built fixed-bed flow reactor from Cambridge Reactor Designs, Figure 2-c. Catalysts were pelletized before use typically approx. 0.24 g unless stated otherwise. The system was set up and purged under the flow of air at 200 °C for 1 hr before the substrate feed was allowed to saturate the system. The substrate and air flow rates were set to their experimental level and left to equilibrate for 1 hr. All reactions were carried out using an air flow of 25 $mLmin^{-1}$, a substrate flow of 15 $\mu Lmin^{-1}$ and at 200 °C unless stated otherwise.

KA oil solutions were made up as a 1:1 weight ratio of cyclohexanol and cyclohexanone and used as the substrate feedstock. An external standard solution of triethyleneglycol dimethyl ether (2 M) in acetone was fed into the off stream of the reactor at the same rate of flow as the substrate. The solution obtained from the off stream was diluted at a ratio of 1:10 with acetone before being subject to GC analysis.

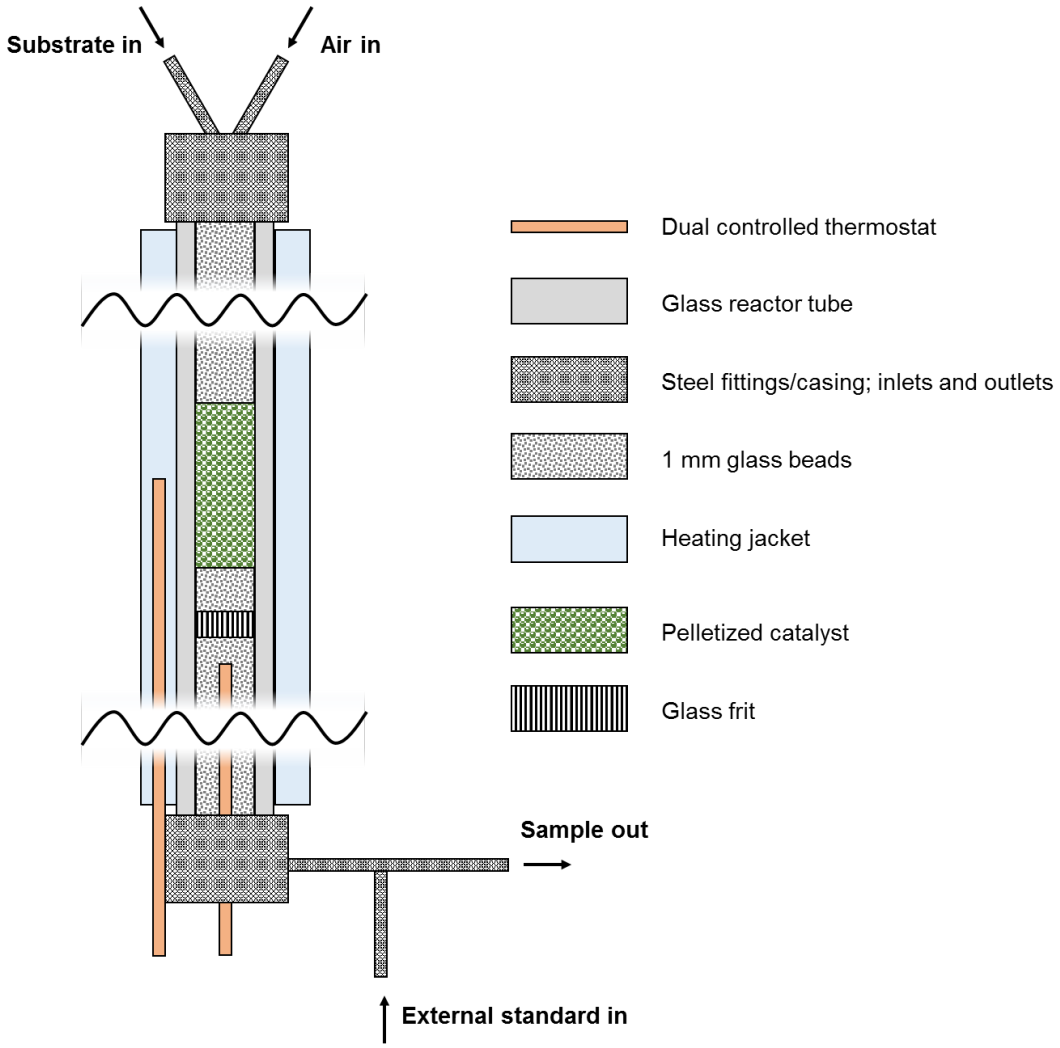

Figure 2-c: Illustration of the fixed-bed flow reactor employed. This representation is not to scale.

2.2.4 Quantitative Analysis of Catalytic Data by Gas Chromatography

Gas chromatography is an analytical technique employed within catalysis to monitor a reaction and quantify its progress. This is done by separation of the reaction contents into the independent chemical species before quantification through the use of independent calibrations for each compound. The separation of compounds is done typically through boiling point and polarity.

In these works the liquid sample is injected into the heated injector port, vaporising the compounds. (NOTE: solids should be removed via centrifugation prior to GC analysis so to not contaminate the injector). This gas mixture is then diluted by and carried into the mobile phase by helium gas. At this point the mixture passes over the stationary phase, the column, while being subjected to the programmed heating regime. This heating regime is individually tailored depending on the column and substances involved in order to achieve the desired peak separation required for accurate interpretation by the flame ionisation detector (FID). The combination of the stationary phase (polarity) and the

heating regime (boiling point) separate the compounds before they reach the FID. The FID consists of a flame, over which the mobile phase passes and is burnt generating ions which are detected as a potential difference across the FID and interpreted as a plot of signal intensity against residence time. See Figure 2-d.

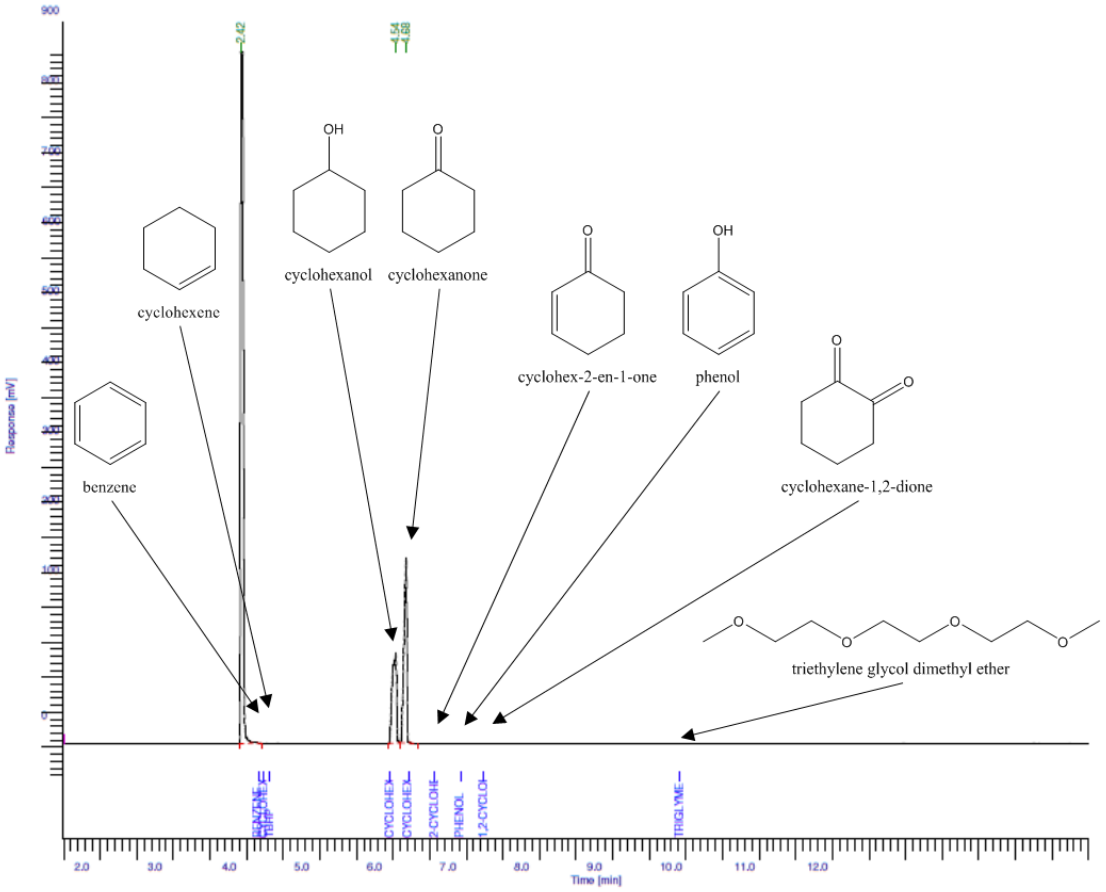

Figure 2-d: Example GC trace of KA oil in acetone with the reaction components and some potential by-products and contaminants highlighted.

Given the GC variables (heating regime, sample size, dilution factor, column type and length etc.) remain constant, solutions of known compounds can be subjected to the GC and generate characteristic response times as depicted for some common (KA oil oxidation) by-products in Figure 2-d. Given the characteristic peak position the area of said peak is directly relatable to the moles of the compound via Equation 15, where the number of moles is simply the peak area multiplied by a constant response factor.

$$Moles(X) = m_X \times Area(X)$$

Equation 15: Equation used to calculate moles of species 'X' in GC sample where m_x is the pre-determined response factor.

In order to maintain reliability of the analysis and to track the process mass balance, a standard must be employed against which the data is interpreted. A standard exists as an

inert substance within (or external to) the reaction whose GC peak area will remain constant, provided no loss of mass has occurred. This rules out any subtle variations in the analytical system affecting the catalytic data as they would impact the peak area of the standard similarly. Therefore, we generate Equation 16 where the response factor for compound '*X*' is now relative to the standard. The rearrangement of which allows the quantifiable interpretation of the moles of '*X*' given the other known values.

$$\frac{Moles(X)}{Moles(std)} = \frac{m_x}{m_{std}} \times \frac{Area(X)}{Area(std)} = Rf_{X/_{std}} \times \frac{Area(X)}{Area(std)}$$

Equation 16: The overall equation for determining the number of moles of 'X' given a known number of moles of the standard (std) where $Rf_{X/std}$ is the response factor for 'X' with respect to the standard.

$$Moles(X) = Rf_{X/_{std}} \times Moles(std) \times \frac{Area(X)}{Area(std)}$$

Equation 17: Rearrangement of Equation 16 allows the determination the number of moles of 'X'.

Equation 16 allows one to calculate the response factor for a given compound and standard by analysis of six or more solutions of known standard and compound ('*X*') concentration. To ensure reliability across the reaction concentration range, these solutions should be made so that the concentration of '*X*' varies across the same range. Analysis of these samples will generate the required variables in order to form a '*y* = *mx* + *c*' plot where the gradient is equal to the response factor as per Equation 16, as shown in Figure 2-e.

Following this, the use of Equation 17 for any reaction (containing these components) can be carried out as the moles of the standard should be known (given an appropriate standard was chosen) and consistent with the time = 0 point. The response factor is now constant and the value calculated previously and the peak areas are generated by the GC analysis of the reaction sample.

All catalysis samples within this work were analysed by GC (PerkinElmer, Clarus 480) using an Elite-5 column equipped with a FID. Products were identified against authenticated standards and quantified by calibration to obtain response factors (R_fs) against the known internal or external standard, di or tri-ethylene glycol dimethyl ether or mesitylene, as described above.

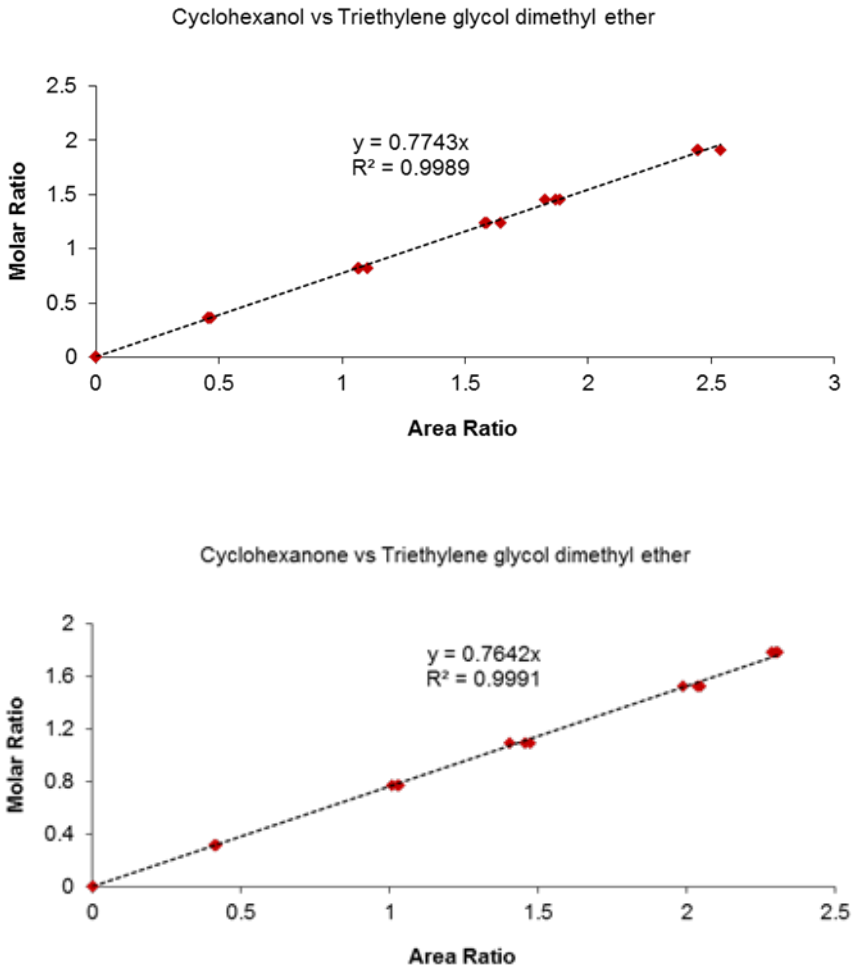

Figure 2-e: Calibration plots for cyclohexanol (above) and cyclohexanone (below) against the external standard employed, triglyme, showing accurate Rfs of 0.7743 and 0.7642 respectively.

2.3 Characterisation Techniques

2.3.1 Powder X-Ray Diffraction

X-rays interact readily with electrons and as a result diffraction of an X-ray beam targeted at an inorganic material will occur. Given the atomic separations are of the same order of magnitude as the X-ray wavelength then constructive and destructive interferences will be generated as a result of the X-ray diffraction within an ordered array of scattering atoms.

The ordered array of scattering atoms is determined by the materials crystal structure, represented by the unit cell, the smallest irreducible 3D unit that can be repeated/translated to represent the entire crystal structure and its symmetry elements. The unit cell is defined (as per Figure 2-f) where dimensions *a*, *b* and *c* are separated by the angles *α* (*bc*), *β* (*ac*) and *γ* (*ab*). For example, for a primitive cubic lattice, *a* = *b* = *c* and *α* = *β* = *γ* = 90 ° but for many other, more complex structures this is not the case. Each lattice plane is labelled with Miller indices (*hkl*), where *h, k* and *l* are integer values and denote the fraction at which the plane dissect the corresponding *abc* dimensions i.e. $\frac{a}{h}$, $\frac{b}{k}$ and $\frac{c}{l}$. The separation of these repeated planes is represented by the *d* term in Equation 18 for a cubic crystal system and more generally in Figure 2-g.

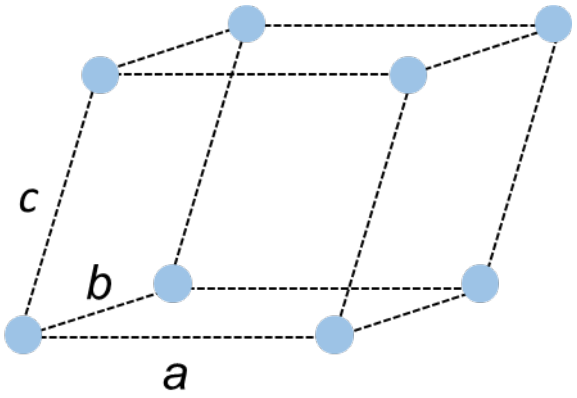

Figure 2-f: Representation of a (triclinic) unit cell.

$$\frac{1}{d^2} = \frac{h^2 + k^2 + l^2}{\alpha^2}$$

Equation 18: d-spacing expression for a cubic crystal system where a represents the unit cell dimension.

This diffraction phenomenon is described by Bragg's law as per Equation 19 and Figure 2-g below. Constructive interference amplifies the resulting signal and occurs as a result of the production of in-phase X-rays resulting from independent scattering events off

atoms contained within repeated crystallographic planes. For examples, points '*A*' and '*C*' in Figure 2-g. This occurs provided the additional difference travelled by the x-ray photon is an integral number of wavelengths. This path difference '*BC* + *CD*' will depend on the lattice spacing's '*d*' of the material and the incidence angle '*θ*'.[195] For integral wavelength differences in path length Equation 20 is true.

$$n\lambda = 2dsin\Theta$$

Equation 19: Braggs law where 'λ' is the x-ray wavelength 'd' is the distance between lattice planes, 'ϑ' is the angle of incidence with the lattice plane and 'n' is an integer.

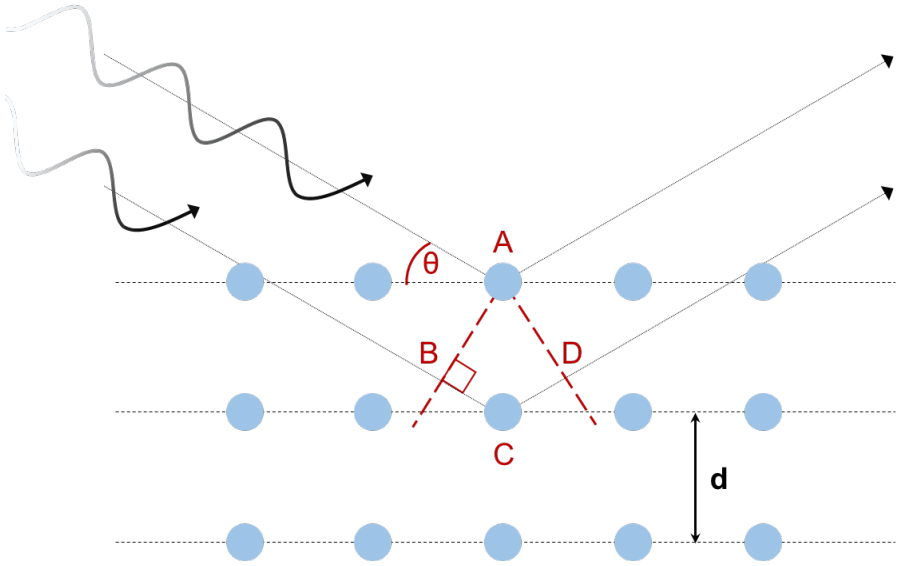

Figure 2-g: Graphical representation of Braggs law.

$$path\ difference = BC + CD = 2dsin\Theta = n\lambda$$

Equation 20: Braggs law where 'λ' is the x-ray wave length, 'd' is the distance between lattice planes, 'ϑ' is the angle of incidence with the lattice plane and 'n' is an integer. BC and CD are determined from Figure 2-g.

Thus, in order to observe diffraction from a given lattice (or inorganic material) Bragg's law can be satisfied by either varying the wavelength or the incident angle. Within these works PXRD was conducted by varying the incident angle on a Bruker D2 Phaser diffractometer using Cu $K_{\alpha 1\&2}$ monochromatic radiation source (λ = 1.5418 Å).

If Equation 20 is not true, destructive interference occurs between the resulting X-rays. This results in the out of phase X-rays dampening each other and becoming negligible in intensity by comparison to those that interact constructively. This allows a 2D diffraction pattern to be generated, usually plotted as intensity vs 2θ (Figure 2-h). The intensity of each signal depends on the electron density of the diffracting plane i.e. atoms with more

electrons scatter X-rays more readily and therefore planes that contain heavier atoms will produce strong diffraction signals.[196] Further, within PXRD multiple crystallographic planes can contribute to a given diffraction signal and therefore this would increase the number of scatterers and in turn the signal intensity. Each individual crystalline phase within a given sample will have a unique diffraction pattern, sometimes termed 'finger prints' by which one should be able to identify the phase. This makes PXRD an ideal tool within heterogeneous catalysis for assessing phase purity of a system, while facilitating the identification of any impurities or unexpected phases present.

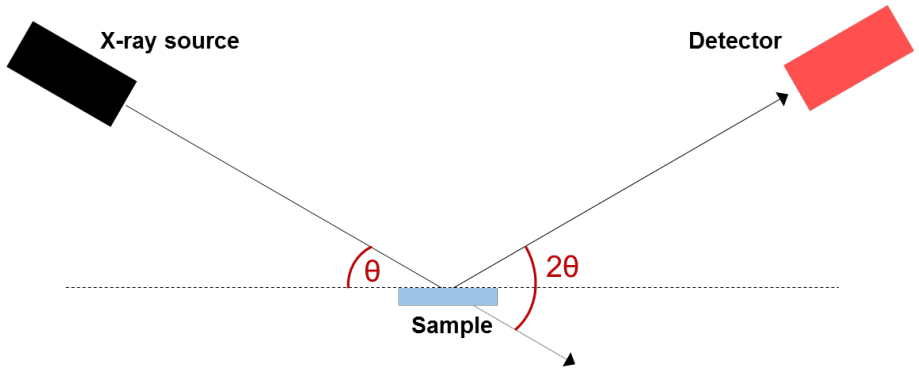

Figure 2-h: 2ϑ is determined by the total angle between the x-ray detector and the incident angle with the sample.

2.3.2 X-Ray Photoelectron Spectroscopy

As highlighted in Section 2.3.1 the interaction between X-rays and electrons can play a pivotal role in enabling chemists to identify material natures. X-ray photoelectron spectroscopy (XPS) is another such technique. Irradiation of a materials surface by a monochromatic X-ray source will cause photoelectrons from within the sample to be emitted due to the photoelectric effect as per Figure 2-i. These emitted photoelectrons will possess kinetic energies (KEs) which are equal to the sum of the energy of the incident X-ray, a spectrometer work function (determined by calibration) and the binding energy (BE) of the ejected photoelectron. Therefore, by measuring the KE of the emitted photoelectrons one can determine their initial binding energies as shown in Equation 21.

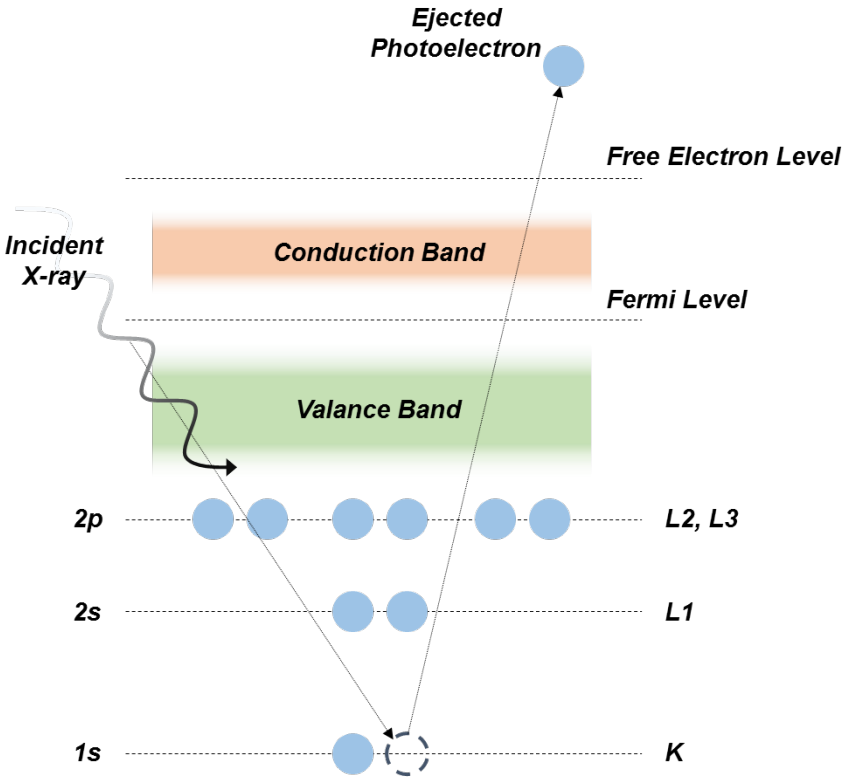

Figure 2-i: Photoemission of electrons.

$$BE = hv - KE - \varphi$$

Equation 21: Binding energy equation where BE is binding energy of the ejected photoelectron, hv is the incident photon energy (h = Planks constant & v = frequency), KE is the kinetic energy of the ejected photoelectron and φ is the spectrometer work function.

These binding energies are specific to the precise electron emitted and are denoted using the electronic configuration from their respective quantum numbers as detailed in Figure 2-j and Table 2-c. This relationship results in photoelectrons that are generated from energy levels with non-zero angular momentum quantum numbers (*p, d* or *f shells*) presenting doublet peaks with characteristic ratios (*p* = 1:2, *d* = 2:3 and *f* = 3:4) as a result of the spin-orbit coupling.

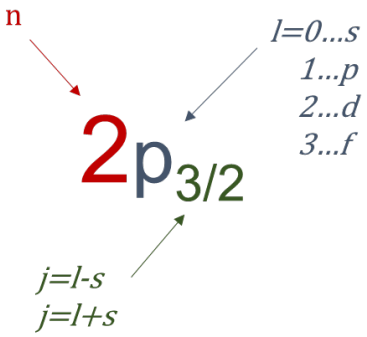

Figure 2-j: Description of spin orbital quantum numbers where n is the principle quantum number, j is the spin-orbit coupling, l is the angular momentum quantum number and s is the spin angular momentum ($s = \pm {}^{1}/_{2}$).

Binding Energy	Energy Level	Electron Configuration	Quantum Numbers
	K	1s	1, 0, $^{1}/_{2}$
	L_1	2s	2, 0, $^{1}/_{2}$
	L_2	$2p_{1/2}$	2, 1, $^{1}/_{2}$
	L_3	$2p_{3/2}$	2, 1, $^{3}/_{2}$
	M_1	3s	3, 0, $^{1}/_{2}$
	M_2	$3p_{1/2}$	3, 1, $^{1}/_{2}$
	M_3	$3p_{3/2}$	3, 1, $^{3}/_{2}$
	M_4	$3d_{3/2}$	3, 2, $^{3}/_{2}$
	M_5	$3d_{5/2}$	3, 2, $^{5}/_{2}$
	N_1	4s	4, 0, $^{1}/_{2}$

Table 2-c: Names of atomic shells in terms of energy shells, electron configuration and quantum numbers.

Typically, XPS spectra are plotted as intensity vs BE (eV) as shown in Figure 2-k. As only electrons close to the surface can escape elastically, the stepped background is due to electrons from deeper within the sample escaping inelastically or undergoing multiple collisions while travelling back to the surface. This results in the typical sampling depth of XPS being on the order of 1 – 10 nm. Meaningful information can be gathered from observing the shifts in the emission lines of the XPS spectra which arise from changes in the local chemical environment and formal oxidation state of the emitting species. Both display BE shifts on the order of < 5 eV. For example increases in oxidation state cause

increases in the BE due to the decrease in the screening of the bound electron from the ion core. This particular feature is used extensively within these works.

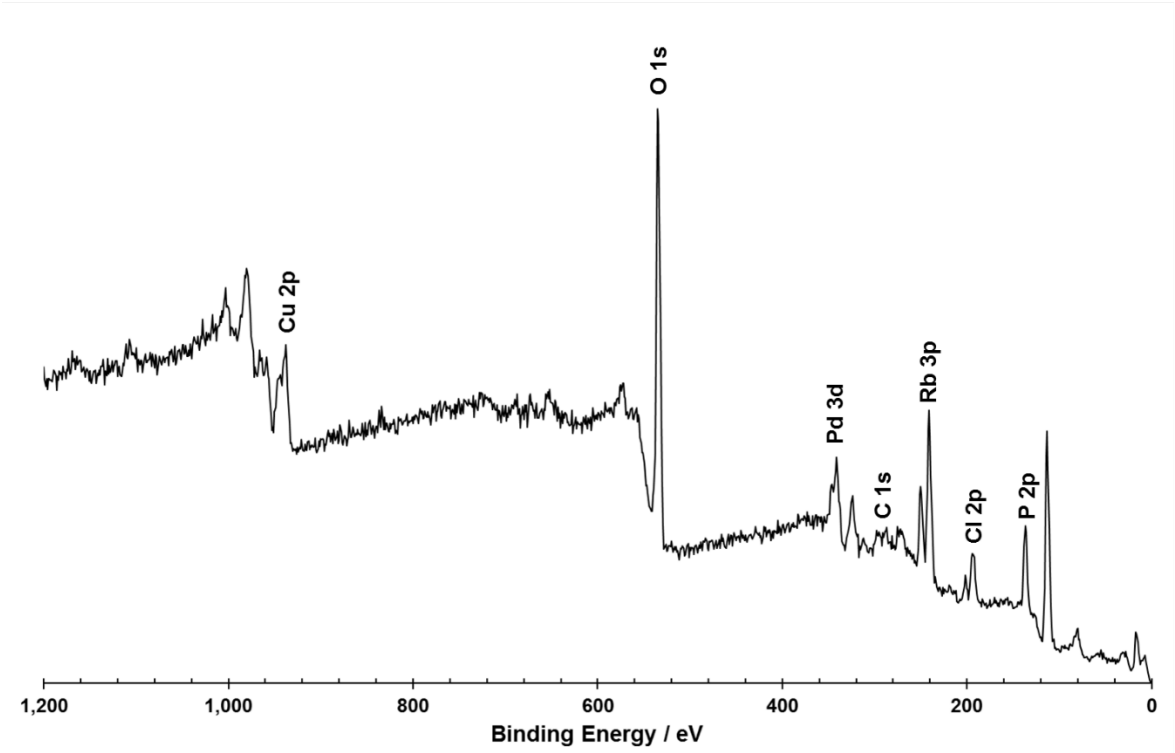

Figure 2-k: Example XPS survey spectra of a material containing: Cu, O, Pd, C, Rb, Cl & P.

Additional features of note within XPS are the generation of shake-up satellite peaks and the emission of Auger electrons. Both of these features can also be used to ascertain meaningful information on the analysed species. The emission of Auger electrons results from a higher energy orbital electron falling to fill the vacancy of the emitted core level electron. This results in the emission of another electron from the same (higher) energy level in order to conserve the energy released by the initial energy level transition, as shown in Figure 2-l. These emissions are often termed using the energy levels of the electron involved, for example if the initial emitted electron is from the 1*s* (K) level and the subsequent two electrons are from the 2*p* (L) level, as depicted in Figure 2-l then this Auger emission line would be a KLL emission. The shake-up process also leads to the generation of emission lines at lower KEs and occurs as a result of additional energy level transitions occurring during the photoelectron emission process as shown in Figure 2-m and Equation 22.

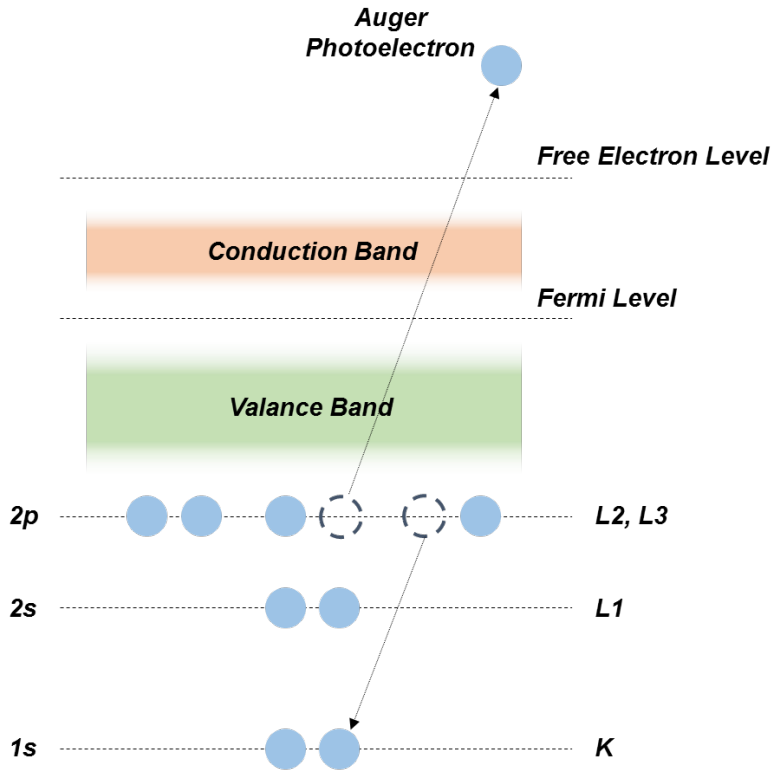

Figure 2-l: Auger electron emission, following the photoemission of a core level electron as per Figure 2-i.

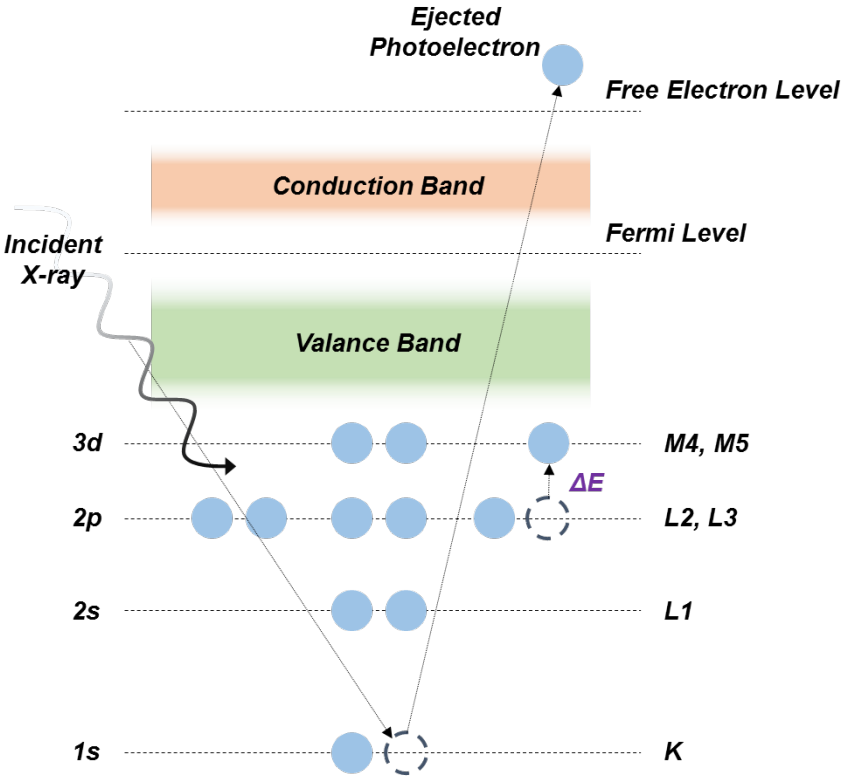

Figure 2-m: Shake-up process that results in the emitted photoelectron processing less kinetic energy than that observed for a primary photoemission as per Figure 2-i.

$$BE = h\nu - KE - \varphi - \Delta E$$

Equation 22: Binding energy equation for shake-up satellite peaks representing the reduced binding energy exhibited by the resulting photoelectron as a result of the energy required to promote an additional lower energy electron to the unoccupied 3d orbital, ΔE in Figure 2-m.

The XPS analysis within this work was performed by Dr Naoko Sano using a Thermo Scientific K-Alpha instrument equipped with monochromated Al K_α source in NEXUS, University of Newcastle. A flood gun was used for charge compensation. A pass energy of 200 eV and a step size of 1.0 eV was employed for all survey spectra while a pass energy of 40 eV and a step size of 0.1 eV was used for high resolution spectra of the elements of interest. All XPS spectra were calibrated against the carbon and/or oxygen 1s peaks, and high resolution spectra were fitted with linear and Shirley backgrounds before peak analysis using the CasaXPS software.

2.3.3 X-Ray Absorption Spectroscopy

X-ray absorption spectroscopy (XAS) is complementary tool to XPS for material analysis and relies on the same underlying phenomenon, the photoelectric effect. Although similar, the two techniques have stark differences, one of which is that XAS is generally measured in transmission and therefore the incident X-rays can interact with any atom within the sample and still be recorded (bulk analysis technique) as opposed to the surface sensitive nature of XPS. Another is the level of detail obtainable from the analysis, in much catalytic research XPS is used primarily to observe oxidation states while also offering some small levels of structural information. XAS on the other hand offers detailed insights into both the oxidation of a particular species and the local structural environment as neighbouring atoms, CNs and bond lengths can all be ascertained.

In order for XAS to be possible the energy of the incident X-ray needs to be greater than that required to perturb, or eject a core level electron of the atom of interest i.e. for the photoelectric effect to occur. The probability of this is termed the absorption coefficient (μ) and this absorption occurs according to Beer's law (Equation 23). Further, for most X-ray energies the absorption coefficient approx. depends on the sample density, the atomic number, atomic mass and X-ray energy according to Equation 24. This strong dependence of the absorption coefficient on both the atomic number and X-ray energy has resulted in the diverse application of X-ray absorption technologies in medicine and other imaging techniques such as tomography.[197]

$$I = I_0 e^{-\mu t}$$

Equation 23: *Beer's law. I_o is the incident X-ray intensity, I is the transmitted X-ray intensity, t is the sample thickness and μ is the absorption coefficient, as per Figure 2-n.*

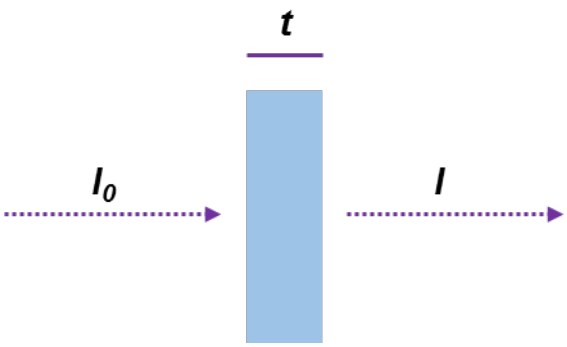

Figure 2-n: *An incident X-ray beam of intensity I_0 passes through the sample of thickness t and the transmitted beam has an intensity I.*

$$\mu \approx \frac{\rho Z^4}{AE^3}$$

Equation 24: *The dependence of the absorption coefficient μ on the sample density (ρ), the atomic number (Z), atomic mass (A) and x-ray energy (E).*

When the incident X-ray has energy equal to, or higher than, that of the BE of a core electron there is a sharp rise in the absorption, this is termed the absorption edge. It is depicted in Figure 2-o. This rise corresponds to the promotion of a core level electron to the continuum and XAS is the measurement of the intensity of *μ* as a function of energy, near and at energies just above the absorption edge. Since the BEs of the core level electrons are well-defined and accurately documented the X-ray energy can be tuned to an appropriate absorption edge, making XAS an element specific technique.

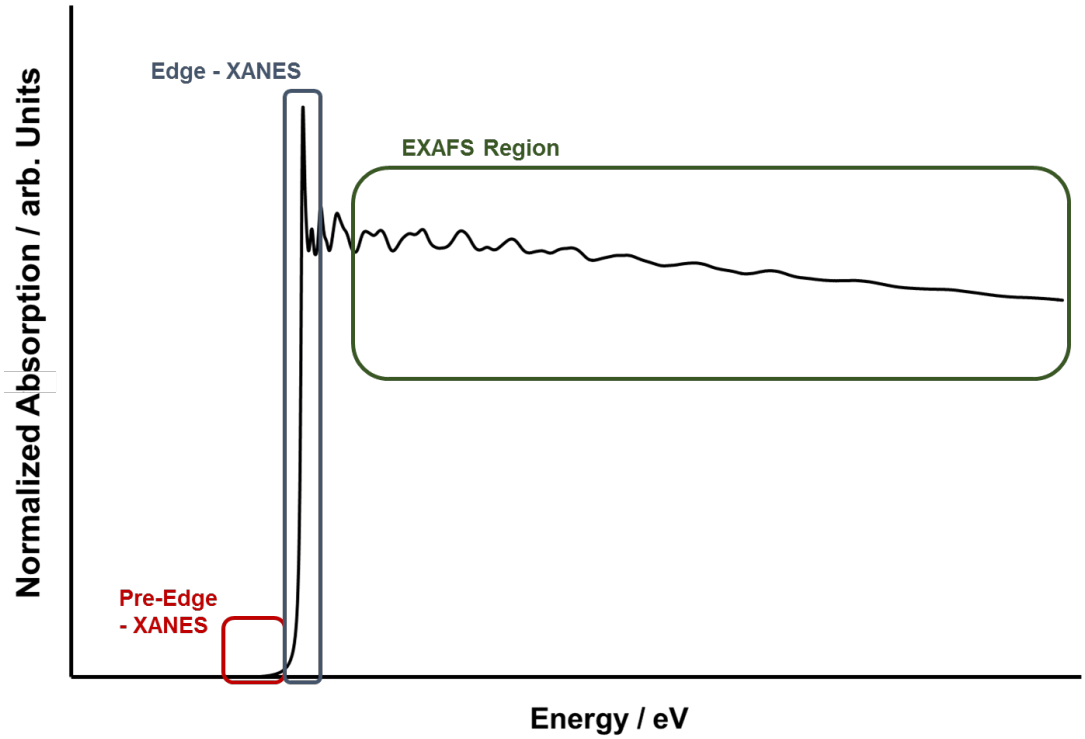

Figure 2-o: Depiction of the different regions within a typical XAS spectrum, μ(E) vs E.

In transmission measurements (as per Figure 2-n) the energy dependence of the absorption coefficient is measured in the form of Equation 25 and the resulting spectrum will be of the form found in Figure 2-o. This spectrum is divided into two sections: the X-ray absorption near-edge spectroscopy (XANES), approx. -50 – 50 eV around the absorption edge, termed – the white line, and the extended X-ray absorption fine structure (EXAFS), approx. 200 – 800 eV above the absorption edge. The former is sensitive towards the formal oxidation state and coordination chemistry (i.e. octahedral, tetrahedral etc.) of the absorbing atom. This is due to features in this region being related to the excitation of the core-level electron to higher energy states below the Fermi level. Therefore, formal oxidation state and coordination environments can have a significant influence over the energy and population of these higher energy states.[12]

$$\mu(E) = \log\left({}^{I_0}/_{I}\right)$$

Equation 25: Energy dependence of the absorption coefficient within transmission XAS measurements.

EXAFS on the other hand is used to determine distances, CN and species of the neighbours of the absorbing atom, due to these features dramatically impacting the oscillatory nature of the propagated photoelectric wave emitted as a result of the initial absorption event. This oscillatory feature stems from the back-scattering of the initial photoelectric wave by the neighbouring atoms. After the absorption event where a

photoelectron is ejected into the continuum, the emitted photoelectrons propagate as spherical waves around the absorbing atom. Back scattering of these waves can occur both in-phase, where the interatomic distances are equal to an integer value of the photoelectron wavelength, or out-of-phase (as shown in Figure 2-p). This then leads to maxima and minima in the EXAFS region of the spectrum, hence its oscillatory nature. These oscillations are represented as a function of the photoelectron wave number *k* and are termed *X(k)* which can be interpreted via the EXAFS equation shown in Equation 26. Using the EXAFS equation to model the recorded data allows one to determine *N* (CN), *R* (bond length) and σ^2 (bond length disorder) knowing the scattering amplitude *f(k)* and phase-shift *δ(k)*.[197]

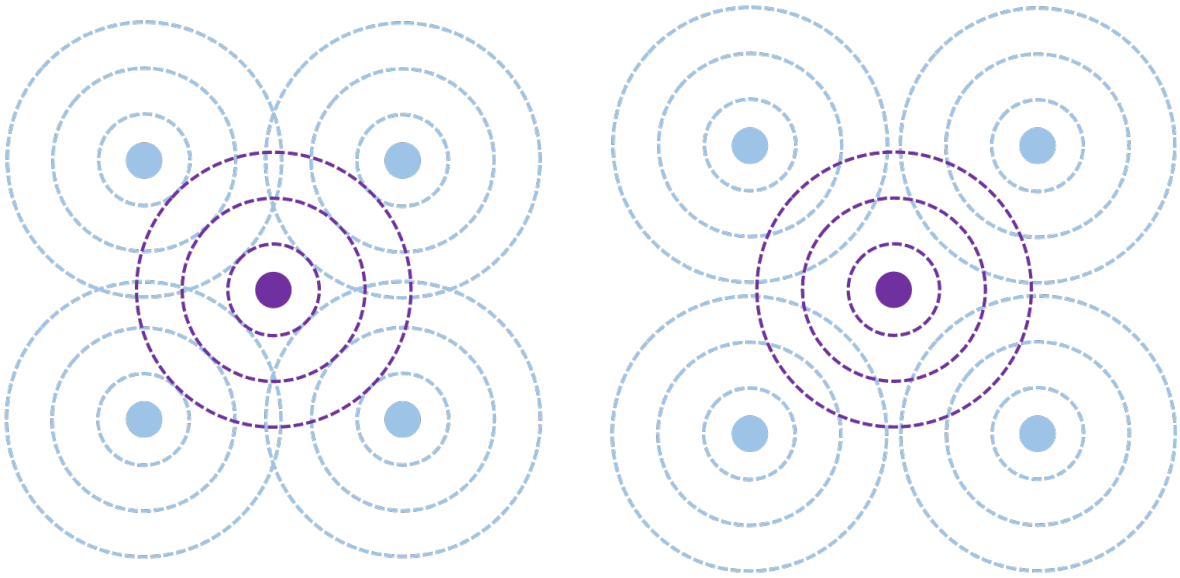

Figure 2-p: In-phase (left) and out-of-phase (right) scattering of photoelectrons leading to maxima and minima in the observed x-ray absorption coefficient.

$$\chi(k) = \sum_j \frac{N_j f_j(k) e^{-2k^2\sigma_j^2}}{kR_j^2} \sin\left[2kR_j + \delta_j(k)\right]$$

Equation 26: The EXAFS equation. f(k) and δ(k) are scattering properties of the neighbouring atoms, N is the number of neighbouring atoms, R is the distance to the neighbouring atoms and σ^2 is the disorder in the neighbour distance.

Au, Pt, Pd and Cu XAS studies within this work were carried out on the B18 beamline at the Diamond Light Source, Didcot, UK. Acquisition of the data was conducted by Dr Peter Wells, as acknowledged, and measurements were performed using a QEXAFS set-up with a fast-scanning Si (111) or Si (311) double crystal monochromator. The normal time resolution of the spectra reported herein was 1 min/spectrum (k_{max} = 16), on average six scans were acquired to improve the signal to noise level of the data. All samples were diluted with cellulose and pressed into pellets to optimize the effective edge-step of the

XAS data and measured in transmission mode using ion chamber detectors. All transmission XAS spectra were acquired concurrently with the appropriate reference foil placed between I_t and I_{ref}. XAS data processing and EXAFS analysis were performed using IFEFFIT[198] with the Horae package (Athena and Artemis).[199] The amplitude reduction factor, S_o^2, was derived from EXAFS data analysis of known compounds, and used as a fixed input parameter.

2.3.4 (Scanning) Transmission Electron Microscopy & Energy Dispersive X-Ray Spectroscopy

Transmission electron microscopy (TEM) is used to reveal the fine structure of solids to a sub-micrometre level of detail, often below 1 nm resolution.[200] This ability to accurately image solids is a valuable tool to a catalytic chemist. Especially when one considers that within heterogeneous catalysis, active surface species often exist within this resolution domain. Species such as nanoparticles for example. Clearly this level of detail would facilitate our understanding of catalytic modes of action and enable the drawing of structure-property correlations as a detailed understanding of the physical structure would be required.

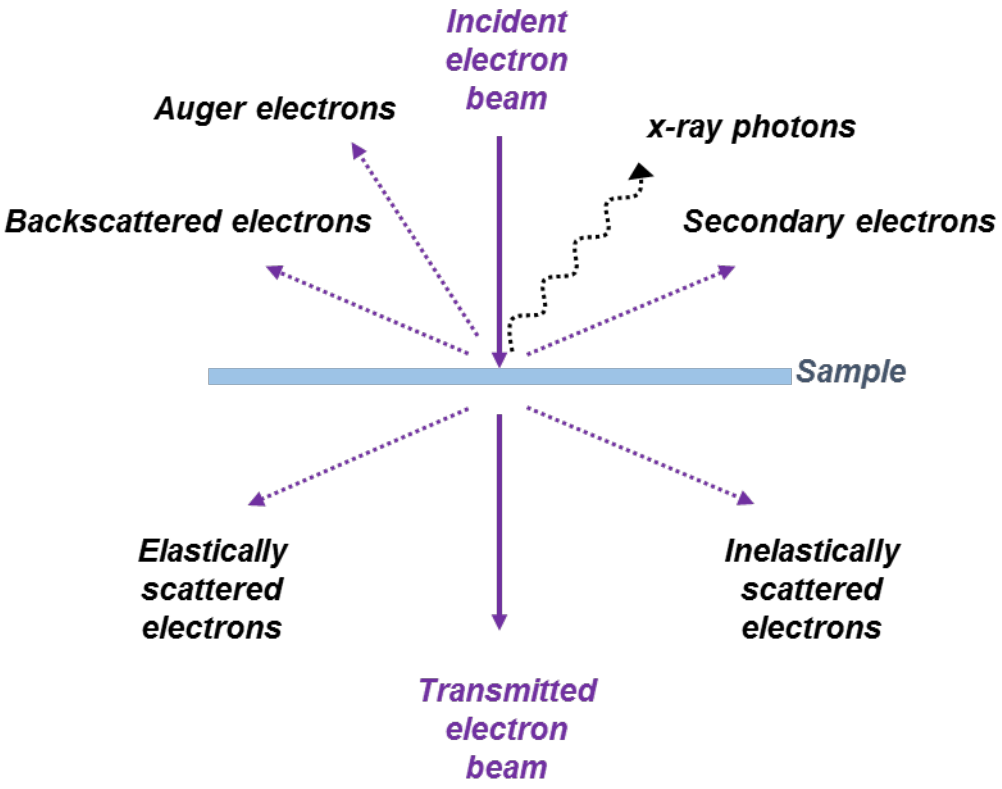

Figure 2-q: The main types of signal generated in the interaction of an electron beam with a specimen in TEM.[12]

Principally the technique involves irradiating the sample with a high energy electron beam which then generates a range of analysable signals from the specimen, as shown in Figure 2-q. Some of these will be discussed later. The two main methods of TEM are the conventional TEM and scanning TEM (STEM). These differ in the nature by which the incident electron beam addresses the specimen. Conventional TEM uses a wide, close-to-parallel electron beam that floods the area of interest. The image is then formed by a measure of the electron density, some of which has been lost through elastic and inelastic scattering. This is done through an objective lens after the thin sample and every image pixel is collected in parallel. STEM on the other hand employs a focussed beam, formed by a probe forming lens before the sample. In this regard each pixel is collected in series as the probe is scanned across the sample.[200]

Irradiation of a sample with a high energy electron beam leads to these high energy electrons (primary electrons) interacting with the atoms within the sample. This either happens elastically (where no measurable energy loss is observed) or inelastically (where measurable energy loss is observed). Typically elastic interactions occur when the incident electrons are diffracted about sample atoms by interactions with their atomic nuclei. These lead to both elastically scattered electrons measured in transmission and measureable backscattered electrons above the sample (Figure 2-q). Inelastic scattering occurs from electron-electron interactions and it is these inelastic scattering events that are primarily used for analysis within TEM. That being said, both of these scattering events lead to changes in electron density within the transmitted electron beam that are recorded to generate the bright field (BF) TEM images. These are typically recorded by a mass/thickness contrast mechanism where, as heavier or a higher abundance of atoms cause more scattering events, areas of low electron density (due to high degrees of scattering, therefore high mass/thickness) appear dark and areas of high electron density (due to low degrees of scattering, therefore low mass/thickness) appear bright.

TEM image resolutions depend on four key parameters: the resolution power of the microscope, the energy spread of the electron beam, the thickness of the sample and its composition/stability. Aberration correction (AC) within STEM facilitates greater image resolution by imparting greater control over the beam energy spread. Passing the electron beam through a spherical aberration following the objective lens allows the reduction of the '*beam tails*' so that a fine beam can be positioned on a specified column of atoms without '*spilling'* significant electron intensity into neighbouring columns, as depicted in Figure 2-r.[200] This offers a significant benefit for STEM techniques, specifically for high angle annular dark field (HAADF) imaging.

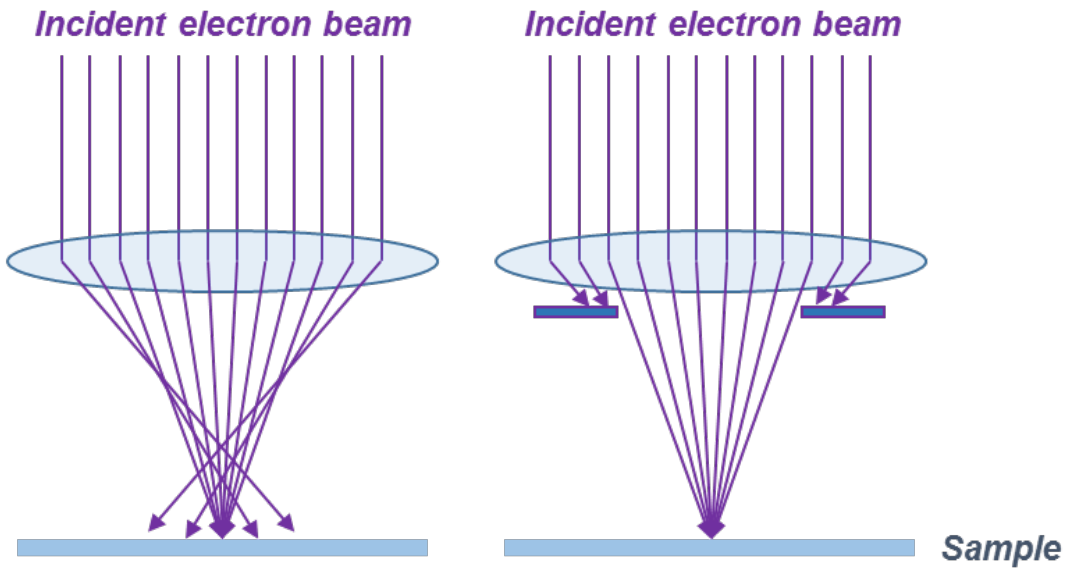

Figure 2-r: Schematic representation of the potential resolution increases offered by spherical lens aberration corrections; STEM (left) and AC-STEM (right).

As eluded to, it is the inelastic scattering events that can lead to additional analysable signals being generated such as X-rays. Inelastic scatting events can lead to the ejection of an inner shell electron from a sample atom, by the primary electron. This then leads to a measurable energy loss in the primary electron and the generation of a secondary electron. The secondary is the sample electron which has now been ejected into the continuum. Following this excitation, the sample atoms will relax, either by emitting a characteristic X-ray or an Auger electron (Figure 2-l). It is the measure of these emitted, characteristic, X-rays that is the principle mechanism for EDXS. When an atom undergoes such a relaxation an outer shell electron (high energy level) will drop to the vacant, lower energy state. In the process emitting an X-ray of well-defined energy, characteristic to the atom of interest. Quantification of these X-rays allows the user to not only measure the elemental composition of a particular AC-STEM pixel (given the appropriate resolution is achievable) but also the abundance of each specific element.

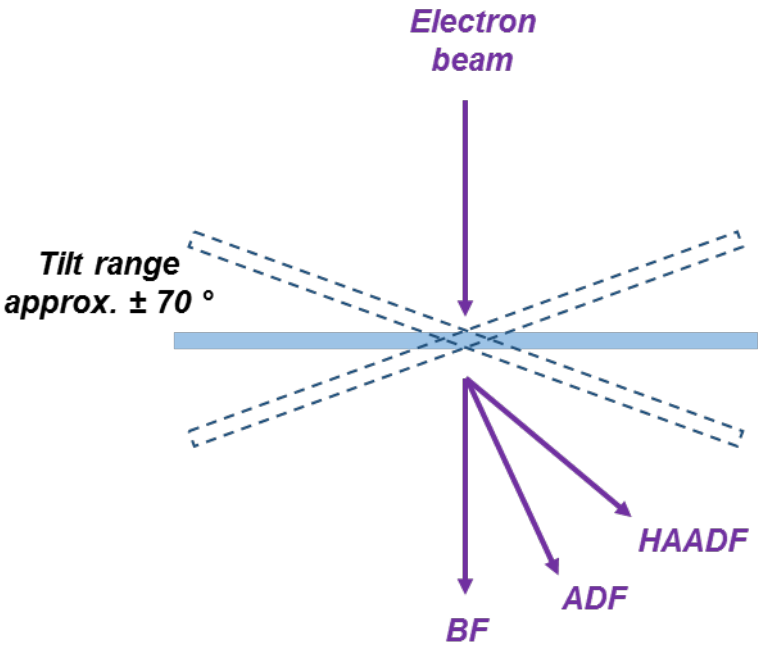

Figure 2-s: Schematic representation of the arrangement in STEM whereby bright-field (BF) as well as annular dark-field (ADF) and high-angle-annular-dark-field (HAADF) images may be recorded.[12]

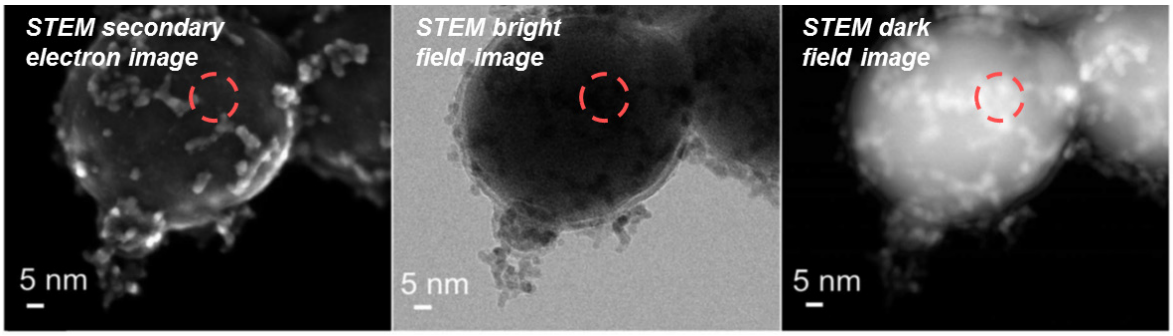

Figure 2-t: Three STEM images highlighting the excellent surface sensitivity of secondary electron STEM, the clear particle contrast in thinner regions offered by BF-STEM and the higher atomic contrast of ADF-STEM facilitating the observation of heavier particles in thicker sample regions.[201]

Further to BF-STEM, other imaging fields are possible, such as annular dark field (ADF) and high angle (HA) ADF, see Figure 2-s. By measuring the transmitted electron beam at high angles, the influence of heavier scattering atoms becomes more significant. In fact, HA scattered electrons are usually insensitive to structure and orientation while being very dependent on the atomic number of the scattering atom.[200] Therefore this particular technique is very useful for imaging samples that contain heavy atoms such as Au, Pt and Pd as these atoms are given increased significance within the image. This feature is further highlighted in Figure 2-t which contrasts imaging techniques of Pd nanoparticles immobilized upon an Fe support. In HAADF the imaging field is inverted so that regions of

high electron density result from highly scattered atoms, and vice versa. This is the opposite of BF-STEM hence the term, dark field.

Within these works, all ADF-STEM and EDXS measurements and processing were conducted by Dr Rowan Leary (University of Cambridge, Cambridge, U.K.) and BF-TEM measurements and particle size distributions by Dr Scott Rogers (UK Catalysis Hub, Research Complex at Harwell, Harwell, U.K) and Dr Gillian Collins (Department of Chemistry and Tyndall National Institute, University College Cork, Cork, Ireland) as acknowledged.

AC-TEM was performed on an FEI Titan3 80-300 STEM equipped with a CEOS CESCOR aberration corrector in the probe forming lens. The Titan was operated at 80 or 300 kV, employing ADF AC-STEM as the primary investigative technique. Samples were prepared for the STEM analysis by dusting the dry powder onto standard Cu TEM support grids with holey carbon support film. Between analyses, samples were stored in a vacuum desiccator with anhydrous calcium sulphate desiccant. Under various combinations of electron beam current, dwell time and pixel size (magnification), and at both 80 and 300 kV, all samples were found to be highly susceptible to beam-induced damage. Considerable care was therefore taken to obtain representative images before overwhelming beam-induced modification of the samples occurred. To ensure correct interpretation, note that some of the ADF images in Chapter 5 show contrast inversion at thicker regions of the sample and often at the larger nanoparticles.

EDXS was performed on an FEI Tecnai Orisis 80-200 STEM operated at 80 kV, equipped with an FEI Super-X EDXS system. Spectral processing by integrating the area under the relevant X-ray peaks, was performed using the FEI TIA and HyperSpy software packages.[202]

BF-TEM images within Chapters 6 and 7 were prepared by dispersing the catalyst sample in ethanol using ultra-sonication. This was then used to load the sample on a holey carbon film supported upon a 300 mesh Cu grid by evaporating the solvent. Measurements were performed by Dr Scott Rogers and Dr Gillian Collins using different JEOL JEM 2100 model microscopes and particle size distributions were produced using the post processing software package, ImageJ.[203]

2.3.5 Inductively Coupled Plasma – Optical Emission Spectroscopy

Within catalysis it is imperative to achieve accurate metal loadings from which to calculate TONs and TOF. Otherwise meaningful comparison with other works cannot be made. A reliable resource in order to achieve this information is the use of inductively coupled plasma – optical emission spectroscopy or ICP-OES. Before ICP subjection samples must

be in the solution or gas phase. Therefore solids must be digested before analysis, this is generally done with strong acids such as hydrochloric, nitric, sulphuric and in some cases hydrofluoric acid. The solution sample is then aerosolised in argon within a nebulizer before being propelled into the ICP. This vaporises the sample and leads to the promotion of the sample atoms to excited states. Relaxation then generates characteristic elemental emission spectra with a relatable concentration relationship, readily interpretable by OES. This can then be used to generate an overall wt. % loading of the analysed elements.

In these works ICP analyses were performed by MEDAC Ltd. Samples were digested using nitric acid, apart from when samples contained gold, in which case, aqua regia was used. Samples were weighed into volumetric flasks and the digestive agent added, once digestion was complete the solution was made up to volume using DI water. Calibration standards and a matrix blank were prepared in the same manner. Analysis was carried out on a Varian Vista MPX ICP-OES analyser following standard operating procedures.

Chapter 3: Contrasting Benign Oxidants for the Selective Oxidation of Benzyl Alcohol using Heterogenized Platinum Nanoparticle Catalysts

This chapter aims to introduce the reader to the copper chloropyrophosphate (CuClP) material along with its characteristics and merits as a nanoparticle host while outlining the generation of supported nanoparticle systems through an extrusion methodology. In order to do this, discussions will focus on the Pt/CuClP catalyst activated under calcination conditions for the selective oxidation of benzyl alcohol to benzaldehyde utilizing both TBHP and molecular oxygen as represented in Figure 3-a. Utilization of X-ray spectroscopic characterization in conjunction with catalytic work highlights the potential for these systems as well as some limitations through determination of structure-property correlations. Through these catalytic studies kinetic measurements are also made in order to facilitate a comparison of these materials with outside systems in the scientific community, offering mechanistic insights.

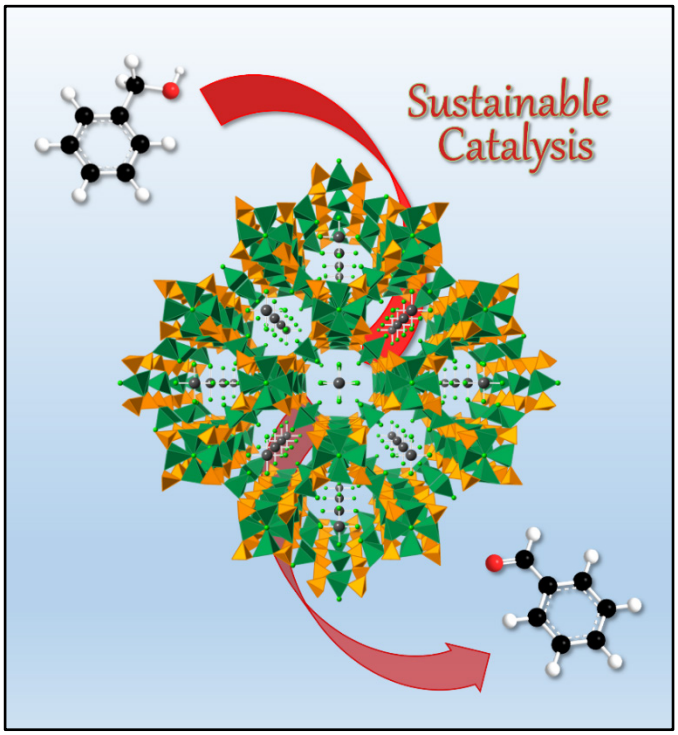

Figure 3-a: Graphical representation of the Pt/CuClP material as a sustainable catalyst for the selective oxidation of benzyl alcohol to benzaldehyde. From C. S. Hinde, A. M. Gill, P. P. Wells, T. S. A. Hor and R. Raja, ChemPlusChem, 2015, ***80****, 1226 – 1230 Reprinted by permission of John Wiley & Sons, Inc.*

Notable contributions:

- Dr Christopher S. Hinde for assistance in the collection of the aerobic oxidation data presented within this chapter.
- Dr Peter P. Wells for his assistance in the collection and fitting of the EXAFS data presented within this chapter.

3.1 Introduction

3.1.1 What are Copper Chloropyrophosphates?

Over many decades, the use of porous open-framework materials, such as zeolites, aluminophosphates (AlPOs), silicon aluminophosphates (SAPOs) and titanium silicates for a range of applications has been vast. The extensive list of applications include: separation science, nonlinear optics, chemical synthesis, electronic devices.[204] Among these topics, heterogeneous catalysis has found extensive use for such materials, owing to their many associated advantages such as; high surface areas, robust natures and structural diversity etc. Development of these systems to include catalytically active metal centres, such as isomorphously substituted AlPOs or encapsulated nanoparticle species, has enabled the catalytic community to exploit the dramatic advantages of site isolation available through use of microporous open-framework materials. This has been discussed in Section 1.2.3.5 and such materials are now well established for a number of catalytic processes.[85,178,205–207]

Similarly, research into another class of open-framework materials, microporous transition metal phosphates, has grown dramatically. These materials possess abundant and cheap transition metals as the key components and thus have become a target for potential use in redox catalysis. The inherent chemical flexibility of these open frameworks originates from the diverse chemistry available to the range of transition metals employed. Specifically, the range of available stable oxidation states and coordination geometries affords them considerable catalytic potential. Examples of such materials include manganese,[208] cobalt[209,210] and iron[211–213] phosphate materials. While there are a small number of studies where catalysis has been carried out over these materials, long term stability appears to be a consistent problem.[212,213] This is a result of the diverse chemistry available, bestowing synthetic limitations such as air/moisture sensitivity as well as poor catalytic stability of the framework. These issues pose significant hurdles for the use of such materials in catalysis. It is therefore apparent that overcoming this stability problem would greatly aid the progression of these materials and recent research into a subclass of the transition metal phosphates has begun to address the issue.

Armstrong *et al*.[214] demonstrated that the incorporation of the highly electro negative fluoride into the metal phosphate framework impacts both structural and compositional aspects of the chemistry. The fluoride (F^-) effectively replaces oxide (O^{2-}) on a metal or phosphorous site allowing for more stable bridging of some metal centres and can lead to the formation of stable terminal fluoride sites within the framework structure. Further, the electron-withdrawing/sigma donor character of the fluoride allows for better stabilization of

higher oxidation states on a transition metal oxide. It also offers greater compositional flexibility of the tetrahedral units within the framework through the formation of (fluoro-)pyrophosphates, $P_2(O,F)_7^{n-}$. All of these features allow significantly more control, flexibility and thus, stability to the open-framework structure of this particular class of transition metal phosphates.

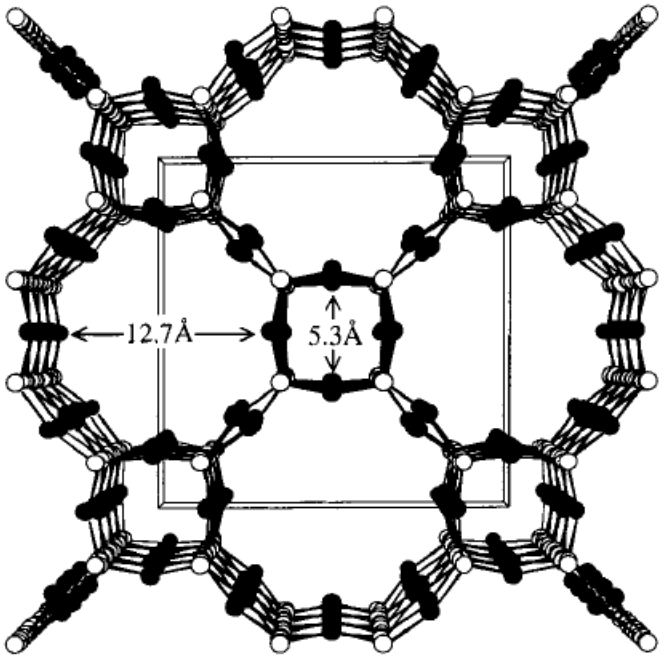

Figure 3-b: Microporous open-framework structure of CU-2 topology. For copper fluorophosphates the black spheres – Cu and white spheres – P with O and other ions omitted for clarity.[215] *Reprinted with permission from Q. Huang, M. Ulutagay, P. A. Michener and S. J. Hwu, J. Am. Chem. Soc., 1999,* ***121****, 10323–10326 Copyright 1999 American Chemical Society.*

Advancement of this research by Weller and co-workers has led to the development of a range of copper(II) fluorophosphates.[216] These structures comprise of Cu^{II} d^9 square-based pyramidal units linked by phosphate species. The Cu centres display elongated apical Cu-O/F bonds due to Jahn-Teller distortion which results in terminal fluoride atoms.[216] These materials are now of great interest due to the low dimensionality and flexibility afforded by the incorporation of the fluoride. These features result in significant ion exchange properties within this class of material. Due to the overall net negative charge on the framework, as a result of its $Cu_3(P_2O_7)_2^{2-}$ composition. Consequently, ionic interaction or hydrogen bonds exist between the group I charge balancing cations or template cations (e.g. K^+, Rb^+, Cs^+ or NH_4^+) and the terminal fluoride ions. The lower charge on the fluoride, in comparison with the oxide, result in relatively weaker coulombic interactions. Therefore, the framework-fluoride influences within these materials provide a facile route for small ion mobility.[214]

Research into the copper fluoro-phosphate materials led onto the development of copper chloropyrophosphates (CuClPs). These materials form hydrothermally with analogous structures but at much more accessible temperatures of 175 °C as opposed to >500 °C.[194] These materials adopt a low dimensionality structure with a CU-2 topology,[215] as seen in Figure 3-b, possessing 12.7 and 5.3 Å 1D channels along the frameworks *c*-axis. The open-framework structure similarly consists of μ^4 chloride ions at the apex of 4 x CuO_4Cl square-based pyramids. Pyrophosphate (P_2O_7) units link these quartets forming analogous 1D channels. The $[CuO_4]_4Cl[P_2O_7]_4$ units are cross-linked via a shared pyrophosphate oxygen atom in the *ab* plane by square-based CuO_4 groups. This produces the square grid of 1D channels approx. 12.7 Å in diameter. The channels are occupied by charge compensating Rb^+, K^+ or NH_4^+ cations and the templating tetrachloro metallate anions such as $[AuCl_4]^-$, $[PdCl_4]^{2-}$ or $[PtCl_4]^{2-}$ as seen in Figure 3-c.[194]

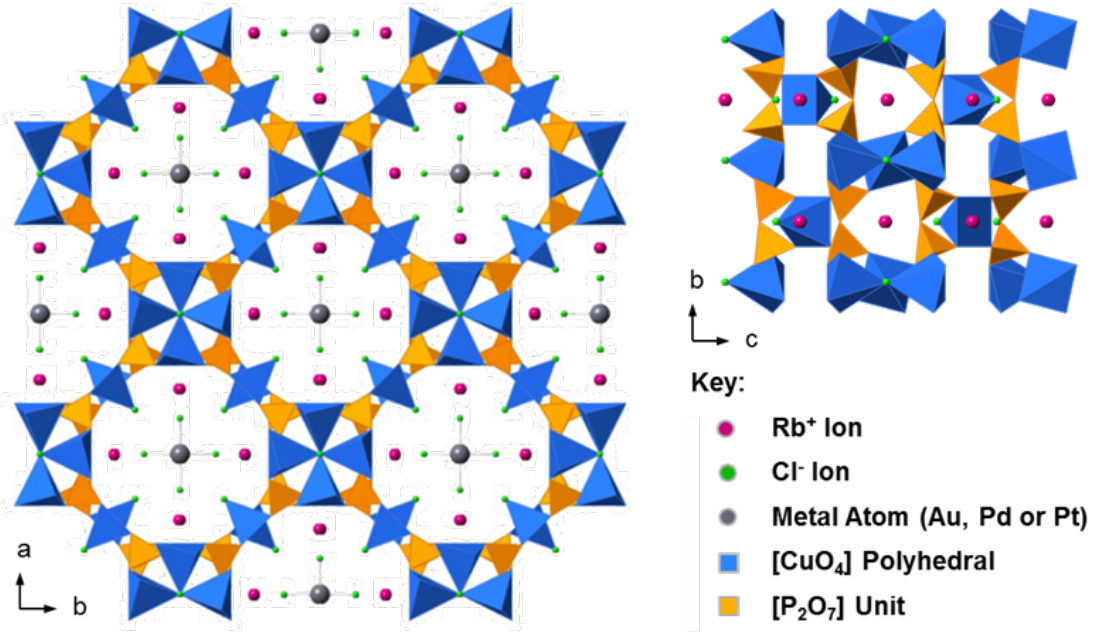

Figure 3-c: Crystal structure of the $[Rb_9Cu_6(P_2O_7)_4(MCl_4)Cl_n]$ framework where M = Au, Pt or Pd and n = 2 for Pt & Pd and 3 for Au. View along the c-axis (left) showing the incorporated metal ions within the 1D channel. View down the a-axis (right) showing the position of the phosphate units within the framework.

Incorporation of these tetrachloro metallate anions is easily achievable through the simple addition of the anion source to the component mixture during the hydrothermal synthesis (e.g. $HAuCl_4$, K_2PtCl_4). This, along with their facile anion exchange capabilities, through simply soaking the material in a concentrated solution of the desired metal salt, has afforded these materials increased potential from a catalytic perspective.[194] This array of anion incorporation, flexibility and the new found stability of the system led to investigations into exploiting these properties as a class of novel hybrid materials. One

can envisage that these properties could thoroughly expand the scope of inbuilt support-site synergies between, for example: a nanoparticle active centre and its supporting microporous framework. Therefore overcoming a number of the drawbacks raised for more traditional supports discussed in Section 1.2.3, allowing for enhanced tailoring of the active site-support-substrate interactions through manipulation of not just the active nanoparticle centre but also the supporting framework. With this in mind, the generation of such nanoparticle systems through the thermal degradation of the hosted chlorometallate anions could prove to be a viable means towards achieving such materials.

3.1.2 Utilization of Copper Chloropyrophosphates as Nanoparticle Supports & the Nanoparticle Extrusion Process

The activity of noble metal species in catalysis has already been highlighted in Chapter 1. Thus, the ability of the CuClP framework to suspend complex anions as known nanoparticle precursors within its porous architecture is a notable attribute. Further, the ability of these systems to form metallic species within/upon the open-framework host via a simple calcination protocol was noted on discovery.[194] Decomposition of the chlorometallate anion can be achieved by simply heating under flow of air. Metallic gold is formed at temperatures above 400 °C, generating Cl_2 gas as the [$AuCl_4^-$] species decomposes, see Figure 3-d. Upon this discovery it was also noted that the interaction between the anion and the supporting framework must be of a stabilizing nature as the decomposition of the $[AuCl_4]^-$ species would normally occur at temperatures close to 200 °C.[194] This demonstrates the significant interactions between the anion and the host framework. Although anion exchange is easily achievable within these systems, there still remains noteworthy material stability outside of the anion exchange conditions.

The discovery of this ability to generate noble metal nanoparticles in a single, post synthetic protocol led to the development of these materials from a catalytic perspective by Hinde *et al.*[217] Their investigations led them to diversify these materials further. Through utilizing the inherent anion flexibility, Hinde and co-workers were able to incorporate gold nanoparticle precursors as well as platinum and palladium. Figure 3-e details the small (approx. 5 nm), uniform, well dispersed and uncapped nanoparticles generated by these systems under the calcination conditions mentioned earlier. It was observed through SEM and PXRD that for all three materials (Au, Pt and Pd/CuClP), the as-synthesised structure existed as a homogeneous distribution of phase-pure cubic crystals. Upon activation, they produced the evenly distributed nanoparticle species detailed in Figure 3-e. These initial findings established that under calcination conditions (2 hr under dry air flow at 500 °C), the controlled generation of metallic nanoparticles with reasonable size distributions (approx. 2 – 10 nm) can be achieved. This demonstrates the

validity of this synthetic methodology and its reliable nature for the production of uncapped, metallic nanoparticles notably from a catalytic perspective, below 10 nm.

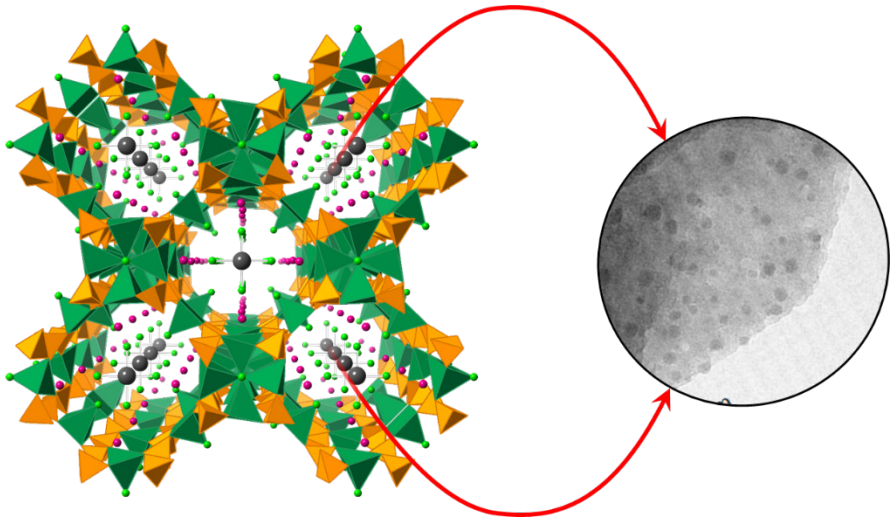

Figure 3-d: Illustration demonstrating the generation of uniform nanoparticle species upon the CuClP framework surface via anion extrusion.

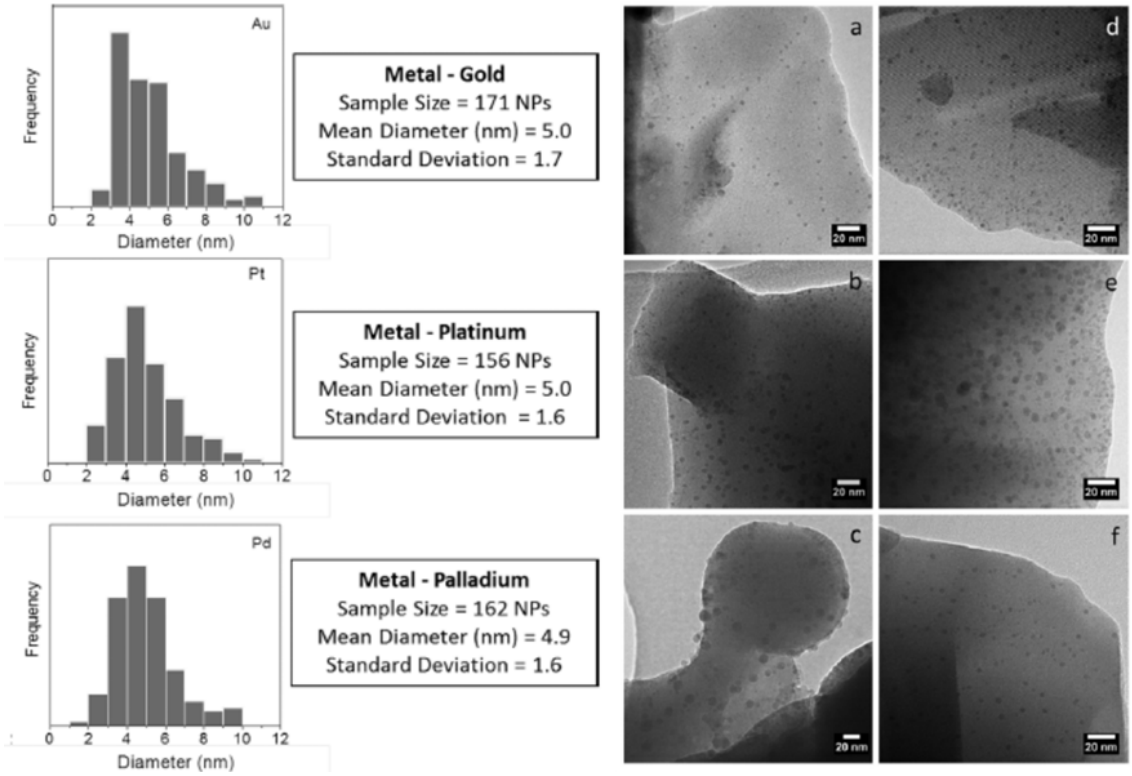

Figure 3-e: Left – Histogram showing the particle size distribution for the Au, Pt and Pd catalysts. Right – TEM images of (a) Au (b) Pt and (c) Pd catalysts after calcination. (d) Au (e) Pt and (f) Pd catalysts after use in the aerobic oxidation of benzyl alcohol.[217]

These findings laid the fundamental building blocks in the development of this novel extrusion technique towards generating supported Au, Pt and Pd nanoparticles within these systems.[217] Under examination as aerobic oxidation catalysts for the benzyl alcohol

to benzaldehyde transformation, it was noted that all three materials, Au, Pt and Pd/CuClP presented very similar levels of catalytic activity: alcohol conversions of 50-60% and benzaldehyde selectivities of 70-80%.[217] Although this observation would appear unanticipated, as one would expect different behaviour from the three metals, it was rationalized due to all three metals having previously shown similarly high levels of activity for this particular reaction at similar nanoparticle size distributions.[136,138,141,142,148,151,218,219] While this may be true, it is rare to find such comparable activity for three such similar systems. Although notably independent, this would suggest that there is a lot more understanding required in order to fully explain this behaviour.

What these catalytic studies did demonstrate however was the highly sought after robustness of these open-framework supported nanoparticle catalysts. Through stringent ICP analysis, metal leaching of the Pt, Au and Pd species was ruled out. Pre- and post-catalysis TEM and PXRD showed the ability of these systems to retain the structural stability and phase purity of the host framework but also the nanoparticle dispersion and size distribution with no notable agglomeration. Further rigorous recycle tests validated the stability by showing no drop in catalytic activity over three recycles.[217]

Following these discoveries, it was postulated that the absence of any nanoparticles from the as-synthesised material and the generation of the nanoparticles in this manner, post synthetically, could in fact pave the way towards control over shape, size and distribution through simply tailoring the extrusion process. It therefore remains to be seen whether one can truly control the nanoparticle formation through this extrusion methodology. Using conditions such as temperature, gas flow rates and/or length of activation to adapt the nature of the active nanoparticle species and apply these materials to other processes.

3.1.3 The Selective Oxidation of Benzyl Alcohol

Oxidation reactions are ubiquitous in the pharmaceutical and fine-chemical industries, and are fundamentally important for introducing oxygen-rich functional groups to organic molecules. For example, aldehyde- and ester-containing molecules are heavily employed as flavouring and fragrance agents owing to their volatility and distinctly aromatic nature.[134] As discussed in Section 1.2.5, benzaldehyde is a key component for most almond-based flavourings while finding other uses as a precursor for plastic additives and as an intermediate in the synthesis of antibiotic drugs such as chloramphenicol and ampicillin, as well as stimulants like ephedrine.[133] Industrially, it is synthesized by the hydrolysis of benzyl chloride. However, the dehydrogenative oxidation of benzyl alcohol is a viable, chloride-free and environmentally benign alternative.[133]

Traditionally, industrial oxidation reactions are based on the use of stoichiometric quantities of inorganic metal-based oxidizing agents such as MnO_2 and CrO_3, or harsh mineral acids like H_2SO_4 and HNO_3, which result in hazardous, corrosive and toxic operating conditions as well as the generation of large quantities of polluting waste by-products.[27] Due to the increased demand for the chemical and related industries to reduce their negative impact on the environment, there is a significant drive to find alternative economic and sustainable oxidation reagents and synthetic protocols.[27] Further details were discussed in Section 1.1.4.

The abundance of molecular oxygen, its high atom-economy in oxidation reactions, low cost and non-toxic reaction conditions make it an appealing candidate as an oxidant.[20] Although high-pressure and relatively high reaction temperatures are often required, since the reaction occurs in the gas phase. Similarly, simple peroxides such as H_2O_2 and TBHP are often considered as alternative green oxidants.[20] Although their use often leads to the generation of larger quantities of by-products in comparison to reactions with molecular oxygen, these oxidants are slightly more reactive due to the lower BDE of the single O-O bond (208 $kJmol^{-1}$ for H_2O_2 and 188 $kJmol^{-1}$ for TBHP)[220] relative to the O=O bond (491 $kJmol^{-1}$),[29] with the added potential to operate under comparatively milder conditions. Nonetheless, suitable catalysts are often still required to activate the oxidants in order to achieve satisfactory activity and selectivity within reasonable reaction conditions.

In recent years, supported noble metal nanoparticle catalysts have shown great promise in the activation of both molecular oxygen and simple peroxides for the selective oxidation of benzyl alcohol, see Table 3-a and Table 3-b. This is due to the zero valent (metallic) Pt, Pd or Au species being the active site for the dissociative adsorption of the alcohol and ensuing β-hydride elimination in the alcohol dehydrogenation process.[121,221] These tables highlight the vast range of different nanoparticle-support systems exploited within this narrow subset of active metals (Au, Pt and Pd). Here the higher temperature required in order to activate molecular oxygen is evident but further to this it is apparent that higher TOFs are more accessible. Therefore, through utilization of molecular oxygen, this could prove significant towards maximising catalytic output. That being said, while higher temperatures appear to facilitate improved catalytic activity with a markedly more reluctant oxidant, they appear to impart losses on the benzaldehyde selectivity. In fact, benzaldehyde selectivities are far lower than desired in the majority of cases with only three examples able to achieve yields of >90% with TOFs upwards of 100 hr^{-1}. Clearly there is an incentive to generate new catalytic systems that are able to achieve both high levels of activity and selectivity with these more sustainable oxidant systems.

While the impact of the oxidant and reaction conditions can be seen from Table 3-a and Table 3-b there is significantly more to consider with regards to nanoparticle catalysts. It is

not simply a case of relating the choice of active metal and oxidant to the catalytic output. As detailed in Section 1.2, nanoparticle morphology and nanoparticle-support synergies play a key role in any catalytic activity. From Table 3-a and Table 3-b, the overwhelming dependence upon impregnation methodologies and metal oxide supports is evident. The preference towards metal oxide supports has already been discussed and is likely down to their simple fabrication, robust nature, economic advantages and their ability to provide reproducible nanoparticle systems through impregnation protocols. However, the over reliance on impregnation methods should be a concern given that they are known to frequently produce nanoparticle systems with high levels of particle mobility at elevated temperatures. Therefore, they often deactivate through agglomeration. Given that this summary also highlights a reluctance to employ organic supports and stabilisers/capping agents, likely due to their limited thermal stability, the need for more adept synthetic protocol for generating these systems is clear.

For alcohol oxidation, specifically the dehydrogenation of primary alcohols, the nature of the support is known to play significant role. Namely, basic conditions can facilitate the initial deprotonation of the alcohol and thus aid in increasing reaction rates. Hence basic nanoparticle hosts are preferred.[121] This was shown by Mori *et al.*[148] when comparing the levels of benzyl alcohol conversion over Pd nanoparticle catalysts; a clear dependence on the basicity of the support was determined. This demonstrates the most basic support, hydroxyapatite, to be the most active (99% conversion) compared to the least basic, carbon (46% conversion), with other metal oxide supports (Al_2O_3 and SiO_2) in between them. Furthermore Fang *et al.*[222] established that the basicity of the nanoparticle host, for Au systems, affects not only the activity but predominantly the selectivity towards the aldehyde. It was determined that either increased numbers of acidic or basic sites upon the support surface would facilitate increased levels of benzyl alcohol conversion. However, only high levels of basic sites would encourage increased aldehyde selectivities. This is in contrast to observations made by Villa and co-workers who observed an inverse relationship between the basicity of the NiO support towards the aldehyde formation. They determined this to be a consequence of the increased basicity of the Au/NiO catalysts encouraging sequential oxidation towards the carboxylic acid.[223] It appears that overall basic conditions will improve catalytic activities by increasing the reactivity of the system. However, one should be wary of over active systems that cause lower levels of aldehyde selectivities due to the over oxidation of the alcohol substrate.

Another key factor to consider amongst these systems is the impact of nanoparticle size. With nanoparticle morphology or more specifically shape generally not reported, it is hard to ascertain meaningful conclusions surrounding its effect. That being said, the impact of nanoparticle size and the volume of under coordinated surface sites has been discussed

in Section 1.2.4. This aspect of nanoparticle morphology also has a significant impact within the oxidation of benzyl alcohol, as expected given the structure-sensitive nature of alcohol oxidation processes.[49,113,120,121] Although subtle, this can be seen within Table 3-a and Table 3-b where the trend towards higher TOFs does roughly correlate with a decrease in nanoparticle diameter. However, this effect is more clearly demonstrated by the research of Chen and co-workers into the impact of Pd nanoparticle size for the oxidation of benzyl alcohol. They demonstrated a clear volcano type size dependence on catalytic activity across a 2.2 – 10.0 nm size range with a constant metal loading: 10.0 nm particles displaying conversions of < 5%; 3.6 nm particles conversions of > 95 % and 2.2 nm particles displayed conversions of 42 %.[224] Similarly, the increase in catalytic activity with decreasing nanoparticle diameter was observed for Au nanoparticle systems by Boronat *et al.*[225] for MgO systems and by Fang *et al.*[222] for hydrotalcite supported systems. This was further supported by computational studies.[225]

Given the preceding discussions, it is clear that the development of such sustainable oxidation catalysts relies on a detailed understanding of the nature of the active sites at a molecular level. This requires a multidisciplinary design-application approach, drawing on strengths of materials chemistry and spectroscopic characterization. By gaining in-depth knowledge of the local structural environment of the active centres within catalytic nanostructures, it is hoped that structure–property correlations can be established, with a view to adopting a more generalized approach for the predictive design of single-site heterogeneous catalysts in industrially significant, sustainable oxidation reactions.

Active Metal	Support	Oxidant	Synthesis	Size (nm)	Time (hr)	Temp (°C)	Benzyl Alcohol Conversion (mol%)	Benzaldehyde Selectivity (mol%)	TOF (hr^{-1})	Ref
Pd	Al_2O_3/SiO_2	Air	CP	3.6	10	70	97	98	167*	224
Au	CeO_2	Air	Imp	3.0 – 4.0	2	90	98	99	123*	142
Pd	SBA-16	Air	Imp	2.0 – 4.0	12	25	99	99	83*	103
Pt	*ZrO_2*	*Air*	*Imp*	-	*N/A*	*90*	*87*	*100*	*46*	226
Pt	**CuClP**	**Air**	**Extrusion**	**5.0**	**6**	**120**	**28**	**100**	**24***	**N/A**
Au	Hydrotalcite	Air	Imp	2.7	24	40	85	92	8*	104
Au	TiO_2	H_2O_2	-	-	3	90	99	85	40*	153
Au	BaO	TBHP	DP	11.5	2	94	53	81	84	152
Pt	**CuClP**	**TBHP**	**Extrusion**	**5.0**	**6**	**65**	**39**	**98**	**82***	**N/A**
Au	CaO	TBHP	DP	9.6	2	94	41	86	78	152
Au	Al_2O_3	TBHP	DP	4.1	2	94	71	65	74	152

*Table 3-a: Table presenting a comparison of heterogeneous nanoparticle catalysed oxidation of benzyl alcohol to benzaldehyde focusing on Au Pt and Pd catalysts. Italics denotes a continuous flow process. Bold denotes the catalysts studied within this work, notably the Pt/CuClP catalyst activated at 500 °C. * shows independent calculation of the TOF based on the information published by the authors. DP – deposition precipitation, CP – coprecipitation, CD – colloidal deposition and Imp – impregnation. Sizes given as approx. mean diameters based on the information presented by the authors.*

Active Metal	Support	Oxidant	Synthesis	Size (nm)	Time (hr)	Temp (°C)	Benzyl Alcohol Conversion (mol%)	Benzaldehyde Selectivity (mol%)	TOF (hr^{-1})	Ref
Au	TiO_2	Oxygen	DP	6.3	5	100	35	55	534	[143]
Au	SiO_2	Oxygen	DP	6.3	5	100	34	59	512	[143]
Pd	Hydroxyapatite	Oxygen	Imp	3.8	1	90	99	100	435*	[148]
Pd	C	Oxygen	Imp	3.8	1	90	46	91	230*	[148]
Pd	SBA-15	Oxygen	CD	5.0 – 10.0	16	120	69	64	221	[150]
Pd	CeO_2	Oxygen	CD	5.0 – 10.0	16	120	50	63	160	[150]
Au	SiO_2	Oxygen	Imp	4.7	2	80	79	94	130	[145]
Pd	SBA-16	Oxygen	Imp	2.0 – 4.0	8	25	99	99	125*	[103]
Pt	C	Oxygen	CD	3.0 – 3.5	3	60	49	79	98	[139]
Au	MgO	Oxygen	Imp	9.0	5	120	56	95	88*	[144]
Au	Al_2O_3	Oxygen	Imp	4.1	5	130	69	65	81	[141]
Au	CuO	Oxygen	Imp	10.9	5	130	28	69	32	[141]
Au	Fe_2O_3	Oxygen	Imp	8.5	5	130	16	100	30	[141]
Pd	C	Oxygen	CD	3.0 – 3.5	3	60	18	91	30	[139]
Au	*SiO_2*	*Oxygen*	*Imp*	*15.5*	*N/A*	*326*	75	*98*	*27**	[146]

*Table 3-b: Table presenting a comparison of heterogeneous nanoparticle catalysed aerobic oxidation of benzyl alcohol to benzaldehyde focusing on Au Pt and Pd catalysts. Italics denotes a continuous flow process. * shows independent calculation of the TOF based on the information published by the authors. DP – deposition precipitation, CD – colloidal deposition and Imp – impregnation. Sizes given as approx. mean diameters based on the information presented by the authors.*

3.2 The Development of Platinum Nanoparticle Catalysts & Their Robust Catalytic Potential for Alcohol Oxidations with a Range of Oxidants

3.2.1 Activation of the Platinum Doped Copper Chloropyrophosphate via Calcination

The CuClP material has the general formula $A_9Cu_6(P_2O_7)_4Cl.[MX_4]Cl_n$ where A is Rb, K or NH_4, M is Cu, Pt, Pd or Au and X is typically Cl or Br as reported by Williams *et al.*[194] This, in its own right, highlights the facile ion incorporation of anionic species and the inherent structural flexibility of these systems. For consistency within these works, the materials studied are the Pt/CuClP systems. These are of the form: $Rb_9Cu_6(P_2O_7)_4Cl.[MCl_4]Cl_2$ where M is Cu in the 'undoped' or 'blank' material and Pt within the nanoparticle containing systems as depicted in Figure 3-f.

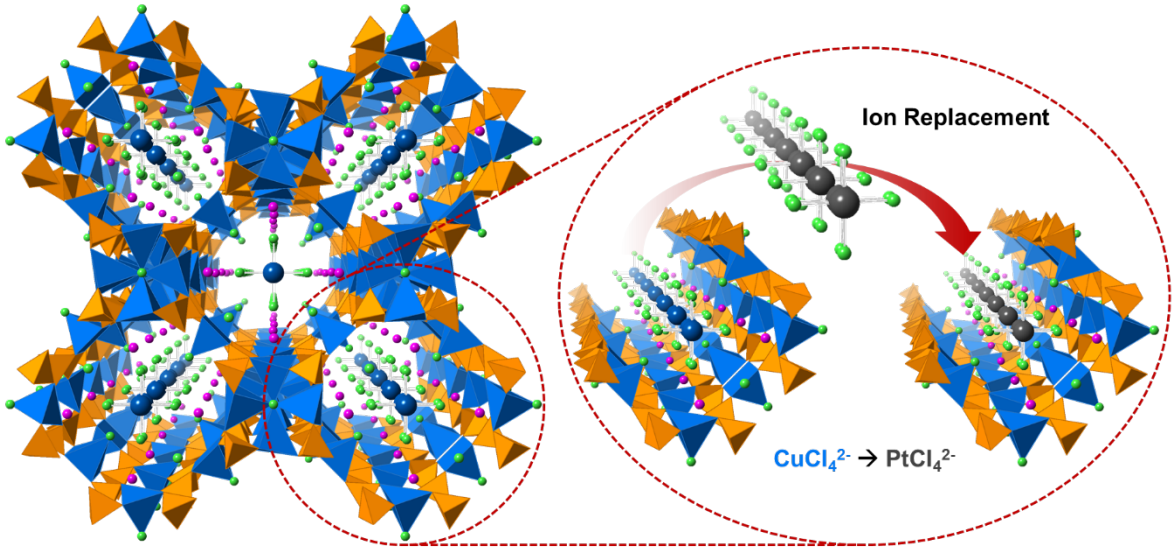

Figure 3-f: Crystal structure of the $[Rb_9Cu_6(P_2O_7)_4(MCl_4)Cl_2]$ framework where M = Cu (blue) or Pt (grey), depicting the replacement of $[CuCl_4]^{2-}$ ions with $[PtCl_4]^{2-}$. Rb – pink, Cl – green and P – orange, oxygen has been omitted for clarity and it's containing units depicted as polyhedra.

Hinde and co-workers have already demonstrated the ability of these materials to form supported nanoparticle systems through a thermal extrusion process. This process involves heating the CuClP framework (for example, in air) and through thermal decomposition of the chlorometallate anion, the metallic species is extruded to the framework surface. The ion decomposition yields both chlorine gas, as the only by-product, and the metallic nanoparticles themselves, as shown in Figure 3-g. Although the

possible existence of small metallic species remaining within the 1D channels of the host framework can't be overlooked, the very restrictive pore diameter of approx. 1.3 nm and lack of evidence for such species make their existence unlikely. Even if they were present within the 1D channels, their access by reactant species would be severely restricted. Therefore it is assumed that the entirety of the metallic species that formed is indeed extruded to the hosts' surface and available for catalysis.

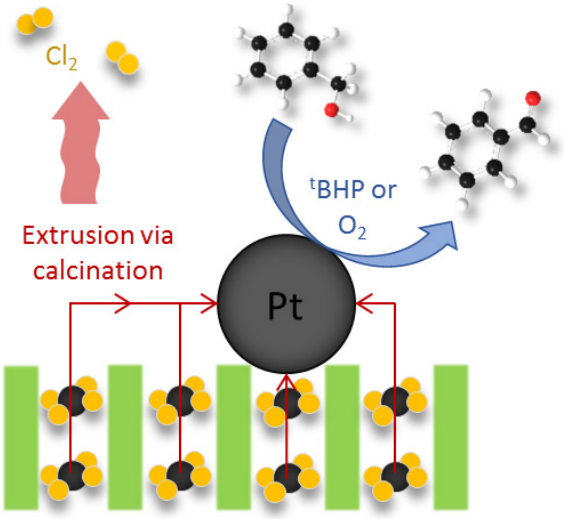

Figure 3-g: Schematic representation of the extrusion process: decomposition of the incorporated chlorometallate anions yielding chlorine gas and catalytically active nanoparticles upon the framework surface.

In comparison with the more traditional supported nanoparticle catalyst synthesis protocols discussed in Section 1.2.3, this extrusion methodology presents without many of the aforementioned limitations. For example, the materials are synthesised hydrothermally and the subsequent nanoparticle generation is carried out in a single and facile step, removing the need for any expensive or elaborate hardware as well as not being particularly labour intensive. This method makes use of well understood nanoparticle precursors and while this results in chloride being present, this is removed in the thermal extrusion and does not appear to cause any significant agglomeration. In fact, the documented mobility that chloride imparts on metallic nanoparticles could be why the extrusion of *chloro*metallate ions from these frameworks occurs easily, no such observations were made for their bromide counterparts.[9,53,194] Another clear advantage over colloidal methods is the way that the nanoparticles generated are uncapped and completely absent of organic moieties. Therefore, this method overcomes the most significant drawback hampering the use of colloidal methods on a larger scale. Further, the nature of the support framework is believed to play a key role in the nanoparticle stability within these systems. Given its ionic nature, one would envisage enhanced Coulombic interactions aiding in the anchoring and stabilizing of the small uncapped

nanoparticles. This is an attribute that could lead to superior catalytic stability over the more common metal oxide supports. Thus, in conjunction with the work conducted by Hinde earlier, it would appear that this methodology provides both good nanoparticle stability as well as consistent, small and narrow size distributions of approx. 5 nm for the Pt/CuClP.[217]

While potential advantages exist for the extrusion methodology over common nanoparticle syntheses protocols, one key aspect that could pose a problem is the control over metal loading. This is one aspect that traditional methods such as impregnation control well and due to the notably low water volume within the hydrothermal synthesis of these materials, mixing by diffusion is significantly limited. This likely leads to an inhomogeneous precursor distribution within the framework channels. The only water present is from the phosphoric acid (85 wt. % in water) and rubidium hydroxide (50 wt. % in water) solutions, just 0.495 g of the total 1.203g. This was addressed by increasing the amount of mixing in the hydrothermal synthesis. The original protocol involved simplistic mixing of the solids with a spatula before the sequential addition of the phosphoric acid and rubidium hydroxide solutions, followed by more manual mixing with a spatula before the heat treatment. As a result, the solid components are now ground together in order to achieve significantly better mixing before the addition of the liquid components and two additional sonication steps have also been introduced for 5 and 15 min after phosphoric acid and rubidium hydroxide addition respectively. This led to an improvement in synthetic yields from approx. 0.15 g (36%) to approx. 0.20 – 0.25 g (48 – 61%) (calculated by weight in accordance to Cu as the limiting reagent) but also good incorporation of the metal precursor into the host framework from the stoichiometries employed 7 ± 1 wt. %.

While improvements have been made towards a more reliable incorporation of the nanoparticle precursor, the pivotal variable for this particular protocol is the extent of the extrusion. Is it possible to completely extrude 100% of the precursor incorporated? If not, is it possible to partially extrude these species in a controlled manor? Determination of these points are key objectives within these works and it can be envisaged that there are many variables inevitably effecting this extrusion process such as time, environment, heating rates, temperature, gas flow rates etc. Therefore, these are all available variables and potential opportunities to tune the process to control the extent of the extrusion and achieve the desired nanoparticle morphology and environment.

3.2.2 Combining X-Ray Characterisation and Catalytic Investigations to Elucidate Structural Properties

Before probing the catalytic properties of these materials and evaluating them against other reported systems one must establish an ideal candidate for the comparison and

address the questions posed in the previous section (Section 3.2.1). Thus, a range of Pt/CuClP catalysts activated under different calcination temperatures (200 – 600 °C) were subjected to XAS analysis. Comparison of these samples has enabled the evaluation of the relationship between the extent of extrusion and the activation temperature, facilitating the quantification of the process and resultantly, nanoparticle formation. The magnitude and imaginary components of the k^3-weighted Fourier transform data and their first shell fits are shown in Figure 3-h, along with the corresponding fitting parameters of the EXAFS data in Table 3-c. The EXAFS data shows a slight but notable increase in Pt-Pt CNs (0.8 – 1.2) and a respective decrease in Pt-Cl coordination (4.5 – 3.7), suggesting a minor correlation between the extent of nanoparticle formation and the calcination temperature. Despite the percentage errors, particularly with the lower CNs being larger than desired, the trend is more evident in the XANES spectra displayed in Figure 3-i.

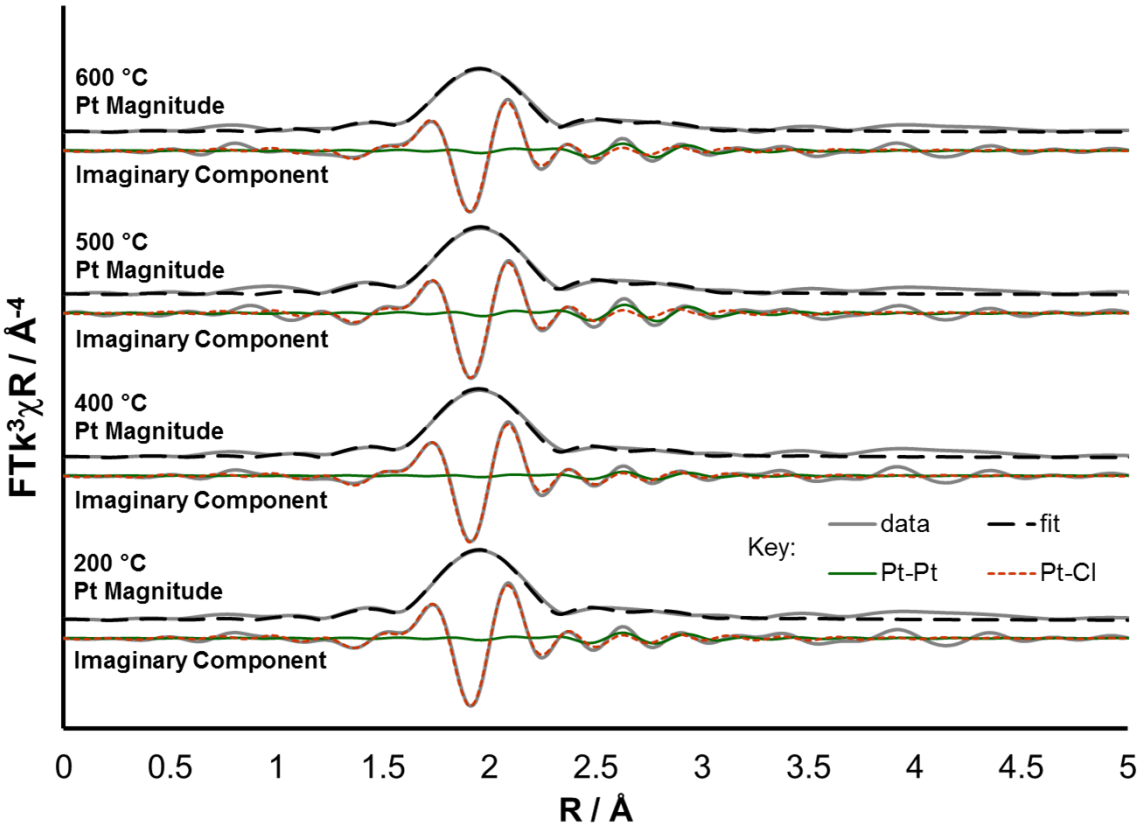

Figure 3-h: Magnitude and imaginary component of the k^3 weighted Fourier transform for the EXAFS data of the Pt/CuClP materials calcined (2 hr) under increasing activation temperature, ascending up the plot. Associated scattering paths are included for the imaginary component.

Sample	Abs Sc	N	R / Å	$2\sigma^2$ / Å^2	E_f / eV	R_{factor}
Pt/CuClP	Pt – Cl	4.5 (2)	2.320 (5)	0.0024 (3)	8.8 (9)	0.010
200 °C	Pt – Pt	0.8 (5)	2.77 (3)	0.004 (2)		
Pt/CuClP	Pt – Cl	5.0 (2)	2.319 (5)	0.0026 (3)	8.8 (9)	0.012
400 °C	Pt – Pt	0.8 (8)	2.78 (4)	0.004 (4)		
Pt/CuClP	Pt – Cl	4.4 (2)	2.320 (6)	0.0026 (4)	9 (1)	0.013
500 °C	Pt – Pt	1.4 (5)	2.78 (2)	0.004 (2)		
Pt/CuClP	Pt – Cl	3.7 (2)	2.317 (5)	0.0025 (3)	9.2 (9)	0.011
600 °C	Pt – Pt	1.2 (5)	2.78 (2)	0.005 (2)		

Table 3-c: EXAFS fitting parameters of the Pt/CuClP materials calcined (2 hr) under increasing activation temperature. Pt sample - $S_0^2 = 0.91$ as deduced by Pt foil standard; Fit range 3<k<12.5, 1<R<3; # of independent points = 12.

Comparison of the XANES data shows a clear depreciation in white line intensity between the Pt/CuClP samples activated at 500 and 600 °C. While the three lower temperature samples demonstrate similar white line intensities, the transition towards the metallic reference between the 500 and 600 °C samples is clear. This suggests a lowering of the average Pt oxidation state (Pt^{IV} – Pt^0) within the sample as the activation temperature is increased across this range. The CNs alone would suggest this transition is minimal (in contrast to the original observations made by Hinde and co-workers) with the majority of the Pt species remaining as the $[PtCl_4]^{2-}$ ion. Nonetheless, it is clear that small levels of extrusion are easy to achieve at lower temperatures, even as low as 200 °C. These are considerably lower than the reported minimum activation temperature for the Au/CuClP material.[194] While this is true, the grouping of the XANES data followed by the clear drop in oxidation state over a relatively narrow temperature window could suggest that an activation barrier is overcome at approx. 500 °C and above, facilitating the beginning of increased levels of extrusion.

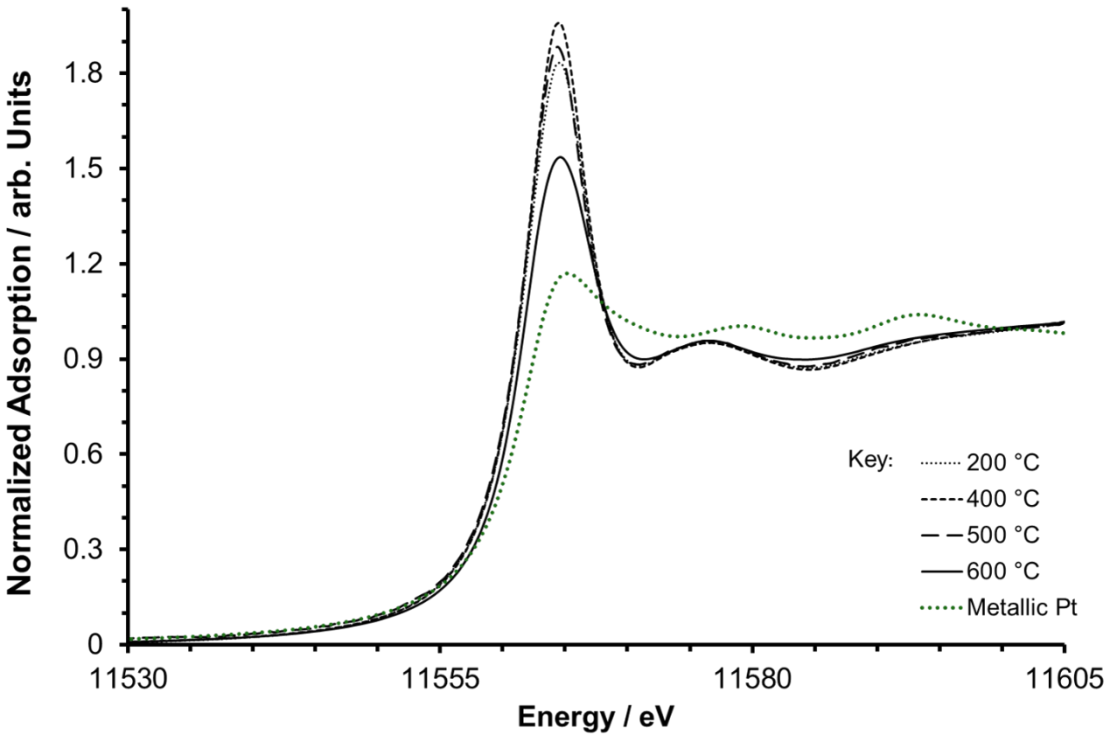

Figure 3-i: Stacked XANES data of the Pt L_{III} edge for the Pt/CuClP materials activated at different temperatures with a metallic platinum reference in green.

This concept of the relationship between calcination temperature and extent of extrusion being key, and not necessarily linar, is also reflected in the catalytic studies. Here we assume that the rate of conversion of benzyl alcohol is directly related to the abundance of platinum nanoparticles and therefore the platinum oxidation state, as discussed above. Given that the blank reactions (no catalyst), carried out at comparatively higher temperatures show no significant benzyl alcohol oxidation (Table 3-d), the conversions shown in Table 3-e display a significant and progressive increase with catalyst calcination temperature. This provides another clear indication that the activation temperature is related to nanoparticle formation (via extrusion), and that this does indeed have a direct influence on the catalytic activity of these materials. There is a 44% increase in the alcohol conversion between the Pt/CuClP samples activated at 400 °C to that at 500 °C and this increases significantly between 500 and 600 °C to 148% suggesting a concomitant trend to that shown by the XANES analysis in Figure 3-i. This evidences that the relationship between the extent of extrusion (average Pt oxidation state or alcohol conversion) is not linear and that there could exist a temperature at which an optimum level of extrusion and nanoparticle formation could be achieved. Whether this is indeed 100% of the $[PtCl_4]^{2-}$ precursor incorporated, is yet to be determined. Undoubtedly, considering the CNs displayed in Table 3-c this optimum temperature would lie upwards of the 600 °C trialled in this study.

Oxidant	Temperature / °C	Time / hr	Conversion / mol%	Benzaldehyde / mol%	Benzoic Acid / mol%
Air[a]	130	5	8	>99	0
TBHP[b]	110	5	6	>99	0

Table 3-d: Full blank reaction results with corresponding conversions and selectivities at the quoted temperature and reaction time. Reaction conditions [a]: benzyl alcohol (9.247 mmol), diglyme as internal standard (6.335 mmol), tertiary butanol (30 mL), air (20 bar), oxidant to substrate molar ratio of 1:0.85. Reaction conditions [b]: benzyl alcohol (4.624 mmol), diglyme as internal standard (2.981 mmol), tertiary butanol (15 mL), TBHP (11.0 mmol in decane), oxidant to substrate molar ratio of 1:0.85.

Catalyst	Conversion / mol%	Benzaldehyde / mol%	Benzoic Acid / mol%	Benzyl Benzoate / mol%
Pt/CuClP 200 °C	15	>99	0	0
Pt/CuClP 400 °C	22	>99	0	0
Pt/CuClP 500 °C	39	98	2	0
Pt/CuClP 600 °C	97	65	34	<1

Table 3-e: Conversions and product distributions from reactions conducted with Pt/CuClP catalysts activated under increasing calcination temperature. Reaction conditions: 65 °C, 6 hr, benzyl alcohol (27.7 mmol), substrate to oxidant (TBHP) mole ratio=1.00:1.15, diethylene glycol dimethyl ether (11.2 mmol) and catalyst (50 mg).

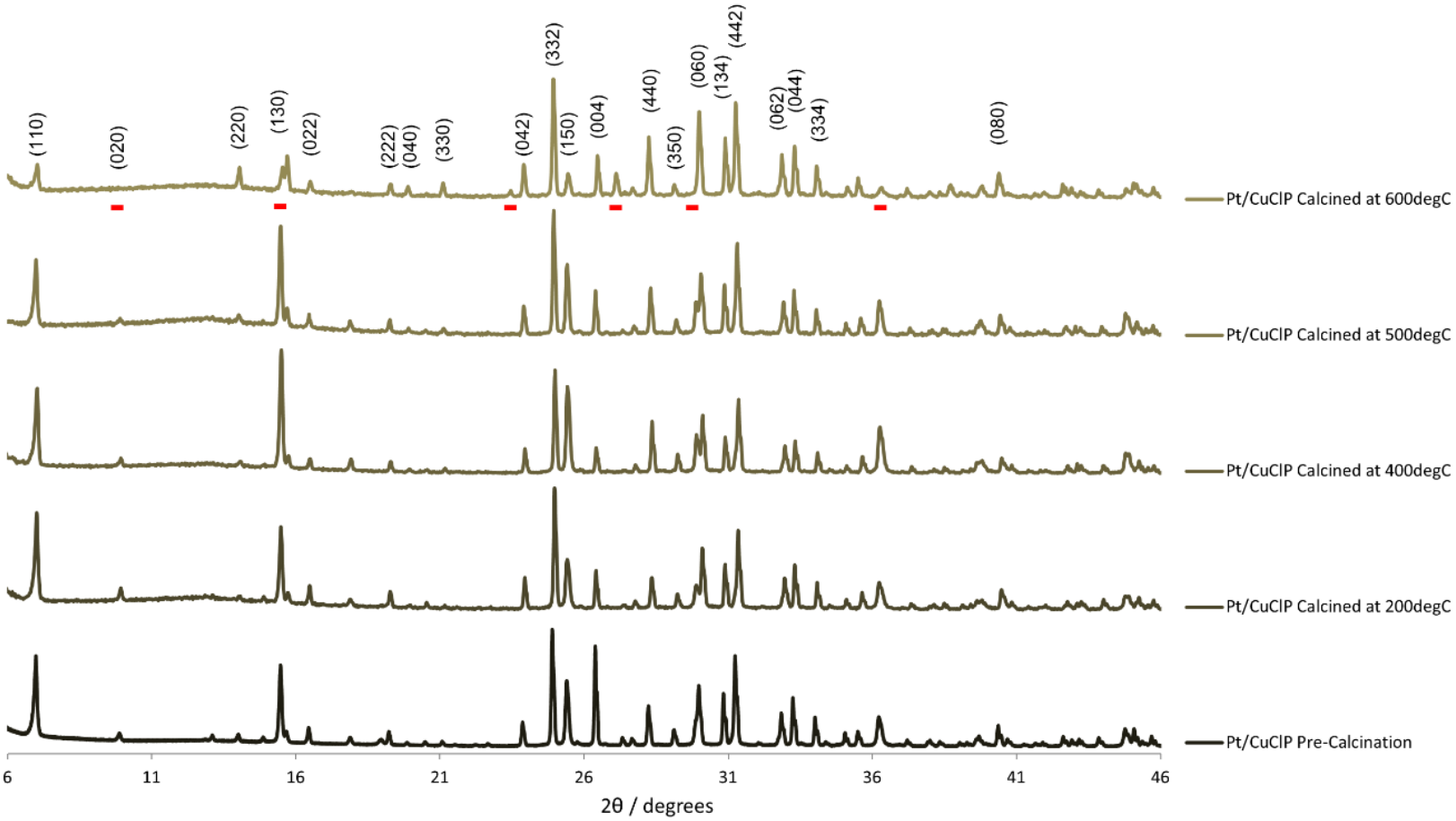

Figure 3-j: Indexed PXRD patterns for the Pt/CuClP under increasing calcination temperature. Data shown for the uncalcined sample through 200, 400, 500 and 600 °C up the plot (all materials were calcined for 2 hr). Changes in the PXRD pattern are observed when the material is calcined at 600 °C which have been highlighted with red markers.

It is also observed that when the calcination temperature exceeds 500 °C, the selectivity of the catalyst drastically diminishes. While it has been noted previously that these materials can undergo thermal degradation at temperatures above 600 °C,[194] the loss of selectivity is also a side effect of over-oxidation. This is a common problem encountered in many oxidation reactions as stated in Sections 1.2.4 and 1.2.5 and has been shown to be associated with the loss of site isolation.[227] Therefore this could be a consequence of the increased quantity of metallic sites available driving an increase in conversion but resulting in the loss of site isolation.[142,228] With this rationale in mind, it is worth noting that although Hinde *et al.*[217] has shown that an abundance of nanoparticles can be produced via activation under similar conditions, the transition in Pt average CN is minimal (approx. 0.5) and well below that expected of 5 nm Pt nanoparticle (> 10).[48,106,107] This is most likely due to the volume of Pt extruded via these means being very small leaving the majority of the Pt species being present in its precursor form. Therefore, while the production of catalytically active nanoparticles is clear from previous works[217] and both the catalytic and XANES data presented in Table 3-d, Table 3-e and Figure 3-i respectively, the loss in product selectivity is more likely due to structural changes within the material as opposed to a consequence of losing site isolation from the '*over*' production of nanoparticles. Indeed, this is further evidenced by inconsistencies in the PXRD of these materials observed in Figure 3-j at elevated temperatures. Consequently, these findings bring into question the stability and true nature of these materials when activated under such high temperatures due to the likely degradation of the host framework.

Therefore, for the purposes of this study and to find an appropriate Pt/CuClP candidate to use for comparing both TBHP and air based oxidations of benzyl alcohol, it can be determined that the complete extrusion of the Pt precursor cannot be attained under these activation conditions. This is due to the activation temperature required to produce meaningful levels of nanoparticle production being above the maximum level allowed by the framework's stability. This has led to the potential degradation of the framework within the most catalytically active sample. As a result, the following kinetic work was conducted with the most active but reliable system. The Pt/CuClP catalyst activated by calcination at 500 °C was used with optimized oxidant to substrate ratios in order to maximize the reaction selectivity towards benzaldehyde.

3.2.3 Kinetics & Mechanistic Insights

A kinetic study was performed for the aerobic and TBHP oxidation of benzyl alcohol by analysis of the conversion rates at different reaction temperatures. Both sets of reactions were run initially for 5 hr to establish the relationship between the benzyl alcohol conversion, product selectivity and time as shown in Figure 3-k and Figure 3-l. For the

aerobic oxidation, the reaction profile of the Pt/CuClP catalyst was zero-order with respect to the conversion of benzyl alcohol, typified by the linear relationship between substrate concentration and time showing little dependence of the substrate concentration on the rate of reaction (Figure 3-k). This is in contrast to the peroxide oxidation where it is interesting to note the deviation from zero-order kinetics, as observed for the O_2 system, even at low levels of conversion: 15 – 20%. The rate of benzyl alcohol oxidation with TBHP decreases over time and thus indicates a dependence on the concentration of the benzyl alcohol and/or TBHP in the reaction (Figure 3-l). In contrast, the selectivity of the TBHP oxidation is maintained at >99% throughout the course of the reaction, whereas benzoic acid is observed as a significant by-product in the aerobic oxidation (Figure 3-k). The higher temperature and pressure required for the O_2 oxidation are likely responsible for the formation of the benzoic acid as the over-oxidation product.

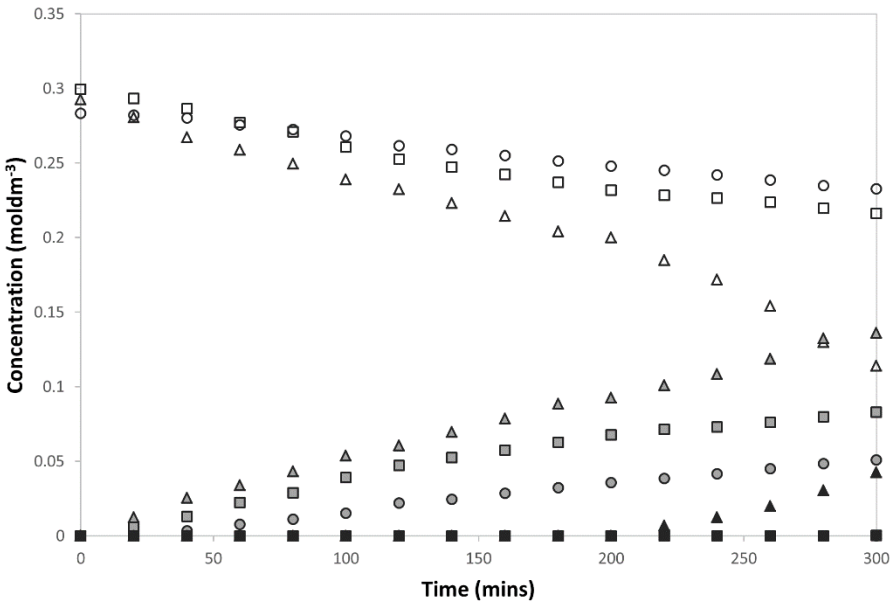

Figure 3-k: Plot showing the change in benzyl alcohol (white fill), benzaldehyde (grey fill) and benzoic acid (black fill) concentration with time in the aerobic oxidation of benzyl alcohol with the calcined (500 °C, 2 hr) Pt/CuClP at 110 °C (circles), 120 °C (squares) and 130 °C (triangles). Reaction conditions: benzyl alcohol (9.247 mmol), catalyst (50 mg), diglyme as internal standard (6.335 mmol), tertiary butanol (30 mL), air (20 bar), oxidant to substrate molar ratio of 1:0.85.

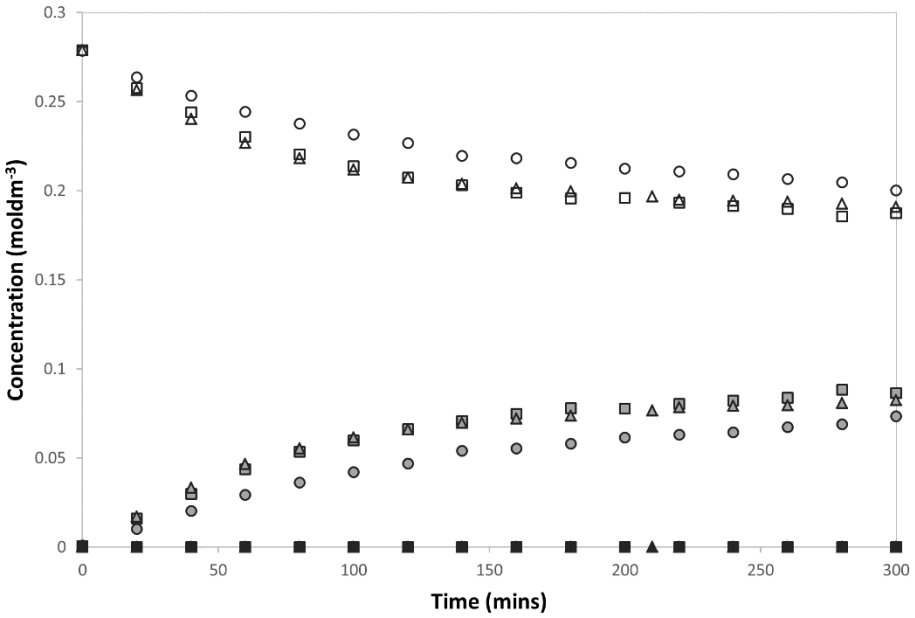

Figure 3-l: Plot showing the change in benzyl alcohol (white fill), benzaldehyde (grey fill) and benzoic acid (black fill) concentration with time in the TBHP oxidation of benzyl alcohol with the calcined (500 °C, 2 hr) Pt/CuClP at 86 °C (circles), 100 °C (squares) and 110 °C (triangles). For reaction conditions (excluding reaction temperature) see Table 3-e.

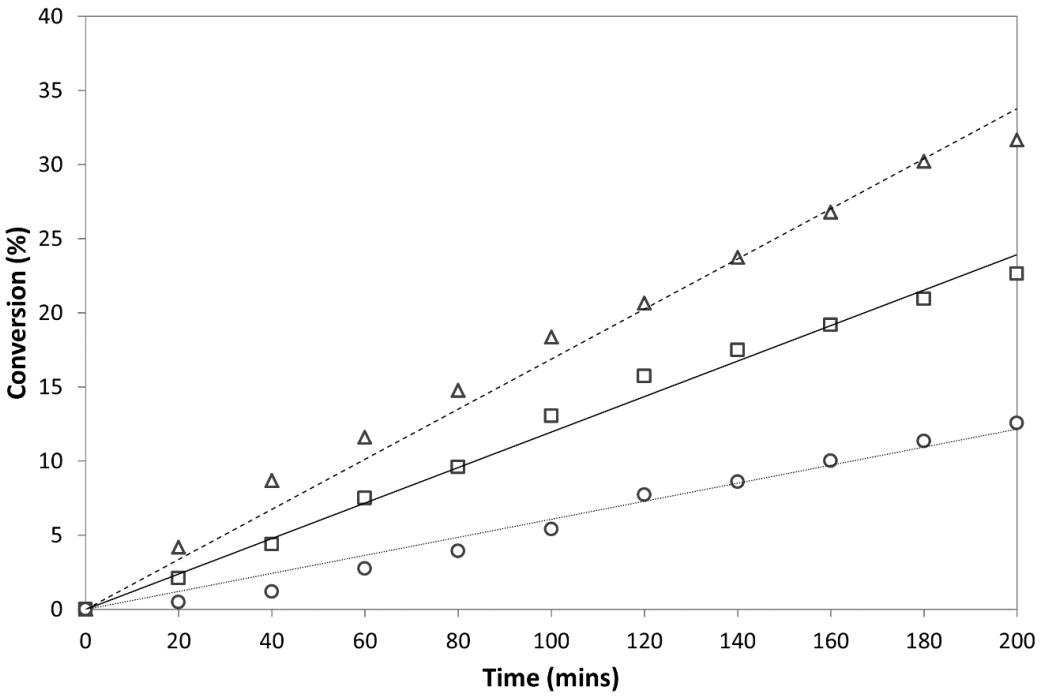

Figure 3-m: Kinetic plot showing conversion of benzyl alcohol by aerobic oxidation with the calcined (500 °C, 2 hr) Pt/CuClP at 110 °C (circles), 120 °C (squares) and 130 °C (triangles). For reaction conditions see Figure 3-k.

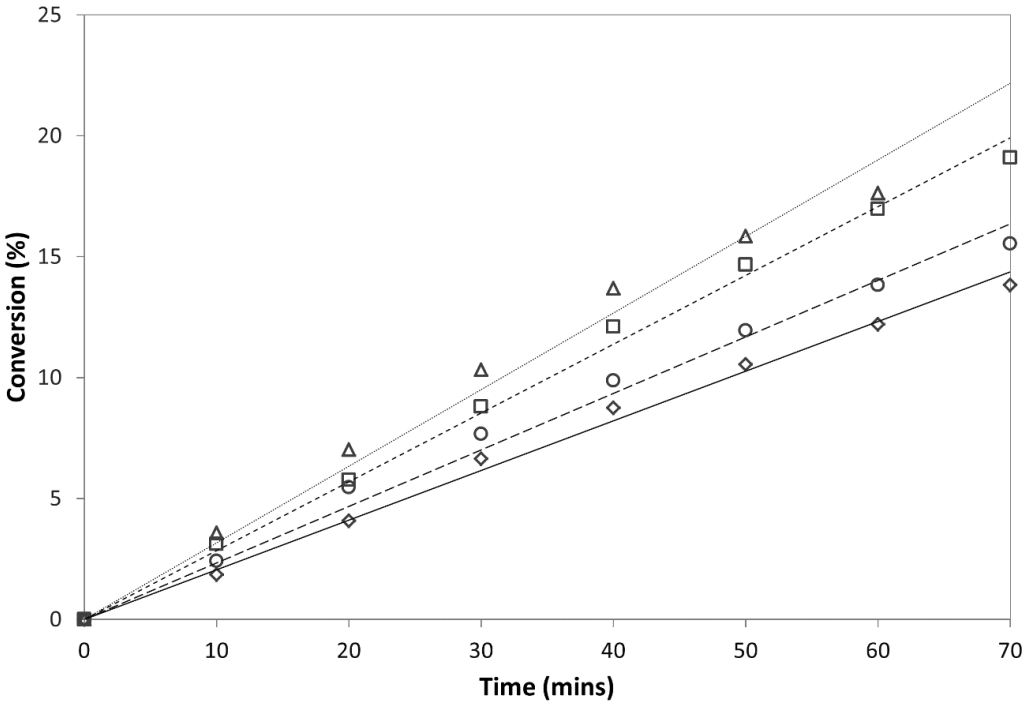

Figure 3-n: Kinetic plot showing conversion of benzyl alcohol by TBHP oxidation with the calcined (500 °C, 2 hr) Pt/CuClP at 87 °C (diamonds) 95 °C (circles), 100 °C (squares) and 110 °C (triangles). For reaction conditions (excluding reaction temperature) see Table 3-e.

In order to calculate the respective activation energies, plots in the form of *[A]* vs *t* needed to be generated. However, due to the relationship between the benzyl alcohol concentration time being non-linear, over the 5 hr time scale for the TBHP system, as displayed in Figure 3-l, the reactions were repeated with smaller sampling divisions. This allowed the representation of the initial linear relationship and the conversion vs time plots for this data. Comparative aerobic data are also represented in Figure 3-m and Figure 3-n. This kinetic data was then used to produce values for *k* at the respective reaction temperatures to construct the Arrhenius plots in Figure 3-o and calculate the activation energies of the two systems.

For the aerobic system (Figure 3-o-a) the activation energy was calculated to be 72.4 $kJmol^{-1}$. This value appears high in comparison with homogeneous nanoparticle systems. Au/PVP,[46] Pd/PVP[46] and Au/P123[228] stabilized systems had activation energies of 25 $kJmol^{-1}$ 33 $kJmol^{-1}$ and 45 $kJmol^{-1}$ respectively. In fact, another bimetallic homogeneous AuPd/PVP system was shown to produce an activation energy as low as 13.7 $kJmol^{-1}$ by Hou *et al.*[229] That being so, the high levels of activity displayed by homogeneous systems have already been discussed in Section 1.1.3 and the Pt/CuClP catalyst compares well against other heterogeneous noble metal catalysts with Pt/ZrO_2[226] and Ru/Al_2O_3[230] displaying activation energies of 78 and 79 $kJmol^{-1}$ respectively. Investigation into the kinetics of the TBHP oxidation of benzyl alcohol using the same calcined Pt/CuClP

catalyst (Figure 3-o-b) revealed an activation energy of 23.6 kJmol^{-1} under analogous substrate to oxidant to catalyst ratios. This is in agreement with the data obtained for similar Au supported nanoparticle materials for the peroxide oxidation of benzyl alcohol at 38[155] and 20[154] kJmol^{-1}, whilst surpassing the values obtained for transition-metal catalysts based on Mn,[231] Mo[232] and W[232] at 30, 84 and 96 kJmol^{-1} respectively. The lower activation energy of the peroxide-based oxidation is not surprising; given the lower BDE of TBHP relative to that of O_2, and as reflected in the activity of the catalyst at temperatures lower than 100 °C. With blank reactions not yielding appreciable conversions (Table 3-d), it is clear that the Pt/CuClP catalyst is able to effectively activate both TBHP and O_2 as oxidants.

With the EXAFS fitting parameters presented in Table 3-c taken into consideration, the Pt-Cl and Pt-Pt CNs clearly show that only a fraction of the chlorometallate anions have been extruded to form metallic nanoparticles on the surface of the materials. As the rate of reaction is correlated with available active sites on the nanoparticle surface and the activation energy directly associated with the rates of reaction, it is noteworthy that the activation energies observed in the 'partially' activated catalysts compete with those reported in the literature with analogous materials.[154,155,226,230] Therefore, with an established method for complete extrusion, in a controlled manor in order to maintain good levels of site isolation, it should be possible to significantly improve on these values.

Oxidation reactions progress either homolytically (single electron transfer) or heterolytically (double electron transfer). Homolytic oxidations are chain reactions involving radicals formed by the homolytic cleavage of an interatomic bond whereas heterolytic oxidation reactions involve the oxidation (by two electron transfer) of a material by an active oxygen compound such as a peroxide, peroxyacid, molecular oxygen itself or by a metal in its high valance state (e.g. Pd^{II} or V^{V} etc.), often stoichiometrically.[27]

For Pt nanoparticles, it is generally accepted that the mechanism of action varies between aqueous and organic media,[139] whereby water facilitates radical-type processes[97,233] and organic media promotes heterolytic mechanisms, in analogy to reactions with Au nanoparticle systems. Through extensive studies on Au nanoparticles, it has been determined that the adsorption of O_2 or peroxides can lead to activated surface-adsorbed superoxide or surface peroxide species that can facilitate the dehydrogenation process (Figure 3-p).[121,142] The subsequent adsorption of the alcohol to form an adsorbed surface alcoholate species then occurs. Abstraction of the β-hydride to the surface of the metal generates the desorbed aldehyde species, with the surface hydrides reacting with the activated surface peroxo species to form water and regenerate sites for adsorption and further catalytic cycles.[46,234] It is likely that similar mechanisms operate also for Pt

nanoparticle systems, including these Pt/CuClP catalysts, in the organic media present for these reactions.

Figure 3-o: Arrhenius plots for the a) aerobic oxidation and b) TBHP oxidation of benzyl alcohol with the calcined (500 °C, 2 hr) Pt/CuClP catalyst. Conversion versus time plots and reaction conditions are given in Figure 3-m (for (a)); Figure 3-n and Table 3-e (for (b)). From C. S. Hinde, A. M. Gill, P. P. Wells, T. S. A. Hor and R. Raja, ChemPlusChem, 2015, ***80****, 1226 – 1230 Reprinted by permission of John Wiley & Sons, Inc.*

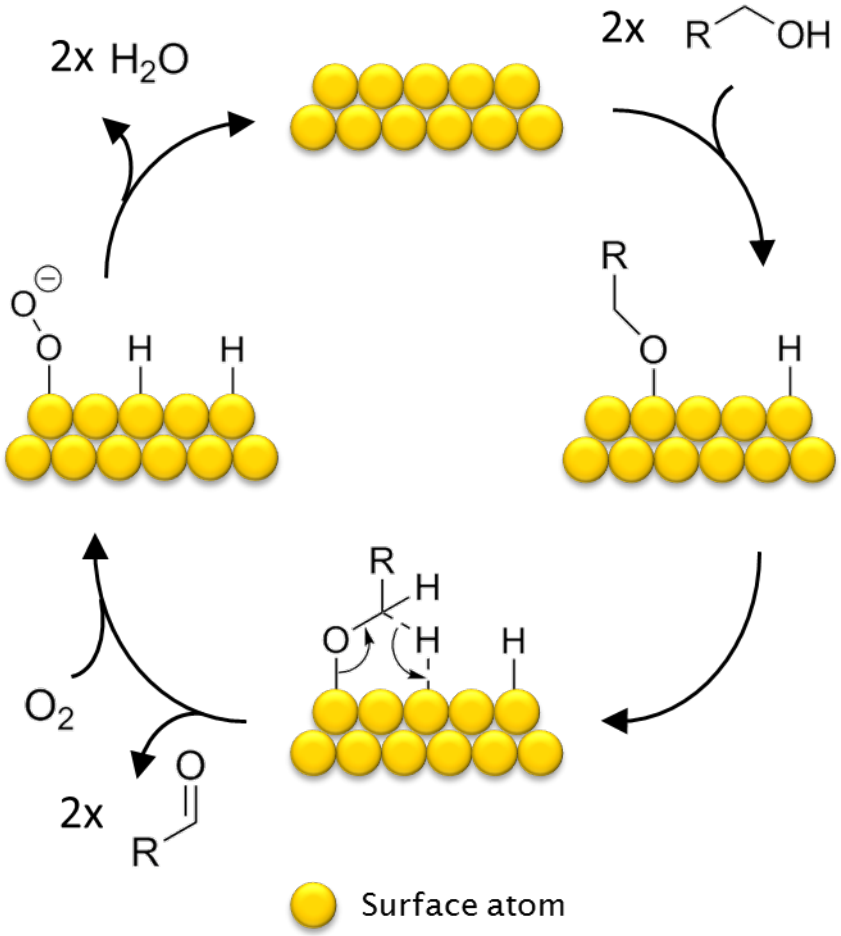

*Figure 3-p: Mechanism for the aerobic oxidation of an alcohol to aldehyde on a metal nanoparticle surface in organic media. From C. S. Hinde, A. M. Gill, P. P. Wells, T. S. A. Hor and R. Raja, ChemPlusChem, 2015, **80**, 1226 – 1230 Reprinted by permission of John Wiley & Sons, Inc.*

3.3 Conclusions

A combination of spectroscopic and catalytic approaches has revealed that activation conditions play a crucial role in controlling the local structural environment of the Pt/CuClP nanoparticle catalysts, which are generated by a one-step extrusion process. Spectroscopic and kinetic analysis further illustrates that the presence of well-defined and isolated nanoparticles is fundamental to activating molecular oxygen for the aerobic oxidation of benzylic alcohols and the ensuing structure–property correlations pave the way for the predictive design of these solid catalysts.

Comparison of activation energies showed a higher value for aerobic oxidation at 72.4 $kJmol^{-1}$ compared with 23.6 $kJmol^{-1}$ for the TBHP oxidation. The aerobic oxidation sustained high rates of conversion with zero-order kinetics and thus negligible influence of substrate concentrations on reaction rates. While the catalyst activated at higher temperatures showed reduced selectivity, with benzoic acid formed as a significant by-product, this only highlights the importance of forming well-defined and isolated nanoparticle sites. In fact it is notable that for all the other catalysts (activated at lower temperatures) including oxidation with TBHP, maintained a high level of selectivity with negligible quantities of by-products formed. However, for the TBHP oxidation this was limited by substrate concentration effects that resulted in considerably lower reaction rates after 4 – 5 hr. The Pt/CuClP nanoparticle catalyst was successful in activating both of these green alternative oxidants, bestowing unique advantages to each process, thereby affording considerable scope for the further exploitation of these catalysts and design strategy.

In order to achieve these targets the activation protocol requires refinement as increased levels of extrusion are still desired in order to maximise catalytic output. Under calcination conditions the activation temperature ceiling has been set at 550 – 600 °C due to the stability of the support framework, witnessed by PXRD and a limited ability to achieve meaningful levels of nanoparticle extrusion is evidenced by the minimal increases in Pt-Pt CNs within the XAS analysis. This therefore justifies the need to review the nature of the activation process. Specific focus should surround the gaseous environment as this could be adapted to better achieve nanoparticle extrusion under more mild conditions.

Chapter 4: The *in situ* Synthesis of Noble Metal Nanoparticle Materials & Their Catalytic Potential

In this chapter, the extrusion process is probed in more detail, under new reductive activation conditions for all three systems: Au, Pt and Pd/CuClP. This yielded the more controlled generation of small and well-defined nanoparticles of Pt, Pd and Au (2-5 nm), as embodied in Figure 4-a.

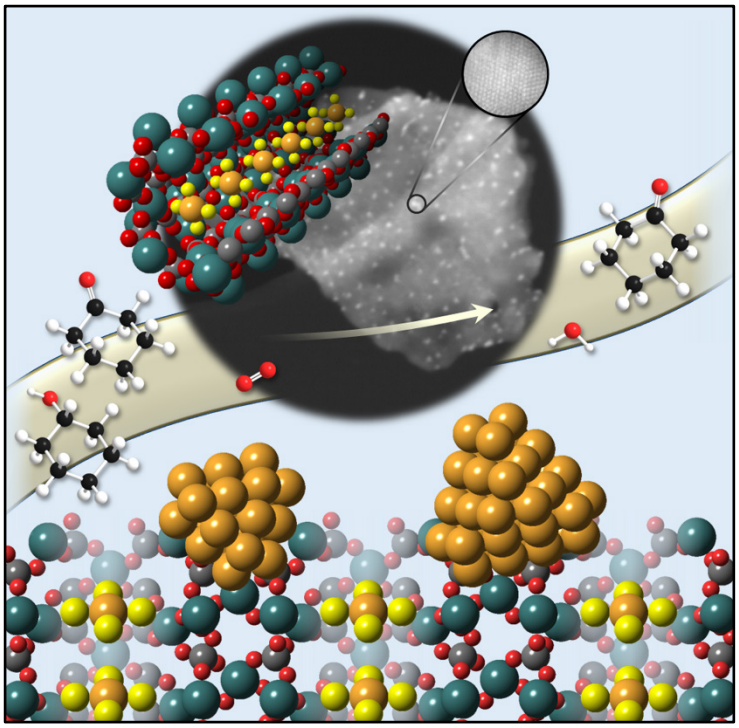

*Figure 4-a: Graphical illustration of the microporous framework architecture containing precursor complexes which result in well-dispersed and isolated metallic nanoparticles upon activation (as visualized by AC-STEM) that are highly active and selective for the aerobic oxidation of KA oil. From A. M. Gill, C. S. Hinde, R. K. Leary, M. E. Potter, A. Jouve, P. P. Wells, P. A. Midgley, J. M. Thomas and R. Raja, ChemSusChem, 2016, **9**, 423 – 427 Reprinted by permission of John Wiley & Sons, Inc.*

In particular, structure-property correlations are drawn through the use of XAS to identify individual characteristics of each Au, Pt and Pd/CuClP system. Further, ADF AC-STEM has been employed to determine the nanoparticle locality and sizes generated under these new activation regimes. This coupled with STEM-EDXS and PXRD has facilitated compositional integrity studies. The structural findings are then rationalized with a view to evaluating structure-property relationships in catalytic studies involving the activation of

molecular oxygen. The stability of these solid nanoparticles and versatility of this approach has been investigated in the aerobic oxidation of KA oil, under continuous flow conditions thereby affording potential scope for the industrial applicability of these catalysts.

Notable contributions:

- Dr Rowan Leary, Prof Paul Midgley and Prof John Meurig Thomas for their collection and processing of the AC-STEM and STEM-EDXS data presented within this chapter.
- Dr Scott Rogers and Dr Peter P. Wells for their assistance in the collection of the XAS data presented within this chapter and discussions with regards to fitting the EXAFS data.
- Dr Naoko Sano and the NEXUS XPS facility at the University of Newcastle for the collection of the XPS data presented within this chapter.
- Andrea Jouve for his assistance and efforts working on the project as a visiting ERASMUS student from the University of Torino, Italy.

4.1 Introduction

4.1.1 Catalytic Performance of Palladium, Gold & Platinum & Nanoparticles Supported on Copper Chloropyrophosphates

Following the progress discussed in Chapter 3, surrounding the activation of the Pt/CuClP material under calcination conditions, the investigation into other activation conditions brought with it a stark contrast in catalyst activity (for the aerobic oxidation of vanillyl alcohol) and material behaviour. Hinde *et al.*[235] subjected the materials to reductive conditions (2 hr under 5% H_2/N_2 flow at 200 °C) and saw the Pt/CuClP material exhibit a dramatically higher level of activity, over the previous calcined materials and the comparative Au and Pd systems as shown in Figure 4-b.

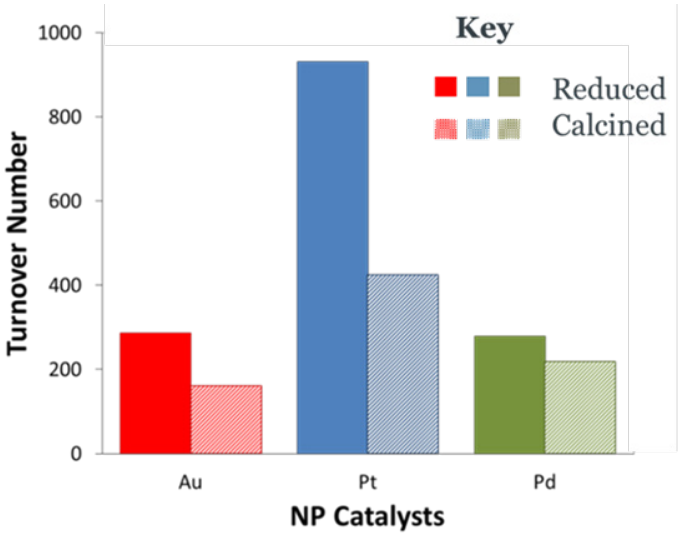

*Figure 4-b: Chart of TONs (calculated after 10 hr) for Au (red), Pt (blue) and Pd (green) reduced (solid); 200 °C, 5% H_2/N_2, 2 hrs and calcined catalysts (patterned); 500 °C, air, 2 hrs. Showing the dramatically more active reduced Pt catalyst for the oxidation of Vanillyl Alcohol.[235] Reprinted with permission from C. S. Hinde, D. Ansovini, P. P. Wells, G. Collins, S. Van Aswegen, J. D. Holmes, T. S. A. Hor and R. Raja, ACS Catal., 2015, **5**, 3807–3816 Copyright 2015 American Chemical Society.*

A combination of XPS, EXAFS, PXRD and TEM analysis, presented in Table 4-a, saw that under these activation conditions the structural integrity of the Pd/CuClP system diminished comparatively with the other materials. A proportion of metallic Pd species were formed but some as particles as large as 50 nm. This coupled with minimal catalytic improvements over the calcined materials would suggest that these activation conditions are too aggressive for the Pd/CuClP system. Both the collapse of the host framework and production of larger nanoparticles were encouraged by the more forceful activation conditions, leading to the diminished catalytic performance.

Technique	Key Findings
PXRD	- Poor structural stability under these activation conditions - Additional crystalline phases introduced, likely due to degradation of the host framework
TEM	- An abundance of larger (20 – 50 nm) particles is present
XPS	- Only partial reduction of the chlorometallate species is achieved with a majority of Pd^{II} remaining under these conditions
EXAFS	- In accordance with the XPS, only partial reduction of the chlorometallate species is achieved with Pd-Cl CNs of 3.3 and Pd-Pd CNs of only 1.3
Catalysis	- Mildly better performance than the comparative calcined materials implies minimal improved formation of catalytically active nanoparticles

Table 4-a: Summary of the structural and catalytic features of the Pd/CuClP activated by reduction at 200 °C under a flow of 5% H_2/N_2 as determined by Hinde et al.[235]

Technique	Key Findings
PXRD	- Excellent structural stability of the host framework under these conditions
TEM	- Evident presence of small Au nanoparticle 2 – 6 nm - Nanoparticles display 0.2 nm fringe spacing's attributed to the Au (200) facet
XPS	- Almost complete extrusion and removal of the Au^{III} species towards complete formation of metallic Au^0
EXAFS	- In contrast with XPS, extrusion appear minimal with only Au-Cl scattering paths present therefore nanoparticle formation should be minimal and limited to the surface regions probed by XPS only
Catalysis	- Mildly better performance than the comparative calcined materials implies minimal improved formation of catalytically active nanoparticles

Table 4-b: Summary of the structural and catalytic features of the Au/CuClP activated by reduction at 200 °C under a flow of 5% H_2/N_2 as determined by Hinde et al.[235]

In contrast, the Au/CuClP material (Table 4-b) showed excellent structural stability but little signs of quantifiable extrusion of the precursor. The EXAFS confirmed that throughout the bulk of the material only the chloride precursor remained present as a Au-Au scattering path could not be incorporated into the data fit. However, both TEM and XPS suggested small amounts of the precursor had formed metallic Au nanoparticles on the surface of the material. This is similar to the observations made in Chapter 3, where small levels of nanoparticle formation were easy to achieve even under less than ideal activation conditions, presumably from surface regions of the host CuClP material. However, the poor catalytic performance is evidence that the production of catalytically active nanoparticles is not achieved under these activation conditions and therefore more

aggressive protocols could be employed to encourage improved extrusion of the $[AuCl_4]^-$ species from within the bulk of the framework.

Comparatively, the Pt/CuClP material (Table 4-c) exhibited the full extrusion of the precursor with no Pt-Cl scattering paths present within the EXAFS data fit. Despite XPS suggesting minor quantities of Pt^{II}, the presence of these species within the bulk of the material was further vindicated by extending the data fit beyond the first shell. This demonstrated purely small, 2.0 – 6.0 nm nanoparticle formation throughout the sample, notably smaller than the approx. 3.5 – 6.5 nm observed under calcination activation. Therefore, it highlights the link between control over nanoparticle formation, the activation conditions and the resulting catalytic activity within these systems. It was therefore concluded that the Pt species could be ideally suited to this synthetic approach.

Technique	Key Findings
PXRD	- Excellent structural stability of the host framework under these conditions
TEM	- Evident presence of small Pt nanoparticle 2 – 6 nm - Nanoparticles display 0.23 nm fringe spacings attributed to the Pt (111) planes
XPS	- Mixed valence (Pt^{II} and Pt^{IV}) species can exist prior to the nucleation and nanoparticle growth - Almost complete extrusion and removal of the Pt^{IV} species towards complete formation of metallic Pt^0
EXAFS	- In accordance with XPS, extrusion appears excellent with no Pt-Cl scattering paths required to establish an accurate data fit
Catalysis	- Significantly better performance than the comparative calcined materials implying improved abundant formation of catalytically active nanoparticles

Table 4-c: Summary of the structural and catalytic features of the Pt/CuClP activated by reduction at 200 °C under a flow of 5% H_2/N_2 as determined by Hinde et al.[235]

In light of the improved nanoparticle formation due to reductive conditions and the observations made in Chapter 3 where it was observed that nanoparticle formation is dependent on the activation temperature, it is hypothesised that a level of control over the nanoparticle environment could be probed through manipulation of the activation temperature. 200 °C under the flow of 5% H_2/N_2 for 2 hr were the conditions utilized by Hinde and co-workers[235] and it was stated that the nanoparticle formation process is not ideal for either the Au or Pd systems. Therefore, it is postulated that tailoring the activation temperature could lead to the complete extrusion of the nanoparticle precursor which in turn would lead to improved catalytic activity.

4.1.2 Current Research into the Selective Production of Cyclohexanone from KA Oil or Pure Cyclohexanol

Following the discussions in Section 1.3, on the potential and current industrial production methods for pure cyclohexanone, much of the current academic research into the production of pure cyclohexanone is focused on the oxidative dehydrogenation or oxidation pathway (Scheme 4-a) and the direct dehydrogenation pathway (Scheme 4-b). These have been highlighted in section 1.3 as the two most promising pathways from an industrial perspective. Much of the current literature on this topic has been reviewed in the tables below, detailing nanoparticle and non-nanoparticle catalysts for cyclohexanol dehydrogenation (Table 4-d and Table 4-f) and similarly for the oxidation pathway (Table 4-e and Table 4-g respectively).

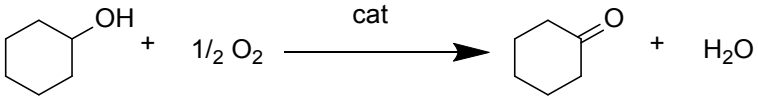

Scheme 4-a: The oxidation of cyclohexanol.

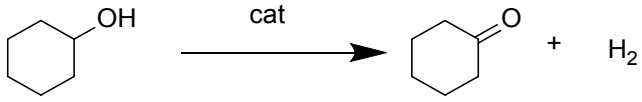

Scheme 4-b: The dehydrogenation cyclohexanol.

Table 4-d and Table 4-f highlight the limitations of the dehydrogenation pathway, as discussed in Section 1.3.1, whereby phenol production is a serious issue for any potential industrial deployment. In contrast to the direct oxidation pathway, regardless of oxidant, the high performing dehydrogenation catalysts possess lower cyclohexanone selectivities, implying the production of phenol as a significant by-product. Thus, it brings with it the prolonged and costly azeotrope separations needed for phenol-cyclohexanone and phenol-cyclohexanol mixtures. While the poor selectivities are clear, it is also apparent that Cu is a mainstay in nearly all of the high performing dehydrogenation catalysts currently being reported by the academic community. This is in contrast to the current industrial employment of copper catalysts, where Cu and Cu_2O are reserved for the production of KA oil mixtures and Pd catalysts for pure cyclohexanone production. This accounts for the typically poor selectivities observed for the Cu catalysts detailed in Table 4-d and Table 4-f.

It has recently been observed that Cu with different oxidation states, namely Cu^I and Cu^0, can indeed catalyse the desired cyclohexanol to cyclohexanone transformation with high selectivities under mild condition.[236] This is apparent from Table 4-d and Table 4-f but the exact role of the individual Cu species has been highly disputed with different authors

quoting each oxidation state responsible for the highly selective activity observed in many nanoparticle and metal oxide systems.[78,237–239] It has now been shown by Wang *et al.*[236] that the reaction mechanisms (Scheme 4-c) are different on Cu(111) and Cu_2O(111) (the most stable facets of each species) but in both cases it is the coordinatively unsaturated sites that are energetically most favourable and carry out all of the catalysis. Specifically on Cu(111), pathway A in Scheme 4-c is more active both thermodynamically and kinetically, in which the hydrogen of the hydroxyl group in cyclohexanol is removed, followed by the abstraction of hydrogen on carbon. Pathway B is dominant on Cu_2O(111).

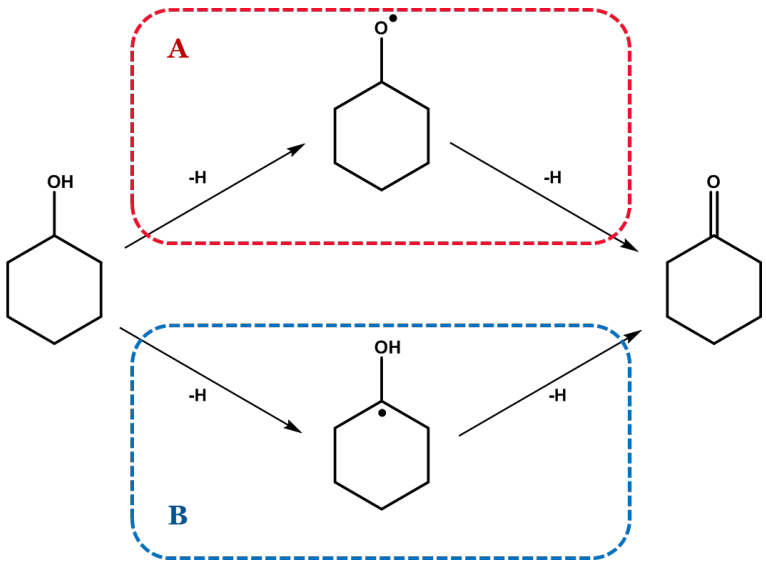

Scheme 4-c: The scheme of two possible reaction pathways of the cyclohexanol dehydrogenation a metal particle surface e.g. copper. Pathway A (red) and pathway B (blue).

While noble metal nanoparticles, including Pt, Pd and Au, have demonstrated a precedent for exceptional activity in a number of selective oxidation reactions,[147,148,159,171,240,241] consultation of existing literature surrounding the selective oxidation of cyclohexanol in particular (Table 4-e and Table 4-g) highlights a number of key points. Firstly, the selectivities towards cyclohexanone are far superior (often above 98%) than the dehydrogenation pathway. This, in part, is due to the larger number of potential by-products for the dehydrogenation process, namely cyclohexene and phenol, as opposed to the direct oxidation process, provided over oxidation products can be avoided. Another significant observation is that while activity of the non-nanoparticle systems is generally higher, these are typically peroxide based systems, catalysed by homogeneous transition metal organometallics. While the higher activity of peroxides is to be expected and is aligned with the observations made in Chapter 3, the drawbacks of such systems have already been discussed in detail (Section 1.1.4). Furthermore, Table 4-e exemplifies the affinity of noble metal nanoparticles towards activating molecular oxygen with the systems contained achieving similar levels of activity to the peroxides. Interestingly, the use of

metal nanoparticles in the oxidation of cyclohexanol and KA oil in particular, under continuous flow conditions is somewhat limited. In fact, only three examples[101,242,243] of a continuous flow process being employed for this transformation were found. One of these; a Au/Cu nanoparticle catalyst[242] is able to produce modest cyclohexanone yields (approx. 75%), but while this is the highest performing example within a continuous flow system, it requires a complex and intensive catalyst synthesis procedure. This includes the generation of a sinter-locked, 3D, micro-fibrous network of Cu fibres as a preform paper followed by the removal of cellulosic binding agents and the subsequent impregnation of the Au nanoparticles. This highlights the significance of developing new such processes and catalysts given the industrial scale advantages of continuous flow systems: reduced reactor volumes, constant production, higher levels of control etc.

Batch based set-ups are in the clear majority over continuous flow systems within the literature reviewed. These include a range of Cu and noble metal based catalysts, as well as other transition-metal variants employing Ti, Co and Mn active centres. However, these have all been shown to require large quantities of co-solvents and basic initiators or co-catalysts (Table 4-e and Table 4-g). This further demonstrates the need for more widespread research into continuous flow methods that avoid the need for such additives. On top of this, to the best of my knowledge, no examples exist where a catalytic process employs a KA oil feedstock for the selective production of cyclohexanone. The merits of such an approach are to diversify the options available within the chemical industry with minimal capital investment through the use of an existing, high volume feedstock (as discussed in Section 1.3.5). Thus, developing the low-temperature, selective oxidation of KA oil could be potentially attractive if cyclohexanone selectivities and yields can rival traditional cyclohexanol oxidation and dehydrogenation pathways.

Active Metal	Support	Synthesis	Additives	Time (hr)	Temperature (°C)	Cyclohexanol Conversion (mol%)	Cyclohexanone Yield (mol%)	TOF (hr^{-1})	Reference
Cu / Co	*SiO_2*	*DP*	*-*	*N/A*	*250*	*96*	*92*	*-*	[244]
Cu	*SiO_2*	*DP*	*-*	*N/A*	*250*	*97*	*84*	*-*	[244]
Cu	*ZnO / SiO_2*	*Imp*	*-*	*N/A*	*300*	*91*	*77*	*-*	[78]
Cu	*Al_2O_3*	*CP*	*-*	*N/A*	*250*	*83*	*66*	*-*	[245]
Cu	*MgO / Cr_2O_3*	*CP*	*-*	*N/A*	*250*	*63*	*63*	*1*	[77]
Pt / Co	*Al_2O_3*	*Imp*	*-*	*N/A*	*250*	*62*	*57*	*3*	[246]
Cu / Ni	*CeO_2*	*CP*	*-*	*N/A*	*350*	*42*	*38*	*20*	[247]
Cu	*CeO_2*	*CP*	*-*	*N/A*	*350*	*32*	*28*	*15*	[247]
Ni	*CeO_2*	*CP*	*-*	*N/A*	*350*	*26*	*24*	*12*	[247]
Rh / Cu	*Al_2O_3*	*Imp*	*-*	*N/A*	*200*	*7*	*5*	*167*	[248]
Cu	*Al_2O_3*	*Imp*	*-*	*N/A*	*200*	*14*	*2*	*-*	[248]
Rh	*Al_2O_3*	*Imp*	*-*	*N/A*	*200*	*8*	*2*	*305*	[248]

Table 4-d: Table (classified by yield) presenting a comparison of heterogeneous nanoparticle catalysed oxidation of cyclohexanol to cyclohexanone by a dehydrogenative pathway. All contained are carried out in absence of any oxidant and within a continuous flow process (italics). TOF left blank when not reported or undeterminable. DP – deposition precipitation, CP – coprecipitation and Imp – impregnation.

Active Metal	Support	Synthesis	Oxidant	Additives	Time (hr)	Temperature (°C)	Cyclohexanol Conversion (mol%)	Cyclohexanone Yield (mol%)	TOF (hr^{-1})	Reference
Au	LDH	DP	Air	Solvent	4	80	93	91	5	[104]
Pt	SiO_2	Imp	Oxygen	Base	22	90	90	90	-	[102]
Au	TiO_2	-	H_2O_2	Solvent	1	90	87	87	87	[153]
Ru	CeO_2	DP	Oxygen	Solvent	8	60	83	81	1	[76]
Pt	-	-	Oxygen	-	24	80	88	78	1	[233]
Au / Ag	-	-	Oxygen	Base	0.25	150	76	76	255	[249]
Au / Cu	*CuO_2*	*Imp*	*Oxygen*	-	*N/A*	*250*	*76*	*75*	-	[242]
Pt	***CuClP***	***Extrusion***	***Air****	**-**	***N/A***	***200***	***74***	***74***	***37***	**-**
Pt	MgO	Imp	Oxygen	Solvent	30	130	67	66	2	[157]
Pd	CeO_2	-	Oxygen	-	12	120	58	57	256	[150]
Pt	BaO	Imp	Oxygen	Solvent	35	130	51	50	1	[157]
Au / Cu	SiO_2	Imp	Oxygen	Solvent	4	80	49	49	1	[145]
Pt	CaO	Imp	Oxygen	Solvent	30	130	47	47	2	[157]
Au	*Porous SiO_2*	*CP*	*Oxygen*	-	*N/A*	*230*	*45*	*45*	*940*	[101]
Fe	Porous Silicate	DP	H_2O_2	Solvent	1	80	38	38	162	[100]
Cu	SiO_2	Imp	Oxygen	Solvent	4	80	38	38	1	[145]
Cu	Nb_2O_5	Imp	Oxygen	*hv*	5	25	30	24	-	[250]
Pd	Porous SiO_2	Imp	Oxygen	-	12	60	23	23	<1	[103]

Continued overleaf…

Active Metal	Support	Synthesis	Oxidant	Additives	Time (hr)	Temperature (°C)	Cyclohexanol Conversion (mol%)	Cyclohexanone Yield (mol%)	TOF (hr^{-1})	Reference
Pt	Aluminosilicate	Imp	Air	Solvent	20	25	21	18	<1	[97]
Pd	***CuClP***	***Extrusion***	***Air****	***-***	***N/A***	***200***	***5***	***5***	***2***	***-***
Pt	SiO_2	Imp	Air	Solvent	20	25	5	5	<1	[97]
Au	***CuClP***	***Extrusion***	***Air****	***-***	***N/A***	***200***	***3***	***3***	***2***	***-***

*Table 4-e: Table (classified by yield) presenting a comparison of nanoparticle catalysed oxidation of cyclohexanol to cyclohexanone. Italics denotes a continuous flow process. Bold denotes the catalysts studied within this work. * denotes a KA oil feedstock as opposed to pure cyclohexanol. TOF left blank when not reported or undeterminable. LDH – layered double hydroxide, DP – deposition precipitation, CP – coprecipitation and Imp – impregnation.*

Active Metal	Species	Additives	Time (hr)	Temperature (°C)	Cyclohexanol Conversion (mol%)	Cyclohexanone Yield (mol%)	TOF (hr^{-1})	Reference
Cu / Cr / Mg / Al	*Mixed Metal Oxide*	-	*N/A*	*330*	*89*	*88*	-	[251]
Cu / La / Mg / Al	*Mixed Metal Oxide*	-	*N/A*	*330*	*86*	*82*	-	[251]
Cu / Mg / Al	*Mixed Metal Oxide*	-	*N/A*	*330*	*86*	*79*	-	[251]
Cu / Mg	*Mixed Metal Oxide*	-	*N/A*	*330*	*83*	*77*	-	[251]
Cu / Zn	*Metal Oxide*	-	*N/A*	*290*	*80*	*75*	*2*	[252]
Cu / Cr	*Metal Oxide*	-	*N/A*	*290*	*80*	*68*	*1*	[252]
Ca	*Metal Oxide*	-	*N/A*	*350*	*90*	*68*	-	[253]
Cu / Zn	*Metal Oxide*	-	*N/A*	*250*	*86*	*60*	-	[254]
Fe / Ti	*Porous Silicate*	-	*N/A*	*240*	*86*	*54*	-	[239]
Cu / Al	*Mixed Metal Oxide*	-	*N/A*	*330*	*48*	*45*	-	[251]
V / Ca	*Metal Oxide*	-	*N/A*	*427*	*75*	*38*	-	[253]
Ti	*Titanosilicate*	-	*N/A*	*150*	*37*	*37*	-	[255]
Al / Si	*Aluminosilicate*	-	*N/A*	*150*	*31*	*31*	-	[255]
Al / Si	*Aluminosilicate*	-	*N/A*	*150*	*31*	*29*	-	[255]
Ti	*TS-1*	-	*N/A*	*150*	*8*	*8*	-	[255]
Fe	*Porous Silicate*	-	*N/A*	*240*	*51*	*6*	-	[239]
Ti	*Porous Silicate*	-	*N/A*	*240*	*86*	*3*	-	[239]

Table 4-f: Table (classified by yield) presenting a comparison of non-nanoparticle catalysed oxidation of cyclohexanol to cyclohexanone by a dehydrogenative pathway. All contained are carried out in absence of any oxidant and within a continuous flow process (italics). TOF left blank when not reported or undeterminable.

Active Metal	Species	Oxidant	Additives	Time (hr)	Temperature (°C)	Cyclohexanol Conversion (mol%)	Cyclohexanone Yield (mol%)	TOF (hr^{-1})	Reference
Cu	Organometallic	TBHP	Solvent	8	50	98	98	7	[93]
V	Mixed Metal Oxide	TBHP	Solvent	6	80	95	94	-	[131]
Co	Organometallic	TBHP	-	8	165	92	92	6	[94]
W	Organometallic	H_2O_2	Solvent	1.5	100	92	89	-	[256]
Cu	Organometallic	TBHP	Solvent	8	50	81	81	<1	[95]
Ru	Mixed Metal Oxide	Air	Solvent	5	25	71	71	2	[257]
Cu	Organometallic	TBHP	Solvent	9	65	69	69	1	[258]
Co	LDH	O_2	Solvent	12	100	67	67	9	[259]
Ru	Tungstosilicate	O_2	Solvent	48	100	83	67	23	[260]
Mn	Aluminophosphate	APB	Solvent	3	60	76	58	-	[207]
Ag	-	*Air*	-	*N/A*	*620*	*58*	*56*	-	[243]
V	Metal Oxide	TBHP	Solvent	8	90	49	49	-	[261]
Ti	TS-1	APB	Solvent	3	60	67	45	-	[207]
Ru	Metal Oxide	Air	Solvent	4	80	43	43	2	[98]
Cu	Aluminosilicate	TBHP	Solvent	8	50	42	42	3	[93]
Co	Aluminosilicate	TBHP	-	8	165	41	41	3	[94]
Mn	Porous Silicate	O_2	-	250	5	52	40	80	[262]
Cr	Metal Oxide	TBHP	Solvent	5	70	38	38	16	[263]

Continued overleaf…

Active Metal	Species	Oxidant	Additives	Time (hr)	Temperature (°C)	Cyclohexanol Conversion (mol%)	Cyclohexanone Yield (mol%)	TOF (hr^{-1})	Reference
Mn	Organometallic	TBHP	-	8	165	38	38	5	[96]
Nb	Metal Oxide	O_2	*hv*	25	5	37	30	-	[250]
Cr	Aluminophosphate	TBHP	Solvent	5	110	30	29	13	[263]
Mn	Organometallic	H_2O_2	-	8	165	27	27	3	[96]
V	Metal Oxide	H_2O_2	Solvent	8	90	26	26	-	[261]
Cr	Aluminosilicate	TBHP	-	10	190	25	25	-	[264]
Ti	Aluminosilicate	H_2O_2	Solvent	3	65	44	24	1	[265]
Cr	Aluminophosphate	APB	Solvent	3	60	71	23	-	[207]
Ti	Aluminosilicate	H_2O_2	Solvent	5	65	10	10	7	[266]

Table 4-g: Table (classified by yield) presenting a comparison of the non-nanoparticle catalysed oxidation of cyclohexanol to cyclohexanone with different oxidants. Italic denotes a continuous flow process. TOF left blank when not reported or undeterminable. LDH – layered double hydroxide and APB - acetylperoxyborate.

4.2 The Thermal Reduction of Chlorometallate Salts in the Presence of Hydrogen & Understanding the Ensuing Structure Property Correlations & Their Catalytic Impact

4.2.1 Extrusion by Reduction: The Case of Palladium

The Pd/CuClP materials, of the form: $Rb_9Cu_6(P_2O_7)_4Cl.[PdCl_4]Cl_2$ were activated between 150 and 200 °C where the extent of the extrusion was investigated through: PXRD, ADF-STEM, STEM-EDXS, XPS and XAS. Despite it already having been shown (Table 4-a) that 200 °C is an insufficient temperature to fully extrude the Pd precursor, one must always maintain the structural integrity of the catalyst in its entirety, this includes the support species. At these activation temperatures the structural integrity of the CuClP framework becomes compromised for the Pd/CuClP catalyst, as shown in Figure 4-c. However, it would be desirable to achieve a catalyst with an optimal level of nanoparticle formation whilst maintaining the host's structural integrity. Therefore, this must be done at temperatures below 200 °C following observations made by Hinde *et al.*[235] and hence the activation study employed herein.

Figure 4-c shows that at reduction temperatures of 150 °C the material maintains its structural integrity but as the temperature increases, small amounts of additional phases are introduced. These phases are present at 175 °C and are becoming increasingly significant at 200 °C. Figure 4-c also highlights these impurities, demonstrating their increasing influence with activation temperature. Comparison of Figure 4-c and Figure 4-d shows that this particular impurity is rubidium phosphate. This is clearly demonstrated by the emergence of the $Rb(PO_3)$: (20-2) and (212) reflections at approx. 25-25.5 °, the (400) at 27.3 °, the (204) at 29.5 °, the (501), (-212) and (412) at approx. 31.8-32.1 ° and the (014), (414) and (020) reflections at approx. 38.3-39.4 °. This phosphate containing phase would be highly detrimental to the structural integrity of the host framework due to its removal of the structurally key phosphate groups. Production of this phase suggests that within the Pd/CuClP analogue, the host CuClP structure has a stronger affinity towards the palladium chloride anions. This is because one would expect the reduction product from the extrusion process to be the less structurally detrimental HCl gas or RbCl. These products are also the most energetically accessible due to their ionic presence and therefore lack of covalent bonds needed to be broken for formation.

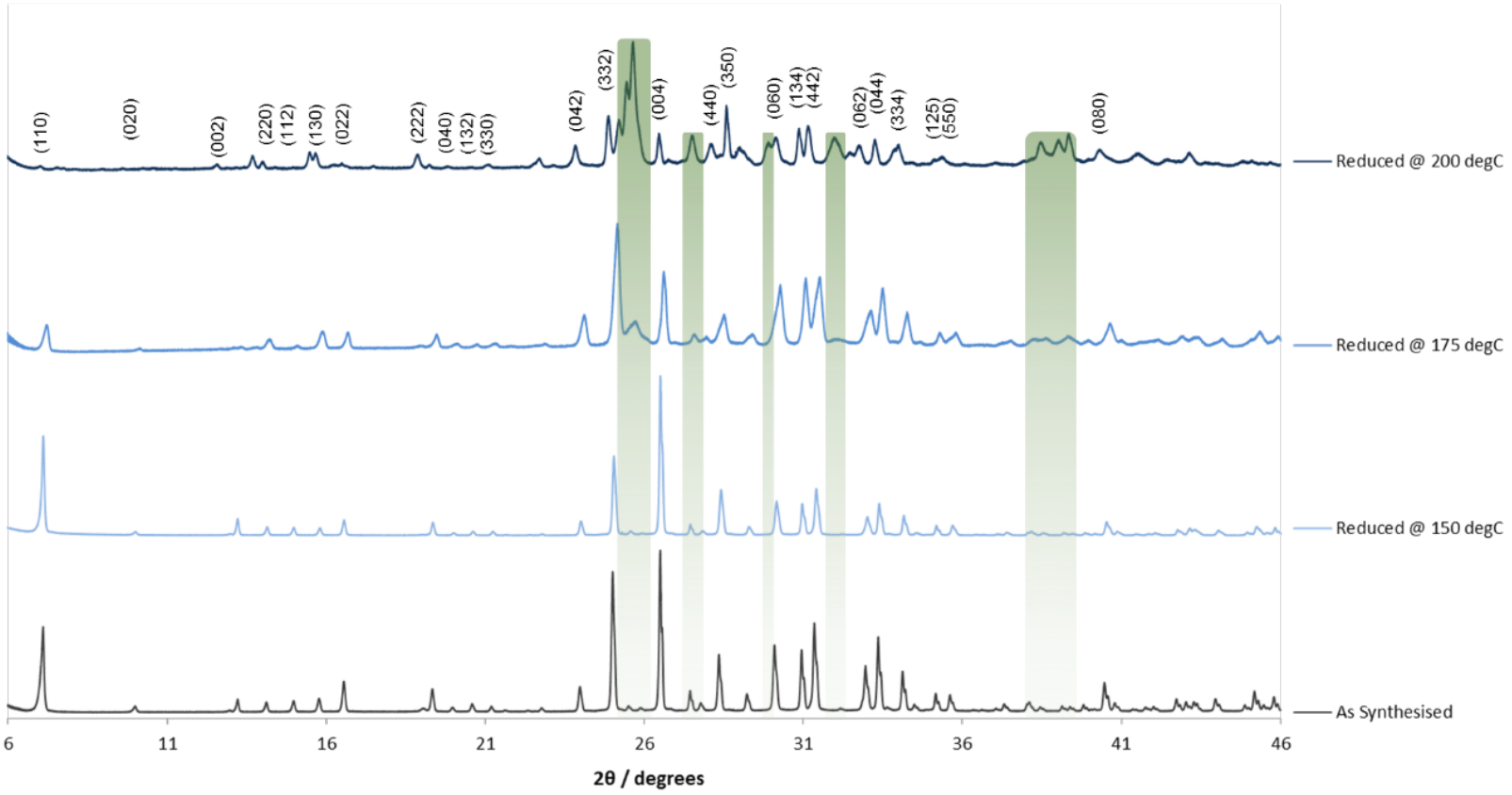

Figure 4-c: Indexed PXRD of the Pd/CuClP materials activated at different temperatures (blue) with the per-activation, as-synthesised sample (grey) for comparison. Impurity rubidium phosphate phase highlighted in green.

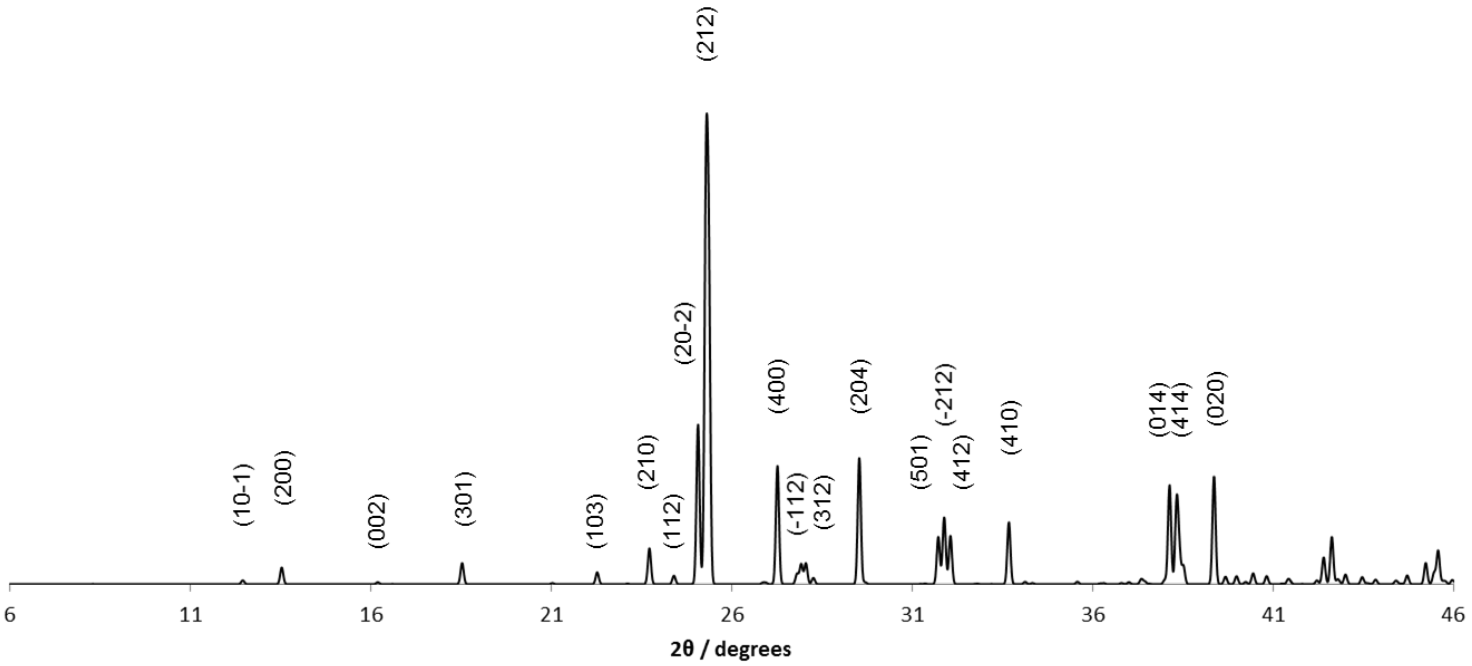

Figure 4-d: Simulated PXRD pattern of rubidium phosphate ($Rb(PO_3)$) with hkl values displayed above the peaks.[267]

Interestingly, this decomposition of the framework occurs at an unexpectedly low temperature. It has been noted that these materials are stable to above 550 °C[194] and similarly in Chapter 3, it was observed that structural changes begin to occur between 500 and 600 °C for the Pt/CuClP system under calcination conditions. It would therefore suggest that this premature decomposition of the Pd/CuClP material could be due to stronger interaction between the $[PdCl_4]^{2-}$ ion and the surrounding channel wall, causing the degradation upon the removal of significant quantities of the palladium chlorometallate anion. These structural implications would suggest that complete extrusion of the Pd species may not be possible without thorough decomposition of the host material.

High-resolution studies using AC-STEM have demonstrated the limited nanoparticle formation in the Pd/CuClP system even at 200 °C, as exemplified in Figure 4-e. Figure 4-e (a) shows the crystalline structure of the framework is rendered visible by the framework lattice planes containing heavy metal atoms. However, in these regions of retained crystallinity there is very limited to no nanoparticle formation observed. This would further imply that the framework degradation is a consequence of the extrusion. Figure 4-e (b and c) highlight the limited nanoparticle formation, suggesting a higher propensity of formation on the surface periphery regions of the support, as highlighted in (c). Further complementary compositional studies using STEM-EDXS also confirmed the well-defined nature of the Pd/CuClP material with a paucity of nanoparticles, Figure 4-f. Therefore, the AC-STEM suggest that there are regions of well-defined structure even when the material is activated at 200 °C, implying that where there is limited nanoparticle formation the composition of the framework remains intact. Coupling this with the PXRD would suggest that there must also be regions of ill-defined structure as while the CuClP framework is still the dominant feature in the PXRD pattern, there must also be rubidium phosphate as a product of fractional nanoparticle formation and consequent framework degradation.

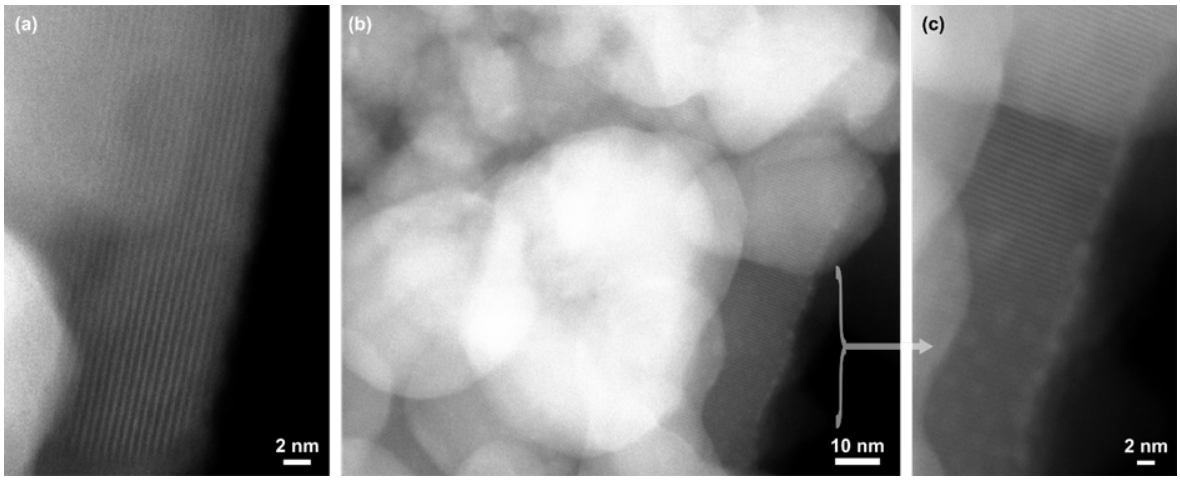

Figure 4-e: ADF AC-STEM images of the Pd/CuClP material activated at 200 °C.

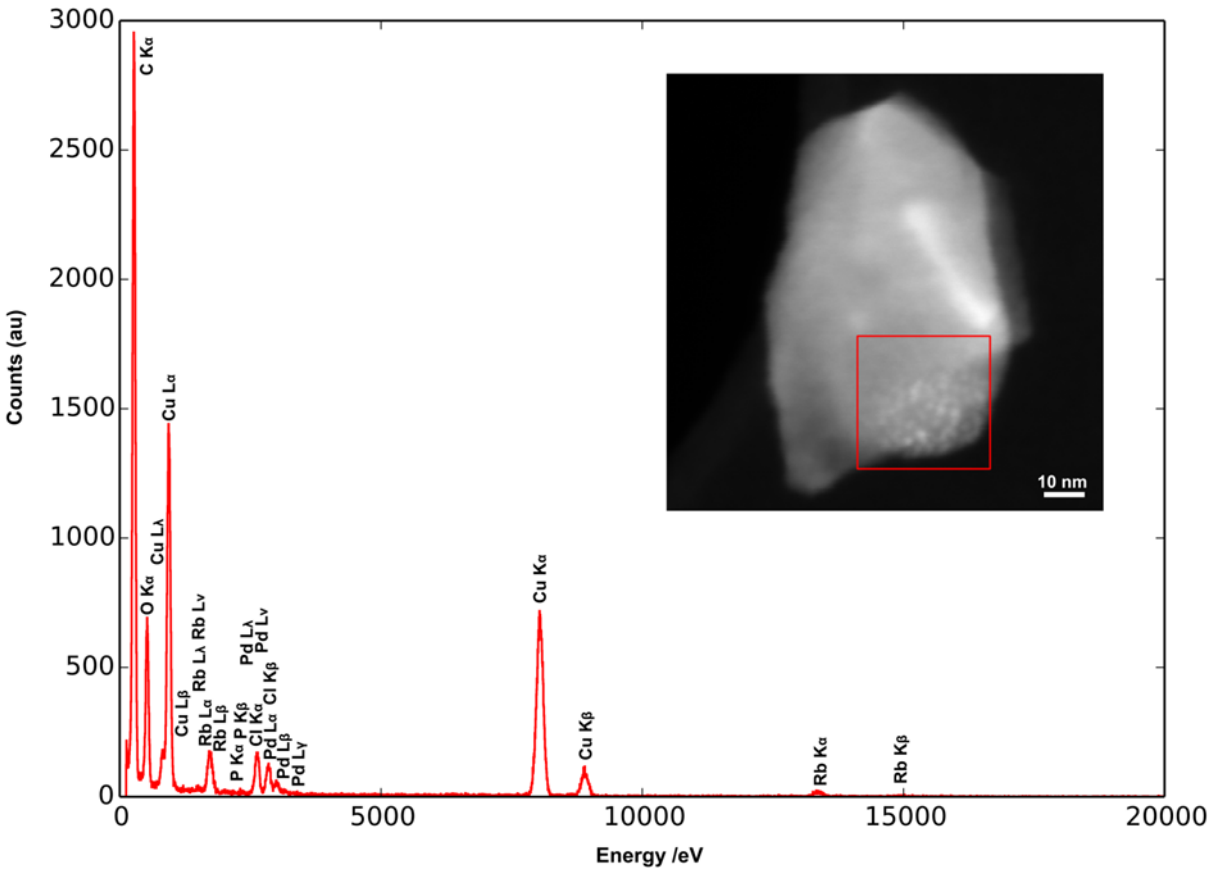

Figure 4-f: EDX spectrum for the Pd/CuClP material activated at 200 °C. The area analysed is indicated by the red box in the inset ADF-STEM image.

XPS analysis of the Pd 3*d* binding region shows progression from metallic Pd^0 towards Pd^{II} with increasing activation temperature. This suggests that, at lower temperatures nanoparticle Pd^0 species could exist. However, at higher activation temperatures the propensity for metallic Pd diminishes. This diminishing quantity of Pd^0 as the activation temperature is increased could also be evidenced by the AC-STEM as minimal nanoparticle formation was observed at 200 °C. This feature is however, somewhat counter intuitive. One would expect increased decomposition of the $[PdCl_4]^{2-}$ species, under the reductive atmosphere, to Pd^0 with the generation of HCl gas and/or RbCl. This would then lead to the increased removal of species from within the channels of support framework causing increased degradation. It could be the case that the Pd species within this system, at the higher activation temperatures, could in fact not be chloride or metallic in nature. Due to the surface sensitivity of XPS (typical sampling depth of < 10 nm, as discussed in Section 2.3.2), these findings are likely limited to surface regions of the samples, similar to the STEM observations.[196,268,269] Therefore, the exploitation of XAS as further bulk structural characterisation is required.

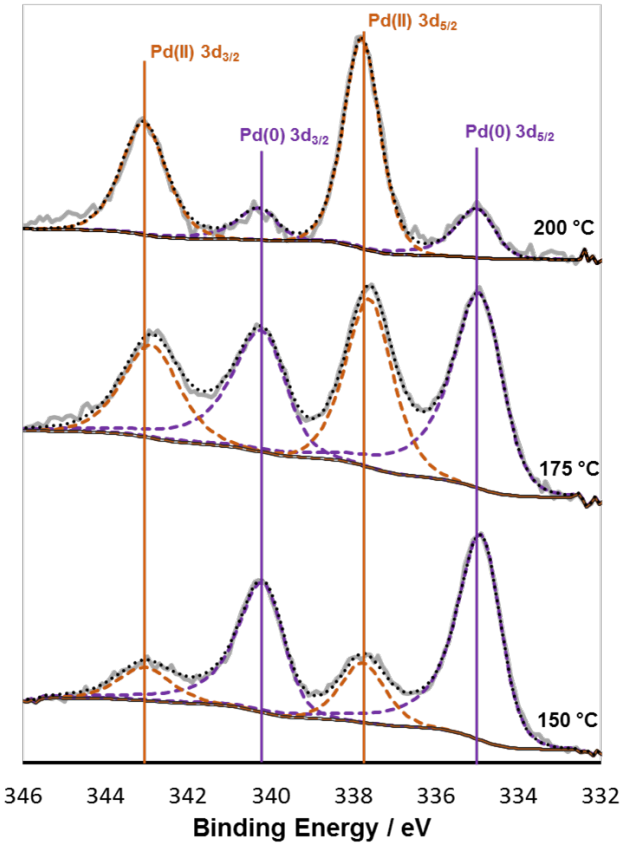

Figure 4-g: Stacked XPS data of the Pd 3d binding region for the Pd/CuClP catalysts activated at different temperatures. The data is shown in grey with the data fit in black, Pd^0 transitions are depicted in purple and the Pd^{II} transitions in orange.

XAS was used to probe the coordination geometry and local structural environment of the Pd centres with a view to gaining a better understanding on nanoparticle formation and exact nature of the Pd species present within these systems, both in the bulk and upon surface fragments. The corresponding XAS data is displayed in Figure 4-h and Figure 4-i, with the EXAFS fitting parameters displayed in Table 4-i. The analysis of this data suggests a slight progression from Pd^{II} to metallic Pd^0 between 175 and 200 °C. This is contrary to the XPS finding however, the XAS does maintain that the majority of the Pd species exists as Pd^{II} even at 200 °C. This is evidenced by the transition of two key features of the Pd K edge XANES towards the metallic standard, the edge feature at 24352 eV and the edge intensity at 24385 eV, both of which transition towards the metallic standard between 150 and 175 °C.

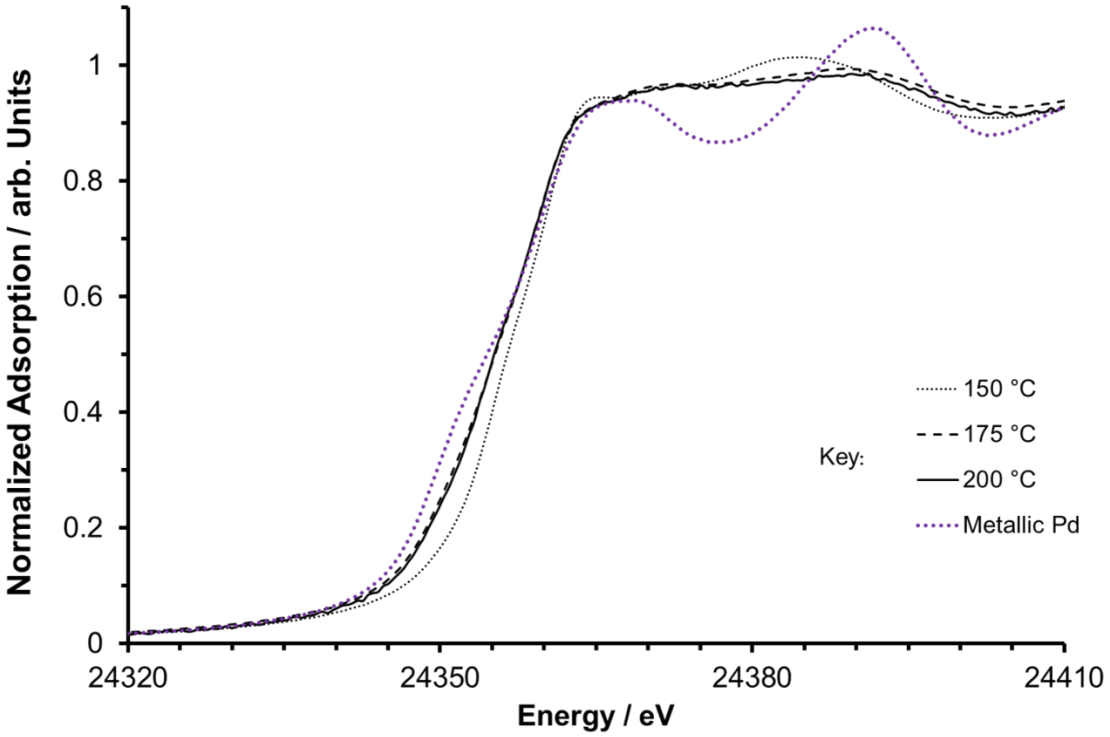

Figure 4-h: Stacked XANES data of the Pd K edge for the Pd/CuClP materials activated at different temperatures with a metallic palladium reference in purple.

Further to the XANES features suggesting a progression towards metallic Pd or at least a reduction in overall oxidation state, the EXAFS data (Figure 4-i and Figure 4-j) and fitting parameters (Table 4-h and Table 4-i respectively) suggest that a significant proportion of chloride persists across all the Pd/CuClP samples. While the fitting parameters also show, analogously to the XANES, a mild progression towards metallic Pd, the quality of these fits in Figure 4-i and Table 4-h depreciate significantly at 175 and 200 °C. This diminishing fit quality reflected by the increasing R_{factor} and the increasing percentage errors, specifically for $2\sigma^2$, stems from the attempt to only use the Pd-Pd and Pd-Cl scattering paths. Reflection of the two proposed fits in R-space (Figure 4-i and Figure 4-j) shows that these two scattering paths do not appropriately fit the region between 2 and 3 Å with a poor fit-data overlap evident in Figure 4-i. Consequently, it is hypothesised that there is a tendency to extrude the Pd as the activation temperature increases, decomposing small fractions of the chloride precursor to form a proportion of metallic nanoparticles on the materials surface. But while this may be true, the specific nature of these Pd species could in fact be significantly more complex than simple monometallic Pd nanoparticles. Justification for this hypothesis comes from the inclusion of a Pd-Cu scattering path, displaying plausible Pd-Cu bond lengths (2.62 – 2.66 Å), considerably improving the data-fit quality in Figure 4-j and Table 4-i.[270]

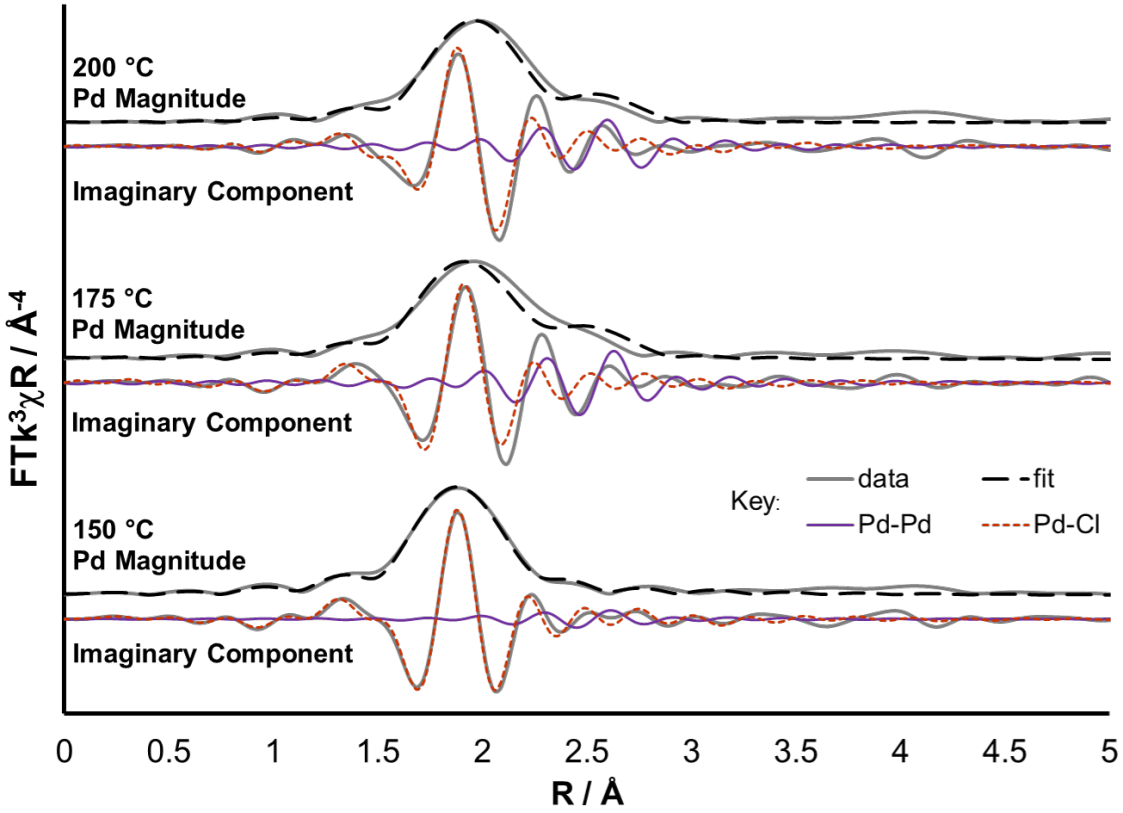

Figure 4-i: *The magnitude and imaginary component of the k^3 weighted Fourier transform for the EXAFS data of the three Pd/CuClP species reduced under increasing activation temperatures. Associated scattering paths are included for the imaginary component and the fitting parameters are displayed in Table 4-h.*

Sample	Abs Sc	N	R / Å	$2\sigma^2$ / Å^2	E_f / eV	R_{factor}
Pd/CuClP	Pd – Cl	4.2 (1)	2.322 (5)	0.0028 (4)	5.2 (7)	0.007
150 °C	Pd – Pd	0.3 (2)	2.76 (3)	0.003 (3)		
Pd/CuClP	Pd – Cl	3.2 (3)	2.35 (1)	0.003 (1)	4 (2)	0.041
175 °C	Pd – Pd	0.9 (4)	2.77 (3)	0.003 (2)		
Pd/CuClP	Pd – Cl	3.4 (3)	2.35 (1)	0.0027 (7)	13 (1)	0.025
200 °C	Pd – Pd	0.9 (4)	2.77 (2)	0.002 (2)		

Table 4-h: *Pd/CuClP EXAFS fitting parameters including Pd-Cl and Pd-Pd. Pd sample - $S_0^2 = 0.82$ as deduced by $PdCl_2$ standard; Fit range 3<k<12, 1<R<3; # of independent points = 11.*

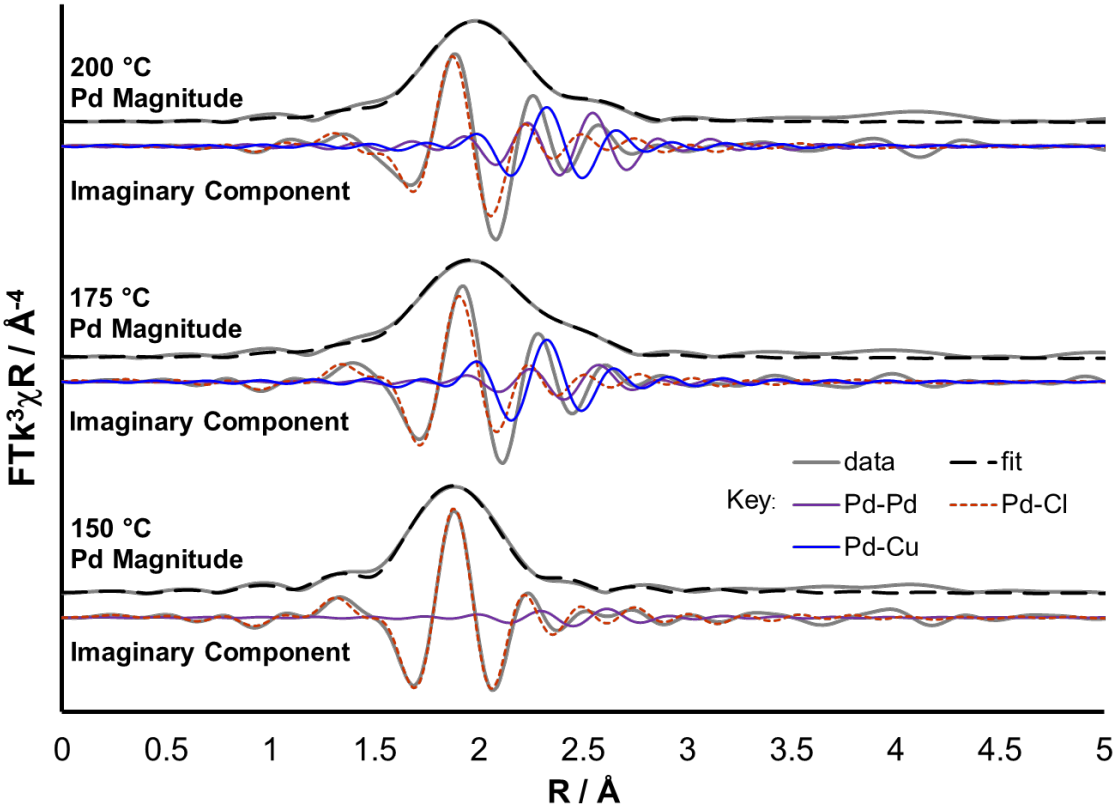

Figure 4-j: *The magnitude and imaginary component of the k^3 weighted Fourier transform for the EXAFS data of the three Pd/CuClP species reduced under increasing activation temperatures. Associated scattering paths are included for the imaginary component and the fitting parameters are displayed in Table 4-i.*

Sample	Abs Sc	N	R / Å	$2\sigma^2$ / Å^2	E_f / eV	R_{factor}
Pd/CuClP	Pd – Cl	4.2 (1)	2.322 (5)	0.0028 (4)	5.2 (7)	0.007
150 °C	Pd – Pd	0.3 (2)	2.76 (3)	0.003 (3)		
Pd/CuClP	Pd – Cl	3.0 (1)	2.335 (7)	0.0029 (4)	2 (1)	0.003
175 °C	Pd – Pd	0.8 (3)	2.71 (2)	0.004 (2)		
	Pd – Cu	1.3 (2)	2.628 (7)	0.003 (1)		
Pd/CuClP	Pd – Cl	3.0 (1)	2.333 (6)	0.0027 (4)	10.0 (8)	0.003
200 °C	Pd – Pd	1.1 (2)	2.71 (2)	0.003 (1)		
	Pd – Cu	1.4 (3)	2.65 (1)	0.003 (2)		

Table 4-i: *Pd/CuClP EXAFS fitting parameters including Pd-Cl, Pd-Pd and Pd-Cu scattering paths. Pd sample - S_0^2 = 0.82 as deduced by $PdCl_2$ standard; Fit range 3<k<12, 1<R<3; # of independent points = 11.*

While the XPS data (Figure 4-g) suggests the increased formation of a Pd^{II} species with activation temperature within surface fragments of the material, the second EXAFS fit depicted in Figure 4-j and Table 4-i demonstrates clearly that a Pd-Cu component exists across the entirety of the material but only when activated at temperatures where the host framework has become vulnerable to degradation. The presence of such a Pd-Cu species

would again coincide well with the framework instability. This is due to the source of copper within the system having to come as a degradation product of the host framework, due to its integral nature within the overriding structure of the CuClP framework. This suggests that the $[PdCl_4]^{2-}$ ions are decomposed as expected at the lower temperatures such as 150 °C producing small proportions of metallic nanoparticles upon the crystalline material surface. This is confirmed by the AC-STEM in Figure 4-e, PXRD in Figure 4-c and prior work by Hinde *et al.*[235] Although, at temperatures above 150 °C the framework becomes increasingly susceptible to degradation. This leads to the production of a rubidium phosphate phase which, in turn, liberates the structurally integral Cu species producing alternative Pd and or PdCu species. The precise nature of which still remains unknown. From a catalytic perspective, this is of lesser importance due to the instability of the support framework rendering these materials undesirable. Furthermore, the congested nature of the nanoparticles produced upon the thin, periphery regions of the host framework, evidenced in Figure 4-e(c), would likely lead to poor site isolation due to the poor distribution and therefore unfavourable catalytic properties could ensue, such as: poor product selectivity (as discussed in Section 1.2). Therefore, the study of the palladium system confirms its structural vulnerability during the nanoparticle formation. This therefore rules it out as a viable oxidation catalyst going forward unless a more suited activation protocol can be designed, wherein the formation of metallic Pd nanoparticles can occur without the seemingly consequential degradation of the support framework.

4.2.2 Extrusion by Reduction: The Case of Gold

The Au/CuClP materials, of the form $Rb_9Cu_6(P_2O_7)_4Cl.[AuCl_4]Cl_3$, were activated at higher temperatures (150-250 °C) than their Pd counterparts, due to the findings of Hinde *et al.*[235] showing that 200 °C was insufficient to observe notable nanoparticle formation (Table 4-b). Similarly to the Pd/CuClP system, the extent of the extrusion was investigated through: PXRD, ADF-STEM, XPS and XAS. However, in contrast to the Pd/CuClP materials, the Au/CuClP maintains its structural integrity across all the activation temperatures investigated, as demonstrated in Figure 4-k. Following the observation of the Pd/CuClP materials, this structural stability is notable given the observations made by XPS in Figure 4-l showing complete formation of metallic Au species at 250 °C. The progressive depreciation of Au^{III} content as a function of activation temperature is evident. This, in conjunction with a shift to lower binding energies of the Au 4*f* signals when activated at 250 °C further vindicates the presence of nanoparticulate species. Such a shift has been observed as a consequence of small as well as increasingly smaller particle size.[137,271–273]

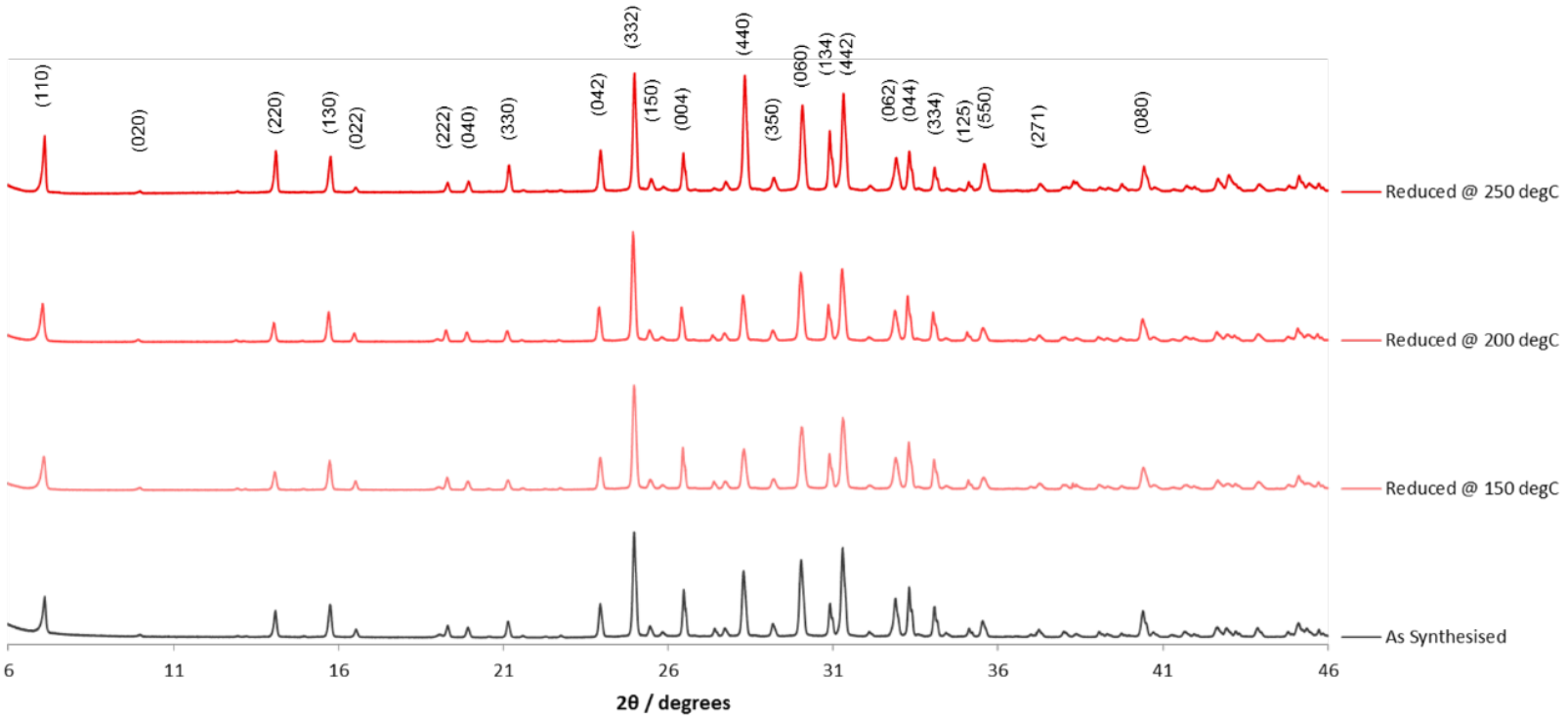

Figure 4-k: Indexed PXRD of the Au/CuClP materials activated at different temperatures (red) with the pre-activation, as-synthesised sample (grey) for comparison.

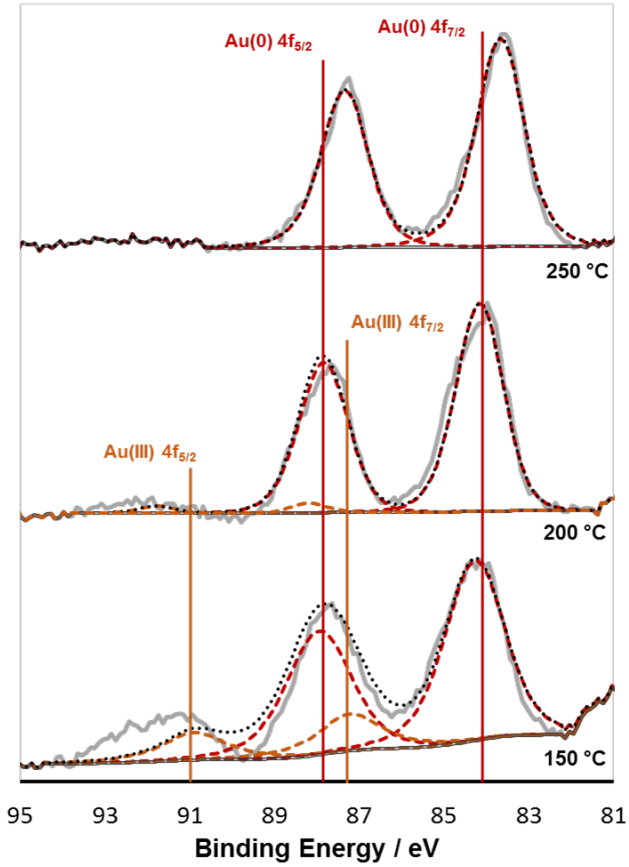

Figure 4-l: Stacked XPS data of the Au 4f binding region for the Au/CuClP catalysts activated at different temperatures. The data is shown in grey with the data fit in black, Au^0 transitions are depicted in red and the Au^{III} transitions in orange.

Thus, it can be observed that metallic Au nanoparticles are achievable upon the host frameworks surface at temperatures as low as 200-250 °C under a reductive activation protocol. This is further supported by AC-STEM studies of the Au/CuClP material, activated at 200 °C, which show that regions of extensive, well-defined and small (approx. 3 nm) nanoparticle formation could be observed for the Au/CuClP at these temperatures in both Figure 4-m (a) and (b). This is similar to the observations made by Hinde and co-workers.[235] Figure 4-m (c) demonstrates that in addition to the small nanoparticles, significant larger nanoparticles (> 10 nm) are also present, even at 200 °C. Consistent with the XPS studies and those observations made for the Pd/CuClP systems, the nanoparticle formation would appear to predominate at thin or surface periphery regions of the framework. Further, STEM-EDXS also confirms the presence of extruded Au species upon the materials surface as observed in Figure 4-n. This suggests that Au nanoparticles are readily attainable through these activation protocols and development of these procedures could lead to enhanced control over the nanoparticle extrusion and characteristics such as size and distribution.

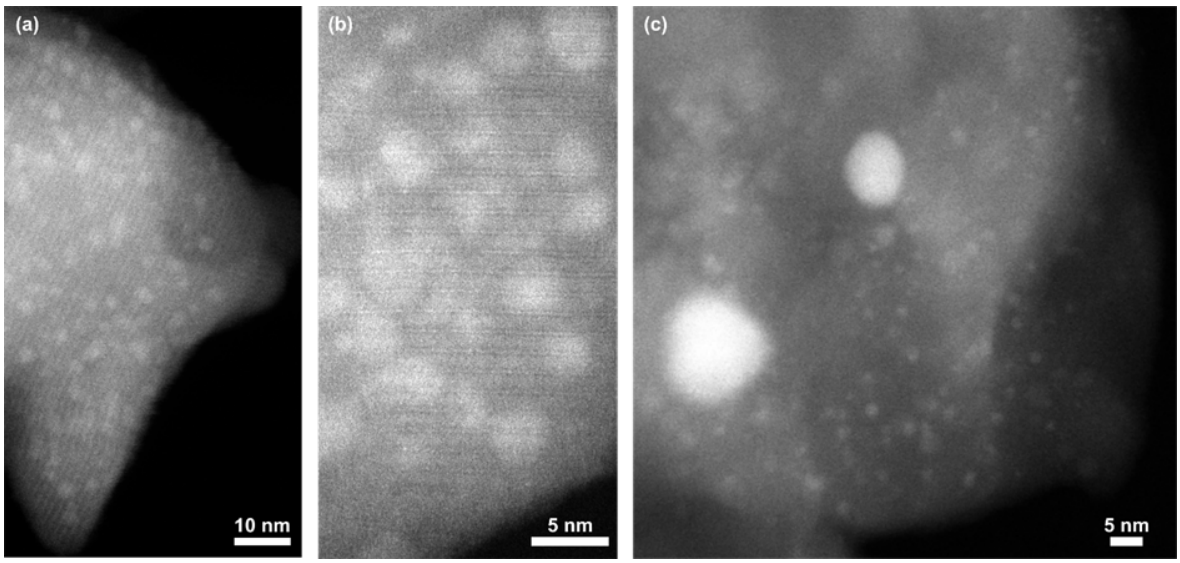

Figure 4-m: ADF AC-STEM images of the Au/CuClP material activated at 200 °C.

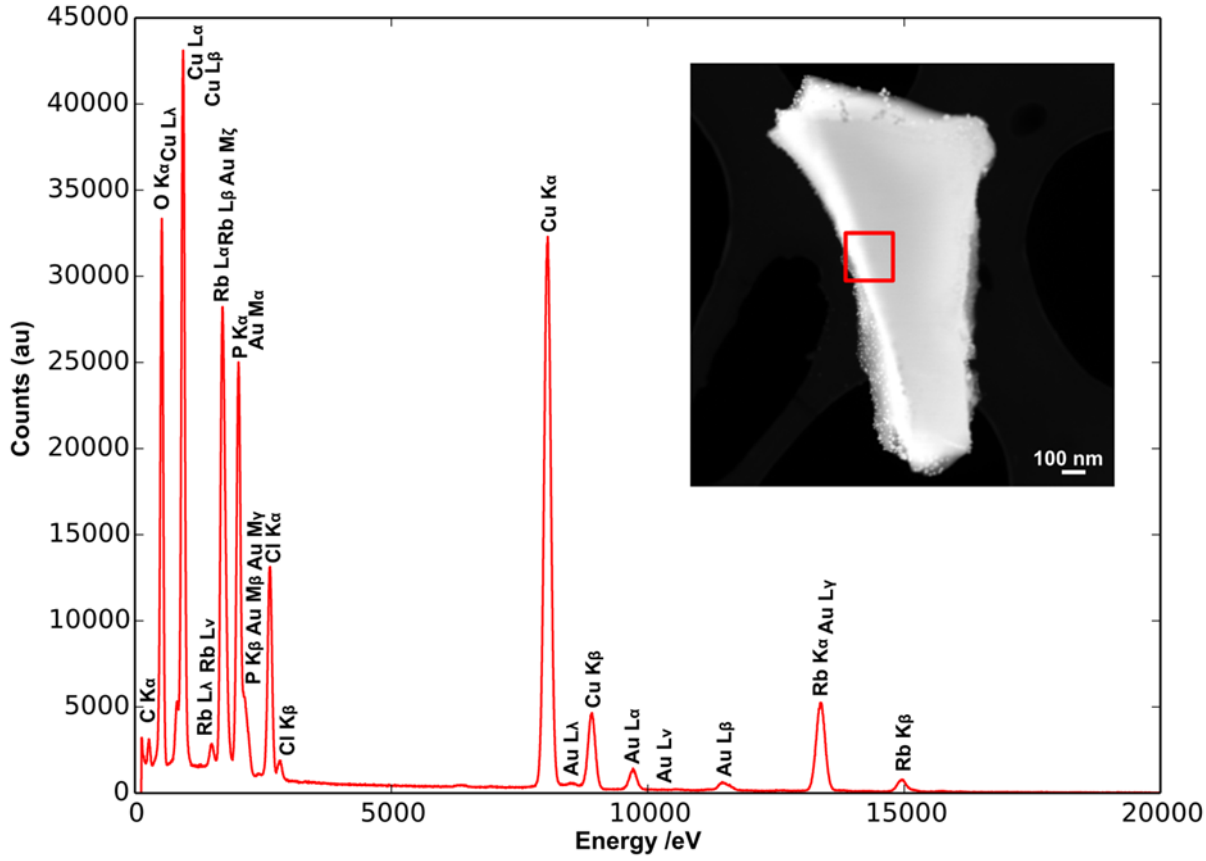

Figure 4-n: EDX spectrum for the Au/CuClP material activated at 200 °C. The area analysed is indicated by the red box in the inset ADF-STEM image.

Following the observable differences between the surface regions of the Pd/CuClP system and the bulk, the Au/CuClP materials were also investigated through XAS. Unfortunately, the Au XAS data (Figure 4-o) was collected on two separate occasions with the 200 °C data being collected individually, slightly detracting from its direct comparability. This is evident from the fitting parameters in Table 4-j as it is clear that the

200 °C data stands out with a comparatively lower Au-Cl CN and bond length, although still within the 2.267-2.290 Å range expected.[274,275] With that said, the EXAFS component does emphasize that within the bulk, minimal metallic Au is present and a significant proportion of the $[AuCl_4]^-$ precursor remains. Consequently, the material requires much higher activation temperatures in order to fully reduce the precursor as no plausible fit was possible with a Au-Au scattering path. Therefore, although the XPS and ADF-STEM show surface nanoparticulate Au species being generated at 200 °C and above, consistent with earlier work by Hinde *et al.*[235] the bulk EXAFS shows that these species are a minority compared to the total volume of Au species within the system. Promisingly, the PXRD (Figure 4-k) shows no sign of diminishing structural integrity and therefore higher activation temperatures should be accessible.

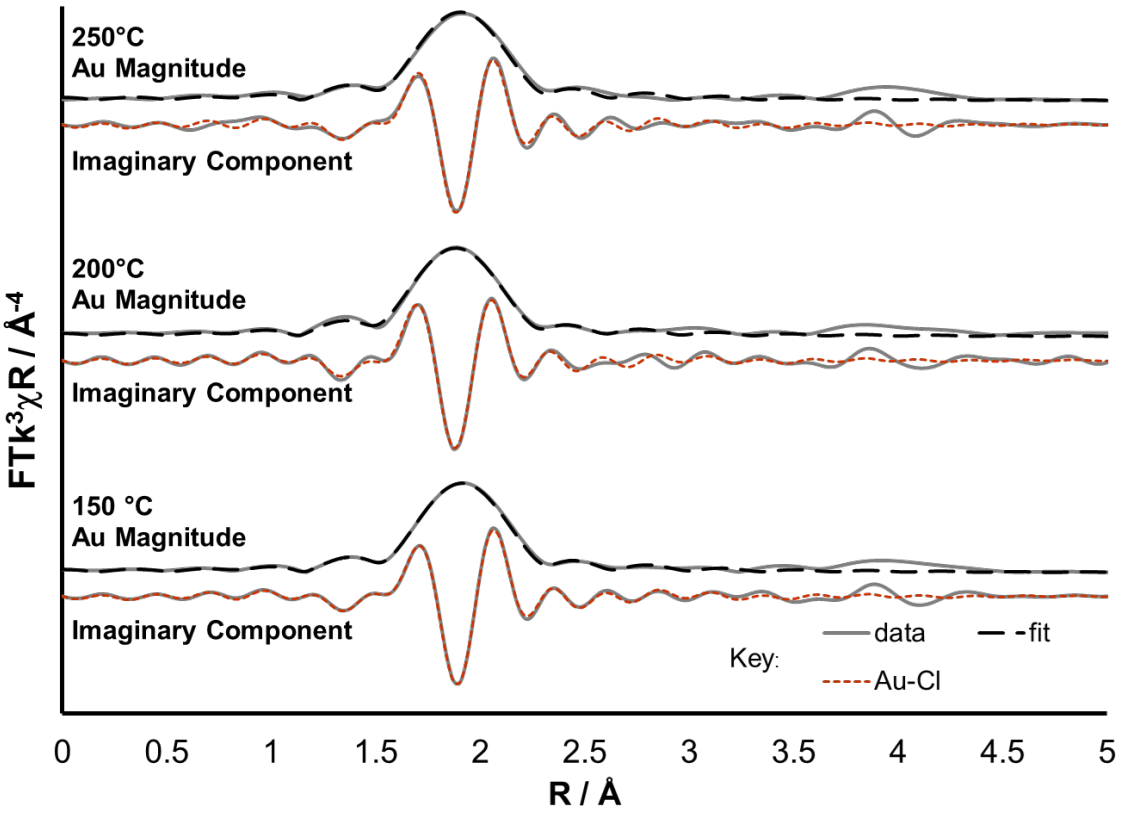

Figure 4-o: The magnitude and imaginary component of the k^3 weighted Fourier transform for the EXAFS data of the three Au/CuClP species reduced under increasing activation temperatures. Associated scattering paths are included for the imaginary component and the fitting parameters are displayed in Table 4-j.

Sample	Abs Sc	N	R / Å	$2\sigma^2$ / Å^2	E_f / eV	R_{factor}
Au/CuClP 150 °C	Au – Cl	3.7 (1)	2.287 (4)	0.0027 (2)	9.9 (6)	0.004
Au/CuClP 200 °C	Au – Cl	2.24 (7)	2.269 (4)	0.0028 (3)	7.3 (7)	0.009
Au/CuClP 250 °C	Au – Cl	3.1 (1)	2.282 (5)	0.0029 (3)	9.4 (9)	0.010

Table 4-j: Au/CuClP EXAFS fitting parameters. Au sample - S_0^2 = 0.75 as deduced by $KAuCl_4$ standard; Fit range 3.5<k<12.5, 1.1<R<3; # of independent points = 10.

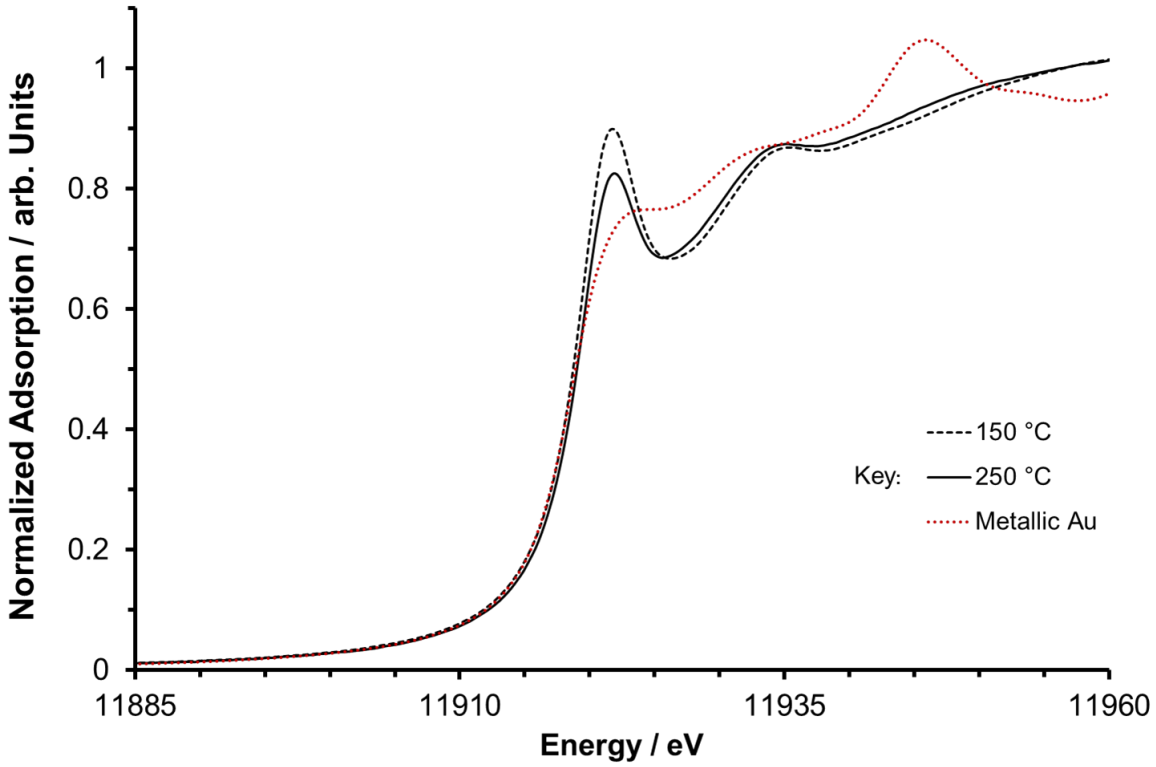

Figure 4-p: Stacked XANES data of the Au L_{III} edge for the Au/CuClP materials activated at different temperatures with a metallic gold reference in red. Note: Au/CuClP activated at 200 °C data was collected on a separate occasion and thus differences in absorption intensity prevents direct comparability.

While no Au-Au scattering path was able to be fitted to the EXAFS data, the XANES data shown in Figure 4-p does support the XPS and AC-STEM findings. The diminishing white line intensity of the Au L_{III} edge is directly proportional to the average oxidation state of all the Au centres within the entire sample. The white line absorption arises from the excitation of Au $2p_{3/2}$ electrons to unoccupied Au 5*d* or 6*s* states thus, as the Au oxidation state increases the 5*d* and 6*s* states become decreasingly populated, allowing more excitations and resulting in stronger white line absorption at this energy.[197] Therefore, the diminishing white line intensity with increasing activation temperature demonstrates the

progression towards a more reduced species. This vindicates the hypothesis that metallic Au species form on the surface of these materials at 200 °C and above but also suggests that higher temperatures and/or alternate activation conditions might be required to achieve complete extrusion of the chlorometallate precursor and in contrast to the Pd/CuClP, this could be possible while maintaining the structural integrity of the support framework.

4.2.3 Extrusion by Reduction: The Case of Platinum

The Pt/CuClP materials, of the form $Rb_9Cu_6(P_2O_7)_4Cl.[PtCl_4]Cl_2$, were activated at the same temperatures (150 – 200 °C) as their Pd counterparts, due to the findings of Hinde *et al.*[235] showing that 200 °C was sufficient to observe complete nanoparticle formation. Similarly to the Au and Pd systems, the extent of extrusion as a function of activation temperature was investigated through: PXRD, ADF-STEM, XPS and XAS. PXRD measurements were performed on all the fresh and activated (i.e. reduced at 200 °C for 2 hr in 5% H_2/N_2 flow) materials and the results are shown in Figure 4-q. Close inspection of the PXRD patterns (with signals of note highlighted in Figure 4-q) show that the peaks at 2θ 15.5°, 25.5° and 36.5° (red boxes in Figure 4-q) display maximum intensity in the as-synthesised catalyst and they then decrease as a function of reduction temperature to a point where they are no longer visible after activation at 200 °C. The depreciation of these peaks is analogous to the observations made in Chapter 3, previously attributed simply to structural changes within the Pt/CuClP materials and potential instability of the framework. Interestingly, it is also apparent that these peaks dramatically increase in intensity with increasing Pt loading (Figure 4-r) and are not present within the PXRD pattern of the un-doped framework (Figure 4-s). Furthermore, the un-doped framework shows no changes under analogous activation conditions which suggests that any changes observed are directly due to the incorporation of the $[PtCl_4]^{2-}$ ions and the ensuing extrusion process. Therefore, we hypothesise that these reflections are from the Pt containing crystallographic planes. Given the comparatively high electron density of Pt, the Pt atoms would be a significant contributor to the volume of x-rays diffracted by Pt containing lattice planes (Section 2.3.1).[196] This explains the depreciation of the associated reflections upon extrusion which result in the removal of the highly electron dense Pt atoms from those specific lattice planes.

This is further evidenced by the emergence of both metallic Pt and RbCl phases, black and blue boxes respectively in Figure 4-q. Both phases are a direct result of the extrusion process and follow the reverse trend to that observed above for the Pt containing CuClP crystallographic planes. The metallic Pt reflection present at 39.6 ° is assigned to the (111) plane and presents with a broad signal suggesting the presence of small crystallites

or nanoparticles.[276] Similarly, the RbCl reflections at 23.3°, 27.1° and 38.7° represent the (111), (002) and (022) planes respectively as seen in Figure 4-t. This is a consequence of the removal of Rb^+ ions from the framework in order to maintain an overall neutral charge through decomposition of the $[PtCl_4]^{2-}$ species.

Ordinarily PXRD would not only offer an insight into any structural changes within the CuClP host framework but it would also offer an excellent means to monitor the size and growth of nanoparticle species within the material due to the relationship between the broadness of the PXRD signal and the size of the crystalline domain, as established by Scherrer *et al.*[276] (Equation 27). The metallic Pt reflection present at 39.6° (Figure 4-q) is unfortunately surrounded by overlapping signals from the host framework. This renders the use of the Scherrer equation impossible due to inaccurate FWHM values and therefore no accurate particle size measurements can be established from this data.

$$\tau = \frac{K\lambda}{\beta cos\theta}$$

Equation 27: *The Scherrer equation.[276] T: the mean size of the crystalline domains, K: the 'shape factor (dictated by the crystallite shape), λ: the x-ray wavelength, β: line broadening or FWHM (rads) and θ the Bragg angle (°).*

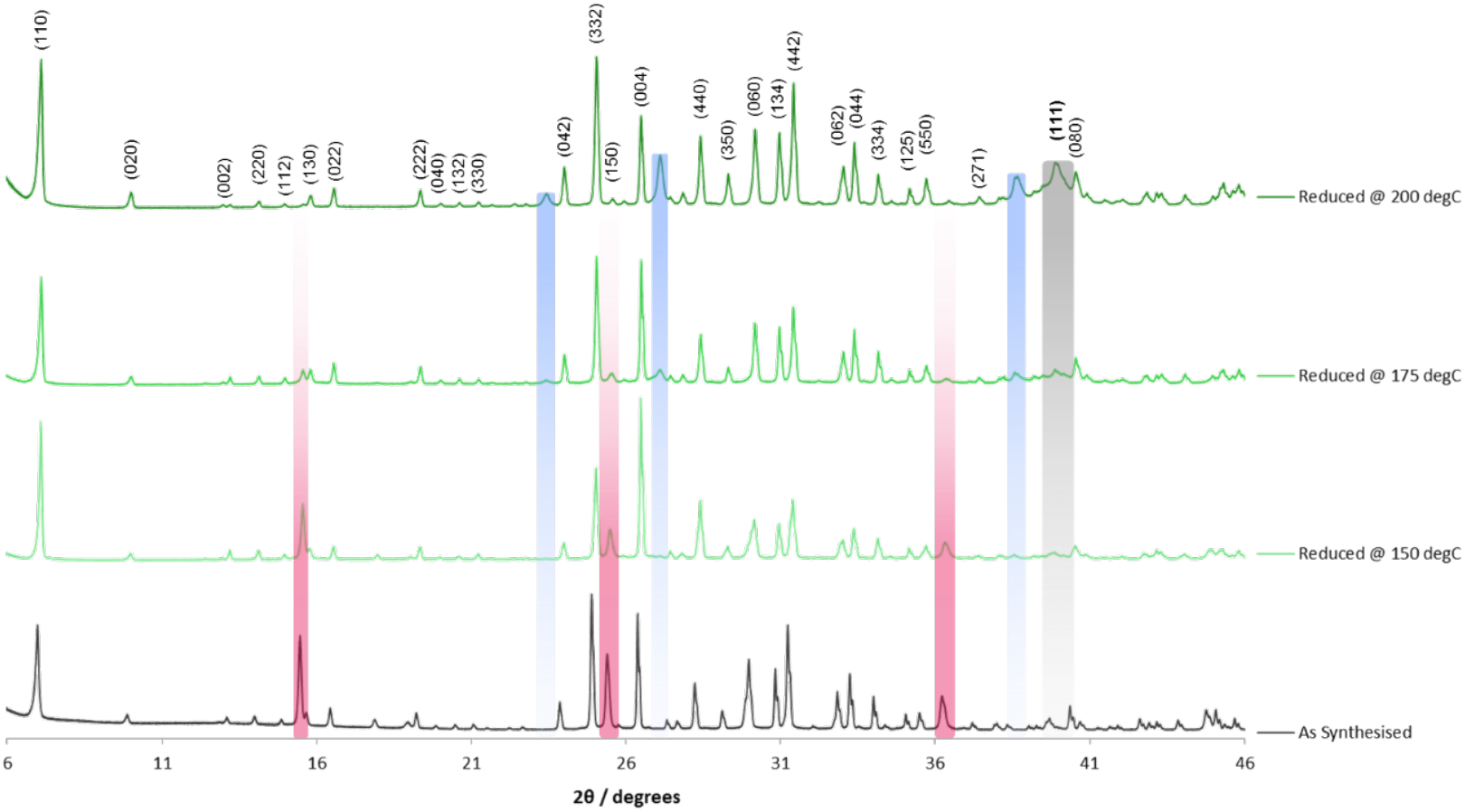

Figure 4-q: Indexed PXRD of the Pt/CuClP materials activated at different temperatures (green) with the pre-activation, as-synthesised sample (grey) for comparison. Impurity rubidium chloride phase highlighted in blue, metallic Pt (111) signal is highlighted in grey and Pt content dependant reflections are highlighted in red.

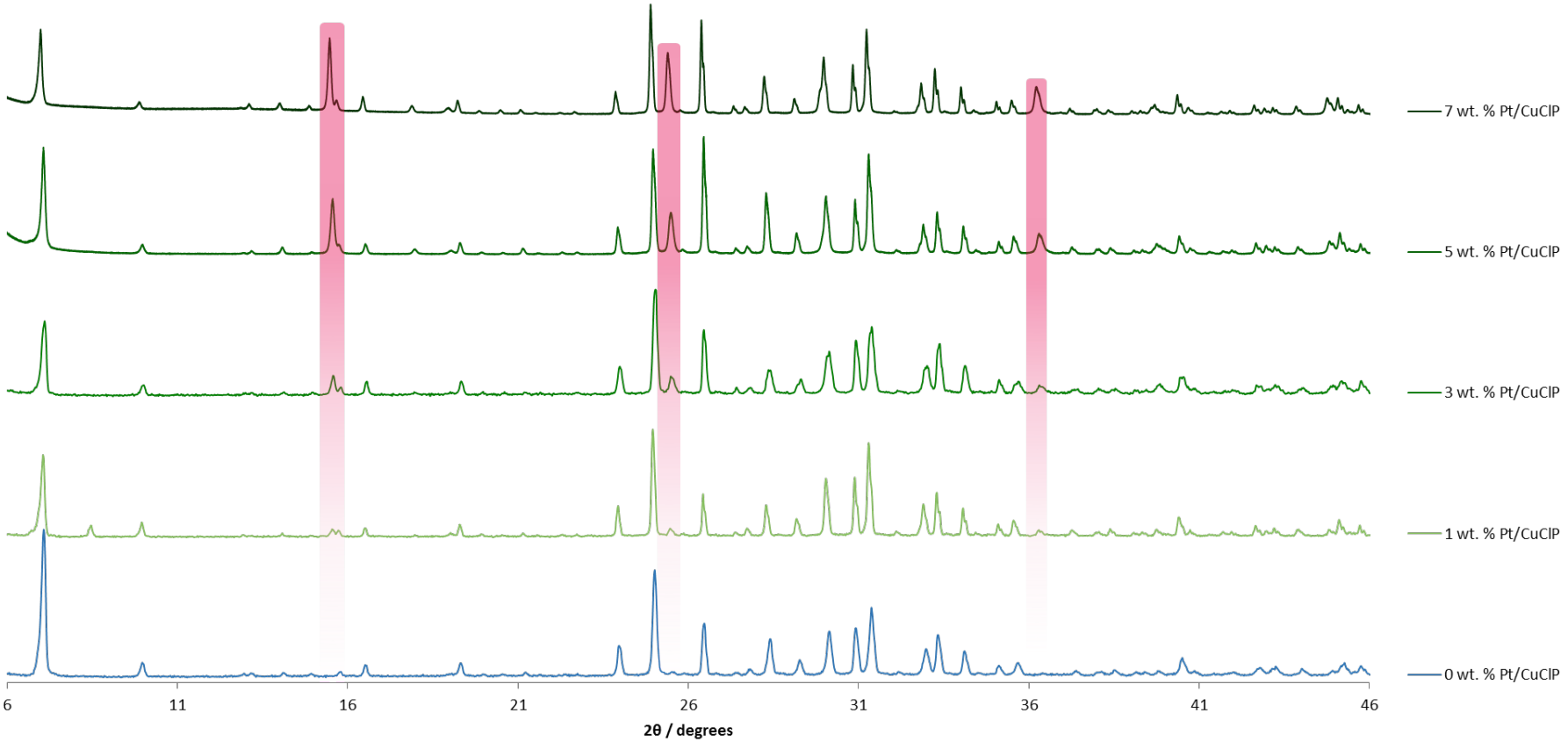

Figure 4-r: PXRD of the Pt/CuClP materials with different Pt loadings pre-activation. Pt content dependant reflections are highlighted in red.

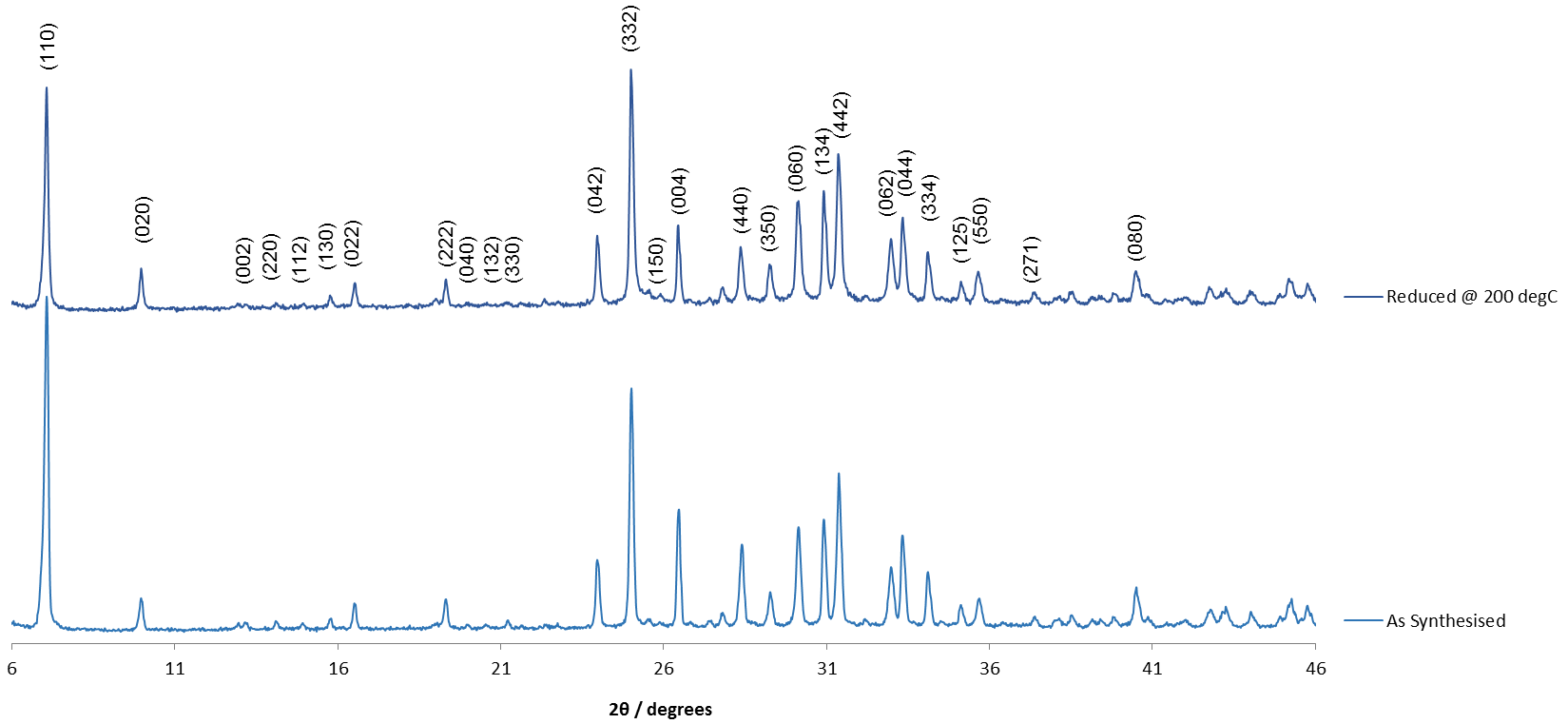

Figure 4-s: Indexed PXRD of the un-doped CuClP materials before and after activation at 200 °C under reduction conditions.

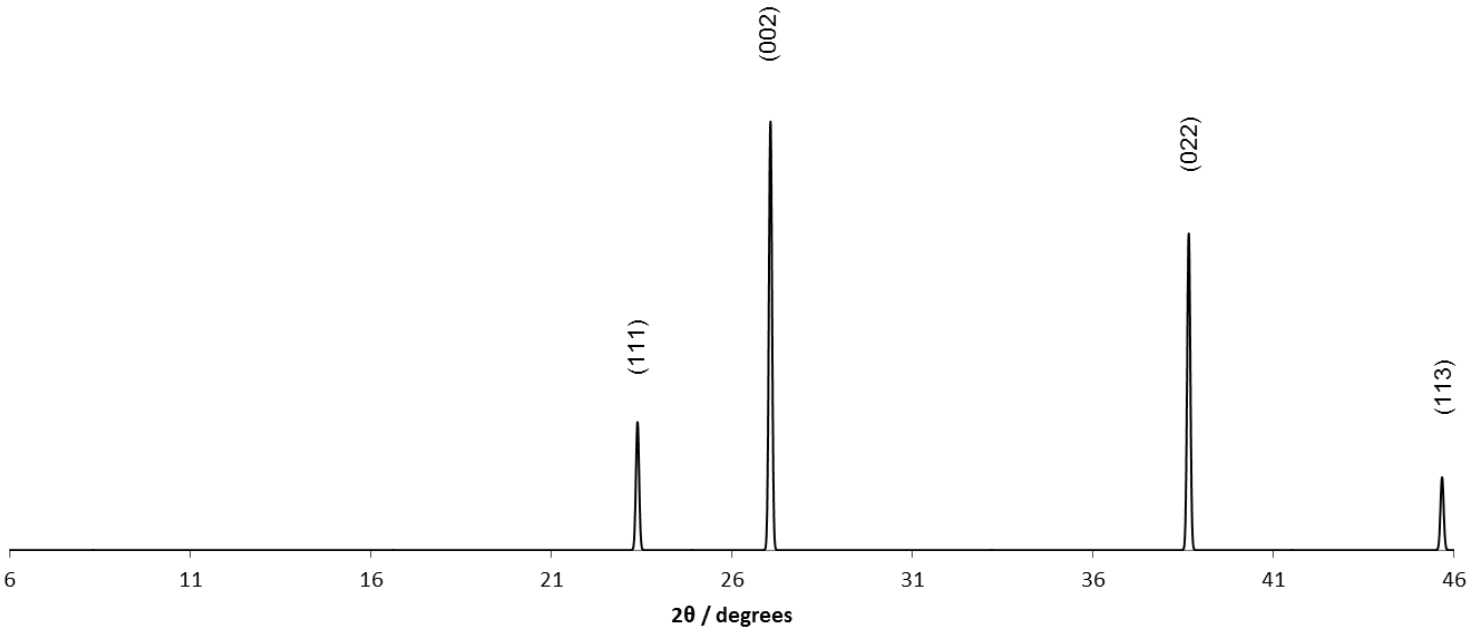

Figure 4-t: Simulated PXRD pattern of rubidium chloride RbCl with hkl values displayed above the peaks.[277]

XPS was employed to probe the nature of noble metal species adjacent to the surface of the microporous framework, with respect to different activation temperatures. A clear trend is observed, consistent with the PXRD findings outlined above. Figure 4-u shows the clear transition from a mixture of Pt^{IV}, Pt^{II} and Pt^{0} with $4f_{7/2}$ peaks at 74.8, 72.4 eV and 70.8 eV respectively, to purely Pt^{0} species, as the activation temperature was progressively increased from 150 to 200 °C. The presence of higher Pt oxidation states, such as Pt^{IV}, has previously been observed under sterically confined environments e.g. within porous networks.[235,256] This would suggests that these species possess a degree of coordinative flexibility which is most likely facilitated by the ionic flexibility of the host CuClP framework. Furthermore, it can be suggested that an activation temperature of 200 °C was sufficient for the complete reduction of the Pt precursors to form nanoparticles under these activation conditions similar to the observations of Hinde *et al.*[235] These observations demonstrate the ability to track the removal of $[PtCl_4]^{2-}$ species from the framework channels and the concurrent metallic Pt nanoparticle formation as a function of reduction temperature across these materials, most successfully with the Pt/CuClP materials.

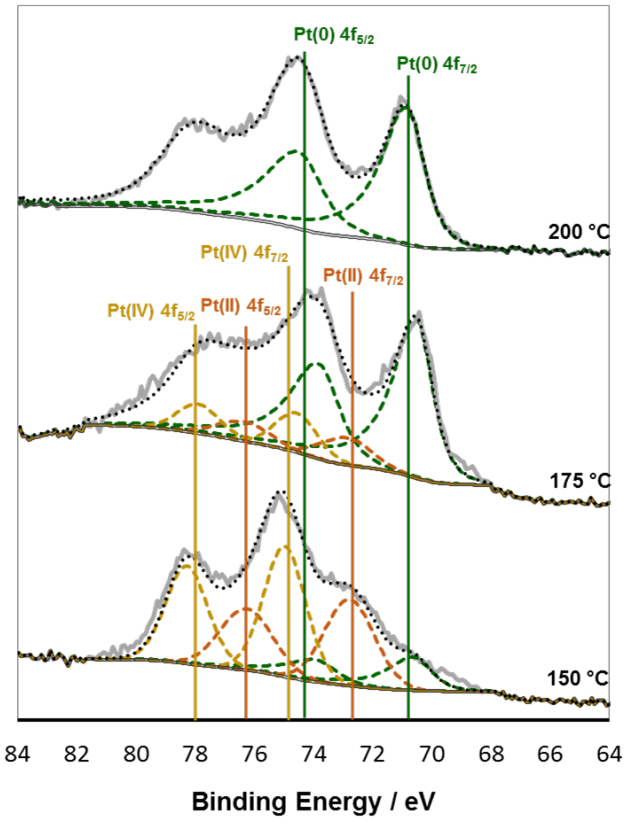

Figure 4-u: Stacked XPS data of the Pt 4f binding region for the Pt/CuClP catalysts activated at different temperatures. The data is shown in grey with the data fit in black, Pt^{0} transitions are depicted in green, Pt^{II} in orange and the Pt^{IV} transitions in mustard. Overlapping Cu 2p transitions have been omitted for clarity.

XAS analysis was required to probe any potential differences, as previously observed for the Au and Pd systems, between the materials bulk and the surface regions observed by XPS. The PXRD strongly suggests that within the Pt/CuClP materials, lies significantly higher levels of reproducibility by contrast with their Au and Pd analogues. Concurrent trends with the XPS and PXRD are exhibited in both the XANES (Figure 4-v) and EXAFS (Figure 4-w and Table 4-k). The progressive reduction of the $[PtCl_4]^{2-}$ precursor species across the bulk of the sample is evident in both. Similarly to Au, due to the direct relationship between the white line intensity of the L_{III} edge and the number of unoccupied Pt 5*d* states, the diminishing white line energies displayed in Figure 4-v suggest that the Pt species are approaching the metallic state with progressive increase in activation temperature. Furthermore Figure 4-w demonstrates the significant decrease in contribution from Pt-Cl neighbouring atoms with a concurrent increase in Pt-Pt neighbours as a function of activation temperature. In addition, Table 4-k shows that Pt-Pt bond lengths remain consistent with that expected of Pt nanoparticles above 2.4 nm (2.76 Å)[278] and that the CNs of the first shell Pt-Pt scattering path are also lower at 9.6(4) than would be expected of bulk Pt metal at 12.[279] This indicates that an overwhelming majority of the $[PtCl_4]^{2-}$ precursor is reduced to its metallic state with the increase in activation temperature, as evidenced by the drastic increase in the average CNs of adjacent Pt atoms around the central Pt species.

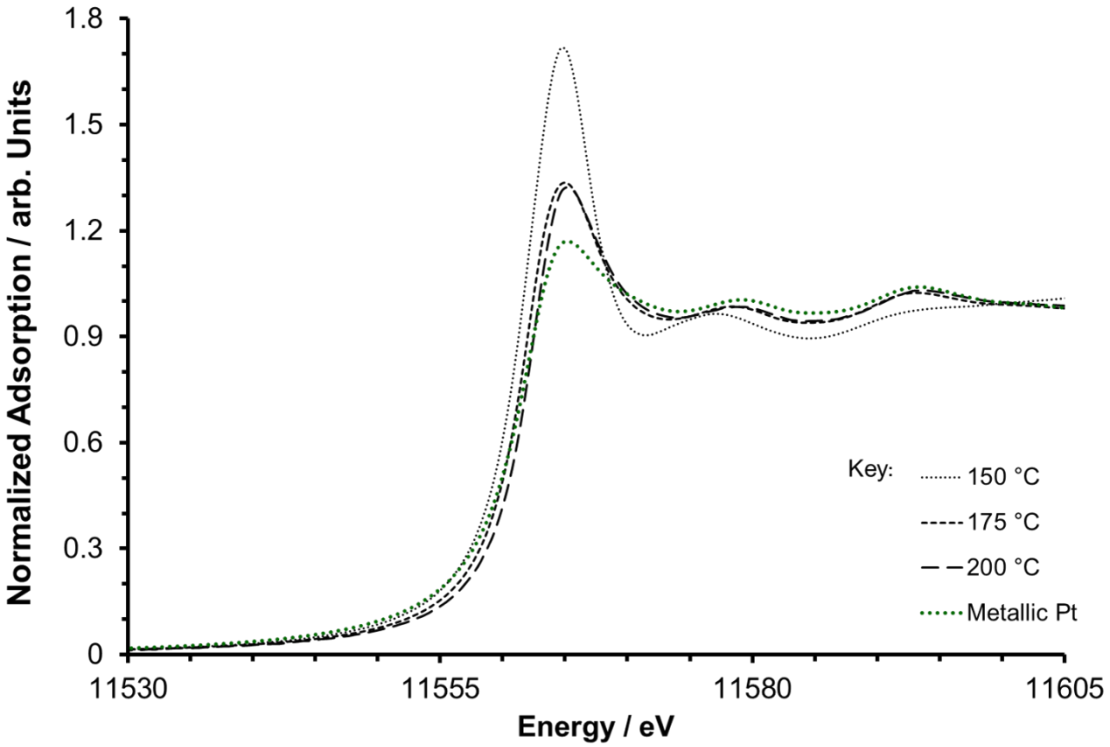

Figure 4-v: Stacked XANES data of the Pt L_{III} edge for the Pt/CuClP materials activated at different temperatures with a metallic platinum reference in green.

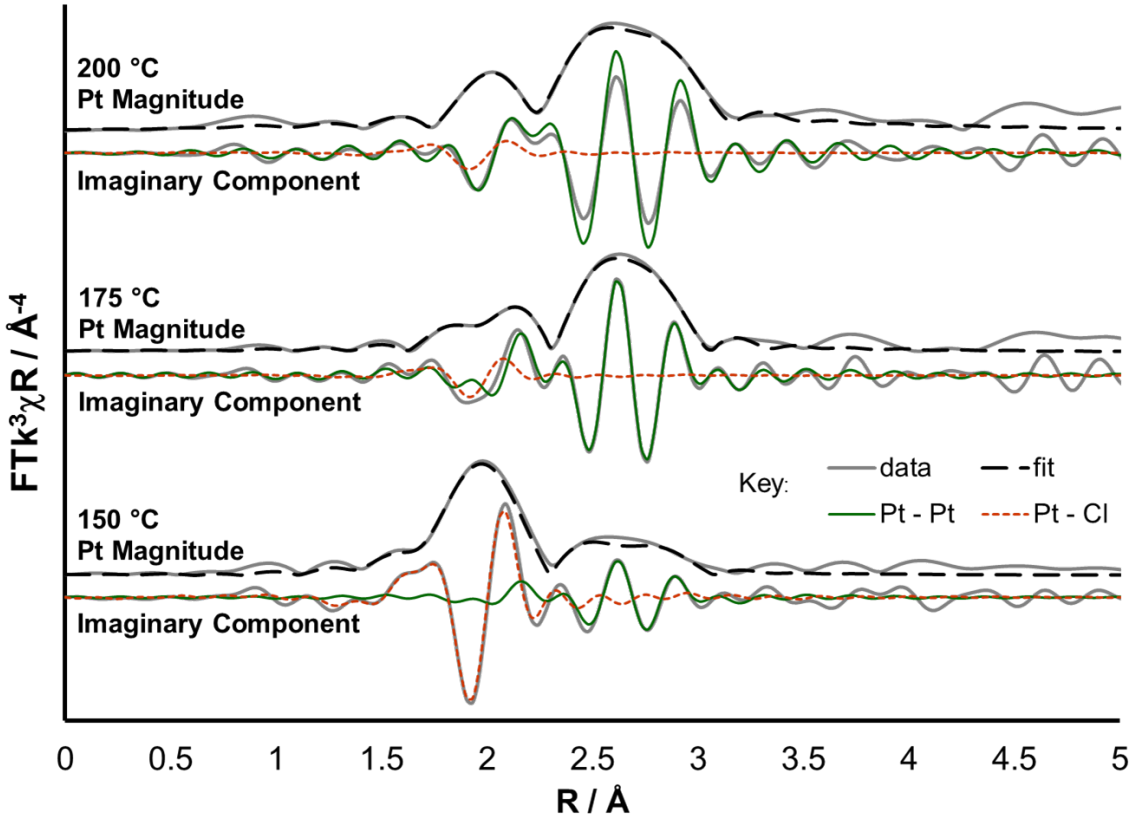

Figure 4-w: The magnitude and imaginary component of the k^3 weighted Fourier transform for the EXAFS data of the three Pt/CuClP species reduced under increasing activation temperatures. Associated scattering paths are included for the imaginary component and the fitting parameters are displayed in Table 4-k.

Sample	Abs Sc	N	R / Å	$2\sigma^2$ / Å^2	E_f / eV	R_{factor}
Pt/CuClP 150 °C	Pt – Cl	3.7 (2)	2.320 (5)	0.0027 (3)	9.5 (8)	0.012
	Pt – Pt	3.4 (5)	2.768 (7)	0.0056 (5)		
Pt/CuClP 175 °C	Pt – Cl	0.8 (1)	2.31 (9)	0.0026 (8)	7.9 (7)	0.006
	Pt – Pt	8.9 (3)	2.76 (2)	0.0059 (1)		
Pt/CuClP 200 °C	Pt – Cl	0.4 (1)	2.32 (2)	0.003 (2)	7.6 (6)	0.006
	Pt – Pt	9.6 (4)	2.760 (3)	0.0059 (2)		

Table 4-k: Pt/CuClP EXAFS fitting parameters. Pt sample - S_0^2 = 0.91 as deduced by Pt foil standard; Fit range 3<k<14, 1.15<R<3; # of independent points = 12.

High-resolution studies, using AC-STEM, have shown in detail the abundant formation of nanocrystalline Pt nanoparticles (2-5 nm in diameter), which are well-dispersed on the CuClP framework, whose crystalline integrity could also be visualized directly (Figure 4-x). In this regard, it is apparent that the atomic number contrast and direct interpretability of ADF STEM imaging, combined with the high-spatial resolution enabled by AC optics (Section 2.3.4), can yield significant insight into the crystallographic structures of both the extruded nanoparticles and the microporous framework. The much more limited and less

defined nanoparticle formation of the Pd/CuClP system has already been highlighted (Section 4.2.1) and emphasizes the effectiveness of the Pt/CuClP material in the controlled production of small (2-3 nm), well-dispersed, surface bound Pt nanoparticles. Complementary compositional studies using STEM-EDXS also confirmed the well-defined nature of the Pt/CuClP, with the abundance of nanoparticles again apparent in Figure 4-y.

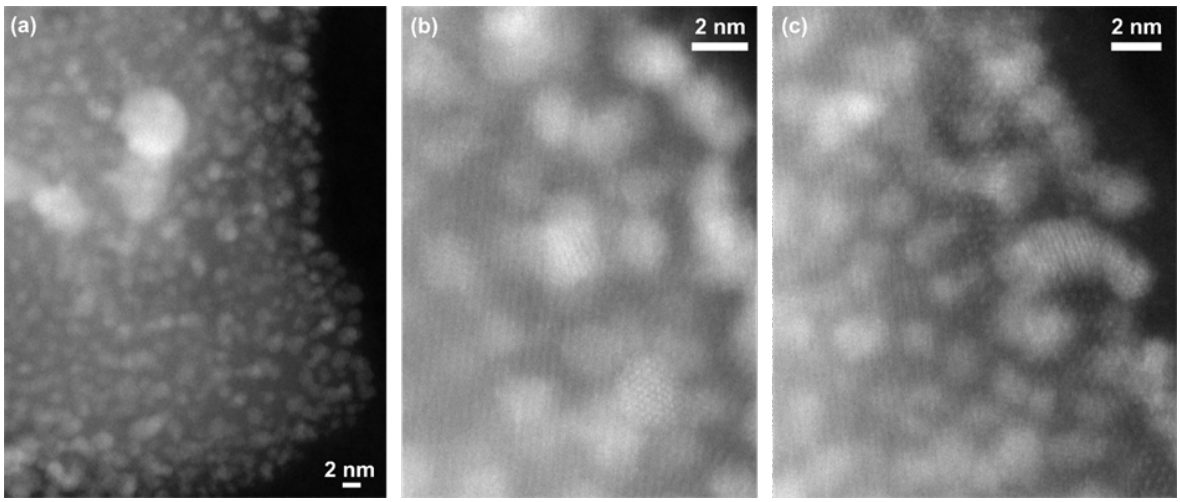

Figure 4-x: ADF AC-STEM images of the Pt/CuClP material activated at 200 °C. (a) Nanoparticle formation across the framework (nanoparticle size in this area approx. 2-3 nm in diameter). (b,c) High-resolution images of the nanoparticles, in which the measured d-spacing's are consistent with nanocrystalline Pt. The crystalline integrity of the framework is also rendered visible, by virtue of the framework lattice planes containing heavy-metal atoms.

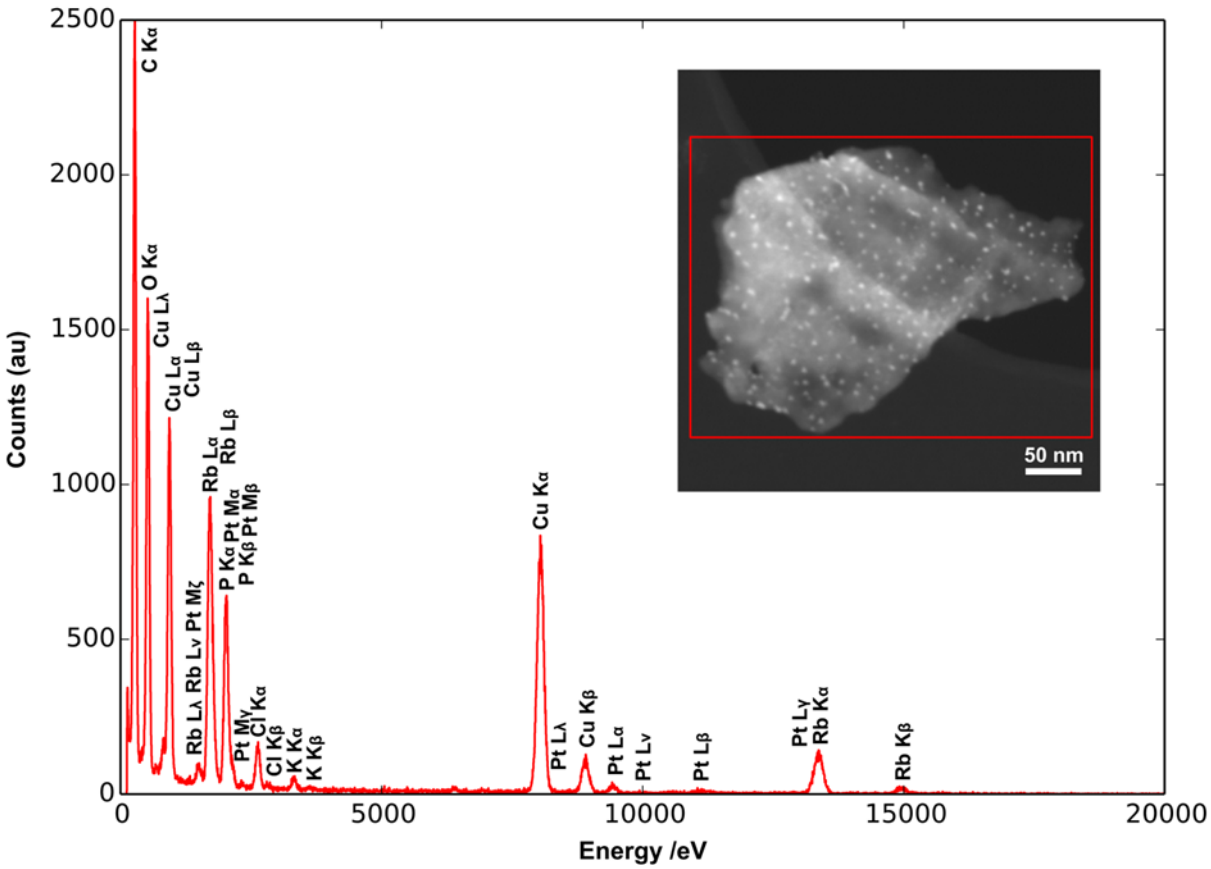

Figure 4-y: EDX spectrum for the Pt/CuClP material activated at 200 °C. The area analysed is indicated by the red box in the inset ADF-STEM image.

4.2.4 The Selective Aerobic Oxidation of KA Oil to Pure Cyclohexanone

The catalytic results for the aerobic oxidation of KA oil with the Pt, Pd and Au/CuClP catalysts, activated under the same conditions as those structurally investigated thus far, are presented in Figure 4-z. This is done with reference to Table 4-l which demonstrates that no cyclohexanol conversion is achieved in the absence of the M/CuClP (M: Au Pt or Pd) catalyst. In fact, Table 4-l further highlights that the host CuClP framework is inactive without the presence of the noble metal nanoparticles. Figure 4-z highlights the superior performance of the Pt/CuClP catalyst over that of its corresponding Pd and Au analogues. Notably, it is remarkable that the selectivity for the desired cyclohexanone was in excess of 99+%. This is an aspect only achieved by two other nanoparticle systems without the presence of additives (Table 4-e) and neither of these possess cyclohexanol conversions over 50%.[101,103] Thus, it highlights the effectiveness of this particular Pt/CuClP catalyst and extrusion process.

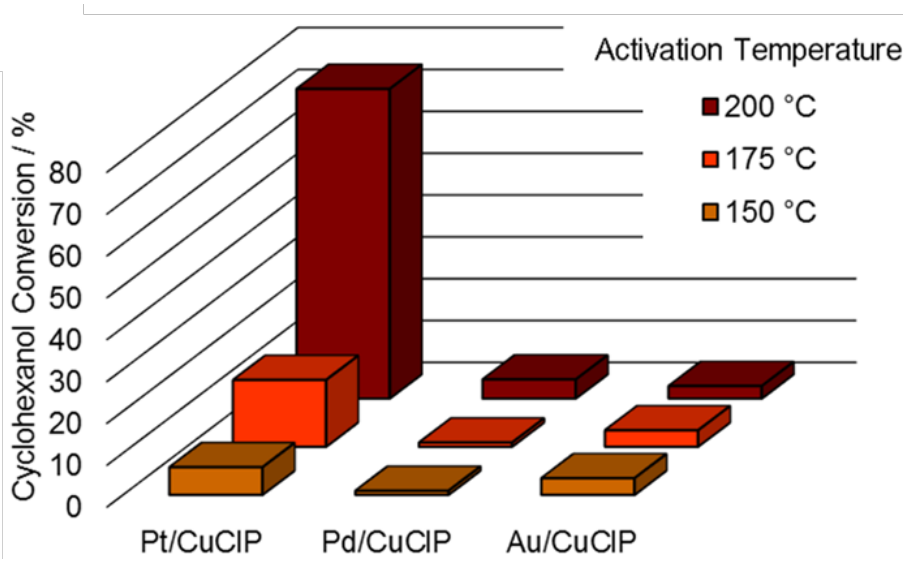

*Figure 4-z: Catalytic results summarizing the activities of Au, Pt & Pd/CuClP catalysts activated at different temperatures in the aerobic oxidation of KA oil. Note – cyclohexanone selectivities were >99% for all data points. From A. M. Gill, C. S. Hinde, R. K. Leary, M. E. Potter, A. Jouve, P. P. Wells, P. A. Midgley, J. M. Thomas and R. Raja, ChemSusChem, 2016, **9**, 423 – 427 Reprinted by permission of John Wiley & Sons, Inc.*

Catalyst	Substrate	Temperature / °C	Cyclohexanol Conversion / mol %	Cyclohexanone Selectivity / mol %
CuClP	Cyclohexanol	200	1	>99
CuClP	Cyclohexanol	300	2	>99
None	Cyclohexanol	200	1	>99
None	Cyclohexanol	300	2	>99
None	KA oil	200	3	>99
None	KA oil	300	3	>99

Table 4-l: Catalytic data from the aerobic oxidation of cyclohexanol and KA oil, showing minimal levels of conversion for both the un-doped framework and the reactions in the absence of catalyst.

Table 4-d and Table 4-e reflect the domination of impregnation methodologies for the production of heterogeneous nanoparticle catalysts utilized within the production of cyclohexanone from cyclohexanol. This is irrespective of whether they employ a dehydrogenation or direct oxidation pathway. This is most likely due to the simplicity and versatility of impregnation methods (discussed in Section 1.2.3.1), although it is clear that the majority of the high performing catalysts are produced by precipitation methods, either deposition-precipitation or co-precipitation. Both of these methods allow much better control over the nanoparticle size and size distribution than impregnation (discussed in Sections 1.2.3.2 – 1.2.3.4), emphasising its importance in these reactions. It is therefore significant that the Pt/CuClP catalyst can be generated in a well dispersed manner, with

small 2-3 nm particle diameters inside narrow size distributions. This therefore vindicates the significance of generating nanoparticle species in a controlled manner as an apparent consequence is improved catalytic activity. Whether that be near 100% selectivity towards the desired product or improved catalytic conversion, these attributes are likely down to the more controlled nanoparticle systems maintaining a better degree of site isolation within the appropriate nanoparticle size range of < 5 nm, as discussed in Section 1.2. Furthermore, while precipitation methods are limited by their maximum metal loadings of approx. 1 – 1.5 wt. %, the CuClP system allows the effective generation of these small nanoparticles at higher, up to 1 – 7 wt. % Pt loadings, facilitating the optimization of the catalysts activity to a wider degree.

Not only is the Pt/CuClP a highly effective and selective aerobic oxidation catalyst (while the undoped framework is inert, Table 4-l), but the robust nature of this material is evidenced by its ability to maintain high levels of activity and selectivity over extended periods on stream (10 hr), as displayed in Figure 4-aa. More importantly, the material retains its structural integrity post-catalysis as evidenced by its sustained phase purity as shown in Figure 4-bb.

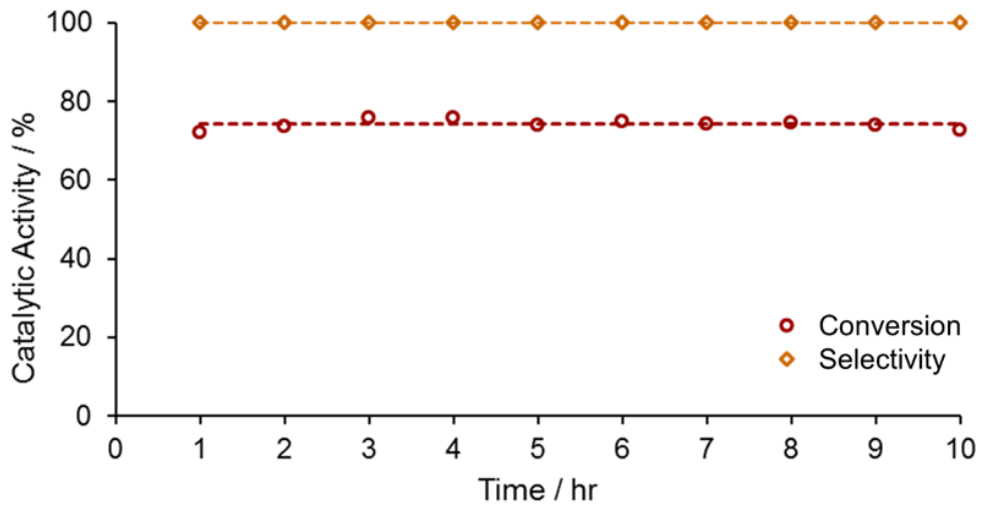

*Figure 4-aa: Influence of time-on-stream on cyclohexanol conversion and cyclohexanone selectivity in the KA oil oxidation using Pt/CuClP (activated at 200 °C) catalyst. From A. M. Gill, C. S. Hinde, R. K. Leary, M. E. Potter, A. Jouve, P. P. Wells, P. A. Midgley, J. M. Thomas and R. Raja, ChemSusChem, 2016, **9**, 423 – 427 Reprinted by permission of John Wiley & Sons, Inc.*

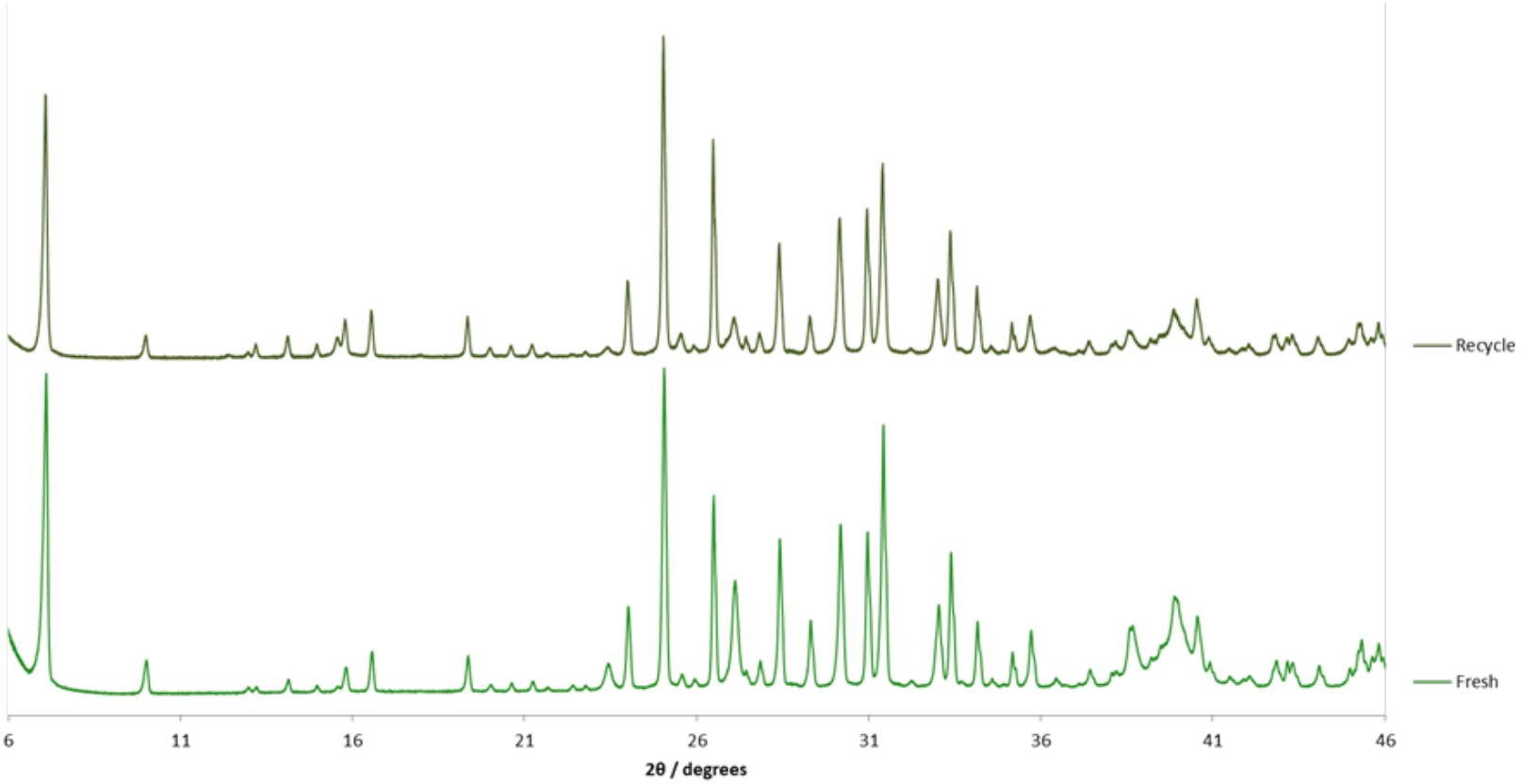

Figure 4-bb: PXRD of the Pt/CuClP materials activated at 200 °C both before (fresh) and after catalysis (recycle) in the oxidation of KA oil for 6 hr signifying the robust nature and extended lifetime of these catalytic materials.

These findings, along with the observed increase in cyclohexanol conversion as a function of activation temperature, something which has already been related to the extent of extrusion and nanoparticle formation, support the hypothesis that the catalytic activity of these materials can be intrinsically linked to the degree of nanoparticle formation. The $[PtCl_4]^{2-}$ precursor shows an excellent propensity for nanoparticle formation over a range of activation temperatures and this, in concert with the surrounding microporous architecture, bestows superior catalytic performance for the aerobic oxidation of KA oil. This is in contrast to the Au and Pd/CuClP systems, which show exceedingly limited activity given that other Au[101,104,145,242,249] and Pd[103,150] nanoparticle catalysts have shown activity for this transformation. This not only supports the relationship between proportion of extruded nanoparticle and the effectiveness of the catalyst, a key factor in describing the activity of the Pt/CuClP system, but it also supports the hypothesis that site isolation is a key feature in the effectiveness of these materials. Both the Au and Pd/CuClP catalysts demonstrated congested nanoparticle formation in small, surface periphery regions only, limiting the nanoparticle dispersion within both systems and in turn lowering their degree of site isolation. Therefore it's apparent that not only is it key to fabricate an abundance of active, small nanoparticle species but the nature and proximity of these sites is key towards achieving highly active and selective catalysts.

The local structural environment and isolated, well distributed nature of the Pt/CuClP active sites is evidently crucial for their superior performance in the aerobic oxidation of KA oil under continuous flow conditions. In fact, this inherent superior catalytic activity is able to approach yields of >90% by adapting a 'closed-loop' system where the ketone to alcohol ratio of the off-stream is reinserted to the reactor as the feedstock (Table 4-m). This clearly demonstrates the ability of the Pt/CuClP catalysts to surpass all other catalytic systems currently under investigation in the academic community for this process (to the best of my knowledge), as discussed in Section 4.1.2.

Cycle	Substrate Feed Molar Ratio (Cyol:Cyone)	Cumulative Cyclohexanol Conversion / mol %	Cyclohexanone Selectivity / mol %
1	1.00 : 1.00	67	>99
2	0.50 : 1.00	81	>99
3	0.10 : 1.00	93	>99
4	0.04 : 1.00	95	>99

Table 4-m: Catalytic data from closed-loop experiments involving the Pt/CuClP catalyst (activated at 200 °C).

4.3 Conclusions

By employing a combination of complimentary structural, spectroscopic and high-resolution microscopy techniques, the varying degrees of Pt, Pd and Au nanoparticle formation have been contrasted under reductive activation conditions (i.e. reduced at 200 °C for 2 hr in 5% H_2/N_2 flow). The key structural findings for Pd, Au and Pt/CuClP materials are displayed in Table 4-n, Table 4-o and Table 4-p respectively. These highlight the superior properties of the $[PtCl_4]^{2-}$ precursor to yield well-defined, isolated nanoparticles (predominantly 2-3 nm) within/upon the microporous CuClP framework architecture via the employed extrusion methodology.

Technique	Key Findings
PXRD	- Structural integrity is maintained up to 150 °C - At temperatures above 150 °C framework degradation occurs leading to the production of a rubidium phosphate ($Rb(PO_3)$) phase
AC-STEM	- Limited nanoparticle formation even at 200 °C - Despite the diminished structural integrity evidenced by PXRD, regions of well-defined structure of the CuClP material are evident at 200 °C - Nanoparticle formation tends to occur at surface periphery regions, likely where the consequential framework degradation also occurs
STEM-EDXS	- Confirms the regions of well-defined Pd/CuClP material and paucity of nanoparticles
XPS	- An abundance of Pd^0 is present at lower activation temperatures within surface regions of the material - A progression from Pd^0 towards more Pd^{II} with increasing activation temperature is evident, suggesting that with the concurrent framework degradation the nature of the Pd species is altered as a consequence
XANES	- Progression of the edge feature at 24352 eV and the edge intensity at 24385 eV towards the metallic reference suggest a progression towards Pd^0 with increasing activation temperature
EXAFS	- A significant proportion of chloride persists across all the Pd/CuClP samples - The fitting parameters also show, analogously to the XANES, a mild progression towards metallic Pd - Incorporating a Pd-Cu scattering path leads to a substantial improvement in the data fit and therefore suggests that at higher activation temperatures the nature of the Pd species could be significantly more complex

Table 4-n: Summary of the structural features of the Pd/CuClP activated by reduction at 200 °C under a flow of 5% H_2/N_2.

Comparisons of Table 4-a (work carried out by Hinde et al.[235]) and Table 4-n demonstrate the development in understanding surrounding the extruded nanoparticle formation by reduction of the Pd/CuClP material. Given the large degree of structural vulnerability of the Pd/CuClP system at reduction temperatures of 200 °C and the uncertain nature of the

Pd species generated, it is clear that lower activation temperatures need to be employed. This has however, proved ineffective at generating the required abundant distribution of small metallic Pd nanoparticles in order to achieve an effective catalytic output. This can be attributed to a number of factors including limited nanoparticle formation, poor site isolation and inadequate control over the nature of the species generated as nanoparticle size distributions are vast with the production of larger particles (> 10 nm) prevalent and the precise composition of the Pd species still unknown. That being said, the XAS and XPS analyses herein have eluded to the more complex nature of the Pd or Pd-Cu species generated under these conditions.

Technique	Key Findings
PXRD	- Maintains its structural integrity across all the activation temperatures investigated: 150 – 250 °C
AC-STEM	- At 200 °C regions of extensive, well-defined and small (approx. 3 nm) nanoparticle formation are observed - In addition to the small nanoparticles, significant larger nanoparticles (> 10 nm) are also present even at 200 °C
STEM-EDXS	- Confirms the presence of extruded Au species upon the materials surface
XPS	- Progressive depreciation of Au^{III} content as a function of activation temperature is evident leading to the complete formation of Au^{0} at 250 °C - A shift to lower binding energies of the Au 4*f* signals when activated at 250 °C vindicates the presence of nanoparticulate species
XANES	- The diminishing white line intensity with increasing activation temperature demonstrates the progression towards Au^{0}
EXAFS	- Minimal metallic Au is present within the bulk of the sample and a significant proportion of the $[AuCl_4]^-$ precursor remains - No plausible fit is possible with a Au-Au scattering path

Table 4-o: Summary of the structural features of the Au/CuClP activated by reduction at 200 °C under a flow of 5% H_2/N_2.

This is in contrast to the Au/CuClP system (Table 4-b and Table 4-o), whereby the limited nanoparticle formation at temperatures < 250 °C has shown no signs of consequential structural instability and therefore suggests that higher temperatures (>250 °C) are required in order to achieve significant levels of extrusion and nanoparticle formation. Akin to the Pt/CuClP material, this could lead to significantly improved catalytic activity.

Technique	Key Findings
PXRD	- Maintains its structural integrity across all the activation temperatures investigated: 150 – 200 °C - Signals at 15.5°, 25.5° and 36.5° appear (approx.) proportional to the Pt content within the framework channels and depreciate as a function of activation temperature or extent of extrusion - RbCl phase is produced as a result of the extrusion process and therefore becomes an increasingly significant impurity with increasing temperature - Similarly, the metallic Pt (111) reflection present at 39.6 ° presents with a broad signal suggesting the presence of nanoparticles
AC-STEM	- The abundant formation of well dispersed nanocrystalline Pt nanoparticles (2-3 nm in diameter) is evidenced - The CuClP framework crystalline integrity could be visualized directly
STEM-EDXS	- Confirmed the well-defined nature of the Pt/CuClP, with the abundance of nanoparticles
XPS	- Clear transition from a mixture of Pt^{IV}, Pt^{II} and Pt^{0} at 150 °C to purely Pt^{0} species at 200 °C
XANES	- The diminishing white line intensity suggest that the Pt species are approaching the metallic state with progressive increase in activation temperature
EXAFS	- A significant decrease in contribution from Pt-Cl neighbouring atoms exists with a concurrent increase in Pt-Pt neighbours as a function of activation temperature - The Pt-Pt bond lengths remain consistent with that expected of Pt nanoparticles above 2.4 nm (2.76 Å) - The CNs of the first shell Pt-Pt scattering path are also lower at 9.6(4) than would be expected of bulk Pt metal at 12, eluding to the nanoparticulate nature of the Pt species

Table 4-p: Summary of the structural features of the Pt/CuClP activated by reduction at 200 °C under a flow of 5% H_2/N_2.

Finally, the Pt/CuClP (Table 4-c and Table 4-p) system has demonstrated its propensity to form an abundance of small (2-3 nm), discrete nanoparticles upon the hosts' surface, as evidenced by AC-STEM. This system displayed none of the aforementioned limitations associated with the Au and Pd materials. The almost complete reduction of the $[PtCl_4]^{2-}$ chlorometallate ion has been demonstrated by XPS, XAS and PXRD where it has become apparent that the deviations in the typical Pt/CuClP PXRD pattern (observed in Chapter 3) can be attributed to changes of the Pt speciation within the system. This also reveals the rubidium chloride by-product of the extrusion process.

In stark contrast with the Au and Pd systems, whose limited and ill-defined nanoparticle generation leads to their catalytic inactivity, the Pt/CuClP material is a highly active and selective oxidation catalyst for the aerobic oxidation of KA oil within a continuous flow system. This catalyst out performed its counterparts and by comparison to the current

academic literature, it has certified its place as the best performing catalytic material for this process, to the best of our knowledge, able to approach yields of >90% by adapting a ’closed-loop’ system. The likes of which have only thus far been achieved by dehydrogenation routes or by the use of solvents and basic additives within oxidation processes. The lack of additives and limited waste generated from the continuous flow system where the off-stream can be re-used as the feedstock, coupled with the exceptional catalytic performance, make this process a significant advance towards a more sustainable production of pure cyclohexanone (in accordance to the discussions in Section 1.1.4) surpassing those already reported.

Chapter 5: The Elucidation of Gold-Copper Alloying Within Gold Doped Copper Chloropyrophosphate Materials

It was shown in Chapter 4 that as you increase the activation temperature of the Au/CuClP catalyst above 200 °C you begin to see interesting structural features that are unique to the Au/CuClP system. Indeed, not only do we observe Au extrusion at these temperatures, but now it can be seen that we also observe Cu extrusion from within the framework. In this chapter, we explore this phenomenon in detail to better understand what drives the extrusion process, what species are generated, what the limitations are, what structure-property correlations we can deduce and how these factors impact on the material's behaviour as an oxidation catalyst.

Notable contributions:

- Dr Rowan Leary, Prof Paul Midgley and Prof John Meurig Thomas for their collection and processing of the AC-STEM and STEM-EDXS data presented within this chapter.
- Dr Naoko Sano and the NEXUS XPS facility at the University of Newcastle for the collection of the XPS data presented within this chapter.
- Dr Peter P. Wells for his assistance in the collection of the XAS data presented within this chapter and discussions with regards to fitting the EXAFS data.
- Sivan Van Aswegen and Tammi Nimmo for their collection and processing of the catalytic oxidation of δ-valerolactam data presented within this chapter.

5.1 Introduction

5.1.1 Cyclic Imides & Glutarimide

Cyclic imides are a highly desirable class of compound, possessing numerous applications in synthetic, biological and medicinal chemistries, with more than 20 kinds of glutarimide based, naturally occurring antibiotics.[280,281] Although there is a wide range of synthetic protocols for the production of imides generally,[282,283] the production of cyclic imides adds another level of complexity which is then enhanced when one takes into account the limitations of methodologies producing specific ring sizes. While it is well established that cyclic imides of a range of sizes can be produced from the dehydrative condensation of a dicarboxylic acid or an anhydride with an appropriate amine (Scheme 5-a), this particular process requires high temperatures (approx. 200 °C) and/or a promoter such as a Lewis acid to achieve yields > 70 %.[280,284] Many alternative routes also suffer similar drawbacks to the cyclisation of amic acids (Scheme 5-b), requiring promotors such as alkali metal salts and operating at low yields < 70 %.[280,285,286]

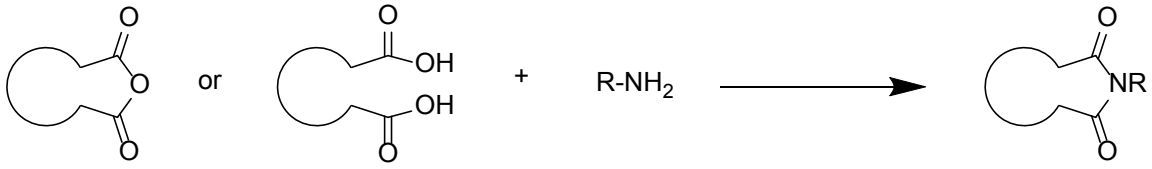

Scheme 5-a: Dehydrative condensation reaction.[284]

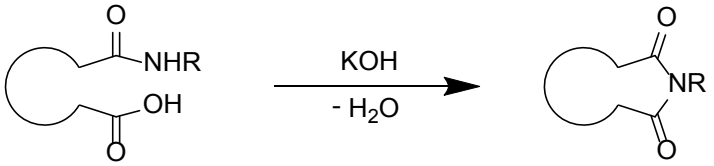

Scheme 5-b: Cyclisation of amic acids.[286]

Scheme 5-c: C-H bond activation.[287]

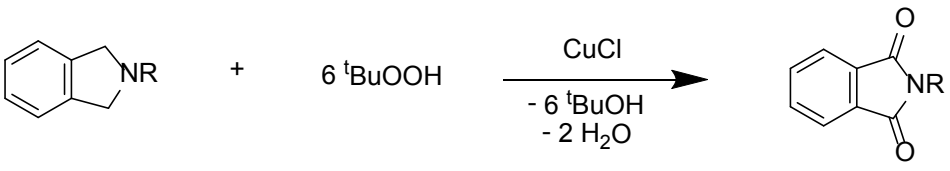

Scheme 5-d: Carbonylation.[288]

Despite several procedures being available, (Schemes 5-a to 5-d), new synthetic methodologies are highly desirable in order to overcome the short comings of the existing processes with a need to use milder conditions with less aggressive reagents and/or promoters while attempting to maximise atom economy.[289] As a result, these processes often employ catalysts. Homogeneous catalytic systems, although suffering from severely limited substrate scope, are common in the synthesis of imides and the works of Trecker and Murahashi have been extensive amongst other examples.[283,287,288] Trecker *et al*.[290,291] employed a peracetic acid-$Mn(acac)_2$ system utilizing TBHP as the oxidant to produce glutarimide in yields of 70 – 80 % from δ-valerolactam. Murahashi *et al*.[292–294] exploited a number of systems, his early work focused on two ruthenium catalysts: $RuCl_2(PPh_3)_3$ with TBHP where glutarimide was produced from δ-valerolactam in yields of 62 % and a $RuCl_3$ catalysts which utilized molecular oxygen under basic conditions to oxidise β-lactams. In his more recent works an $IrH_5(P\mathit{i}Pr_3)_2$ catalyst was employed in order to produce functionalised glutarimides from nitrile complexes in yields of over 90 % (Scheme 5-e).

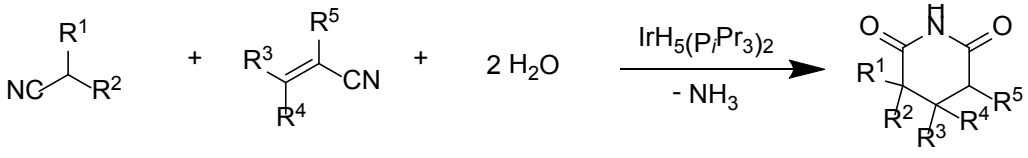

Scheme 5-e: Nitrile hydrolysis and cyclisation of the resulting amide and remaining nitrile.[294]

Aside from the homogeneous routes described, other more diverse methodologies have been explored such as ozonolysis,[295,296] a $MnCl_2$ catalysed microwave irradiation process[297] and a combination of molecular oxygen and subcritical water.[298] The latter two examples produced glutarimide from δ-valerolactam in yields of 85 and 60 % respectively. Heterogeneous catalytic production of cyclic imides has been limited and only recent exploration has highlighted its exceptional potential for development, especially with a view to achieving high atom economies. Namely, recent investigations employing some metal oxides have been explored as Lewis acid catalysts for the synthesis of cyclic imides via the dehydrative condensation pathway (Scheme 5-a) with a Nb_2O_5 catalysts proving to be a promising candidate, producing imide yields typically > 80 %.[284]

5.1.2 Bimetallic Catalysts & the Advantages of Multi-metallic Nanoparticle Systems

The vast majority of research on nanoparticle catalysts has employed nanoparticles which are comprised of a single metal. Now, as the understanding of the reactive centre and its interaction with the desired substrate is expanding the desire to design more complex systems as superior catalysts has also increased. This has led to the introduction of a second and in some instances, third metal to the composition of the nanoparticles

explored. The introduction of this second metal allows the chemist to further tune both physical and electronic properties of the catalysts active site. Development of such systems has picked up significant traction since just prior to the turn of the century.[299] However, as is often the case for catalytic research, early investigations were of an observational capacity where the improved catalytic properties were noted and the development of their understanding was to come later. As more detailed and accurate characterisation techniques were developed and applied to these multi-metallic nanoparticle systems, it was discovered that bimetallic nanoparticles can take on a variety of morphologies from simple heterostructures or segregated alloys to pure alloys and core/shell structures, as seen in Figure 5-a.[32,300,301]

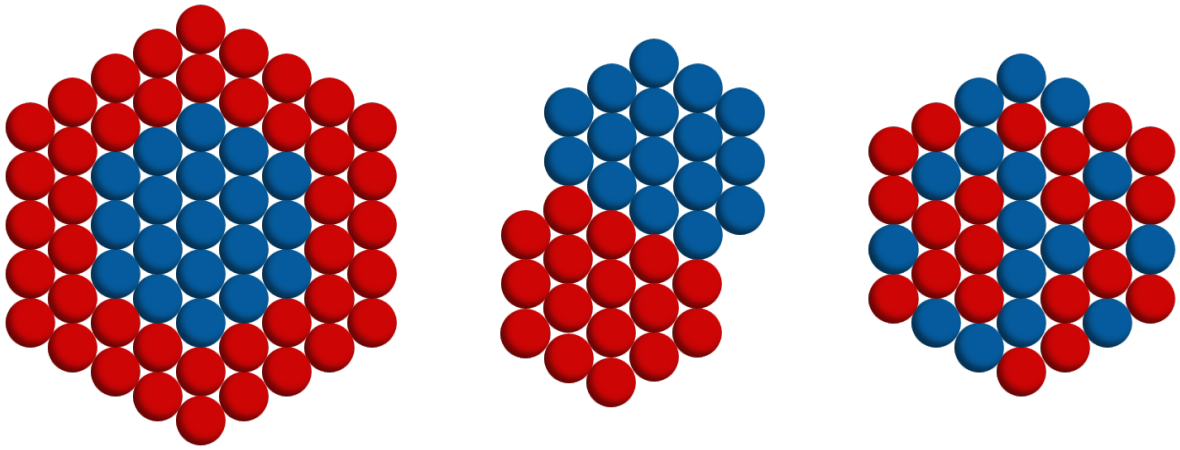

Figure 5-a: Bimetallic nanoparticles with different structures: left – core/shell, centre – heterostructure (segregated alloy), right – true alloyed structures.

Alloyed and segregated nanoparticles are typically generated through simultaneous reduction of the two respective metal-salts with the nature of the resulting nanoparticle depending primarily on the compatibility of the two metals. For example, metals that share similar chemistries, crystal structure and lattice bond lengths are more likely to form stable alloyed structures. As the most thermodynamically stable state will form, the specific chemistries of the metals as well as the outside influences such as solvents/additives, concentration, temperature and pH all play a role in determining the final nature of the multi-metallic nanoparticle.[300,301] Core/shell particles are commonly prepared via epitaxial growth through the sequential reduction of the secondary metal upon the preformed monometallic seed crystals. This is typically done in two separate steps but provided the redox potentials of the metals allow, it can be done in a single step as the metal with the higher redox potential will deposit first followed by the metal with the lower redox potential conveniently forming a core/shell structure by design.[300,301]

There exists an array of metal combinations within the field of bimetallic nanoparticle catalysis with each combination demonstrating individual catalytic characteristics,

including: transition metal-transition metal (Fe, Co, Ni, Cu, Rh, Ru), pure group 10 (Ni, Pd, Pt), pure group 11 (Cu, Ag, Au), group 10-group 11 hybrids to main group combinations with those already mentioned.[31–33] Nonetheless, primary attention will be targeted towards noble metal containing nanoparticle systems given their known catalytic activity for oxidation processes and the focuses of these works.[121] One notable group's research efforts, have in particular, highlighted the potential of bimetallic noble metal nanoparticles. Hutchings and co-workers have focused primarily on Au-Pt, Au-Pd and Pt-Pd bimetallic systems demonstrating the clear synergistic enhancement of these materials on various supports (e.g. C, TiO_2 and MgO) for a range of alcohol oxidation processes. These include: benzyl alcohol,[136,139,147,219] cinnamyl alcohol,[139,147] octanol,[139,147] glycerol[302] and others.[147] They have also shown superior catalytic properties for the much more challenging C-H activation where the aerobic oxidation of toluene was carried out over such materials achieving conversions in excess of 90%.[171] Further to this, they have also explored the potential of Au-Pt-Pd trimetallic nanoparticle systems as oxidation catalysts.[149] The clear synergistic enhancement in catalytic conversion is frequently coupled with enhanced aldehyde selectivity for alcohol oxidations, in contrast to many other observations of improved activity in similar systems. Often the improvements in activity are coupled with poorer product selectivity, as observed in Chapter 3. Through sol-immobilisation (or colloidal deposition) methods, Hutchings and co-workers have shown the immense significance of both particle size and composition. Through exploiting synthetic variables such as solvents, pressures, concentrations and temperatures, a range of alloyed and core/shell particles have been generated.[136,139,219,303] These demonstrate that these compositional differences along with the support influence and particle size effects have a dramatic impact over the resulting catalytic performance, which is always substrate specific. These findings have thus allowed methods to be established for the generation of, specifically Au-Pd bimetallic nanoparticles of different morphologies with varying catalytic properties.[40] Therefore, it demonstrates the need for clear compositional and morphological understanding in order to fully rationalize the ensuing catalytic behaviour.

While there is clear scope for the employment of purely noble bimetallic nanoparticle catalysts, the utilization of more abundant and economical alternatives is desirable, provided sufficient catalytic activity can be bestowed. As eluded to, group 11 bimetallic systems are on the current research agendas of many chemists but specifically Au-Cu systems have shown a lot of promise and given their shared FCC crystal structure and similar lattice spacing's, random or true alloy particles form readily.[304] A notable species, given the composition of the CuClP material and its ability to house both Cu and Au precursors species. Both Cu[305] and Au[7,306,307] have independently shown exceptional activity as oxidation catalysts but given the propensity for metallic Cu to oxidise under

some oxidative conditions and the frequently documented poor stability of Au nanoparticle systems, a marriage of the two has often found to drastically improve the overall material stability without detriment towards their catalytic applications.[308,309] Further to this, the poor affinity of metallic Au towards molecular oxygen is documented and hence Au nanoparticles are regularly supported upon metal oxide supports in order to facilitate the binding of molecular oxygen.[310] Another way to circumvent this, is to alloy Au with another metal, one which can more readily bind molecular oxygen and Cu is one such example.[311] Consequently, Au-Cu nanoparticle systems have demonstrated exceptional potential in a range of oxidation processes from the water-gas-shift reaction[312] and CO oxidation[304,310,311,313] to a range of selective alcohol oxidations including: methanol,[314] HMF,[308] benzyl alcohol[242] and others.[242] Thus, there exists a great desire to fabricate new AuCu nanoparticle systems given their highly compatible chemistries and ensuing catalytic perspective. Not only that but given the diversity of the individual monometallic variants there could exists abundant scope for applications further afield from those listed above, with more complex oxidative transformations in mind such as the selective oxidation of cyclic lactams.

5.2 Investigating Structural & Chemical Features within the Gold Nanoparticle Systems: The Fine Balance between Alloying & Over-Extrusion

5.2.1 Structural Characterisation: Annular Dark Field Aberration Corrected Scanning Transmission Electron Microscopy & Energy-Dispersive X-Ray Spectroscopy

To investigate the effects of the different activation temperatures (200, 250 & 350 °C) on the morphology and composition of the Au/CuClP materials, further ADF AC-STEM imaging and STEM-EDXS investigations, to those in Chapter 4, were undertaken. From Figure 5-b it is observed that extensive regions of well-defined, small nanoparticle formation, are present upon the surface of the Au/CuClP material activated at 200 °C, analogous to the Pt/CuClP system described in Chapter 4. The small nanoparticle formation is visibly localised upon the periphery of the sample fragments, as highlighted in Figure 5-b: b and d. Despite the majority of the fragments displaying small, defined nanoparticle formation a limited number of larger nanoparticles are visible, shown in Figure 5-b: d.

The smooth intensity of the image contrast for the support framework, demonstrated in Figure 5-b, is indicative of a highly pristine surface. This feature however, is not consistent across all the samples. Au/CuClP activated at 250 °C and 350 °C, shown in Figure 5-c and Figure 5-d respectively, show variation in the image contrast throughout the bulk of the framework, therefore suggesting morphological and compositional re-distributions as a result of the activation process. This demonstrates an analogous trend to that observed for the Pd/CuClP materials described in Chapter 4 where, as the activation temperature increases, so does the extent of the extrusion of both the noble metal and the structurally vital Cu species causing the integrity of the framework to become increasingly compromised.

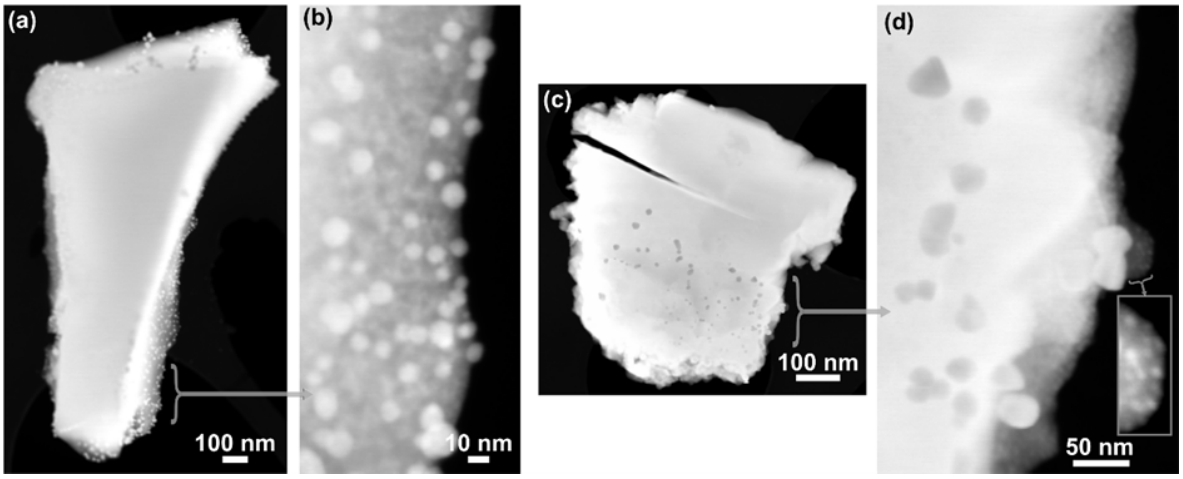

Figure 5-b: ADF-STEM images revealing the morphology of the Au/CuClP sample activated at 200°C.

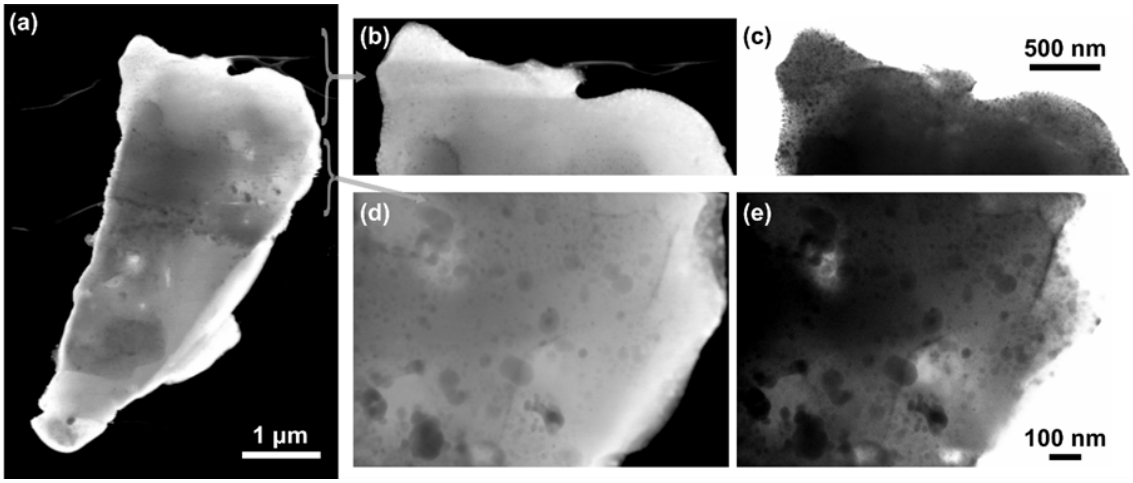

Figure 5-c: ADF (a,b,d) and bright-field (c,e) STEM images revealing the morphology of the Au/CuClP sample activated at 250°C.

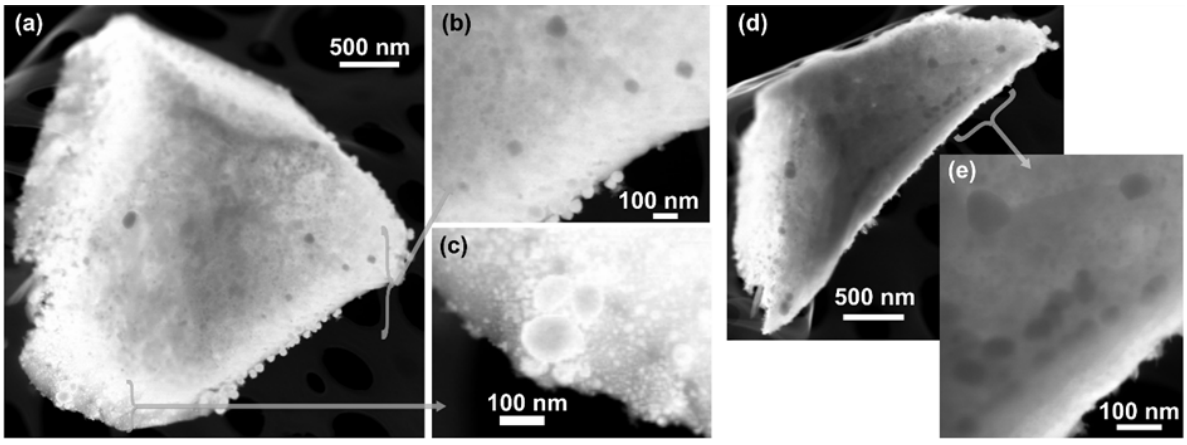

Figure 5-d: ADF-STEM images revealing the morphology of the Au/CuClP sample activated at 350°C.

It is apparent by comparison of Figure 5-b, Figure 5-c and Figure 5-d that the increase in abundance of larger nanoparticles is directly related to the activation temperature. This, coupled with the image contrast, suggests compositional redistribution with increasing temperature would clearly point to the increased levels of extrusion having a detrimental effect on the structural integrity of the host framework. This is perhaps unsurprising, as one would expect the removal of structurally integral species, such as Cu from the framework to be detrimental to its structural integrity, as it was for the Pd/CuClP system. That being said, there is still evidence to support the abundance of small nanoparticulate species present on the materials activated at higher temperatures, evident from Figure 5-c: e and Figure 5-d: c. These larger particles then must exist alongside the smaller particles (< 10 nm) and therefore add to the range of potential active centres present upon the surface of these materials.

In addition to this, it is apparent that the elevated temperatures and/or increased level of extrusion has a clear influence on the precise nature of the nanoparticle species generated at the materials surface. This is further supported by the EDXS analysis (Figure 5-e, Figure 5-f and Figure 5-g) which shows increased quantities of Cu when compared to the abundance of Au, suggesting an decreasing Au:Cu ratio. Thus, supporting the concept of a dual extrusion process of both Au and Cu, with Cu extrusion becoming increasingly significant at elevated temperatures.

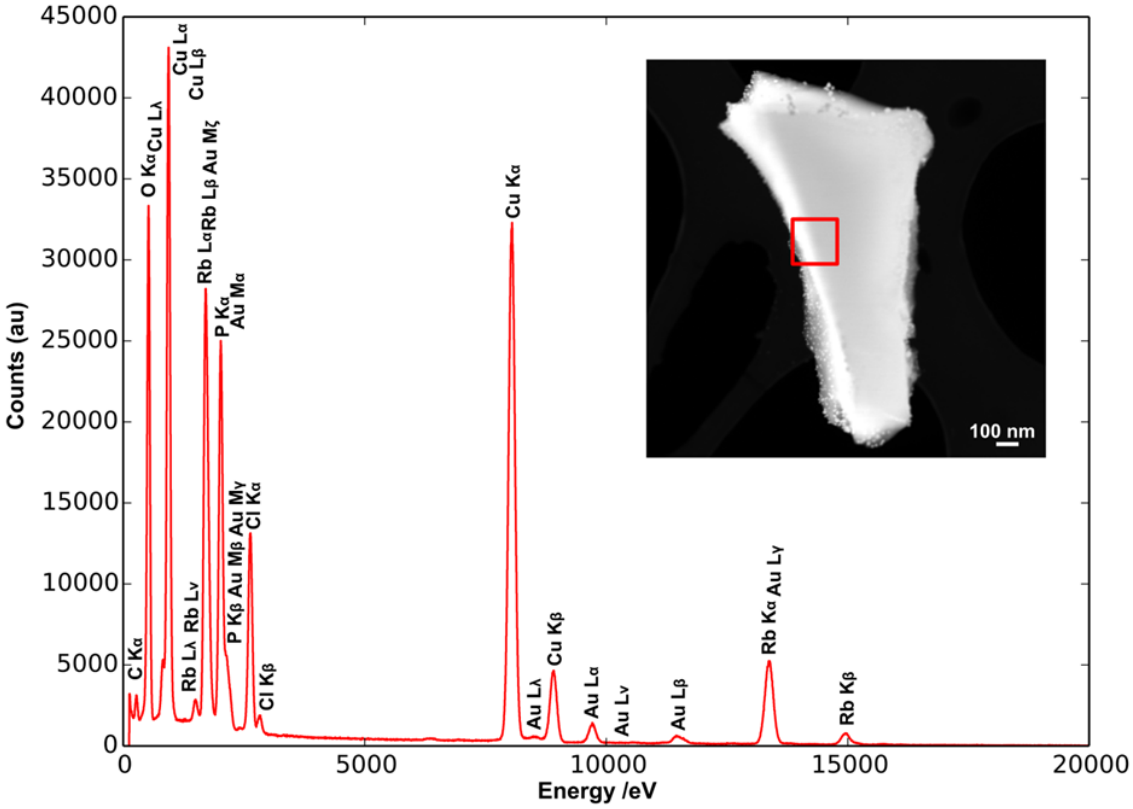

Figure 5-e: EDX spectrum for the Au/CuClP material activated at 200°C. The area analysed is indicated by the red box in the inset ADF-STEM image.

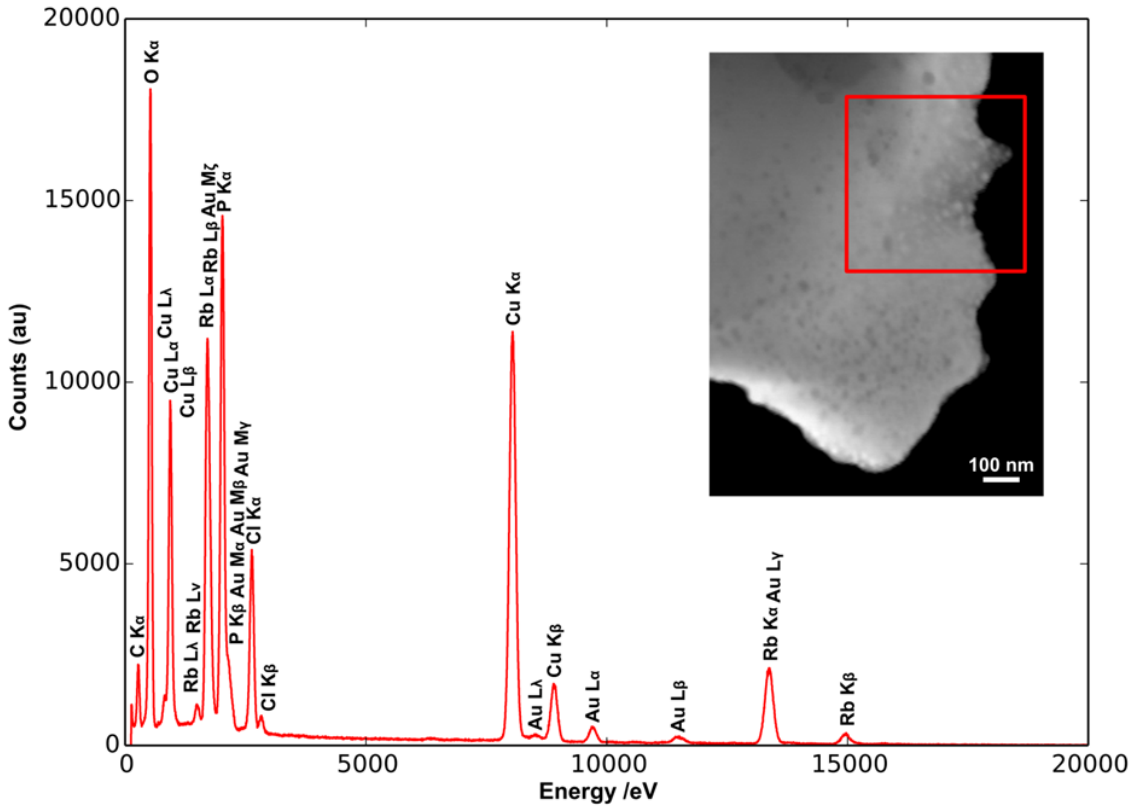

Figure 5-f: EDX spectrum for the Au/CuClP material activated at 250°C. The area analysed is indicated by the red box in the inset ADF-STEM image.

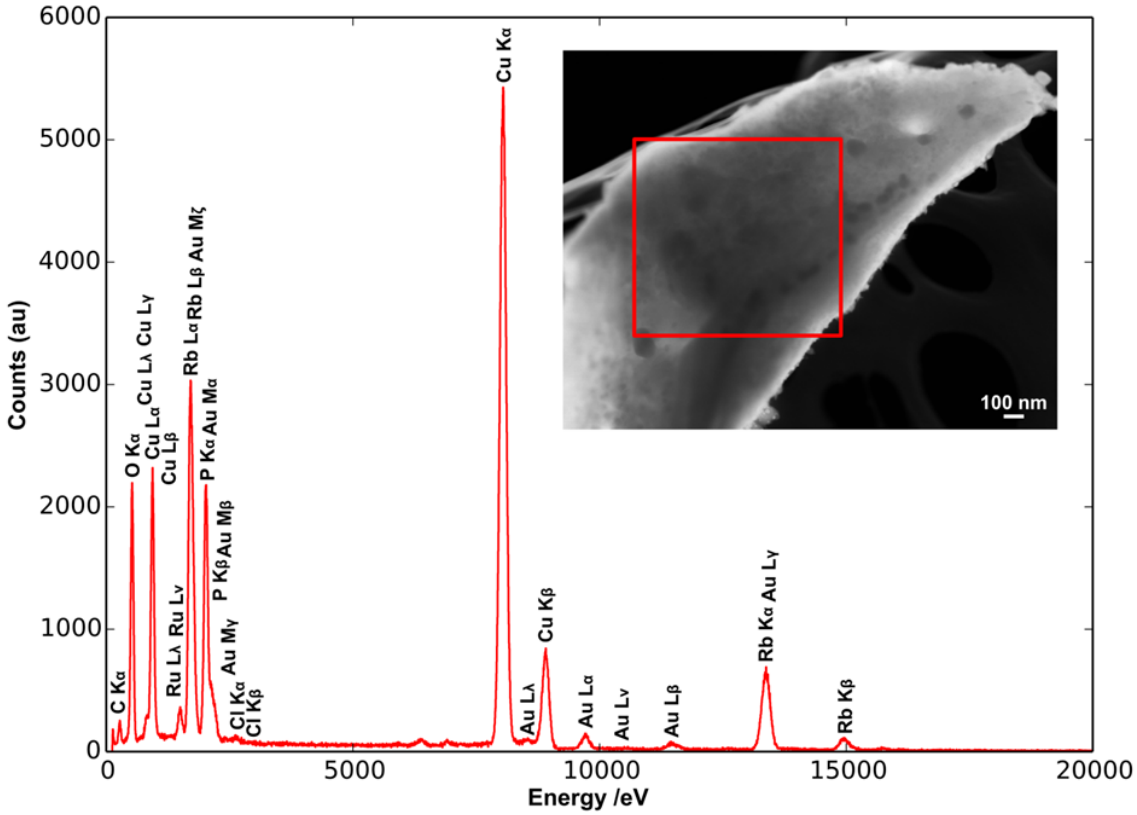

Figure 5-g: EDX spectrum for the Au/CuClP material activated at 350°C. The area analysed is indicated by the red box in the inset ADF-STEM image.

Further to the structural imaging, a combination of STEM-EDXS point spectra, line scans and spectrum images were performed to probe the chemical identity of the nanoparticles and distribution of elements within the framework. These confirmed, in many cases, the identity of smaller (2-5 nm) and larger (> 10 nm) nanoparticles as predominantly Au. Exemplary elemental maps in this regard are shown in Figure 5-h and Figure 5-i for the Au/CuClP material activated at 250 and 350 °C respectively. These show clearly that the large faceted nanoparticles here are Au, while the supporting framework is Cu rich with the other elements evenly distributed across the framework. Further, Figure 5-i conclusively highlights the effectiveness of the extrusion process, at the elevated 350 °C for completely removing Au from regions of the framework.

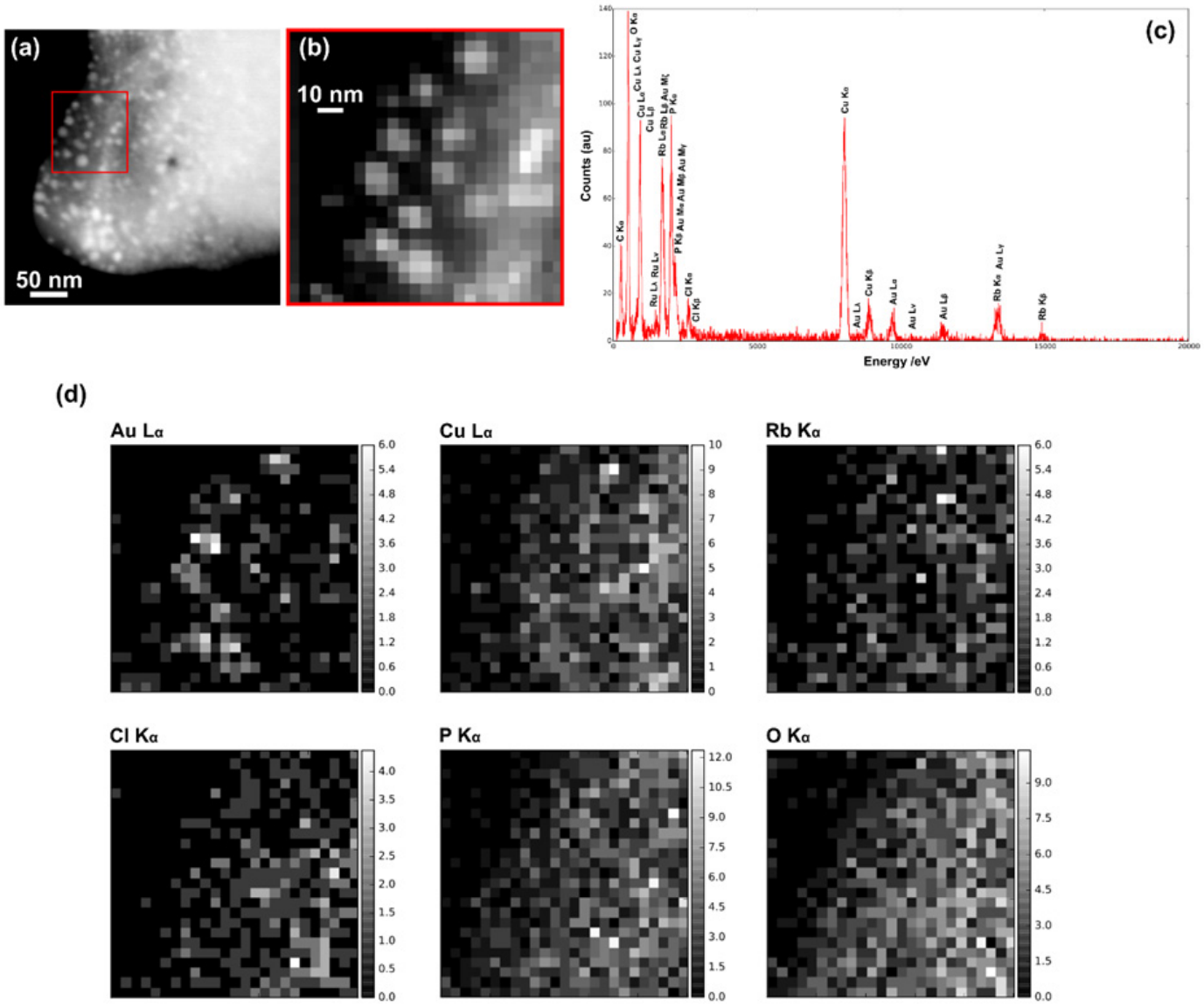

Figure 5-h: STEM-EDXS mapping of the small nanoparticles in the Au/CuClP sample activated at 250°C. (a) ADF image of the region analysed prior to EDXS. (b) ADF image acquired simultaneous to EDXS mapping. (c) EDXS sum-spectrum, obtained by summing all spectra from the spectrum image. (d) Elemental maps obtained from the spectrum image by peak integration.

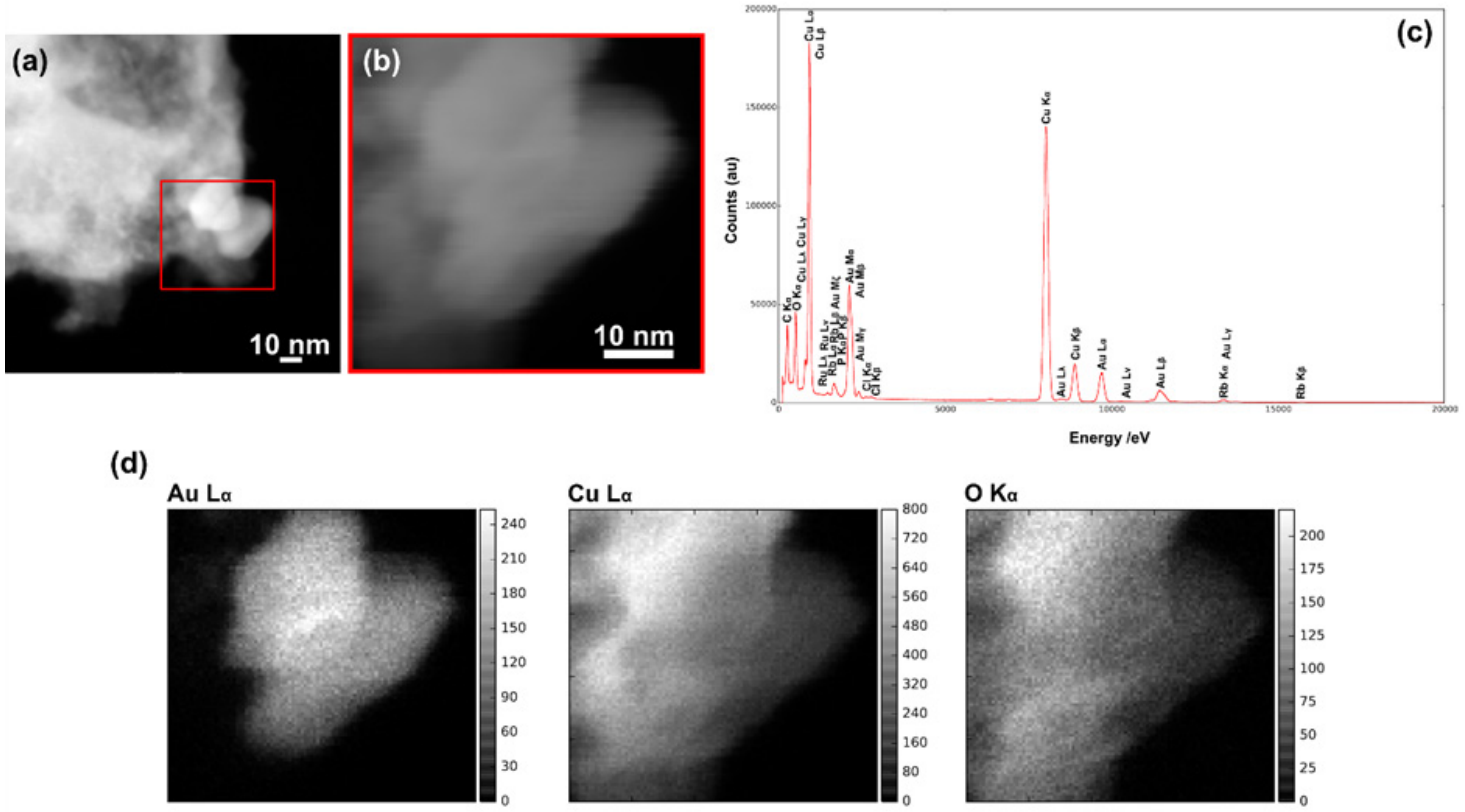

Figure 5-i: STEM-EDXS mapping of the large faceted nanoparticles in the Au/CuClP sample activated at 350°C. (a) ADF image of the region analysed prior to EDXS. (b) ADF image acquired simultaneous to EDXS mapping. (c) EDXS sum-spectrum, obtained by summing all spectra from the spectrum image. (d) Elemental maps obtained from the spectrum image by peak integration. Rb, P and Cl maps not shown here due to peak overlap and dominance of the Au signal in this spectrum image.

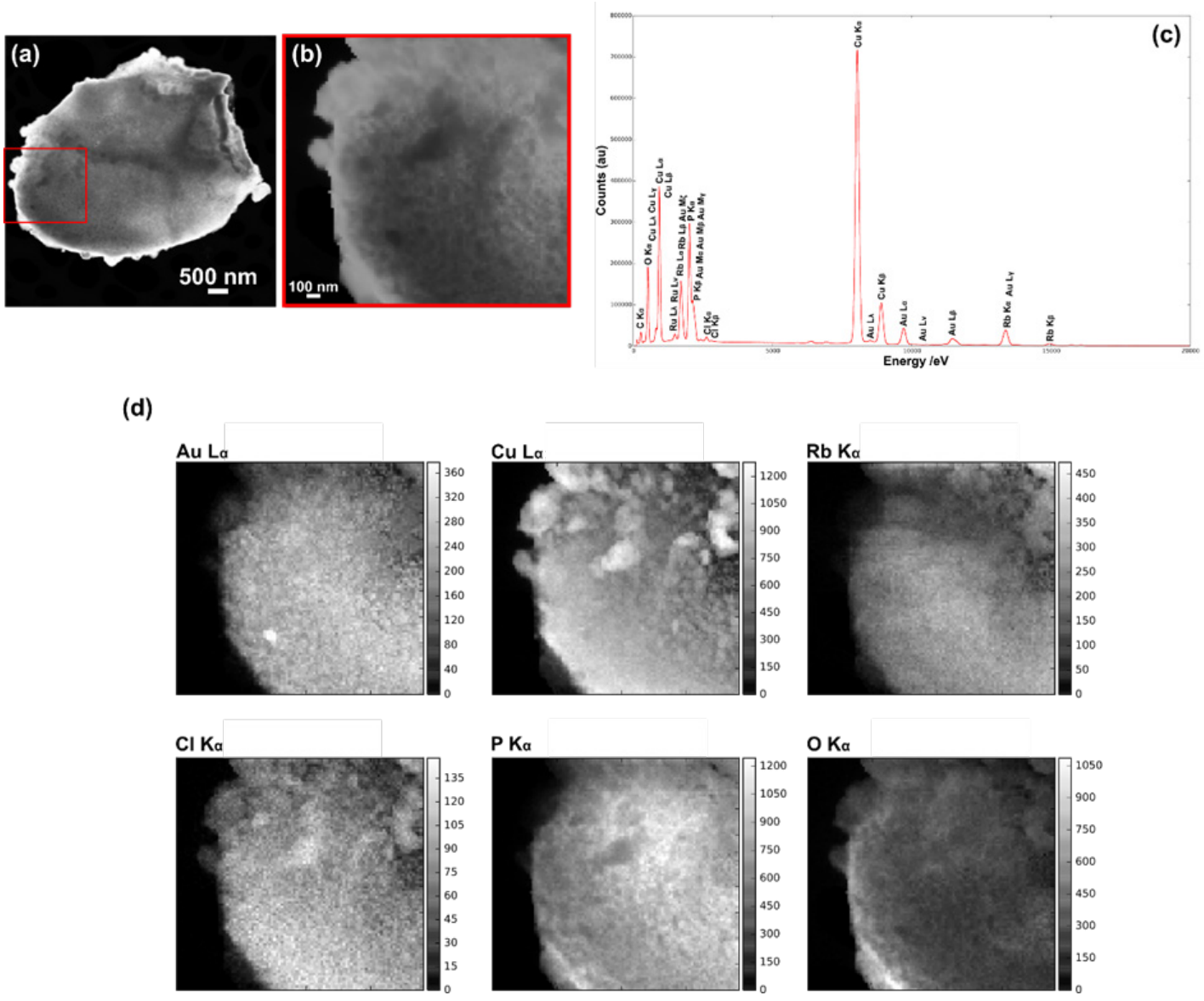

Figure 5-j: STEM-EDXS mapping of the large nanoparticles and agglomerations of the framework support in the Au/CuClP sample activated at 350°C. (a) ADF image of the region analysed prior to EDXS. (b) ADF image acquired simultaneous to EDXS mapping. (c) EDXS sum-spectrum, obtained by summing all spectra from the spectrum image. (d) Elemental maps obtained from the spectrum image by peak integration.

Furthermore, these spatially resolved STEM-EDXS studies also reveal the presence of predominantly Cu nanoparticles, often associated with substantial agglomeration of elements from the framework, as exemplified in Figure 5-j. However, the slightly mottled appearance of the Au map suggests that the formation of the smaller Au nanoparticles occurs upon the surface of the sample activated at 350 °C together with the formation of larger Cu nanoparticles. The immediate vicinity of these two species would form significant sites upon the materials surface where Au nanoparticle-support-Cu nanoparticle synergies could exist.

ADF imaging and spatially resolved STEM-EDXS then clearly offer an insight into possibility of Au-Cu alloying and co-existing discrete Au and Cu nanoparticles. Indeed, the presence of the increased extrusion of both Au and Cu, with some degree of intermixing, has been demonstrated. It therefore appears that the Au/CuClP materials have the potential to possess a range of active species, including small extruded Au nanoparticles on the surface as well as larger Au, Cu or Au-Cu nanoparticles. Further evidence is therefore required in order to ascertain the exact nature of the nanoparticulate species or range of species present within these systems.

5.2.2 Structural Characterisation: Powder X-Ray Diffraction

PXRD has been used to analyse the crystallinity, phase purity and extent of any framework degradation of the bulk material as a result of the activation process. Figure 5-k shows the Au/CuClP material in all the forms studied within this chapter, as synthesised and activated at 150, 200, 250, and 350 °C increasing up the plot. Firstly this plot highlights the high crystallinity and phase purity of the bulk material up to at least 250 °C. This suggests that any framework degradation that occurs, as indicated in Section 5.2.1, is minimal and most likely exclusive to small surface regions of the material thus, not effecting the bulk material. With this in mind we do begin to observe a mild, qualitative, drop in crystallinity, evident from the peak intensity/definition. Further we begin to see the introduction of additional phases, akin to those in the Pd/CuClP material discussed in Section 4.2.1, at temperatures above 250 °C. These observations align well with those made in Section 5.2.1, that reorganisation of the host framework begins to occur at these elevated temperatures, suggesting an upper limit to the activation protocol for these materials.

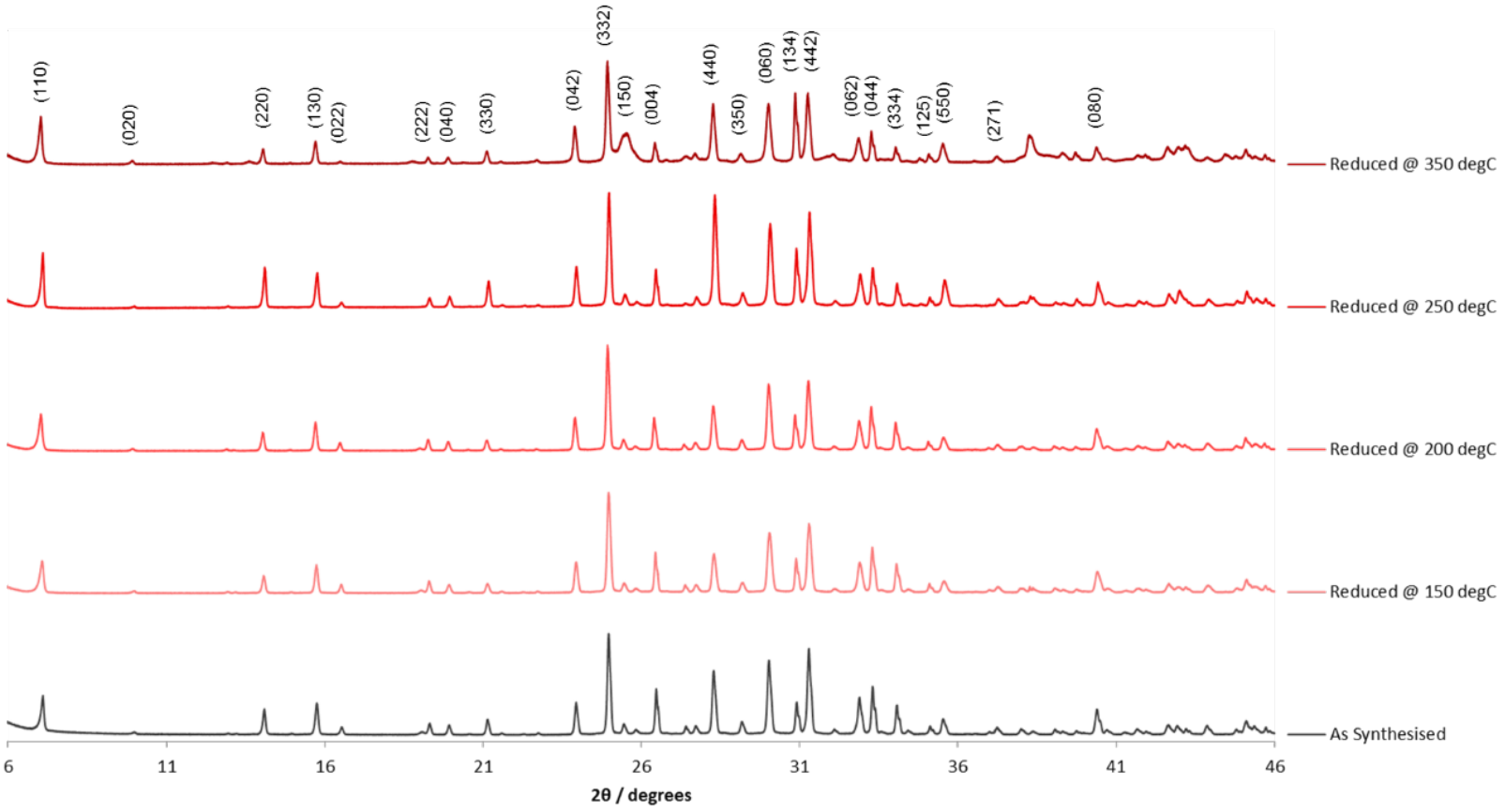

Figure 5-k: Indexed PXRD of the Au/CuClP materials activated at different temperatures (red) with the pre-activation, as-synthesised sample (grey) for comparison.

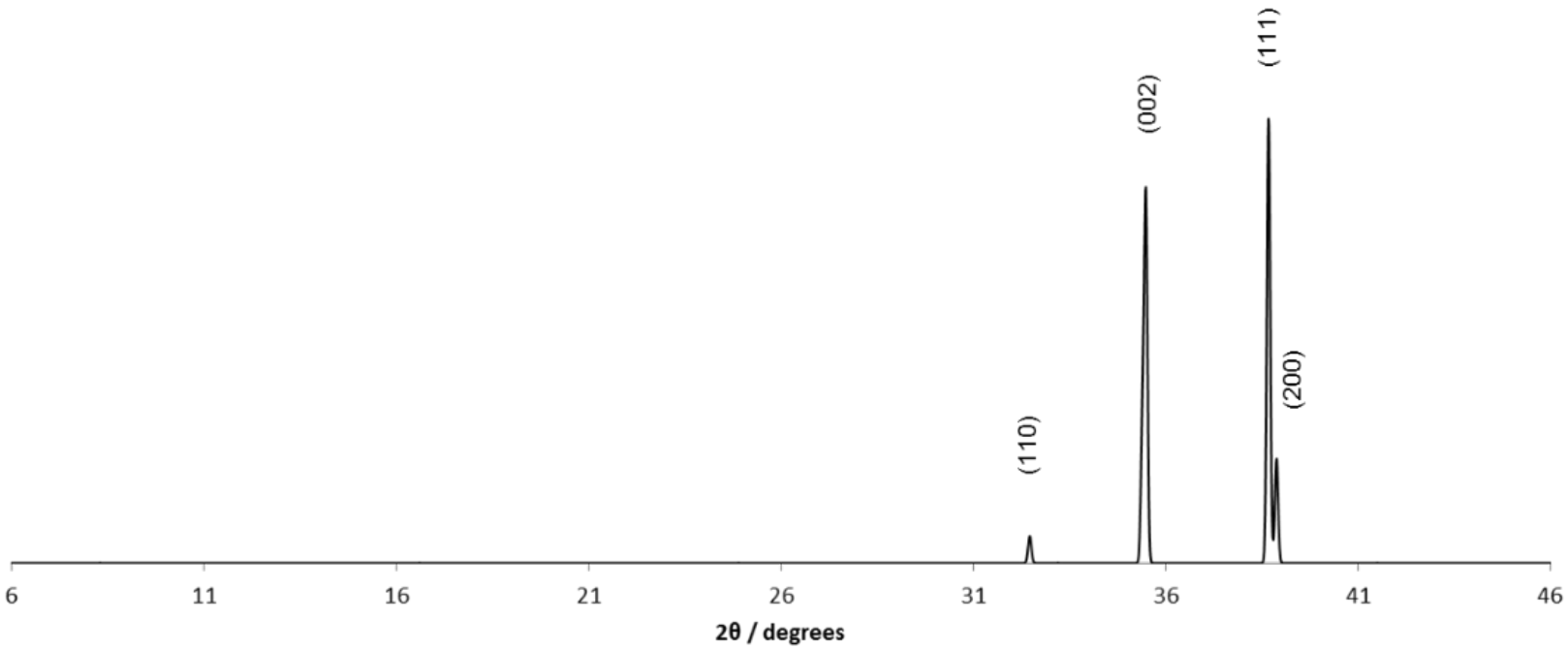

Figure 5-I: Simulated PXRD pattern of copper oxide (CuO) with hkl values displayed above the peaks.[315]

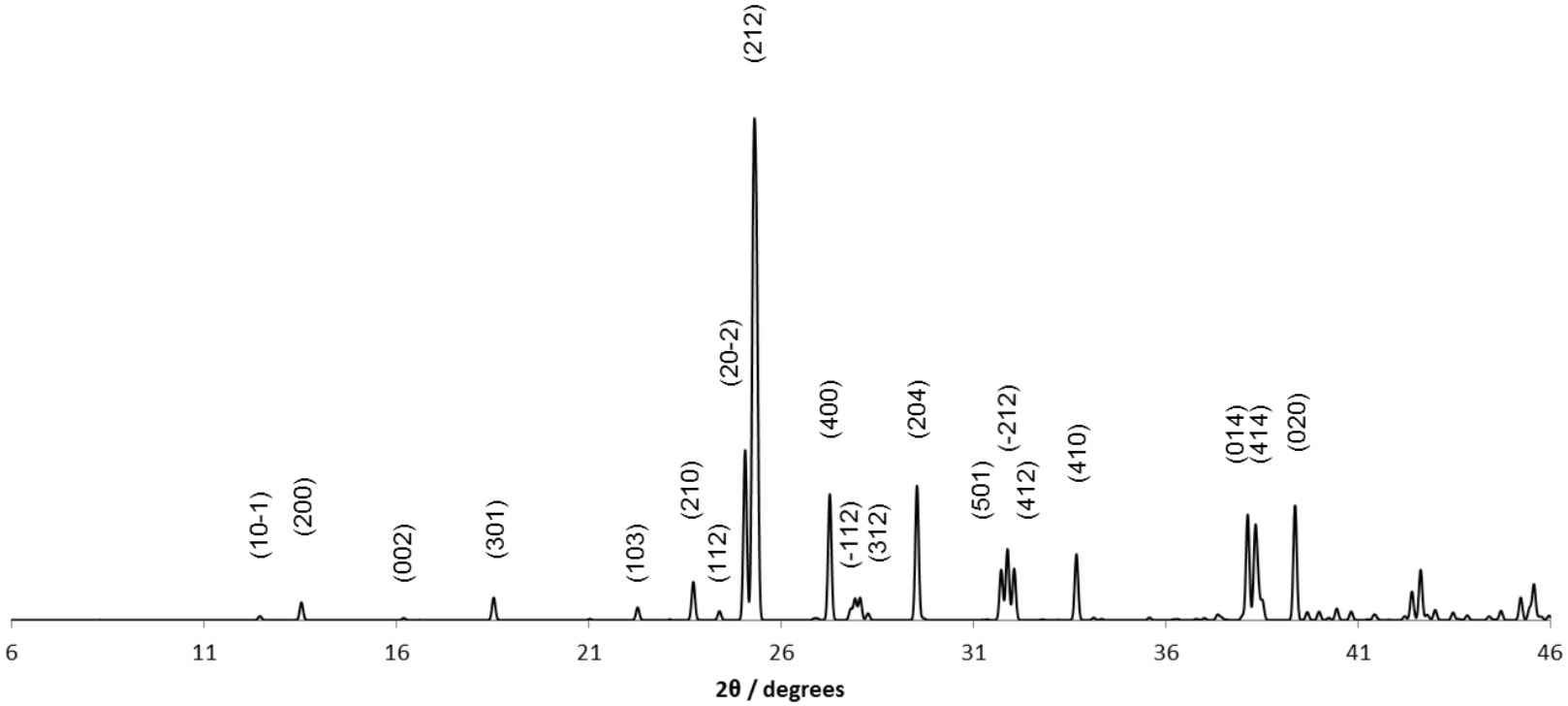

Figure 5-m: Simulated PXRD pattern of rubidium phosphate ($Rb(PO_3)$) with hkl values displayed above the peaks.[267]

Figure 5-l and Figure 5-m detail the two potential impurity phases present in the Au/CuClP sample activated at 350 °C, which are copper oxide and rubidium phosphate respectively. Within the PXRD pattern of the Au/CuClP samples, there are two significant peaks that are introduced at the higher temperature. These are a broad signal centred around 25.6 ° and a sharper signal at 38.4 °, which have been attributed to rubidium phosphate and copper oxide respectively. Copper oxide (Figure 5-l) presents three significant signals within the range analysed and the CuO (111) and (200) planes appear in a similar region to the observed impurity, at 38.6 and 38.8 ° respectively. Furthermore, the CuO (002) plane presents directly underneath the Au/CuClP (550) plane and given the small volume of the impurity, this is enough to hide the signal from the PXRD pattern. Similarly to the copper oxide, the quantity of these impurities makes their identification challenging due to only observing faint influences from only their most intense signals. The rubidium phosphate presents with one such signal, 25.3 ° very similar to the broad signal observed in our materials 25.6 °. In fact, the rubidium phosphate peak in this region has a second signal adjacent (25.0 °). A combination of these signals and the Au/CuClP (150) signal could be causing the broad nature of this signal. In addition, the other significant $Rb(PO_3)$ signals, (014) and (414), are hidden beneath the CuO (002) signal and close observation of the Au/CuClP material activated at 350 °C pattern shows a subtle broad signal at 31.9 ° which most likely is due to the $Rb(PO_3)$ (501), (-212) and (412) signals.

Considering the possible decomposition products of these materials, these two impurities appear to be the most likely. Not only do their PXRD patterns closely match that observed within our systems, but in contrast to the Pt/CuClP system described in Chapter 4, these impurities incorporate key elements from the host framework e.g. the phosphate unit, copper and oxygen, which can only come from the parent framework and not simply from charge balancing ions. Further to these findings, it is worth noting that the spatially resolved STEM-EDXS maps in Figure 5-j rule out the possibility of the larger surface bound Cu nanoparticles in fact being CuO which could be inferred from the PXRD. Consultation of the O K_α map shows that oxygen is restricted to the framework regions only.

5.2.3 Structural Characterisation: Spectroscopy – Gold

XPS and XAS have been employed to directly evaluate the nature of both the surface and bulk Au species, contrasting any differences. Figure 5-n shows the XPS data of Au 4*f* binding region of the Au/CuClP materials under analogous activation conditions to those studied in Sections 5.2.1 and 5.2.2. Figure 5-n shows exclusively Au^0 suggesting the complete reduction of the Au^{III} species to the metallic species across all samples, upon the samples surface. This is in agreement with the ADF-STEM (Figure 5-i), demonstrating

that the extrusion occurs extensively on the materials peripheries. This was expected as prior XPS on these materials showed entirely metallic gold from a reduction temperature of 150 °C, (Chapter 4).

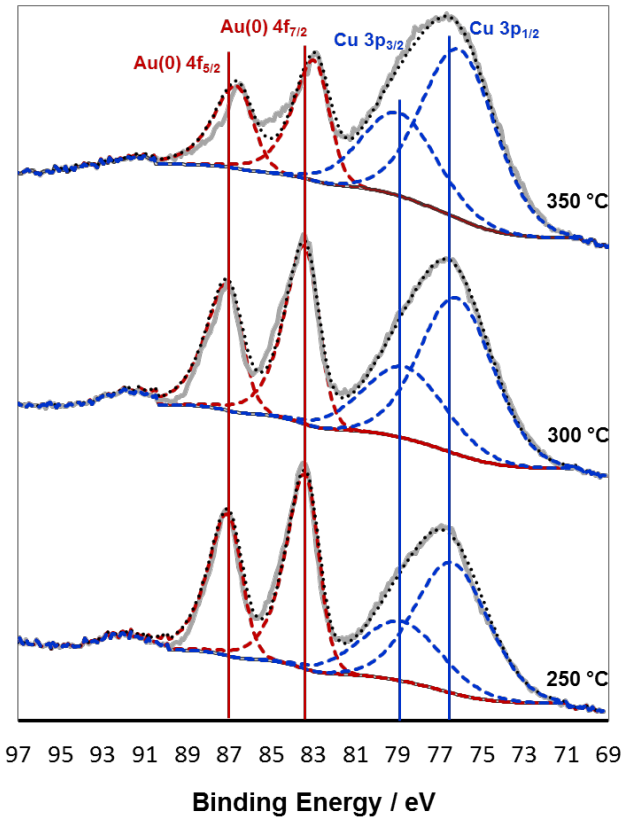

Figure 5-n: Stacked XPS data of the Au 4f binding region for the Au/CuClP catalysts activated at different temperatures. The data is shown in grey with the data fit in black, Au^0 transitions are depicted in red and the overlapping Cu 3p in blue.

Despite the clear indication of metallic Au throughout, there are two significant features of note when contrasting the spectrum of the sample activated at 350 °C with the lower temperature samples. One, there is a clear shift to lower BE of the Au 4*f* signals of approx. 0.5 eV. Two, there is a change in the peak shape of the Au 4*f* signals, notably at approx. 84.5 eV. Both suggest that the electronic nature of the Au species within the 350 °C sample is different by comparison to the other two, potentially due to the introduction of Au-Cu interactions altering the electronic state of the Au centres. Au 4*f* shifts to lower binding energies have been attributed to both smaller Au particles with a higher percentage of low occupancy sites[316] and Au-Cu alloying directly.[317] Alloying causes electron transfer from Cu to the more electro negative Au causing Au core levels to shift to lower BE. Thus, the latter appears more applicable in this case due to the former being disputed[137,271,318] and the high resolution ADF-STEM suggesting a progression towards larger particles with increasing activation temperature. Further, Ou *et al.*[319] suggested that reducible Cu species have the potential to stabilise ionic $Au^{\delta+}$ species which would

present with $4f_{7/2}$ signals at 84.5 eV, accounting for the peak shapes observed in Figure 5-n. That being said, attempts to fit the data with such parameters were unsuccessful due to difficulties modelling the appropriate $4f_{5/2}$ signal within the data. Despite this, the above discussions would clearly suggest that there is a change in the electronic character of the Au sites within the 350 °C sample or potentially the production of a range of Au species upon the surface, likely due to the introduction of Cu species, supported by the ADF-STEM.

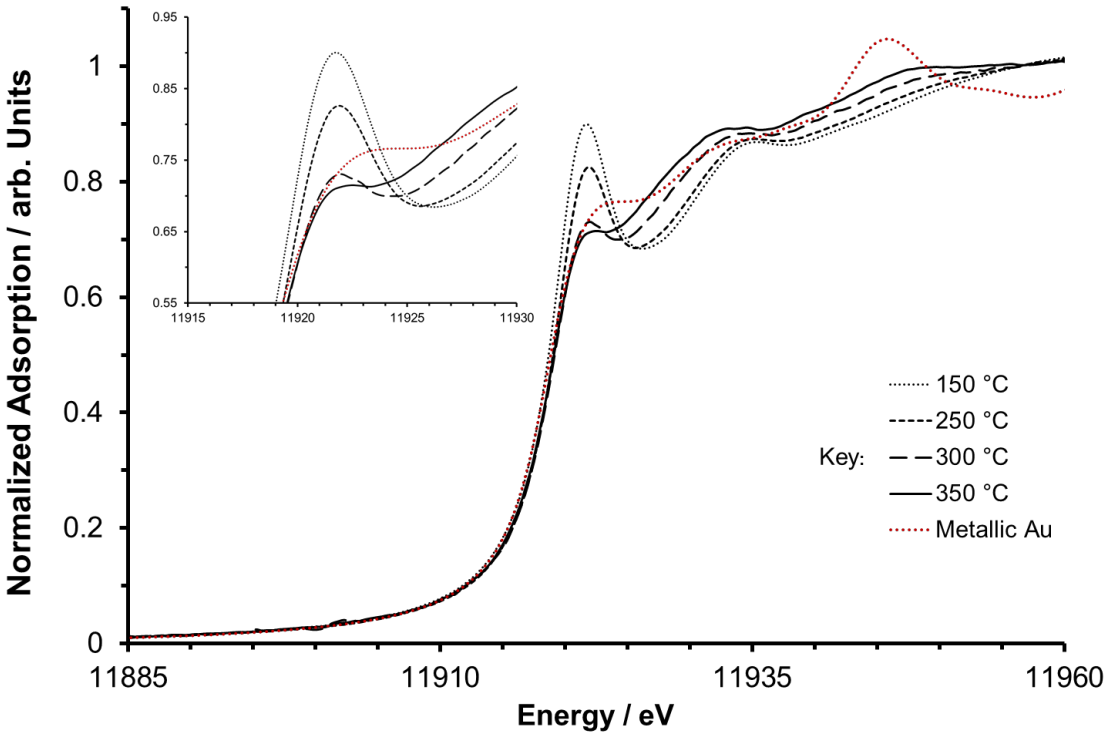

Figure 5-o: Stacked XANES data of the Au L_{III} edge for the Au/CuClP materials activated at different temperatures with a metallic gold reference in red. Inset image shows a closer view of the white line absorption differences between the samples.

Following the XPS analysis above, concomitant findings were established through use of XAS. As discussed in Chapter 4, the white line intensity of the Au L_{III} edge XANES is directly proportional to the average oxidation state of all the Au centres within the sample. Figure 5-o clearly shows the depreciation of the white line intensity as the activation temperature increases, demonstrating a progression toward the metallic Au. Further to this, the apparent weaker white line intensity (300 & 350 °C), than that displayed by the metallic reference (red), can be attributed to the nanoparticulate nature of a proportion of the Au species.[320] This is due to overlap of the *s, p* and *d* bands in bulk gold resulting in a depletion of the 5*d* orbitals causing a slightly more intense absorption.[321] Additional trends towards the metallic reference can also be seen at 11923 (inset) and 11946 eV, further supporting the progression towards metallic Au. The XANES therefore strongly agrees

with XPS analysis while highlighting the differences in Au oxidation between the surface of the sample and the bulk. Clearly, the reduction of the gold salt is more achievable in surface regions of the sample, leaving a significant proportion of chlorometallate ion present within the bulk. It is therefore in agreement with the ADF-STEM findings and supported by the following EXAFS analysis: Figure 5-p and Table 5-a.

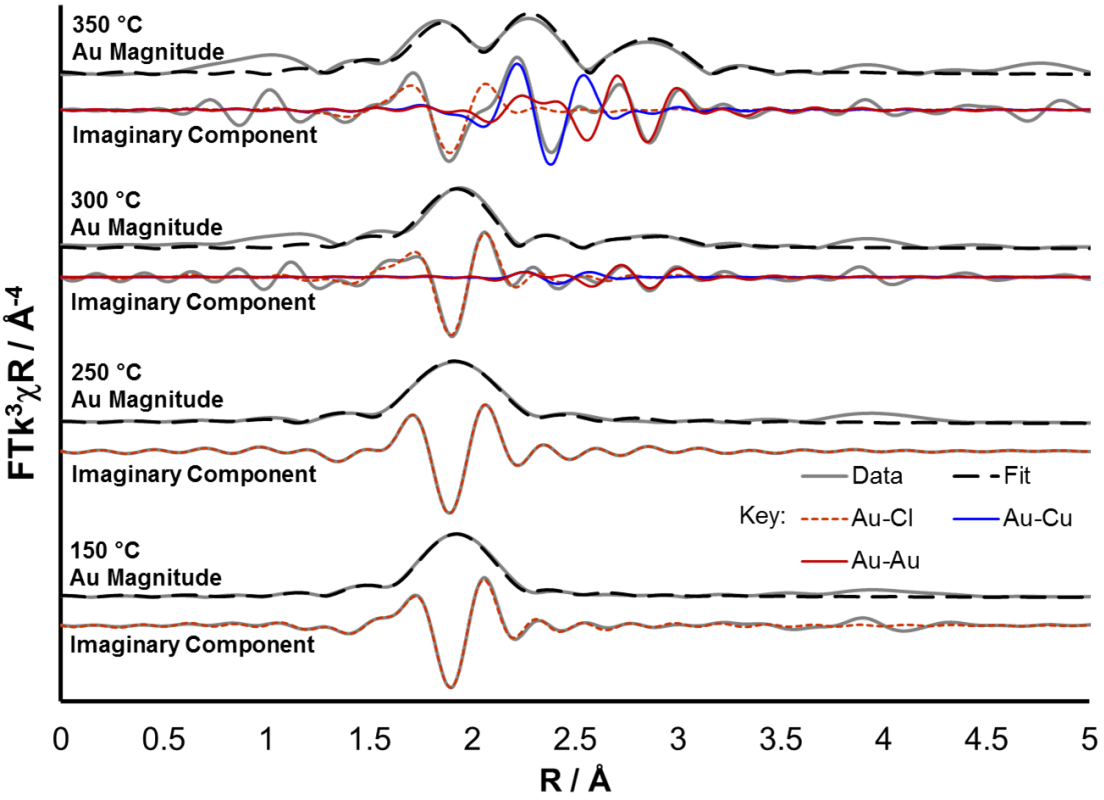

Figure 5-p: The magnitude and imaginary component of the k^3 weighted Fourier transform for the EXAFS data of the three Au/CuClP species reduced under increasing activation temperatures. Associated scattering paths are included for the imaginary component and the fitting parameters are displayed in Table 5-a.

Sample	Abs Sc	N	R / Å	$2\sigma^2$ / Å^2	E_f / eV	R_{factor}
Au/CuClP 150 °C	Au – Cl	3.53 (9)	2.286 (3)	0.0025 (2)	9.6 (5)	0.005
Au/CuClP 250 °C	Au – Cl	2.97 (7)	2.286 (3)	0.0024 (2)	9.6 (4)	0.006
Au/CuClP 300 °C	Au – Cl Au – Cu Au – Au	2.2 (2) 0.3 (3) 1.2 (8)	2.294 (9) 2.69 (4) 2.87 (2)	0.0034 (6) 0.0038 (5) 0.005 (2)	11 (1)	0.030
Au/CuClP 350 °C	Au – Cl Au – Cu Au – Au	1.3 (1) 1.7 (2) 3.1 (5)	2.28 (1) 2.647 (9) 2.84 (1)	0.0045 (9) 0.0053 (7) 0.0072 (9)	7 (1)	0.020

Table 5-a: Au/CuClP EXAFS fitting parameters. Au sample - S_0^2 = 0.75 as deduced by $KAuCl_4$ standard; Fit range 3<k<14, 1.1<R<3; # of independent points = 13.

The Au EXAFS data shown in Figure 5-p further demonstrate a progression to a more metallic species with increasing activation temperature. The fitting parameters are shown in Table 5-a and comparison of the Au-Cl CNs clearly show a depreciating trend with the increase in activation temperature. This supports the hypothesis that the $[AuCl_4]^-$ extrusion is proportional to the activation temperature while also supporting the contrast between the materials bulk and surface with the chlorometallate species still present in significant volume when activated at 350 °C. Further, inclusion of Au-Au or Au-Cu scattering paths in the data fits of the lower temperature samples detracted from the fit quality and this can be seen qualitatively from the magnitude components displayed in Figure 5-p, showing no significant scattering components above 2.3 Å. This advocates for the interaction between the Au and Cu species, as the inclusion of Au-Cu scattering paths is required in order to achieve a plausible fit for the EXAFS data, akin to the findings from the XPS investigations.

Closer inspection of the fitting parameters shows similar Au-Cl, Au-Cu and Au-Au bond lengths to that observed in the literature, reinforcing the reliability of the data fit employed.[271,322] Comparison of the Au-Cu and Au-Au CNs also suggests increasing Cu content of the nanoparticles with increasing activation temperature, approx. a quarter of the metallic Au coordination at 300 °C and a half at 350 °C. While this may suggest increasing Cu content, examination of the bond lengths could suggest nanoparticles with Cu rich shells as the Au-Au bond lengths are similar to those observed for bulk Au (approx. 2.86 Å) and the Au-Cu bond lengths are smaller than that expected of bulk AuCu alloys (approx. 2.65 Å) but similar to other surface Cu rich bimetallic AuCu nanoparticles.[322,323]

The characterisation discussed above strongly suggests that as the activation temperature increases not only does the extrusion of the chlorometallate ion to metallic Au occur but also there exists a proportion of Cu extrusion. Whether these Cu species are extruded from within the 1D channels of the framework as $[CuCl_4]^{2-}$ ions or from the framework itself is not yet clear. One thing to highlight would be that the extrusion of the Cu species is much more significant in the sample activated at 350 °C, this particular detail has been evident across all techniques employed. In addition, despite the exact nature of the final Au, Cu or Au-Cu species not being clear there does appear to be some interaction between the two metal centres which again is much more prominent in the sample activated at 350 °C as opposed to the lower temperature samples.

5.2.4 Structural Characterisation: Spectroscopy – Copper

Spectroscopic analysis of the Cu environment is complicated by the vast majority of the Cu species being integral to the framework. These present as predominantly Cu^{II} with a proportion of Cu^{I} while the target Cu^{0} species of interest is significantly lower in volume.

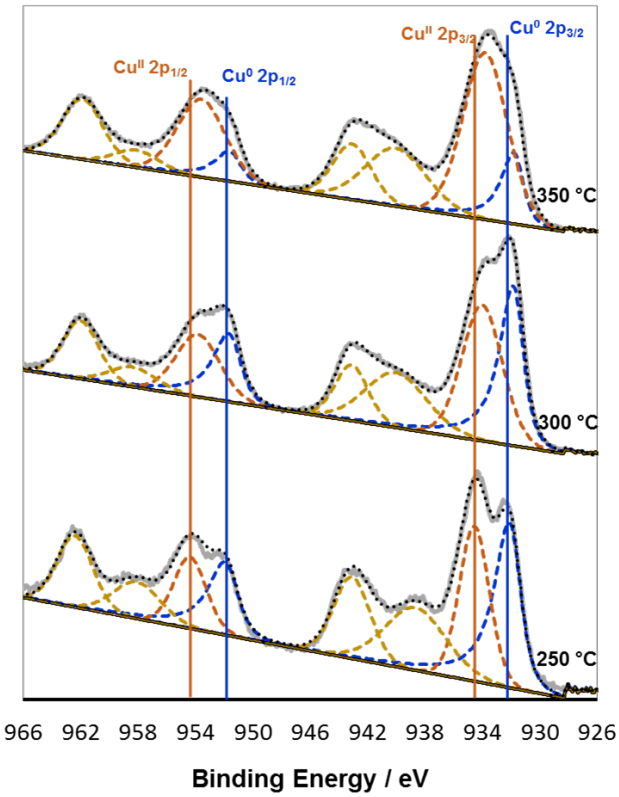

Figure 5-q: Stacked XPS data of the Cu 2p binding region for the Au/CuClP catalysts activated at different temperatures. The data is shown in grey with the data fit in black, Cu^{I}/Cu^{0} transitions are depicted in blue, the Cu^{II} in orange and the associated satellite peaks are shown in mustard.

Figure 5-q shows the XPS data of the Cu 2*p* binding region. Cu^{I} & Cu^{0} are notoriously difficult to differentiate between through XPS, presenting with analogous 2*p* binding energies (narrow signals $2p_{3/2}$ approx. 933 eV and $2p_{1/2}$ approx. 953 eV, shown in orange) with no satellite peaks.[316,324] Cu^{II} presents with broader signals at $2p_{3/2}$ approx. 934 eV and $2p_{1/2}$ approx. 954 eV with the addition of two satellite peaks as a result of its open shell $3d^{9}$ configuration (shown in beige).[325–327] As the Cu speciation within the framework is expected to be Cu^{II}, these XPS findings would support a combination of Cu species, Cu^{I}/Cu^{0} and Cu^{II}. Despite the 2*p* binding region suggesting a depreciation in the Cu^{I}/Cu^{0} component, it should be understood that there exists a range of Cu species within the framework itself, five coordinate $[CuO_4Cl]$ polyhedra, residual $[CuCl_4]$ units within the framework channels and potentially other disrupted species as a result of the extrusion process. It could therefore be true that one particular low oxidation state Cu species is

changing in nature which results in this depreciation, i.e. both production of Cu^0 and the oxidation of Cu^I to Cu^{II} could be occurring simultaneously.

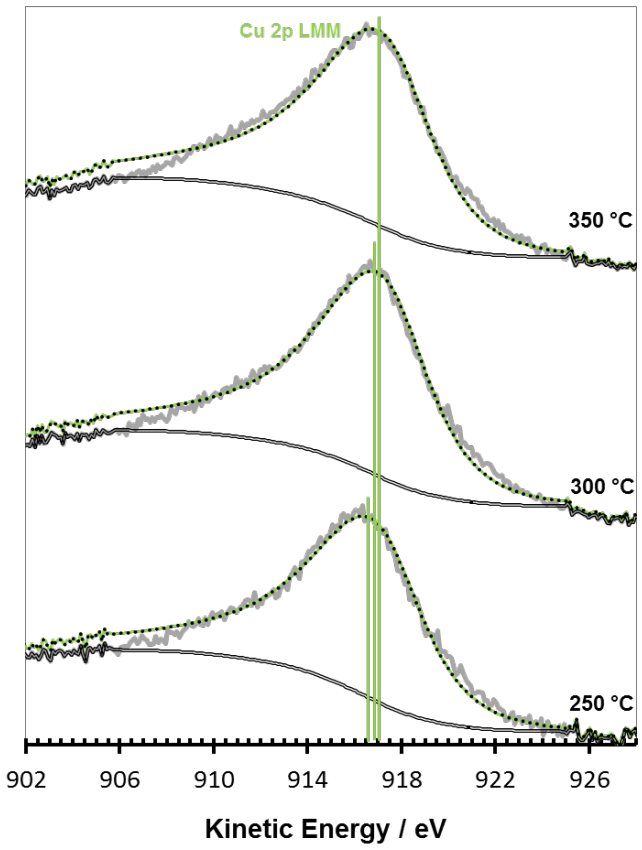

Figure 5-r: Stacked XPS data of the Cu LMM binding region for the Au/CuClP catalysts activated at different temperatures, plotted in KE. The data is shown in grey with the data fit in black and the Cu LMM transition shown in green.

Due to these difficulties, it would be more appropriate to view the overall impact of the extrusion process as a function on the overall oxidation state of Cu. This is possible through the Cu LMM Auger feature and the Cu K edge XANES (Figure 5-r and Figure 5-s respectively). The Cu LMM transitions display a shift towards higher KE (approx. 916.5-917.2 eV in KE) as the activation temperature increases. This is widely attributed to a decrease in the overall Cu oxidation state with typical values for Cu^{II}, Cu^I and Cu^0 of 916.8, 917.7 and 918.6 eV respectively.[324,326,328] The observed low KE when compared to the literature for metallic Cu could be due to the large excess of framework Cu by comparison, resulting in any changes in the average Cu oxidation state being minimal. While this could be the case, comparison with the other characterisation discussed and the XANES data below would show contrasting trends. The Cu K edge XANES spectra depicted in Figure 5-s show an analogous trend to the Cu XPS of the 2*p* binding region, a slight increase in the Cu oxidation state. This is evident from comparison with the metallic standard (blue) and the concomitant decrease in the associated pre-edge feature (8977 eV) coupled with the increase in white line absorption, all indications of increasing Cu

oxidation state.[329–331] Further to this, as expected, we observe clear indications of predominantly Cu^{II} environments due to the overwhelming majority of the framework Cu. The wide post edge shoulder is characteristic of Cu^{II} and is due to the 1*s* to 4*p* transition.[331,332] Therefore, the slight increase in the Cu LMM Auger feature is more likely due to the dramatic increase in Cu nanoparticle diameter as demonstrated by the high resolution ADF-STEM and shown by Shin *et al.*[333] to be a feature of widening *d*-band width of larger Cu particles.

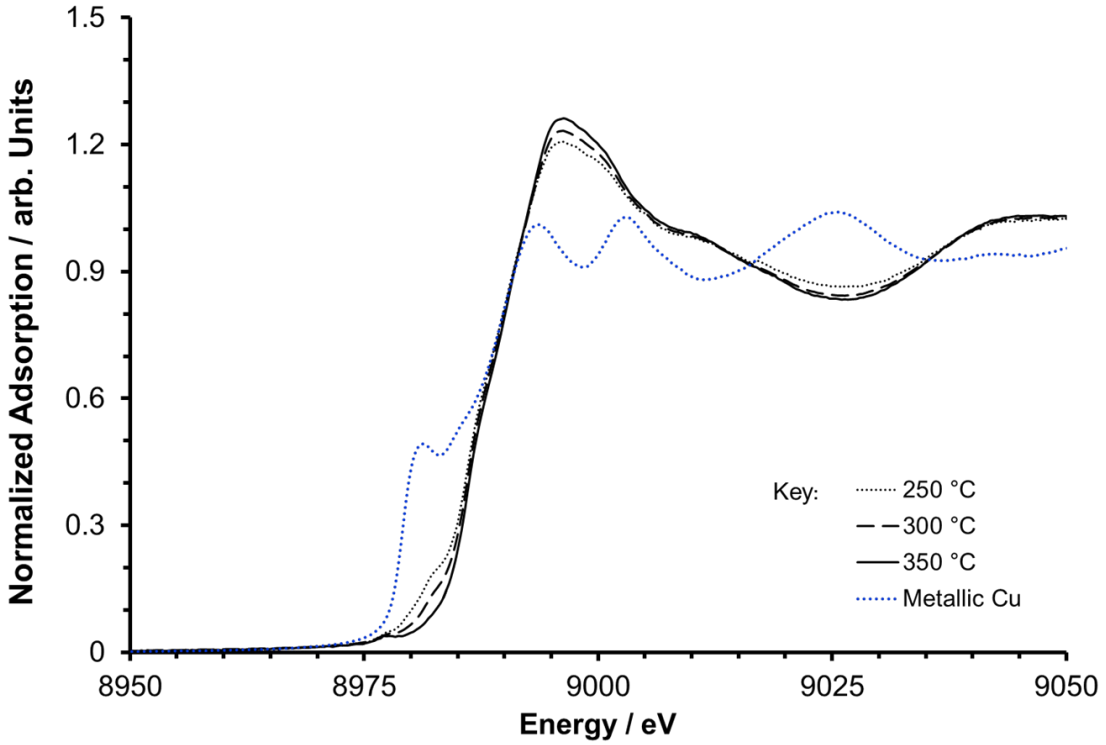

Figure 5-s: Stacked XANES data of the Cu K edge for the Au/CuClP materials activated at different temperatures with a metallic copper reference in blue.

Analysis of the Cu speciation within these samples suggests a mild increase in oxidation state which would appear counter intuitive given the reductive environment and nature of the extrusion process which has already been shown to produce metallic Cu species. Having said that, direct quantification of the Cu species is made extremely difficult due to the very small proportion of the target species in comparison to the bulk framework species. Thus, one important conclusion to draw is that this process does indeed change the nature of a proportion of the Cu species within the material. Whether this is fundamental framework species (which the PXRD could suggest) or simply residual copper chloride from within the channels is not known. Nevertheless, what does appear apparent is that the extrusion of this Cu species has an impact on the nature of the Au species on the supports surface and that this is most influential at 350 °C when compared to the lower temperature samples.

5.2.5 The Oxidation of Valerolactam to Glutarimide & Other Catalytic Potential

As discussed in Section 5.1.1, the production of imides such as glutarimide is a highly desirable concept especially if the substrate scope can be expanded slightly. For example, the use δ-valerolactam as a substrate for the production of glutarimide has been limited with only a handful of examples present. These were also discussed in Section 5.1.1. Through the utilization of these Au/CuClP catalysts this objective has been realised. Not only has this been done without the common drawbacks of more traditional routes such as the use of additives, co-catalysts or promoters but with an environmentally friendly oxidant (TBHP). Table 5-b demonstrates the competitive yields of approx. 60% achieved by these materials with notable levels of selectivity in excess of 99%, clearly highlighting their catalytic potential for such transformations.

Catalyst	Valerolactam Conversion / mol %	Glutarimide Selectivity / mol %	Benzyl Alcohol Conversion / mol %	Benzaldehyde Selectivity / mol %
CuClP 200 °C	2	>99	6	99
Au/CuClP 150 °C	17	>99	19	84
Au/CuClP 250 °C	22	>99	22	88
Au/CuClP 350 °C	60	>99	52	72

Table 5-b: Catalysis data for two independent reactions, the oxidation of valerolactam and benzyl alcohol with Au/CuClP catalysts activated at different temperatures utilizing TBHP as an oxidant. Undoped framework shown for comparison.

Table 5-b also highlights the low catalytic activity observed at lower activation temperatures followed by the clear jump in the conversion between the samples activated at 250 and 350 °C. This is something which is also observed for the TBHP oxidation of benzyl alcohol under similar conditions. This trend aligns well with the characterization discussed previously. We have established the limited existence of small (2-5 nm) Au nanoparticles at 250 °C and below, evidenced by both XPS, HR ADF-STEM and Chapter 4. The catalytic studies suggest that although the presence of Au nanoparticles upon the materials surface alone does impart some catalytic activity (comparing the blank CuClP vs the Au/CuClP activated at 150 °C), it is not enough to produce impressive yields of the imide and significant levels activity. Thus, this in conjunction with the observed increase in catalytic activity at 350 °C would suggest that the nature of the catalyst changes upon activation above 250 °C.

Further vindication of this evolution of the catalytic active site can be found when these catalysts were also tested, under similar conditions, in the oxidation of benzyl alcohol (Table 5-b). Clearly in this case, the changes in the catalytic active site causes over-oxidation products such as benzoic acid to be produced in significant quantities. Despite the catalysts activity towards benzyl alcohol not being impressive in its own right, it does serve to highlight the versatility of these materials as catalysts allowing them to be applicable to at least primary alcohols and cyclic lactams but potentially a much broader range of prospective substrates.

Indeed, it has been recognised that there is a significant difference in the nature of the catalytic nanoparticle species between activation at 250 and 350 °C. The presence of a range of small (2-5 nm) and larger (> 10 nm) nanoparticles that are exclusively metallic Au in nature at 250 °C has been demonstrated by the ADF AC-STEM investigations within this chapter. This has been corroborated by the ensuing XAS, XPS findings which support the solitary presence of metallic Au nanoparticles upon the CuClP frameworks surface, in line with the discussions in Chapter 4. Upon activation at 350 °C the evolution of the catalytic species follows. ADF AC-STEM demonstrated that at these temperatures the metallic Au (2-5 nm and > 10 nm) nanoparticles remain but they are accompanied by the introduction of large, > 10 nm metallic Cu nanoparticles and these species predominantly form in the periphery regions of the CuClP framework.

Further, these more aggressive activation conditions imparted a small degree of structural degradation (evidenced by both the PXRD and the image contrast of the ADF AC-STEM) and an increase in the density of the larger Au nanoparticles. This resulting vulnerability of the CuClP host is thought to be a result of removing the structurally integral Cu species as observed for the Pd/CuClP in the previous chapter. That being said, these structural changes and introduction of Cu species have a clear impact on the catalytic performance of these materials and the spectroscopic investigations established why this might be. Both EDXS and EXAFS demonstrated an increase in the Au:Cu ratio at the material surface which was suggested by the ADF AC-STEM. While the EXDS-STEM elemental mapping might suggest that these Au and Cu species exist discretely, observations of the XPS (Au 4*f* binding region) and EXAFS (Au-Cu CNs) strongly suggest otherwise. The presence of a clear shift to lower BE of the Au 4*f* XPS signal can be attributed to an electron transfer interaction from Cu to the more electro negative Au atoms and the requirement of Au-Cu scattering paths in order to achieve a plausible Au L_{III} edge EXAFS data fit stand as significant evidence for interactions between the Au and Cu centres. Whether they exist as truly alloyed nanoparticles is still to be established, but the significant nature of the Au-Cu CN (1.7) would suggest an extensive degree of Au-Cu bonding and thus support the hypothesis of a proportion of bimetallic AuCu nanoparticles

existing. Nevertheless, one can confidently suggest that it is these Au-Cu sites in conjunction with the host framework that are imparting the significant catalytic enhancements observed. Further still, noteworthy catalytic contribution from the introduction of discrete large Cu particles is not thought to be significant as they are > 10 nm in diameter. Given the pre-existence of the monometallic Au nanoparticles at the lower reduction temperatures, one can confidently suggest that it is the introduction of Cu rich and/or bimetallic AuCu species and their consequential nanoparticle-support synergies that are responsible for the catalytic enhancement observed, analogous to the observations made in Section 5.1.2 with similar bimetallic systems.

5.3 Conclusions

By employing a combination of complimentary structural, spectroscopic and high-resolution microscopy techniques, the degree of Au nanoparticle formation has been established to the point where the Au/CuClP material beings to break down, similarly to the Pd system, under reductive activation conditions (i.e. reduced at 200 °C for 2 hr in 5% H_2/N_2 flow). Through these investigations, a unique characteristic of the Au/CuClP material has been established; its ability to form catalytically active Cu rich species, potentially as bimetallic Au-Cu nanoparticles. The production of such species, existing alongside both large (>10 nm) and small (<10 nm) monometallic Au nanoparticle species has been evidenced by XAS, XPS and ADF-STEM, see table Table 5-c. These observations, coupled with the catalytic investigations, suggest that the introduction of increasing quantities of Cu species and the Au-Cu synergies that ensue, have a dramatic impact on the catalytic behaviour of these systems, bestowing vastly superior levels of activity in both the TBHP oxidation of benzyl alcohol and δ-valerlactam. Further, in the case of δ-valerlactam oxidation, the resulting increased activity does not cause a depreciation of the catalysts selectivity. This suggests that these unique materials could offer new, selective, and more environmentally friendly pathways to the synthesis of the commercially valuable cyclic imide, glutarimide.

It has therefore been demonstrated, that the Au/CuClP materials have the potential to possess a range of active species provided the activation protocols are appropriately designed. The generation of small (2-5 nm) extruded Au nanoparticles on the surface as well as larger (> 10 nm) Au, Cu and/or Au-Cu nanoparticles, with the later demonstrating significant catalytic implications, has been evidenced. These findings have therefore not only shown the Au/CuClP material to be an effective catalyst for oxidation processes in its own right but also indicate the potential for tailored Au/Cu alloying or combined extrusion, which enhances the prospects for exploiting bifunctional, multi-metallic catalysis in the future.

Technique	Key Findings
ADF AC-STEM	- At 200 °C regions of extensive, well-defined and small (approx. 2-5 nm) nanoparticle formation are observed - Significant density of larger nanoparticles (> 10 nm) is also present even at 200 °C and these increase in abundance with activation temperature - Image contrast suggests retention of the pristine framework at 200 °C alongside increasing degradation at 250 and 350 °C
EDXS	- Confirms the presence of extruded Au and Cu species upon the materials surface - Shows the Au:Cu ratio decreases with activation temperature - Thus, Cu becomes increasingly dominant at the materials surface with increasing activation temperature
STEM-EDXS	- Confirms the identity of smaller (2-5 nm) and larger (> 10 nm) nanoparticles as predominantly Au at 250 °C - Smaller Au nanoparticles exist upon the surface of the sample activated at 350 °C together with the formation of larger Cu nanoparticles - Conclusively highlights the effectiveness of the extrusion process, at elevated 350 °C, for completely removing Au from within surface regions of the framework
PXRD	- Demonstrates the Au/CuClP system maintains its structural integrity across activation temperatures of: 150 – 250 °C - Small quantities of additional phases (copper oxide and rubidium phosphate) are present at 350 °C
XPS	- Exclusively shows complete formation of Au^0 at ≥ 250 °C - Demonstrates that extrusion occurs extensively on the materials peripheries - Changes in the electronic environment of the Au species are introduced at 350 °C - Electron transfer from Cu to Au leads to Au core levels shifting to lower BEs, indicating AuCu alloying at 350 °C or at least Au-Cu interactions
XANES	- The diminishing white line intensity with increasing activation temperature demonstrates the progression towards Au^0 - Reduction of the gold salt is more achievable in surface regions of the sample, leaving a significant proportion of chlorometallate ion present within the bulk - Weaker white line intensity at 300 & 350 °C than the Au^0 reference can be attributed to the nanoparticulate nature of a proportion of the Au species
EXAFS	- Au-Cl CNs clearly show a depreciating trend with the increase in activation temperature - Au-Cu and Au-Au CNs suggests increasing Cu content of the nanoparticles with increasing activation temperature, akin to EDXS - Advocates for the interaction between the Au and Cu species as the inclusion of Au-Cu scattering paths is required

Table 5-c: Summary of the structural features of the Au/CuClP activated by reduction under a flow of 5% H_2/N_2.

Chapter 6: Performance Optimization of the Platinum Catalyst for the Selective Production of Cyclohexanone & Mapping the Catalysts Deactivation

In this chapter, the experimental variables for the oxidation of KA oil by the Pt/CuClP catalyst are examined. This led to the optimization of the overall catalytic process within the continuous flow system employed, following the material investigations discussed in Chapters 3 and 4. In addition, the typical deactivation pathways for nanoparticle catalysts are reviewed in order to objectively apply the findings to the Pt/CuClP system.

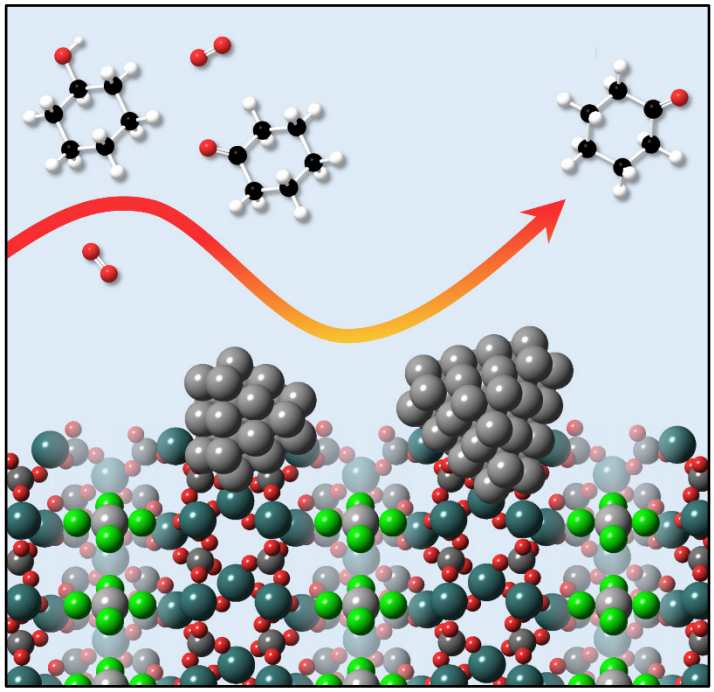

*Figure 6-a: Graphical illustration of the microporous CuClP framework containing $[PtCl_4]^{2-}$ precursor complexes which result in well-dispersed and isolated metallic Pt nanoparticles upon activation that are active for the selective aerobic oxidation of KA oil within a continuous flow system. From A. M. Gill, C. S. Hinde, R. K. Leary, M. E. Potter, A. Jouve, P. P. Wells, P. A. Midgley, J. M. Thomas and R. Raja, ChemSusChem, 2016, **9**, 423 – 427 Reprinted by permission of John Wiley & Sons, Inc.*

In particular, alternative Au, Pd, Pt and other transition metal nanoparticle catalysts upon different supports are contrasted against the highest performing Pt/CuClP catalyst. This was done in order to establish a comparison of performance for the selective aerobic oxidation of KA oil against other catalysts with meaningful research potential. Following

these comparisons and the establishment of the Pt/CuClP catalysts authority within this particular system, the reaction parameters are refined in order to maximise the overall performance of these materials. Further, in order to fully understand these materials and this particular catalytic system, the catalysts' deactivation pathway is assessed. This is done through the utilization of catalytic observations in conjunction with detailed structural analysis in the form of XAS, PXRD and TEM.

Notable contributions:

- Dr Jaime Garcia-Aguilar for his provision of the catalysts used in Table 6-a.
- Prof Richard Adams for his provision of the catalysts used in Table 6-b.
- Dr Scott Rogers for his provision of the catalysts used in Table 6-c and the collection and processing of the TEM data presented within this chapter.
- Andrea Jouve for his efforts working on the project as a visiting ERASMUS student from the University of Torino, Italy.
- Sophie Wood for her assistance, efforts and notable contributions to the catalysis whilst working on the project as a third year student within the University of Southampton.

6.1 Introduction

6.1.1 Deactivation Pathways for Nanoparticle Catalysts

Poisoning and deactivation of a catalyst, while largely considered to be detrimental, can benefit the ensuing catalytic process, with several examples, including industrial processes, citing the benefits of controlled catalytic deactivation. These often present by limiting the activity of a catalyst and consequently improving the desired selectivity, often within oxidation processes. For example, in the formation of CO from ethylene by silver catalysts, small degrees of chlorination aid in preventing the over oxidation to CO_2 while over chlorination leads to complete deactivation. Similar observations have also been made for some sulphur and nitrogenous compounds within metal catalysed oxidations and hydrogenations.[12] That being said, typical poisoning of a catalyst leads to deactivation and reduced catalytic lifetimes. Known harmful poisons for Pt catalysed hydrocarbon oxidations include: Pd, P, Zn, SO_2 and Fe, none of which would be expected to have a significant impact within this particular process provided the substrate stream is sufficiently pure of these species.[334]

Catalysts can deactivate via a number of pathways: the active sites can be poisoned/blocked by the adsorption of impurities (from the substrate stream); the fouling of the surface active sites by carbonaceous materials from the breaking down of hydrocarbon reaction components; the loss of reactive surface area through sintering via the agglomeration and growth of the catalysts particles; physical loss of the active species such as leaching or the chemical transformation of the active site within the catalyst itself.[12,334] For nanoparticle catalysts, all of these deactivation pathways are tenable. However, depending on the conditions and species of interest, some are more common than others. In particular, leaching (due to poor particle-surface adhesion) and sintering (due to the high surface energy of nanoparticles) are amongst the most common and prominent, due to their irreversible nature for nanoparticle materials. It is also noteworthy that these two features, in particular, share principles with the discussions formed around the stabilisation of nanoparticle systems upon their fabrication (Section 1.2). Therefore these are two significant hurdles for the fabrication of highly active and robust nanoparticle systems. However, within vapour phase systems, like those under investigation within these works, dissolution of the active metal species is severely hindered and therefore leaching is less commonly observed. Furthermore, given the oxidative nature of this particular system, surface oxide formation, coking and agglomeration are to be more prominent.

Over oxidation of an alcohol substrate is a common cause of catalytic deactivation for Pt-group metal catalysts. This typically occurs according to Scheme 6-a, for primary alcohols, or for secondary alcohols, via the C-C bond cleavage and generation of adsorbed carbonate species. As seen in Scheme 6-b for the decomposition of 2-propanol over Pd catalysts.[28,335,336] This not only produces pollutants in the form of adsorbed larger carbonaceous materials, but also the typically, strongly adsorbed, CO a very common and highly detrimental pollutant for Pt based systems.[28,337–339] These strongly adsorbed species block the catalytically active sites and therefore the catalysts effectiveness progressively diminishes as the sites are blocked leading to complete deactivation. Typically, deactivation by this particular pathway is reversible by simple reactivation of the catalyst under highly oxidative conditions; high oxygen concentrations and high temperatures can typically burn off the pollutants and regenerate the catalytic species, provided the thermal stability of the system allows.[339,340]

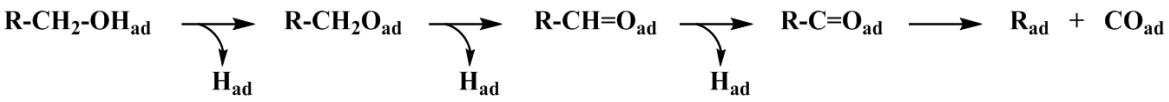

Scheme 6-a: Simplified general route for the transformation (decomposition) of a primary alcohol on the Pt-group metal surface.[337]

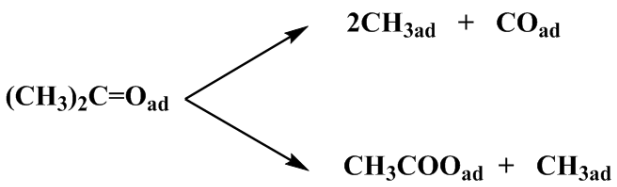

Scheme 6-b: Simplified route for the transformation (decomposition) of 2-propanol on a Pd (111) surface.[336]

Another common means of blocking the catalytic active sites, frequently observed for Pt systems under oxygen atmospheres, is the generation of a PtO_x layer upon the particle surface.[28,339] This has been well documented and it is often accepted that while in many cases the active Pt species is the adsorbed Pt-O species, over oxidation of the Pt surface leads to the prevention of substrate binding. Therefore, it is key to avoid excessive volumes of oxygen in order to maintain a balance between the generation of the active adsorbed oxygen species, while facilitating the binding of the alcohol substrate.[335,339,341] While this presents as a serious consequence of oxygen rich environments, it is often reversible by simply exposing the catalyst species to a reductive environment in order to regenerate the active metallic Pt species.[341,342] However, in some cases it has been reported that oxygen atoms can penetrate the Pt lattice and form sub-oxide species that are not easily reduced.[342]

Finally, and arguably, the most significant possible deactivation pathway for Pt nanoparticle catalysts is the migration of the surface Pt species and the agglomeration of the particles to form larger, inactive species. Not only is this commonly observed across many nanoparticle systems but it is also completely irreversible.[28,334,341,343] This thermodynamic phenomenon stems from the fact that larger particles or bulk metals are more stable than small isolated particles with high percentages of surface atoms. This is due to lower surface area systems possessing a lower surface energy and are therefore more energetically favourable.[344] This thermodynamic favourability to enhance particle size means that if the migration of the metallic species is facilitated in any way then the particles will tend to coalesce. Due to its favourable energetics, this phenomenon is not only hard to prevent but it is also facilitated by a number of factors, such as: temperature, atmosphere, metal dispersion and the surface area/porosity of the support. The growth of metal crystallites occurs through two primary routes at the temperatures close to and within the ranges studied within these works: migration of entire crystallites and atomic migration.[334] Due to their thermodynamic nature, both of these mechanisms are facilitated by elevated temperatures. This involves the transport of individual Pt atoms by chelating molecules towards larger particles (Oswald ripening) and is further encouraged by a number of factors. Highly acidic or basic conditions encourage the dissolution of metal atoms as M^{n+} species which can then readily migrate in solution. Also, high oxygen concentrations facilitate the migration of metallic species and often lead to the aggregation and enlargement of the metallic particles.[28,334] Ostwald ripening occurs readily at temperatures as low as RT but predominantly acts within liquid phase systems. This process has been known to impact Pt nanoparticle systems, leading to activity losses in alcohol oxidations through nanoparticle diameter increase of > 30%.[343,345,346]

Agglomeration of the active nanoparticle species has been to the detriment of a range of catalytic applications: from Ru/TiO_2,[347] Co/Al_2O_3[348] and $CoPt/SiO_2$[349] catalysed Fischer-Tropsch syntheses, Au/CeO_2[340] and Au/TiO_2[350] catalysed CO oxidation, Pt/C[351] catalysed ethanol oxidation, Pt/CeO_2[352] catalysed methane oxidation to the more curious Pd/C catalysed dehydrogenative coupling of hydrosilanes and amines.[353] With this in mind, it is important to consider the factors affecting agglomeration pathways, particularly for Pt based systems, such as those studied within these works. It is known that sintering rates increase rapidly with temperature and metal loading (or inversely with the surface dispersion of the metal) and typically one would expect crystallite migration to dominate at low temperatures and atomic migration at higher temperatures.[334,354] It is also well established that for Pt nanoparticle systems, particle sintering is favoured in oxygen rich environments over hydrogen or nitrogen.[28,334] Therefore despite sintering processes predominantly occurring at high temperatures (i.e. > 500 °C), the oxygen rich atmosphere, high metal loadings and the presence of chloride ions (known to facilitate the migration of

M^{n+} species) could be detrimental to the stability of the Pt/CuClP system.[28,334,354] However, sintering rates are lower for nanoparticles supported on porous supports and this has been shown to decrease further as the nanoparticle diameters approach those of the pores of the host material.[334] This is a consequence of different nanoparticle positions upon a surface having different levels of stability. For example, a nanoparticle within a surface 'valley' position or at the apex of a pore mouth would be stable and thus less likely to migrate whereas an 'on-top' position, one residing upon a flat, pristine surface is highly unstable and would favour migration.[355] Therefore, there are a number of key factors influencing the potential agglomeration of Pt nanoparticles upon the CuClP framework and the more favourable nanoparticle-support interactions available for the Pt/CuClP systems could aid in the catalysts stability. Given this array of factors and the vast number of potential deactivation pathways for catalytic systems, such as Pt nanoparticles beyond agglomeration, it is a vital commodity to understand which is the most prominent for a given system if one is to design and develop not just an active catalyst but one which is also robust in nature.

6.2 A More Detailed Study of the Pt/CuClP Catalyst for the Aerobic Oxidation of KA Oil

6.2.1 Contrasting the Pt/CuClP Catalyst against Other Catalytic Systems

While development of the Pt/CuClP catalyst, and comparisons against the Au and Pd analogues, have been detailed in Chapters 3 and 4, direct comparisons with other, similar catalytic systems has thus far been lacking. Table 6-a, Table 6-b and Table 6-c contrast the catalytic performance of the Pt/CuClP material against some other heterogeneous catalysts. Table 6-a details silica supported Pt, Pd, Au, Ru and V catalysts prepared via a sol-gel method by Dr Garcia-Aguilar *et al.*[356] Table 6-b details MCM-41 supported Ir and Bi clusters prepared by Prof Adams *et al.*[357] Table 6-c details titania supported Pt, Pd and Au nanoparticle catalysts prepared via a sol-immobilisation method with differing H_2O/EtOH ratios by Dr Rogers *et al.*[358] Please note that due to the quantities of materials supplied it was not possible to run all reactions under analogous conditions, unfortunately as a result, differing catalyst quantities were employed and therefore each table should be considered independently of the others.

Catalyst	M / wt. %	Cyclohexanol Conversion / mol%	Mass Balance / mol%	Cyclohexanone Selectivity / mol%	TOF / hr^{-1}
Pt/CuClP[a]	7	58	98	>99	67
Pt/Al_2O_3[b]	1	56	67	>99	449
Pt/SiO_2[b]	1	36	89	91	302
Au/SiO_2[b]	1	2	96	>99	20
Pd/SiO_2[b]	1	40	79	88	178
V/SiO_2[b]	1	3	99	>99	7
Ru/SiO_2[b]	1	54	90	86	235
RuV/SiO_2[b]	1	53	80	86	167

Table 6-a: Contrasts the Pt/CuClP catalyst against silica supported Pt, Pd, Au, Ru and V catalysts prepared via a sol-gel method by Dr Garcia-Aguilar et al.[356] *Catalyst: 0.10g, a – synthesised by A. Gill, b – synthesised by J. Garcia et al.*[359,360] *Air flow: 25 $mLmin^{-1}$, KA flow: 15 $\mu Lmin^{-1}$ WHSV: 4.20-4.30 hr^{-1}, temperature: 200 °C. Others: benzene, phenol, 2-cyclohexene-1-one or a mixture thereof.*

Catalyst	M / wt. %	Cyclohexanol Conversion / mol%	Mass Balance / mol%	Cyclohexanone Selectivity / mol%	TOF / hr^{-1}
Pt/CuClP[a]	7	74	89	>99	57
Ir_3Bi/MCM-41[b]	3	25	84	71	143
Ir_5Bi_3/MCM-41[b]	3	6	93	99	12

Table 6-b: Contrasts the Pt/CuClP catalyst against MCM-41 supported Ir and Bi clusters prepared by Prof Adams et al.[357] *Catalyst: 0.15g, a – synthesised by A. Gill, b – synthesised by R. Adams et al.*[357] *Air flow: 25 $mLmin^{-1}$, KA flow: 15 $\mu Lmin^{-1}$ WHSV: 2.80-2.90 hr^{-1}, temperature: 200 °C. Others: benzene, cyclohexene, 2-cyclohexene-1-one or a mixture thereof.*

Catalyst	M / wt. %	Cyclohexanol Conversion / mol%	Mass Balance / mol%	Cyclohexanone Selectivity / mol%	TOF / hr^{-1}
Pt/CuClP[a]	7	72	91	>99	36
Pt/TiO_2[b]	1	39	73	>99	137
Au/TiO_2[b]	1	4	97	>99	2
Pd/TiO_2[b] (A1)	1	66	94	64	228
Pd/TiO_2[b] (A4)	1	32	83	53	113
Pd/TiO_2[b] (B1)	1	25	82	>99	88

Table 6-c: Contrasts the Pt/CuClP catalyst against titania supported Pt, Pd and Au nanoparticle catalysts prepared via a sol-immobilisation method with differing H_2O/EtOH ratios by Dr Rogers et al.[358] *Catalyst: 0.24g, a – synthesised by A. Gill, b – synthesised by S. Rogers et al.*[358] *Brackets refer to variations in synthesis protocol.*[358] *Air flow: 25 $mLmin^{-1}$, KA flow: 15 $\mu Lmin^{-1}$ WHSV: 1.75-1.85 hr^{-1}, temperature: 200 °C. Others: benzene, cyclohexene or a mixture thereof.*

Inspection of these tables clearly highlights the activity of Pt in particular for the aerobic oxidation of KA oil. This is independent of the fabrication procedure, as Pt catalysts produced via different means clearly demonstrate superior levels of activity than the other active metals: Au, Pd, Ru, V, Ir and Bi. This is similar to the observations made for Au and Pd/CuClP catalysts. While the synthesis procedure doesn't appear to carry significant impact on the catalysis, there is a clear influence, by the support specifically, affecting the catalysts selectivity. In particular, the Pt/SiO_2 system (Table 6-a) shows notably lower levels of selectivity when compared with the other supports: CuClP, Al_2O_3 and TiO_2. Not only do the Pt systems demonstrate superior levels of cyclohexanol conversion over other metallic systems, but they also exhibit significantly higher levels of ketone selectivity over the other systems. Contrastingly, Au and V systems appear inactive and while Pd and Ru catalysts show good activity, they suffer from poor product selectivity, demonstrating a

propensity to form the 2-cyclohexen-1-one product. While these observations suggest Pt to be specifically active for this particular oxidation, some highly active Pt catalysts show poor mass balances, suggesting significant levels of tar and CO_2 production. This further highlights the need to restrain ultra-reactive centres that can cause over oxidation and the undesirable loss of product selectivity. With that said, this is not observed for the Pt/CuClP system which demonstrates the highest combined levels of cyclohexanone selectivity, cyclohexanol conversion and mass balance (overall yield), vindicating its impeccable performance within this process.

6.2.2 Optimization of the KA Oil Oxidation Reaction Parameters

Following the works discussed in Chapters 3 and 4, which detailed the catalytic improvements centred on refinement of the catalyst itself, here the optimization of the reaction parameters is reviewed to establish the most effective system possible with the Pt/CuClP catalyst. Figure 6-b details the impact of the catalyst bed loading on the activity. Catalyst masses ranged from 0.10 – 0.24 g encompassing the maximum conversion range for the system. Throughout the study, cyclohexanone selectivity was consistent at >99 % for all samples and a steady mass balance of 85% ±5% is achieved below WHSVs of 3.5 hr^{-1}. The maximum cyclohexanol conversion was found to be at 0.175 g of Pt/CuClP, equivalent to a WHSV of approx. 2.5 hr^{-1}, before which increasing mass (decreasing WHSV) saw a progressive increase in conversion. That being said, increases in catalyst mass above this point demonstrated no catalytic advantage in terms of cyclohexanol conversion. Therefore, the conversion profile suggests that there is little need to load the catalyst bed above 0.18 g. Thus, material could be saved by reviewing the previously employed catalytic protocol employing 0.24 g of catalyst.

The increasing catalyst mass also caused a concurrent decrease in TOF. Therefore, it implied that while the total number of active sites is increasing, this can also have negative implications. It is understood within catalysis that while certain active sites can work in tandem, it is often the case that site isolation is key to achieve high levels of activity. Increases in the amount of catalyst would cause a loss of site isolation and therefore this could be why the number of moles of cyclohexanol converted in this case are not sufficient to keep a constant, linear TOF relationship.[85] Therefore, using a higher mass is unfavourable industrially due to a reduction in TOF. Thus, given its ideal cyclohexanol conversion and sustained TOF, 0.175 g was established as the ideal catalyst-bed mass giving a WHSV of approx. 2.5 hr^{-1} at the given substrate flow rate. Furthermore, the reduction in catalyst mass in contrast to the 0.24 g previously employed would be more attractive industrially due to its enhanced reaction efficiency.

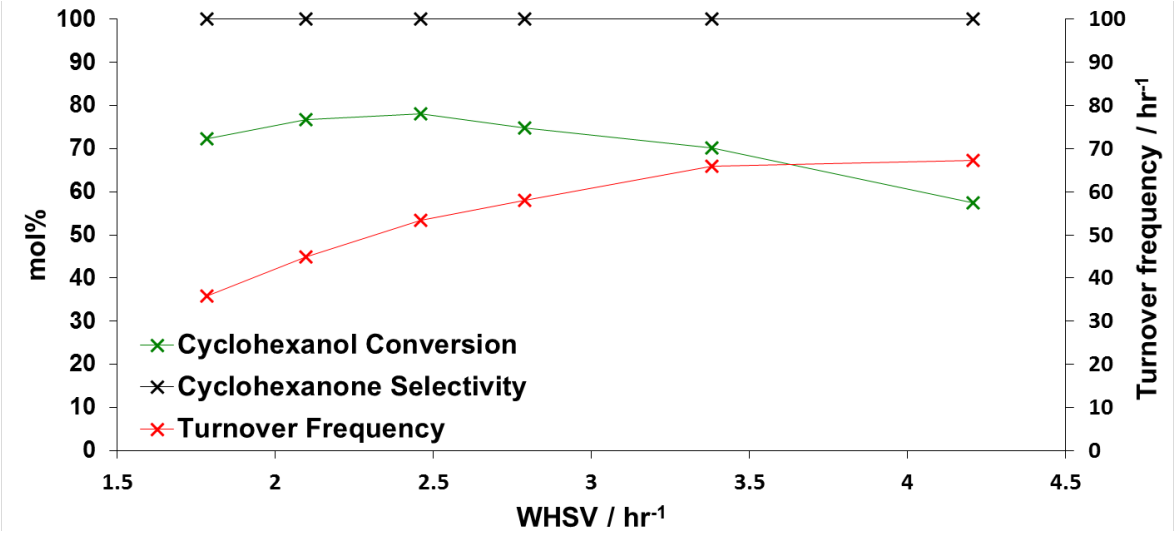

Figure 6-b: The effect of changing the mass of Pt/CuClP catalyst (0.1 - 0.24 g) employed on the oxidation of KA oil. Temperature 200 °C, KA oil flow: 15 µLmin^{-1}, air flow: 25 mLmin^{-1}.

Given the vapour phase nature of this process and the boiling points of cyclohexanol and cyclohexanone being 162 and 156 °C respectively, the effect of the reaction temperature, shown in Figure 6-c, was contrasted from 170 – 230 °C. There appears to be little effect on conversion above 190 °C although the mass balance depreciates gradually above 200 °C to approx. 65% at 230 °C. Therefore, the higher kinetic energy observed for the system at 200 °C is beneficial by comparison with lower temperatures resulting in slightly higher levels of cyclohexanol conversion and therefore the pre-existing operating temperature should be maintained given the depreciation in mass balance beyond this point.

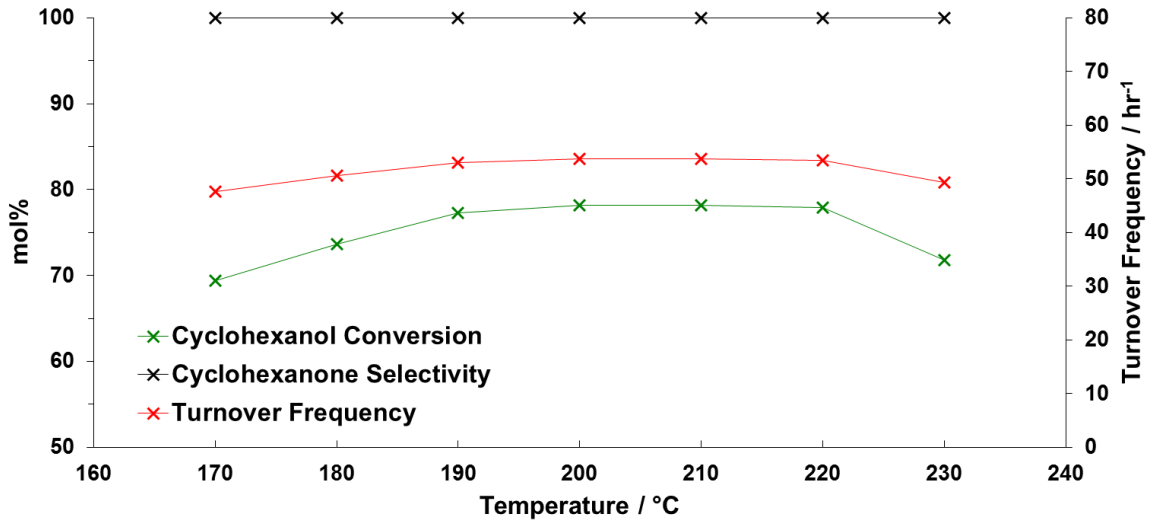

Figure 6-c: The effect of changing the temperature on the Pt/CuClP oxidation of KA oil. 0.175 g of catalyst, KA oil flow: 15 µLmin^{-1}, WHSV: 2.45 hr^{-1}, air flow: 25 mLmin^{-1}. NOTE: mol% axis ranges from 50 – 100%.

Changing the air flow rate, as displayed in Figure 6-d, shows a clear and steady increase in cyclohexanol conversion to above 80% at approx. 30 mLmin^{-1}. This is followed by a sharp drop in conversion at higher air flow rates. With oxygen as the active oxidant being 21% by volume, Figure 6-e shows the conversion as a function of substrate to oxidant, ratio which displays an analogous trend to that of Figure 6-d. Oxygen is only required in a stoichiometry of 0.5 (section 1.3.4) for the alcohol to ketone transformation to occur. The steady, almost linear increase up to a ratio of 3.5:1.0 suggests an order of more than one with respect to oxygen within this process. This implies that the saturation of the catalysts' surface with oxygen is key for higher rates of reaction. It also implies that the formation of the by-product, water, and its abstraction of the hydrogen generated by the transformation followed by its subsequent desorption could be the rate determining step for the process. This is in concurrence with the discussions in 6.1.1, where it was highlighted that the active site within the Pt catalysed alcohol oxidation processes, is often the adsorbed Pt-O species.[335,339,341] This is further supported by the concurrent trend observed for the TOF of the system with respect to the air flow (Figure 6-d). The sudden and drastic drop in cyclohexanol conversion, whilst unanticipated, could be due to the over saturation of the catalysts' surface, inhibiting substrate binding. Furthermore, coupling this with the fact that as the air flow rate and concentration of air in the system at any given time is increasing then the consequence of this is the decrease in cyclohexanol concentration. Thus, not only is the binding of the substrate being inhibited by saturation of the catalysts surface with oxygen, but the overall concentration of the substrate is decreasing, further verifying the decline in catalytic activity.

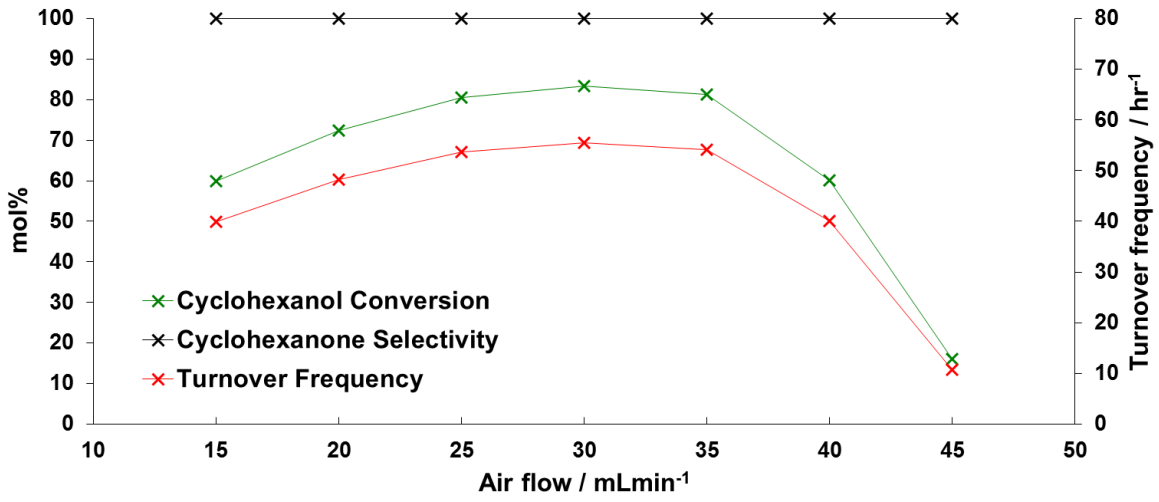

Figure 6-d: The effect of changing the air flow rate on the Pt/CuClP oxidation of KA oil. Temperature: 200 °C, 0.175 g of catalyst, KA oil flow: 15 µLmin^{-1}, WHSV: 2.45 hr^{-1}.

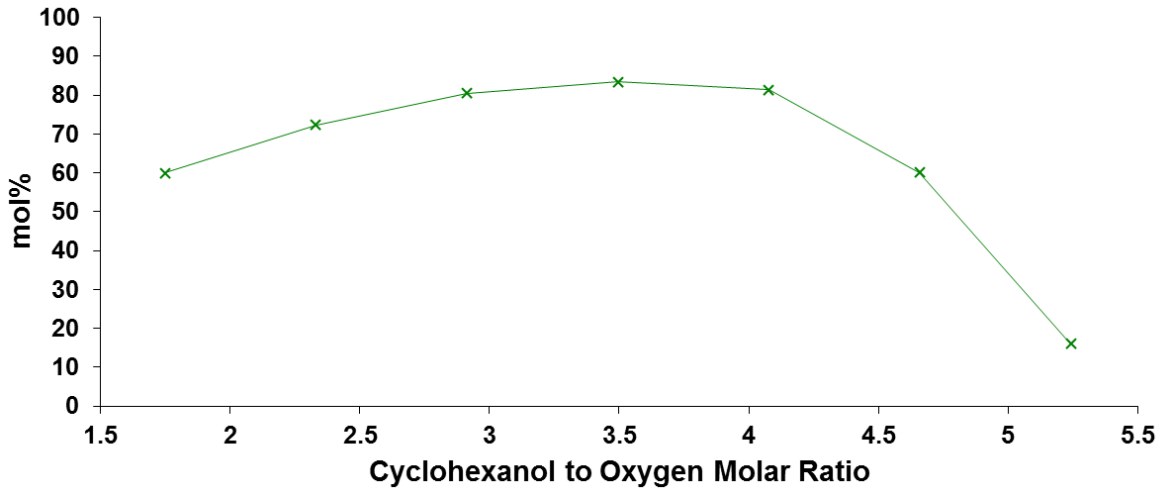

Figure 6-e: The effect of changing the air flow rate on the Pt/CuClP oxidation of KA oil plotted as the substrate to oxidant ratio. Temperature: 200 °C, 0.175 g of catalyst, KA oil flow: 15 µLmin^{-1}, WHSV: 2.45 hr^{-1}.

The effect of substrate flow variation is displayed in Figure 6-f, depicting a steady decrease in cyclohexanol conversion from > 90 – < 40 % after which point further increases to the KA oil flow rate have little impact on the overall catalytic conversion. This depreciation in activity is most likely due to the increasing cyclohexanol concentration and not the inadequate activity of the catalyst. In fact, the TOF increases rapidly with flow rate, demonstrating the capacity of the catalyst to accommodate the added substrate within the system. However, a maximum is reached at approx. 3.2 hr^{-1} (equivalent to a KA oil flow rate of 20 µLmin^{-1}) after which the drop in TOF suggests that beyond this point the catalyst becomes rapidly less efficient. This is likely due to a lack of binding sites available to the excess cyclohexanol or the detrimental displacement of oxygen by cyclohexanol upon the catalysts' surface, the significance of which has just been highlighted.

Another consideration is that at lower WHSVs there is a smaller flow of cyclohexanol. Consequently the molecules have a longer contact time with the catalyst as per Equation 28. This increased contact time with the catalysts' surface results in a higher probability that the cyclohexanol will react, thus justifying the observed higher conversion at lower WHSV. Furthermore, while the highest conversion is achieved at the lowest substrate flow (WHSV = 0.8 hr^{-1}), this occurs with the lowest process mass balance of approx. 55%. This can be attributed to over oxidation as a longer contact time may lead to the over oxidation of the desired cyclohexanone product into unwanted, non-detectable (by GC) by-products, such as tars, dibasic acids and/or carbon dioxide.[335] Therefore in order to achieve a plausible compromise between the process mass balance and catalytic TOF and given the linear decline in conversion, a flow rate of 17.5 µLmin^{-1} (WHSV of 2.85 hr^{-1}) was established as the improved operating parameter.

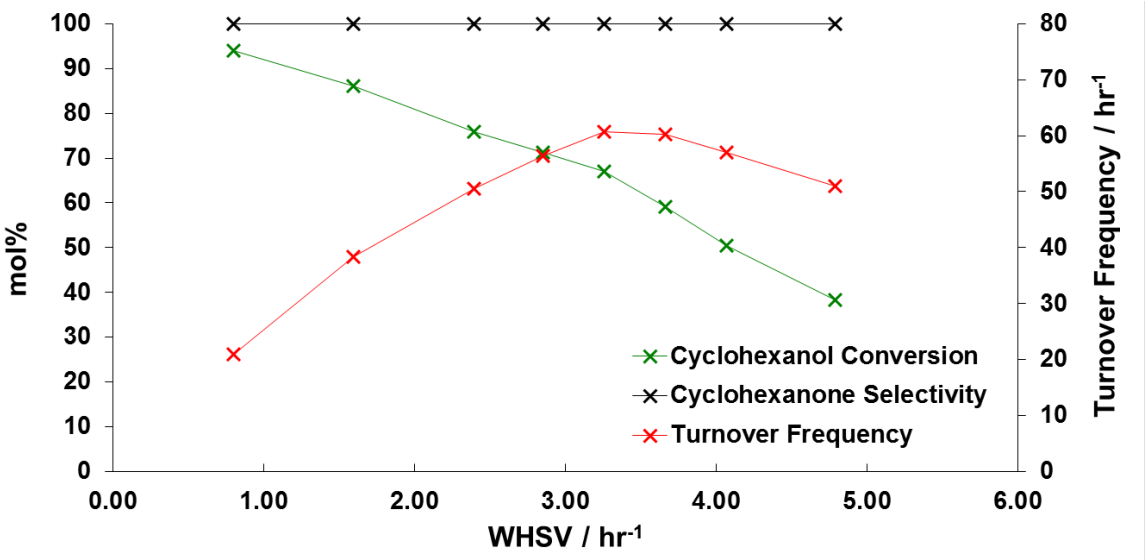

Figure 6-f: The effect of changing the substrate flow rate on the Pt/CuClP oxidation of KA oil. Temperature: 200 °C, 0.175 g of catalyst, KA oil flow: 5 – 30 µLmin^{-1}, air flow: 25 mLmin^{-1}.

$$Contact\ time\ (min) = \frac{Volume\ of\ catalyst\ (\mu L)}{Flow\ rate\ (\mu L min^{-1})}$$

Equation 28: Contact time.

As detailed in Section 2.2.3, the catalyst is prepared in pelletized form before being subjected to the reaction. These pelletized fragments are sieved to minimise any influence of particle size / catalysts surface area for a given mass on the catalytic performance. Across the range studied, detailed in Table 6-d the catalyst particle size shows little influence. Still, the data could subtly elude to the logical conclusion that smaller particle size leads to greater conversion although given the narrow nature of the study due to the equipment available these observations remain speculative.

Particle Size / mm	Cyclohexanol Conversion / mol%	Cyclohexanone Selectivity / mol%	TOF / hr^{-1}
2.0 – 0.5	78	>99	52
2.0 – 1.0	78	>99	53
1.0 – 0.5	83	>99	56

Table 6-d: The effect of particle size on the Pt/CuClP oxidation of KA oil. Temperature: 200 °C, 0.175 g of catalyst, KA oil flow: 15 µLmin^{-1}, WHSV: 2.45 hr^{-1}, air flow: 25 mLmin^{-1}.

Given the findings from the refinement of the reaction parameters for this KA oil oxidation process, a new and improved set of reaction conditions were attained: a reaction temperature of 200 °C, 0.175 g of catalyst (1.0 – 0.5 nm), a KA oil flow of 17.5 µLmin^{-1} (WHSV: 2.85 hr^{-1}) and an air flow of 35 mLmin^{-1}. While the refinements focused on the

individual parameters under investigation, a contrast between these improved conditions and those employed previously can be found in Table 6-e below. There is an evident improvement in both the TOF and cyclohexanol conversion suggesting a much more active and efficient system being achieved under the improved reaction parameters. This both vindicates the study and not only emphasises the potential for the Pt/CuClP material as a catalyst for this reaction but also, by contrast with other catalytic systems (Section 6.2.1), begins to establish its' dominance for the process as a whole.

Conditions	Cyclohexanol Conversion / mol%	Cyclohexanone Selectivity / mol%	TOF / hr^{-1}
Original	72	>99	36
Refined	92	>99	73

Table 6-e: Contrasting the Pt/CuClP catalysts performance under the original and refined reaction conditions. Original: temperature: 200 °C, 0.240 g of catalyst, KA oil flow: 15.0 µLmin^{-1}, WHSV: 1.75 hr^{-1}, air flow: 25 mLmin^{-1}. Refined: temperature: 200 °C, 0.175 g of catalyst, KA oil flow: 17.5 µLmin^{-1}, WHSV: 2.85 hr^{-1}, air flow: 35 mLmin^{-1}.

6.3 Ascertaining the Pt/CuClP Catalysts Deactivation Pathway

6.3.1 Time-on-Stream & Reaction Profile

With the discussions from Section 6.1.1 in mind, the catalytic profile of the Pt/CuClP catalyst, activated at 200 °C and operating under the refined reaction conditions, is presented in Figure 6-g below. The consistency of this system, over a 10 hr period, has already been discussed in Chapter 4 so it is therefore interesting that from Figure 6-g three clear stages of the catalytic life-cycle are present. There is an initial period of continued, consistent high performance (1 – 10 hr), a middle section of slight but progressive performance decline (10 – 20 hr) and a final section of rapid and terminal performance decline (20 – 24 hr). Within this chapter, a study to ascertain the deactivation pathway of these materials will be discussed. The use of PXRD, XAS and TEM analysis will aid in distinguishing between agglomeration and other catalyst deactivation pathways such as coking, sintering or leaching.

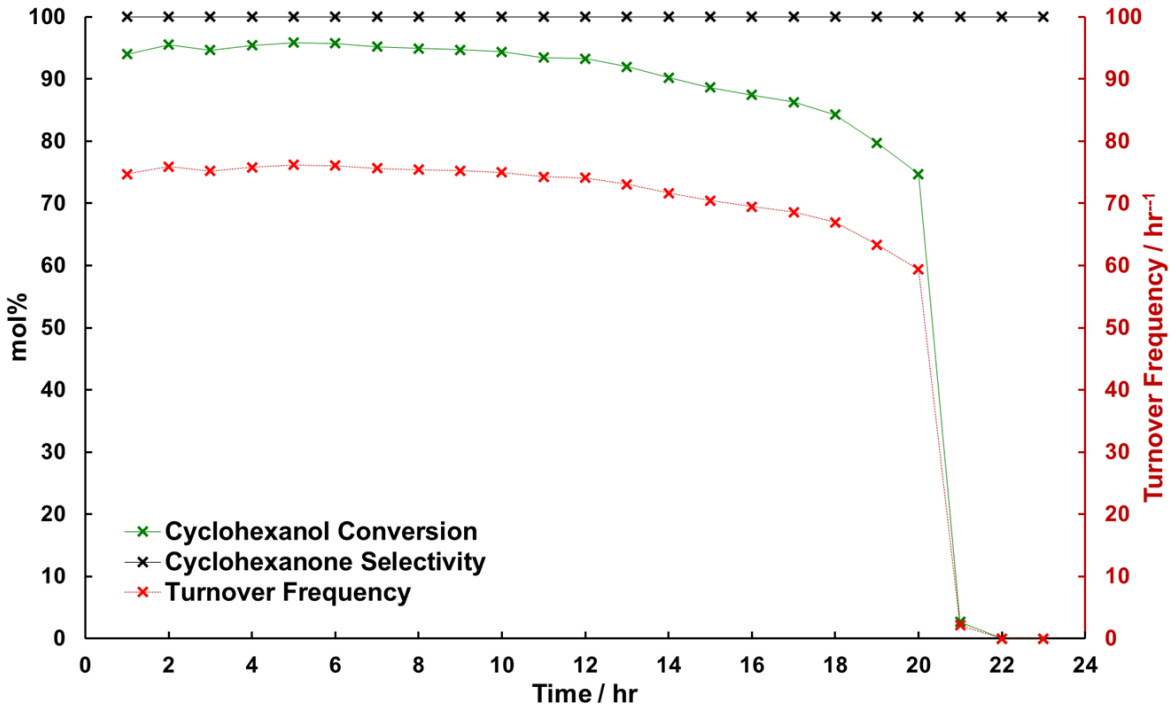

Figure 6-g: Pt/CuClP oxidation of KA oil catalysis plot demonstrating the catalysts deactivation profile over a 24 hr on stream. Temperature: 200 °C, 0.175 g of catalyst, KA oil flow: 15 µLmin^{-1}, WHSV: 2.45 hr^{-1}, air flow: 25 mLmin^{-1}.

In order to accurately monitor the nature of the nanoparticle species throughout the process, a series of reactions were run to obtain four independent samples of varying degrees of deactivation, mirroring the three stages discussed above. From a single batch

of Pt/CuClP, four experiments were run to four separate points of deactivation, or conversion: 95-90%, approx. 85%, 75-70% and 0% as depicted in Figure 6-h. These reactions were then terminated and the catalyst extracted for analysis.

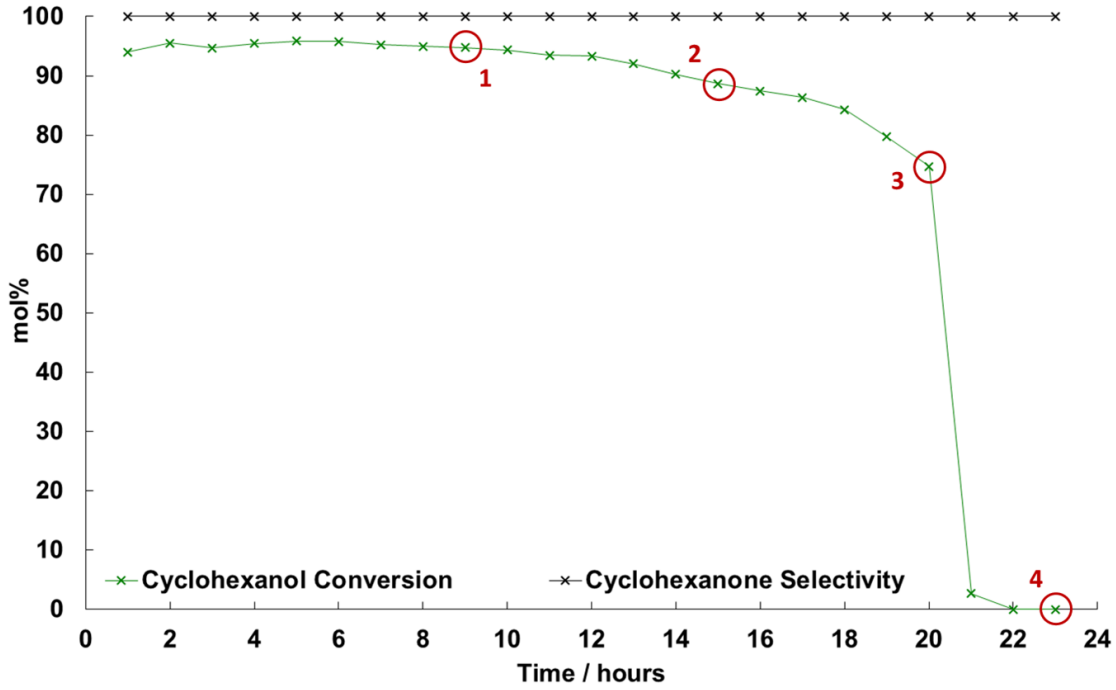

Figure 6-h: Pt/CuClP deactivation profile with the catalyst samples extracted for characterization at particular levels of conversion shown in red. Temperature: 200 °C, 0.175 g of catalyst, KA oil flow: 15 µLmin^{-1}, WHSV: 2.45 hr^{-1}, air flow: 25 mLmin^{-1}.

6.3.2 Structural Characterisation: Powder X-Ray Diffraction

PXRD offers an insight to any structural changes within the CuClP host framework that could lead to catalytic deactivation. Full indexed PXRD patterns of all four samples can be found in Figure 6-i alongside the fresh (activated sample, pre-catalysis) and the as-synthesised materials for comparison. The metallic Pt reflections present at 39.6° and at 46.3° are assigned to the (111) and (200) planes respectively. However, as discussed in Chapter 4, these reflections are unfortunately surrounded by overlapping signals from the host framework rendering the use of the Scherrer equation impossible due to inaccurate FWHM values. Therefore, observation of the peak broadening must be qualitative. However, Figure 6-j demonstrate this broadening from the fresh sample to the deactivated catalyst quite clearly, with the Pt (111) reflection presenting a much narrower and intense signal, representative of larger, more crystalline domains. This therefore implies a significant growth of the nanoparticles (for it to be observable via PXRD) between the fresh and deactivated materials.

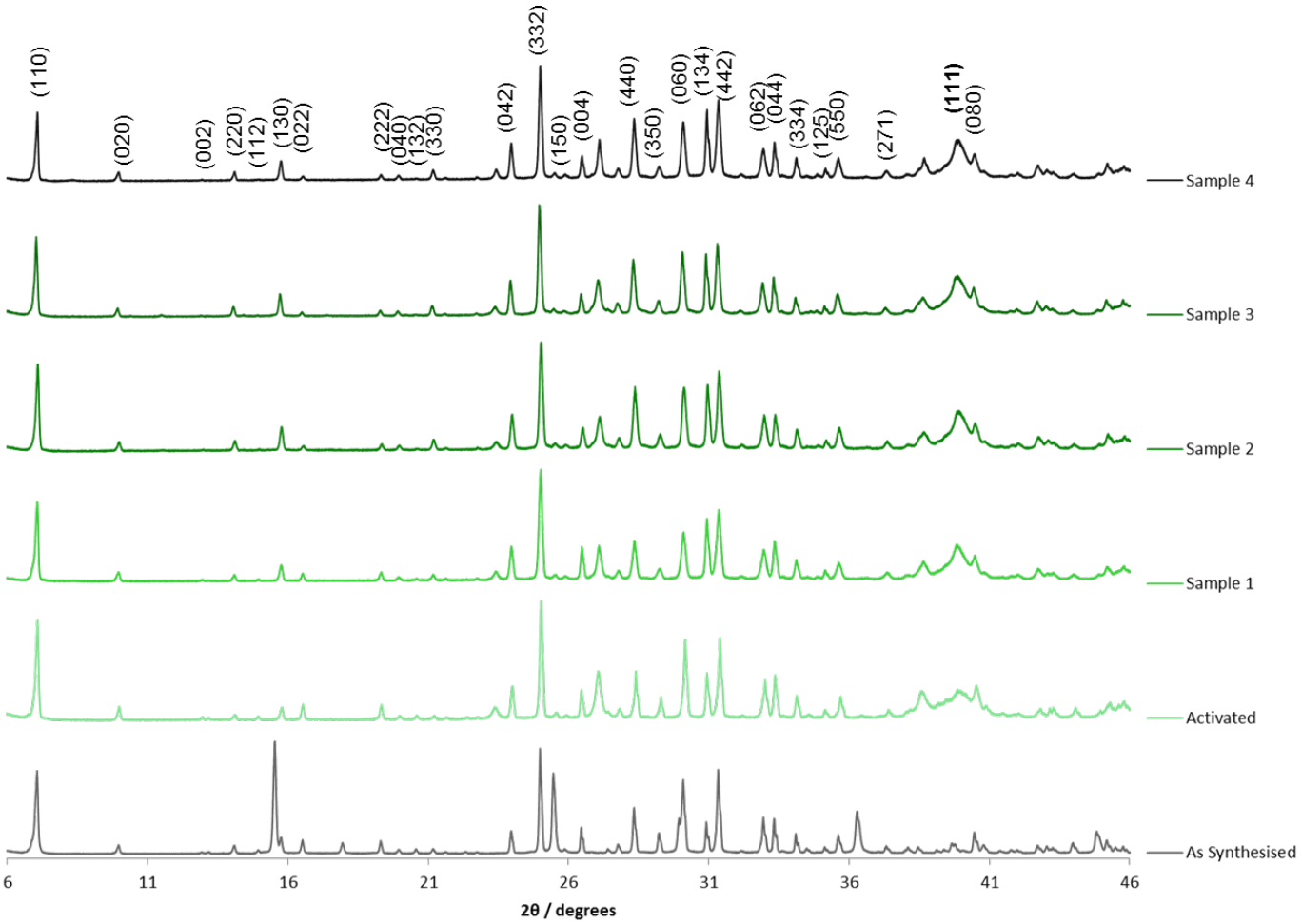

Figure 6-i: Indexed PXRD of the Pt/CuClP materials at different stages of deactivation (green), as per Figure 6-h. As-synthesised sample (grey) for comparison. Metallic Pt (111) signal is highlighted in bold.

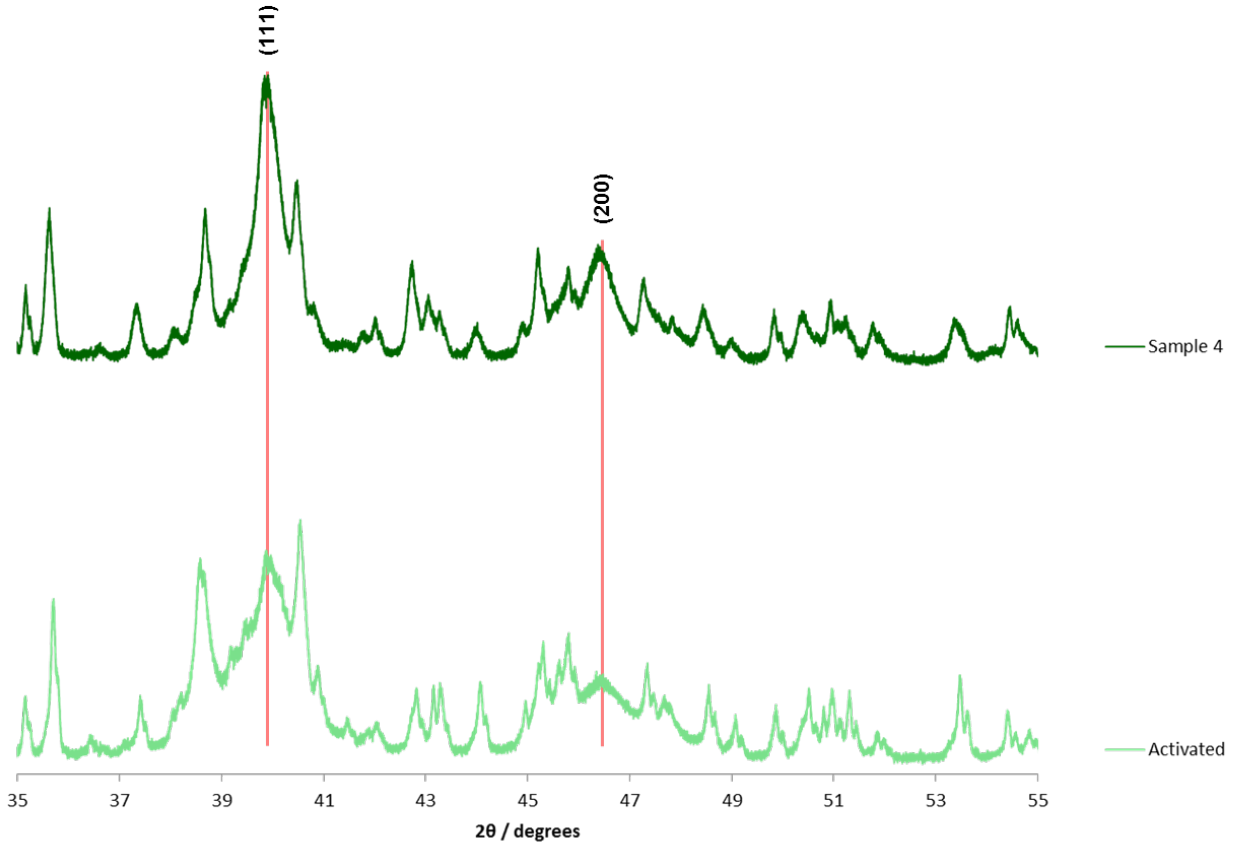

Figure 6-j: PXRD of the Pt/CuClP materials at different stages of deactivation (green), as per Figure 6-h. Comparison of the fresh/activated material and the deactivated sample allow the qualitative comparison of the Pt(111) peak width, highlighted with red.

6.3.3 Structural Characterisation: X-Ray Absorption Spectroscopy

Given the sensitive nature of XAS, it was employed as an ideal candidate to explore nanoparticle growth in light of the PXRD observation but also to probe the presence of any carbonaceous deposits upon the Pt surface. Due to its heightened sensitivity, XAS provides an insight into any small scale (< 2.5 nm) nanoparticle growth as opposed to the larger scale observations made by PXRD. The Pt/CuClP Pt L_{III} edge XANES (Figure 6-k and Figure 6-l) show excellent overlap with the metallic reference for all samples with minimal changes observed across the samples that underwent catalysis. Although a very slight transition towards the metallic reference is evident between the fresh sample and samples 1-4, this is very slight and could be a result of mild thermal reduction of any fractionally remaining $[PtCl_4]^{2-}$ towards a more metallic species or other electronic influences.

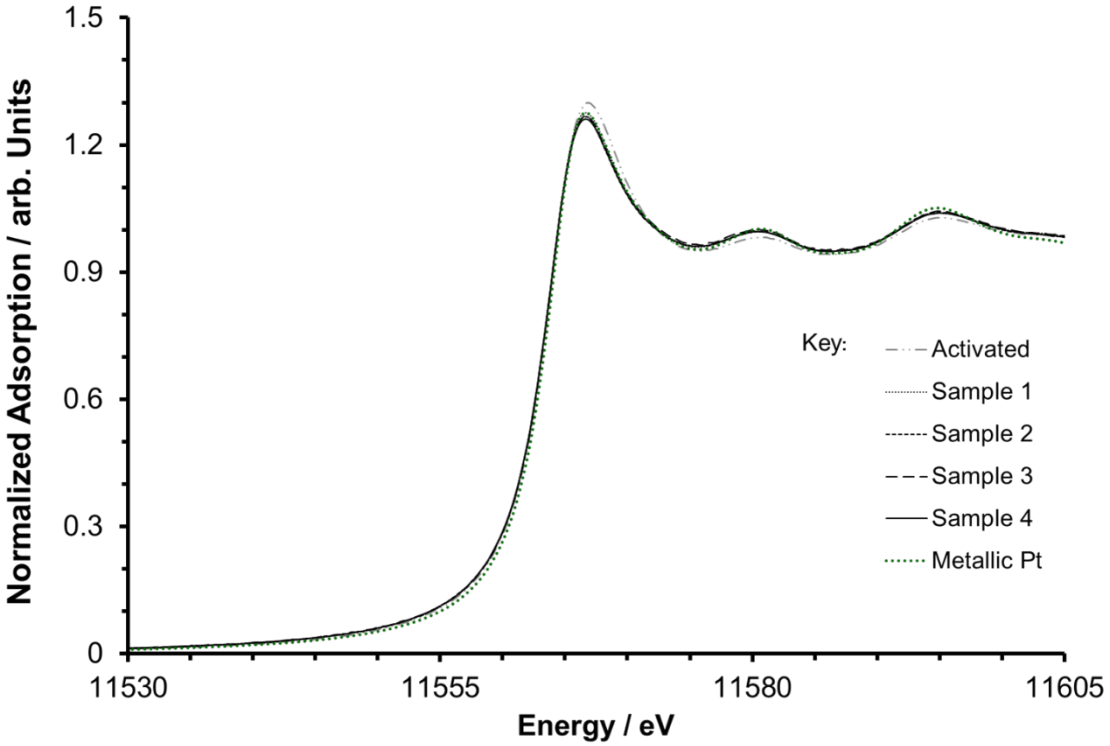

Figure 6-k: Stacked XANES data of the Pt L_{III} edge for the Pt/CuClP materials at different stages of deactivation, as per Figure 6-h with a metallic platinum reference in green.

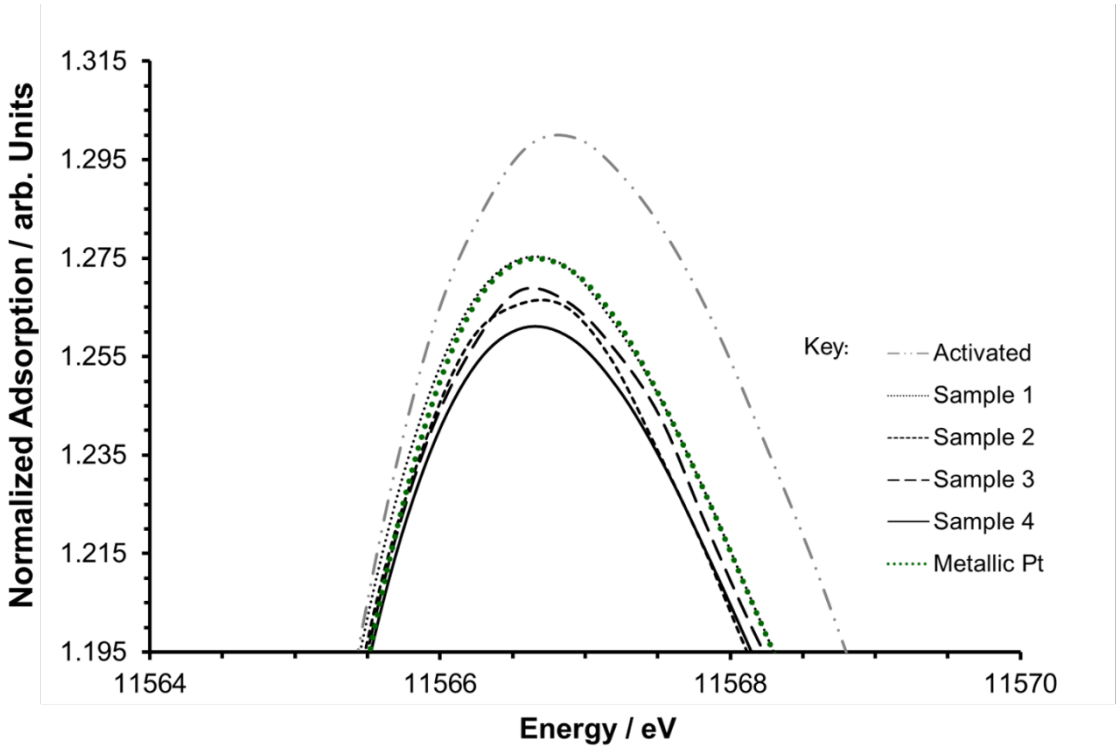

Figure 6-l: Zoomed in view of the stacked XANES data at the absorption maxima of the Pt L_{III} edge for the Pt/CuClP materials at different stages of deactivation, as per Figure 6-h with a metallic platinum reference in green.

The Pt EXAFS displayed in Figure 6-m and the corresponding fitting parameters in Table 6-f suggest minimal changes to the Pt environment upon catalysis. In fact, all data fits for the post catalysis samples are almost analogous with only 0.02 Å changes to the Pt-Pt bond lengths and deviations of approx. 0.5 in the CNs occurring and no overarching trend apparent. Additionally, no evidence in the form of light weight scatterers such as carbon or oxygen (at approx. R < 2.0 Å)[127,361–363] could be found within or fit to the data. Moreover, the depreciation of the Pt L_{III} edge absorption energy, although slight, further contradicts any oxide formation. Deactivation through chemisorption of feedstock impurities or the lay down of carbonaceous materials would lead to a gradual linear decline in activity. This, coupled with the observations outlined above, would suggest that coking, impurity adsorption and/or oxide formation are not the primary causes of the ensuing Pt/CuClPs catalytic deactivation.[12,363]

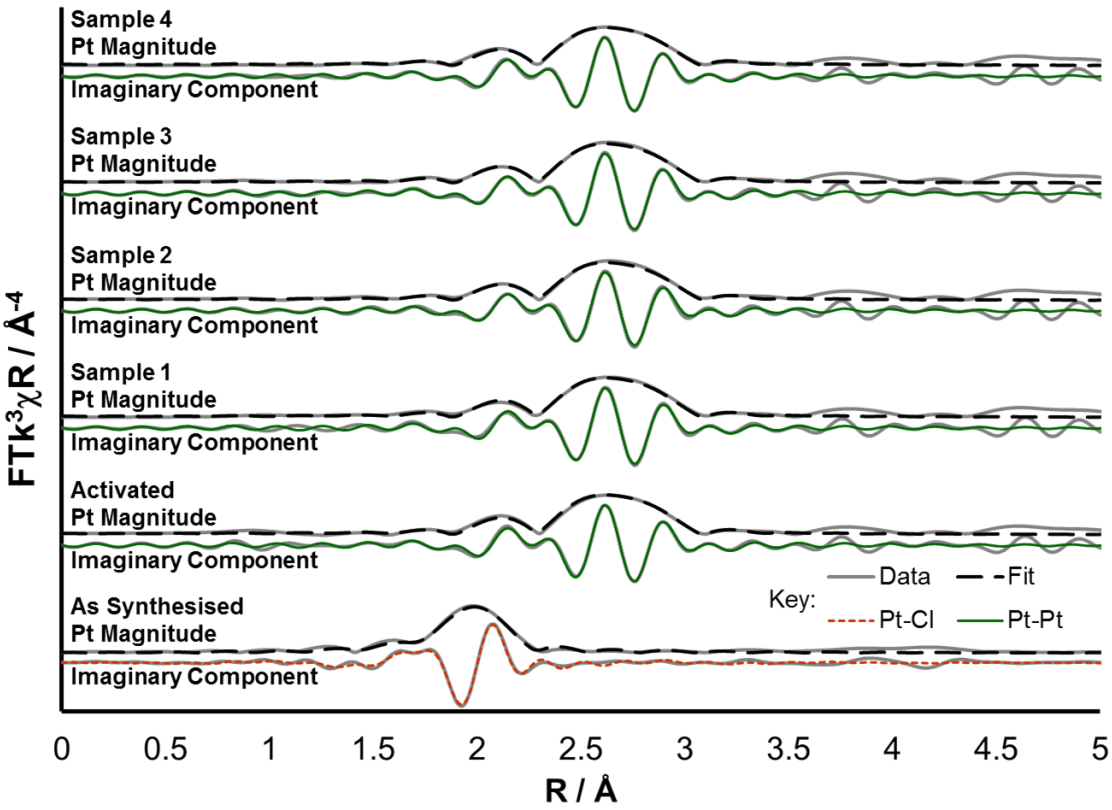

Figure 6-m: The magnitude and imaginary component of the k^3 weighted Fourier transform for the EXAFS data of the Pt/CuClP catalyst at different stages of deactivation, as per Figure 6-h. Associated scattering paths are included for the imaginary component and the fitting parameters are displayed in Table 6-f.

Sample	Abs Sc	N	R / Å	$2\sigma^2$ / Å^2	E_f / eV	R_{factor}
As Synthesised*	Pt – Cl	4.8 (2)	2.321 (5)	0.0022 (3)	9.5 (7)	0.013
Fresh	Pt – Pt	9.0 (4)	2.760 (4)	0.0058 (2)	7.9 (9)	0.013
Sample 1	Pt – Pt	10.3 (4)	2.761 (4)	0.0058 (2)	7 (1)	0.017
Sample 2	Pt – Pt	10.8 (4)	2.785 (4)	0.0058 (2)	8.4 (8)	0.012
Sample 3	Pt – Pt	10.9 (3)	2.785 (3)	0.0057 (1)	8.3 (7)	0.008
Sample 4	Pt – Pt	10.4 (3)	2.758 (3)	0.0057 (1)	7.6 (7)	0.009

Table 6-f: Pt/CuClP EXAFS fitting parameters. Pt sample - $S_0^2 = 0.91$ as deduced by Pt foil standard; Fit range 3<k<14, 1.15<R<3; # of independent points = 12. (Fit range 3.75<k<15.80, 1.15<R<3.10; # of independent points = 13).*

In order to observe changes in CN and relate them back to changes in the nanoparticle diameter as per Table 6-g and Figure 6-n (work by Jentys *et al.*[106]), one would require the

changes to be predominantly in the region of 2.5 nm and below. Nanoparticle agglomeration to particle sizes above this region would be highly difficult to observe (Table 6-g and Figure 6-n) and given the Pt CNs of approx. 10.5 post catalysis, one would suggest that these particles lie outside of the observable region with approx. diameters of > 3.5 nm. Further, given the nature of XAS providing information of the average Pt environment, the presence just a few larger >10 nm particles would significantly skew the data making it increasingly difficult to identify agglomeration via this technique. In fact, with the notable observations of larger particles within the Au and Pd systems, this could indeed be the case. That being said, there is evidence of mild agglomeration upon the material being subjected to the reaction environment as the fresh sample displays a CN of 9.0 as opposed to approx. 10.5 for the post catalysis samples. This corresponds to an initial particle size of approx. 2 nm according to Table 6-g and Figure 6-n, consistent with the ADF AC-STEM discussed in Chapter 4 and the previous works of Hinde *et al.*[235]

Diameter / nm	Number of Atoms
0.8	13
1.4	55
1.8	135
2.0	201
2.2	249
2.6	459
3.1	767
3.3	959
4.2	2171
5.3	4321
6.3	7419

Table 6-g: Size and contained number of atoms of spherical Pt clusters. Adapted from that published by Jentys et al.[106]

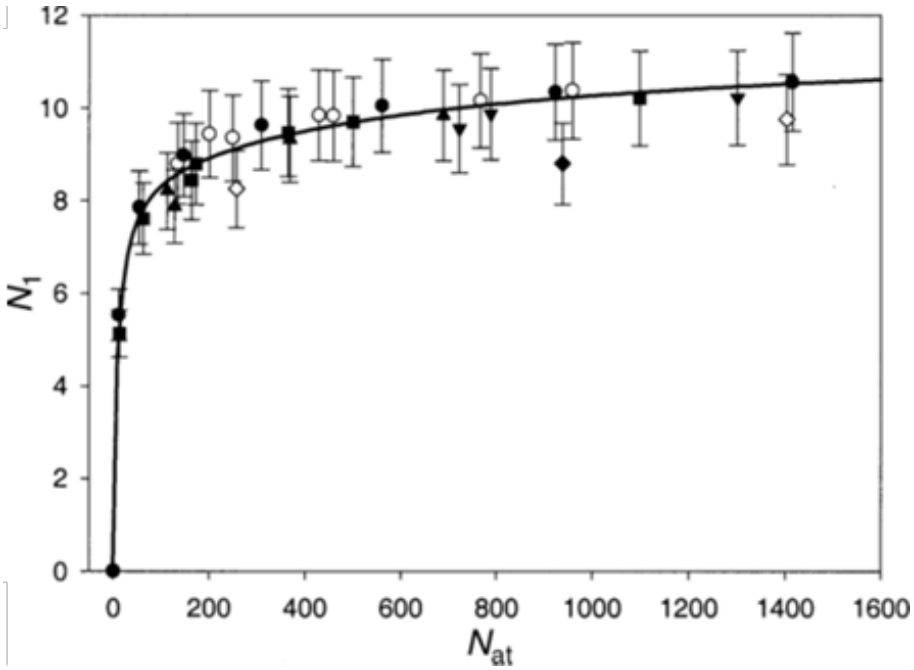

*Figure 6-n: Average coordination of the first coordination shell (N_1) as a function of the number of atoms. The differing data labels represent different particle shapes. Reproduced from A. Jentys, Phys. Chem. Chem. Phys., 1999, **1**, 4059–4063 with permission from the PCCP Owner Societies.*[106]

6.3.4 Structural Characterisation: Transmission Electron Microscopy

In summary, the XAS analysis showed no signs of carbon deposits or oxide formation and indicates that the particle sizes lie at approx. 2 nm, before catalysis and above 3.5 nm after catalysis. Furthermore, this progressive growth of the nanoparticles is observed via PXRD through the significant narrowing of the metallic Pt reflections, evidencing that the changes within these particles are in size regimes above 2 – 5 nm. Therefore, TEM analysis should prove a telling technique to further evidence any agglomeration taking place. Figure 6-o contrasts the TEM images and nanoparticle size distributions of the fresh and deactivated materials. Clearly, from these observations, larger nanoparticles with a much broader size distribution are generated as a result of the material being subjected to the catalytic conditions. Further, the micrographs of sample 4 and its nanoparticle size distribution histogram evidence the production of several significantly (> 15 nm) larger particles. Consistent with the predictions made following the XAS and PXRD analysis, the clear increase in the mean nanoparticle diameter from 2.5 nm to 6.4 nm and accompanied dramatic increase in particle size distribution are clear evidence for the agglomeration of the active Pt nanoparticles. This agglomeration appears to consequently lead to the deactivation of the catalyst. Furthermore, the apparent abundance of nanoparticles present within sample 4 (Figure 6-o) rules out any significant

degree of Pt leaching from the system as this would have been exposed by a drastic decrease in nanoparticle abundance.

Following these observations, reactivation of the catalyst by calcination in air (200 °C) or reduction (5% H_2/N_2, 200 °C) proved ineffective, demonstrating cyclohexanol conversions of < 3%. This further justifies this hypothesis as reactivation should be possible if the catalyst deactivates through coking, impurity adsorption and/or oxide formation as discussed in 6.1.1.[339–341,355]

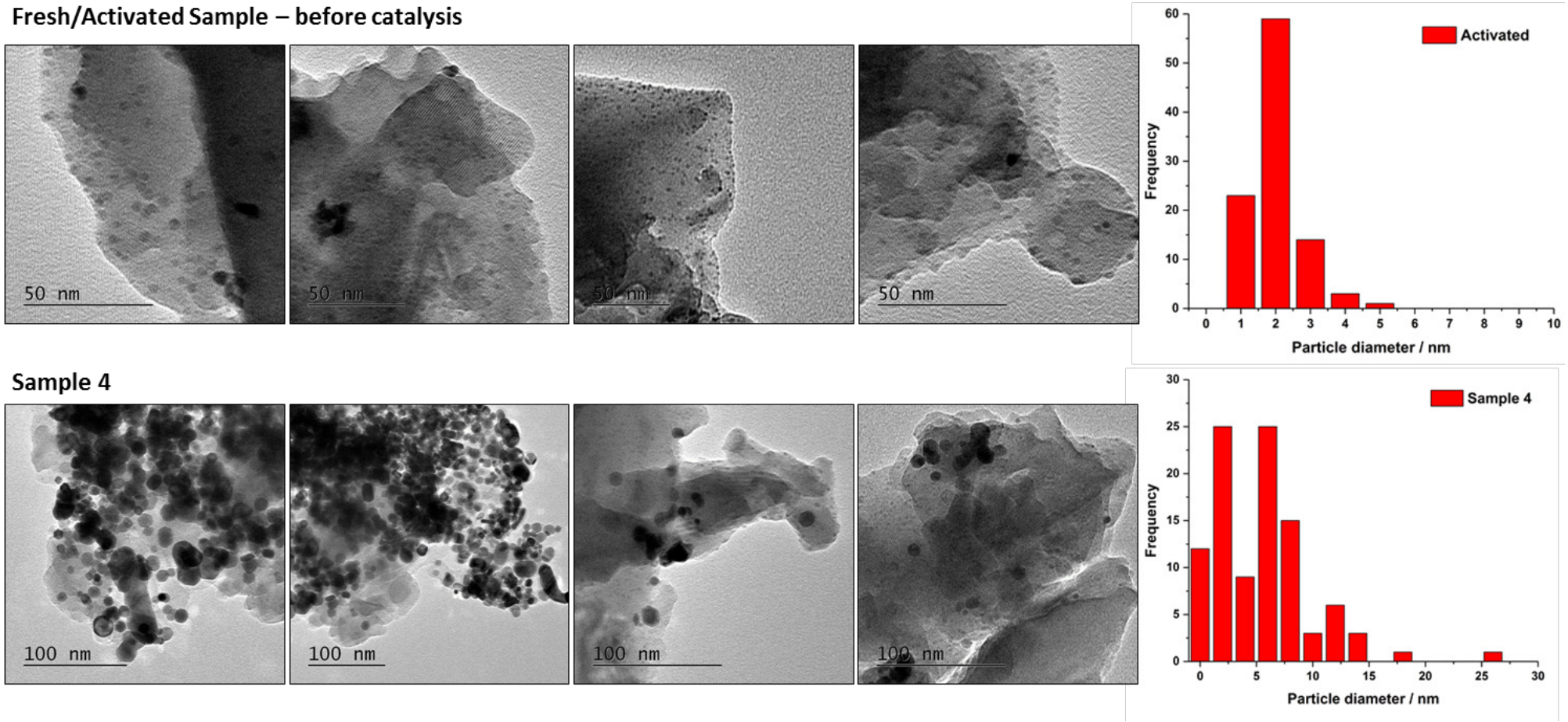

Figure 6-o: BF-TEM images (left) and nanoparticle size distributions (right) of the Pt/CuClP materials at different stages of deactivation, as per Figure 6-h. Above – pre-catalysis. Below – post-deactivation. NOTE: differing scale of the particle size distribution x-axes.

6.4 Conclusions

The generation of a new, improved set of reaction parameters (200 °C, 0.175 g of catalyst (1.0 – 0.5 nm), a KA oil flow of 17.5 μLmin^{-1} (WHSV: 2.85 hr^{-1}) and an air flow of 35 mLmin^{-1}) has significantly enhanced the catalytic performance of the Pt/CuClP materials, evident from Table 6-e. This refinement of the reaction conditions has led to a 20% increase in alcohol conversion, while maintaining the desired > 99% ketone selectivity, with a reduced catalyst bed loading which has led to a two fold increase in the catalysts TOF, demonstrating a vast improvement in the catalysts efficiency.

Not only have improvements been made to the effectiveness of these materials but an enhancement of our understanding has been presented. The four potential deactivation pathways were discussed in section 6.1.1: poisoning of the active sites by substrate impurities, fouling of the active sites by carbonaceous materials produced in the reaction, the loss of reactive surface area through sintering and the physical loss of the active species by leaching. Initial observations of the catalytic profile (Figure 6-g) suggested that deactivation presented after 10 hr on stream and was initially minimal and linear whereas after 20 hr the catastrophic deactivation of the system occurred after which no activity was displayed.

By products, such as the aldol condensation product of cyclohexanol and cyclohexanone, are known poisons for Pt group metal catalysts.[28] However, evidence for such poisons was not found by GC analysis (displaying cyclohexanone selectivities of > 99 %) or XAS. XAS analysis of the Pt/CuClP catalyst at various degrees of deactivation demonstrated that active site saturation via oxide formation or fouling by carbonaceous deposits could not be the case as no Pt-O or Pt-C scattering paths could be incorporated into the EXAFS data fit. Further, the XANES analysis displayed no increase in the average Pt oxidation state, something that would be evident if platinum oxide species were present. Deactivation through poisoning of a catalyst's surface by substrate impurities would also appear unlikely due to the non-linear activity profile depicted in Figure 6-g. One would expect deactivation via the progressive introduction of poisonous species to produce a linearly decreasing catalytic profile, due to their progressive and linear introduction to the system, proportionally to the substrate stream. However, the catalytic profile in this case demonstrated an abrupt and catastrophic drop in activity upon deactivation, something which is characteristic of nanoparticle sintering.[355] This occurs once the particle diameters raise to a point whereby they become inactive, causing the abrupt deactivation. This was, in fact, demonstrated to be the case by a combination of PXRD and TEM. These techniques conclusively established that these materials deactivate through the

agglomeration of the < 3 nm nanoparticles to > 6 nm, rendering them irreversibly inactive. This irreversible nature of the deactivation is another feature frequently attributed to agglomeration as opposed to some poisoning and fouling pathways which can be readily regenerated, as discussed in section 6.1.1.[339–341,355]

Chapter 7: Conclusions & Future Work

Throughout these works, the use of an inorganic microporous copper chloropyrophosphate framework to both host and produce well-defined and isolated noble metal nanoparticles of Au, Pt and Pd through an innovative extrusion methodology has been vindicated. The most adept material, Pt/CuClP, demonstrated it's ability to exploit a variety of environmentally sustainable oxidants (TBHP and molecular oxygen) for the selective production of benzaldehyde. Under these conditions, the Pt/CuClP catalysts, activated by calcination, were able to demonstrate comparable activation energies (aerobic oxidation, 72.4 $kJmol^{-1}$, TBHP oxidation: 23.6 $kJmol^{-1}$) to other similar nanoparticle catalysts currently under academic investigation. This was achieved while the M/CuClP systems were in their relative infancy, as further enhancement of the extrusion protocol has now been achieved through utilizing reductive atmospheres of 5% H_2/N_2 within the activation process. These advances yielded the more controlled generation of small and well-defined nanoparticles of Pt, Pd and Au (2-5 nm). Through these means, the host-nanoparticle synergies in play within each system have been illuminated, with each individual M/CuClP catalyst bestowing unique structure-property correlations upon the ensuing catalytic behaviours. These unique characteristics were realised through the exploitation of the industrially relevant KA oil feedstock within a continuous flow system for the selective and catalytic production of a pure cyclohexanone product. Through these investigations, our understanding of each system grew. The structural vulnerability of the Pd/CuClP system eluded to the consequences of an overly aggressive extrusion process - the production of ill-defined Pd species resulting in significant degrees of framework decomposition into other phases such as rubidium phosphate. The catalytic superiority of the Pt/CuClP was understood through its necessary, complete, production of small (2-3 nm) and well isolated nanoparticle species achieving yields of >90% by adapting a 'closed-loop' system, surpassing other clean (solvent and additive free) oxidation processes within the field. The propensity for the Au/CuClP system to produce a variety of active species has been evidenced. These species range from isolated, monometallic Au nanoparticles, to the catalytically significant bimetallic AuCu species and are a unique consequence of the inherent nanoparticle-host synergies available to this material.

Not only have the distinctive natures of each individual extrusion process been investigated, but through these endeavours the catalytic substrate diversity has been demonstrated through the consistent use of notably green oxidants: TBHP and molecular oxygen. Through the use of such oxygen containing compounds, the selective oxidations of primary (benzyl) and secondary (cyclohexanol) alcohols as well as lactams such as δ-

valerolactam have been achieved in a more sustainable manor. Although these developments of the M/CuCIP systems have facilitated our understanding of their characteristics and their growth in standing within the catalytic community by demonstrating their catalytic potential, the propensity for nanoparticle sintering within these systems, specifically the prospective Pt/CuCIP system (2.5 nm to 6.4 nm after 24 hr on stream) has now been recognised. This stands as the next challenge facing the development of these materials. However, with the plethora of variables available to tackle this barrier such as metal loading, nanoparticle composition, better control over nanoparticle size, shape and distribution, developments in the nanoparticle-support interactions or influences of elemental changes to the host CuCIP framework, their extended application would seem promising. These factors could prove significant in the progression of these materials toward a more established catalytic standing within the current oxidation processes, not to mention the potential of these systems within those catalytic applications that are yet to be investigated.

Notable contributions to the works within Chapter 7:

- Andrea Jouve for his assistance and efforts working on the project as a visiting ERASMUS student from the University of Torino, Italy.
- Dr Gillian Collins for acquisition and processing of the TEM images presented within this chapter.
- Dr Martin J. Taylor and Dr Georgios Kyriakos for their collection and processing of the catalytic acetalisation of furfural data presented within this chapter.

7.1 Probing the Impact of the Pt Content within Pt/CuClP Systems

The relationship between the metal loading and (closely related) surface dispersion, towards the tendency of a supported nanoparticle system to undergo sintering has been established in Section 6.1.1. Therefore, one could expect that by tailoring the metal loading to below the values currently employed 7 wt. %, this could be a means towards improving the on-stream stability of these materials. Further, to improve catalyst stability, one could envisage that through manipulating the metal loading in the correct way the resulting Pt/CuClP system could impart new levels of catalytic efficiency. These would lead to increased TOFs, more in line with the 1 wt. % Pt catalysts discussed in Section 6.2.1, while maintaining its characteristically high levels of ketone selectivity.

A range of these materials have already been synthesised and eluded to in Section 4.2.3. Figure 4-r demonstrated that through a range of Pt loadings (1 – 7 wt. %) the Pt/CuClP system maintains its structural integrity pre-activation, while also suggesting that the Pt loading can be observed through the peak intensities of the Pt containing crystallographic planes. Furthermore, Figure 7-a demonstrates that the structural integrity is maintained post activation across a similar range of metal loadings. Also, the corresponding Pt containing crystallographic planes are removed upon extrusion, analogous to the observations made for the 7 wt. % system in Chapter 4. Initial catalytic investigations suggest a close relationship between the Pt loading and the ensuing TOFs. Figure 7-b suggests that while the Pt loading relationship with cyclohexanol conversion may be linear, the TOF increases dramatically below 5 wt. %. It is noteworthy that the relationship between conversion and metal loading appears to be linear. This feature allows us to predict the TOF for other metal loadings, see Figure 7-c. This predicts a TOF profile increasing rapidly at lower metal loading, as expected, provided the linear relationship in cyclohexanol conversion is followed. That being said, the 1 wt. % Pt/CuClP material displays minimal catalytic activity which demonstrates the need for moderate Pt loadings in order to achieve meaningful levels of nanoparticle extrusion and thus, substantial catalytic performances.

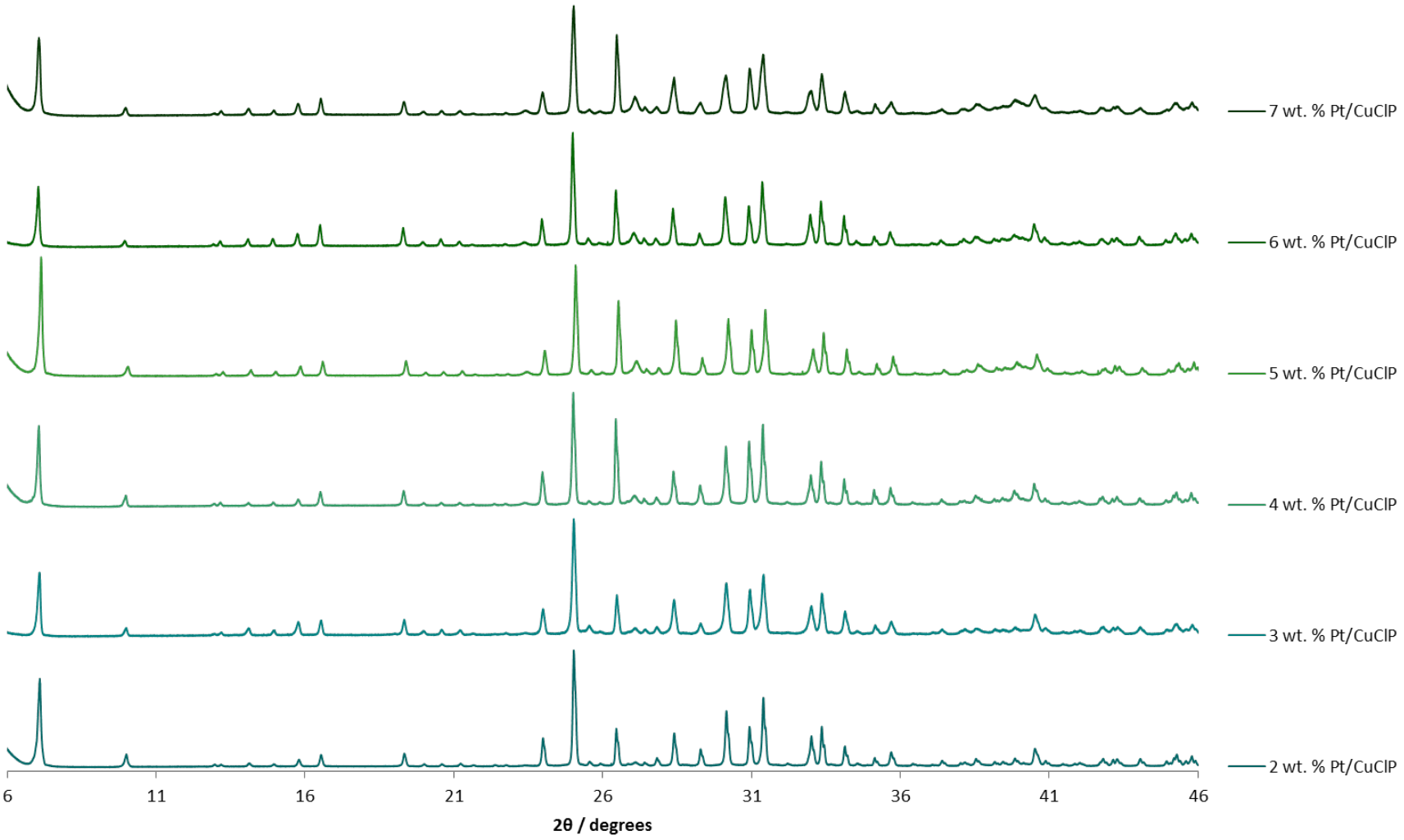

Figure 7-a: PXRD of the Pt/CuClP materials with different Pt loadings post-activation at 200 °C under reduction conditions.

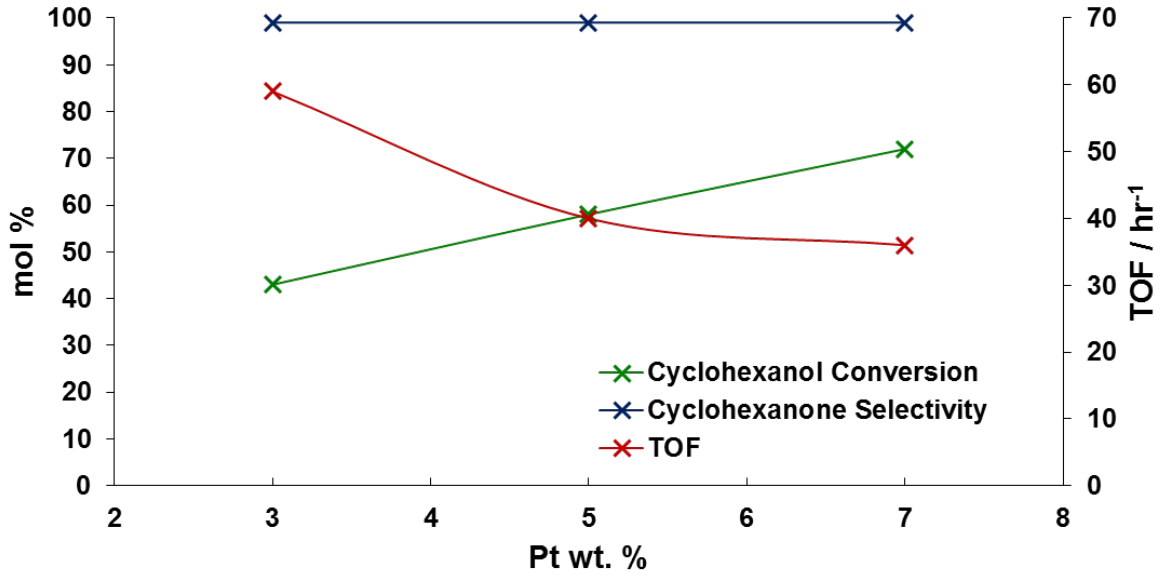

Figure 7-b: Comparison of Pt metal loading within the Pt/CuClP catalysts. Catalyst: 0.24g, air flow: 25 mLmin^{-1}, KA flow: 15 µLmin^{-1} WHSV: 2.80-2.90 hr^{-1}, temperature: 200 °C.

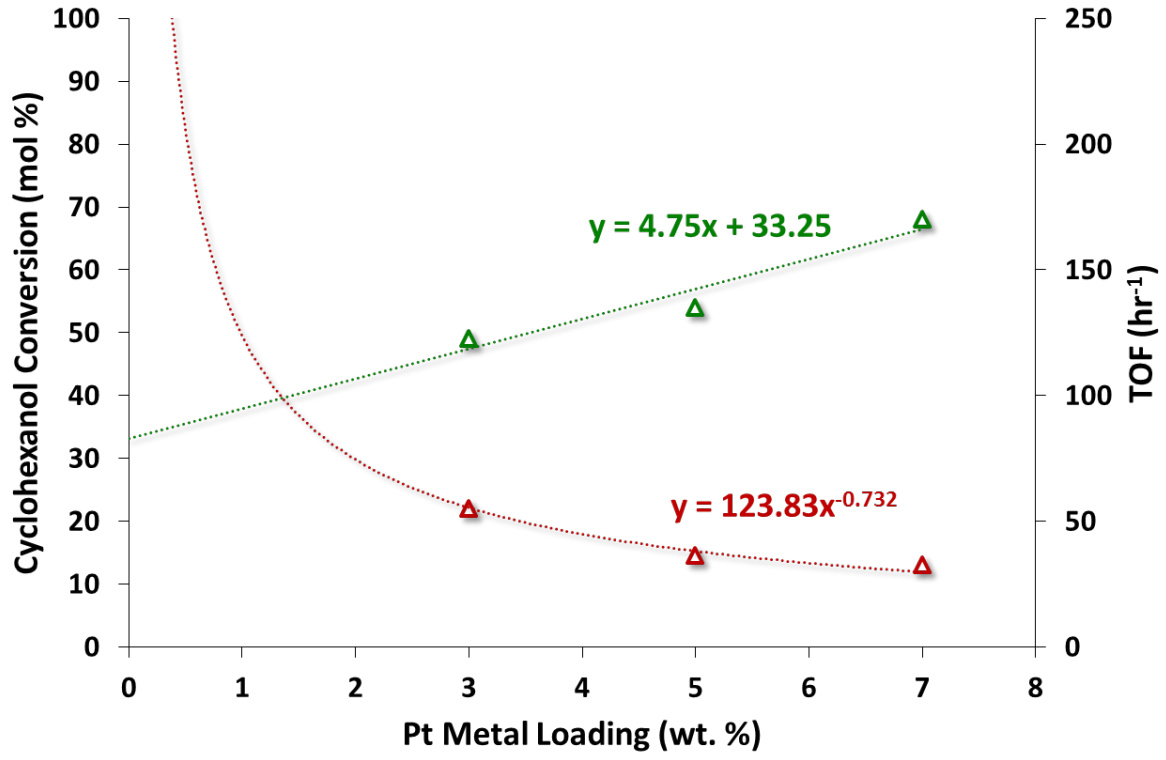

Figure 7-c: Predicted relationship between the Pt metal loading and the resulting TOF (red) and cyclohexanol conversion (green).

Following these preliminary investigations, efforts should be made to contrast the life-time of these catalysts with lower Pt loadings to establish a relationship (if any) between the metal loading and on-stream catalysts lifetime. Further, nanoparticle size distributions are required not just pre- and post-catalysis, but throughout the catalyst lifecycle to establish

meaningful structure-property correlations that relate to the deactivation of these materials and whether these are consistent across the range of Pt loadings proposed. At what specific size does the catalytic activity cease? Do the nanoparticle size distributions increase after deactivation? Thus, is the catalytic process responsible for the nanoparticle agglomeration or is it the reaction environment? XPS analysis could also elude to any changes in the electronic environment of the Pt centres throughout the deactivation process, potentially eluding to a more in-depth explanation of the dramatic catalytic drop-off observed for these materials.

7.2 Improving the Control over Nanoparticle Morphology via Extrusion

As discussed in Chapter 1, the controlled production of a known nanoparticle morphology is intrinsic to facilitating a thorough understanding the catalysts' mode of action. Through this understanding, one would facilitate a means towards refining and improving the catalytic output of said species. Given the nature of the extrusion process, there is sufficient, unexplored potential to improve the levels of control over the growth rate of the Pt nanoparticles within these systems.

It is known that for nanoparticle formation, the nucleation stage is generally rapid, requiring high reaction rates in order to proceed.[48] That being said, these conditions are not ideal for the controlled growth of metallic nanoparticle species, as they favour anisotropic growth rates which are detrimental towards controlling the resulting morphology. Therefore, one can envisage that slower growth rates could lead to heightened levels of morphological control. Thus, given that sufficient control over the rate of growth could be achieved, one can foresee the controlled production of different nanoparticle morphologies. With very slow controlled growth rates, cubic or octahedral morphologies could be produced displaying the Pt (100) or (111) planes respectively. With intermediate growth rates, spherical particles could be produced displaying both the Pt (100) and (111) planes. With rapid accelerated growth rates more irregular morphologies could be generated. It's logical to assume that such contrasting morphologies would demonstrate catalytic differences which could enhance the systems potential and would better our understanding of the Pt/CuClP materials and the extrusion process.

One way in which to probe such a theory, could be to monitor the extrusion process, under analogous and later different conditions, via thermogravimetric analysis with a live GC-MS analysis of the gases produced. Through this real time analysis, one could probe a range of H_2/N_2 ratios, flow rates, heating rates etc. to attempt to control the extrusion process more precisely and in turn potentially offer greater levels of control over the nanoparticle morphology and resulting catalytic profiles. Through these investigations not only would it become apparent at precisely what temperature does the extrusion process occur and how rapidly, but one could accurately monitor the extent of the extrusion if one can precisely observe the chloride release from the system. This has the potential to offer the removal of unnecessary prolonged thermal treatments which are likely detrimental to the resulting nanoparticle size and potentially morphology.

With developments in the nanoparticle extrusion process, the desire to observe the ensuing impacts via different means becomes increasingly apparent. The reliance upon

PXRD, XPS, XAS and TEM within these works is evident. While each technique affords unique insights into the nature of the M/CuClP materials and the progression of the extrusion process, new investigative means should be explored in order to widen our understanding of the multitude of interactions in play, within this complex system. For example, the use of DRUV-vis to monitor the extrusion process (akin to PXRD but from a complementary perspective) could be possible. Through tracking the copper environments and their related charge-transfer interactions with the surrounding oxygen and chloride atoms as well as the similar charge-transfer transition that should exist between the platinum and chloride atoms, meaningful structural insights into the mechanism of the extrusion process could be made.[364,365]

7.3 Bimetallic Nanoparticle Catalysts upon Copper Chloropyrophosphate Materials

The design strategy outlined in Chapters 4 and 5 now offers adequate scope for the creation of multi-metallic (e.g. Au–Pt) and multifunctional heterogeneous catalysts in our continued quest for the activation of molecular oxygen and renewable feedstocks in sustainable catalytic processes. The justification for multi-metallic nanoparticle systems bestowing catalytic enhancements upon a variety of systems can be found in 5.1.2. Furthermore, the incorporation of a second metal within nanoparticle systems has often led to a labouring of the nanoparticle sintering phenomena.[334,354,355] Therefore, the stage is set for these M/CuClP materials to grow their existing catalytic potential through the introduction of bimetallic nanoparticles and overcome a significant barrier to their wider employment within the catalytic community.

Simply by incorporating both K_2PtCl_4 and $HAuCl_4$ precursors into the synthetic protocol in a 1:1 ratio (3.5:3.5 wt. %), the production of metallic species of both Pt and Au upon the catalysts surface is possible. This is evidenced by the Au and Pt 4*f* binding regions within the XPS spectra presented in Figure 7-d. Figure 7-d shows that the production of both metallic Pt and Au exists across all the activation temperatures employed (200 – 350 °C) with no evidence of remaining Pt^{II} or Au^{III} precursors present within surface regions of the materials. This is expected at reduction temperatures above 200 °C, in concert with Chapter 4. Further to this, the BR-TEM images of the AuPt/CuClP materials activated at 250 °C display an excellent distribution of small (approx. < 5 nm) nanoparticles across the materials surface. In accordance with observations made in Chapter 4, this distribution of nanoparticles appears to dominate around thin periphery regions and less pristine areas of the support surface. This apparently consistent nanoparticle distribution and reproducible nanoparticle morphology of the AuPt/CuClP materials appears unique to the system, activated at 250 °C, within these preliminary investigations. Therefore, this is the active sample carried forward within these investigations to date.

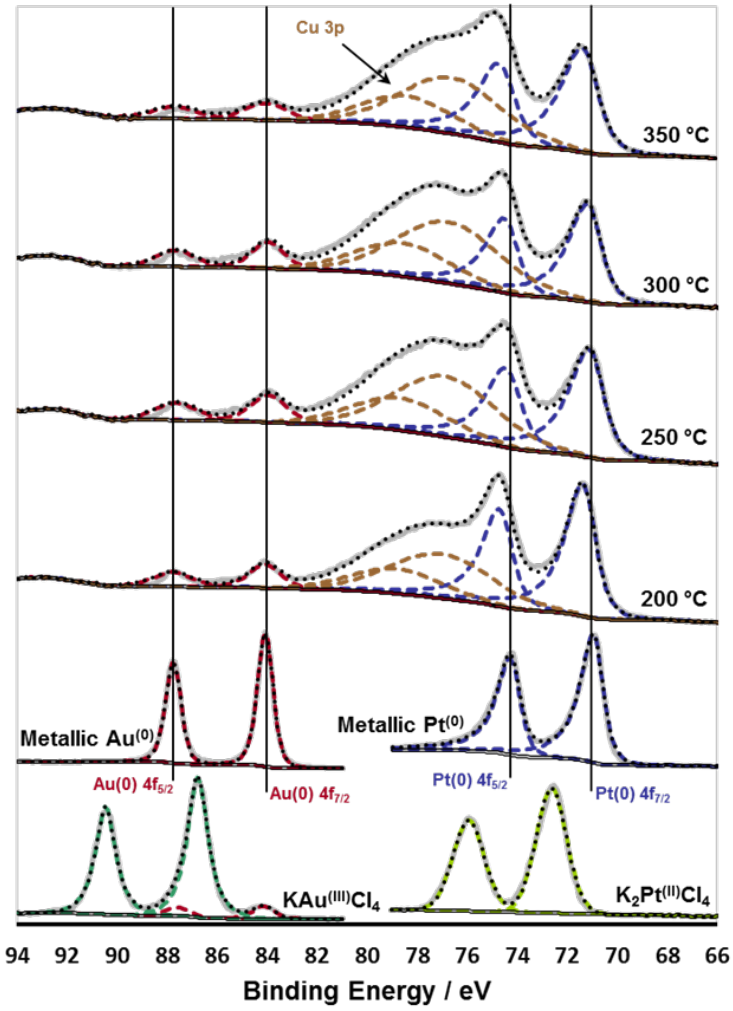

Figure 7-d: Stacked XPS data of the Pt 4f and Au 4f binding regions for the AuPt/CuClP catalysts activated at different temperatures. The data is shown in grey with the data fit in black, Pt^0 transitions are depicted in blue, Au^0 in red and the Cu 2p transitions in mustard.

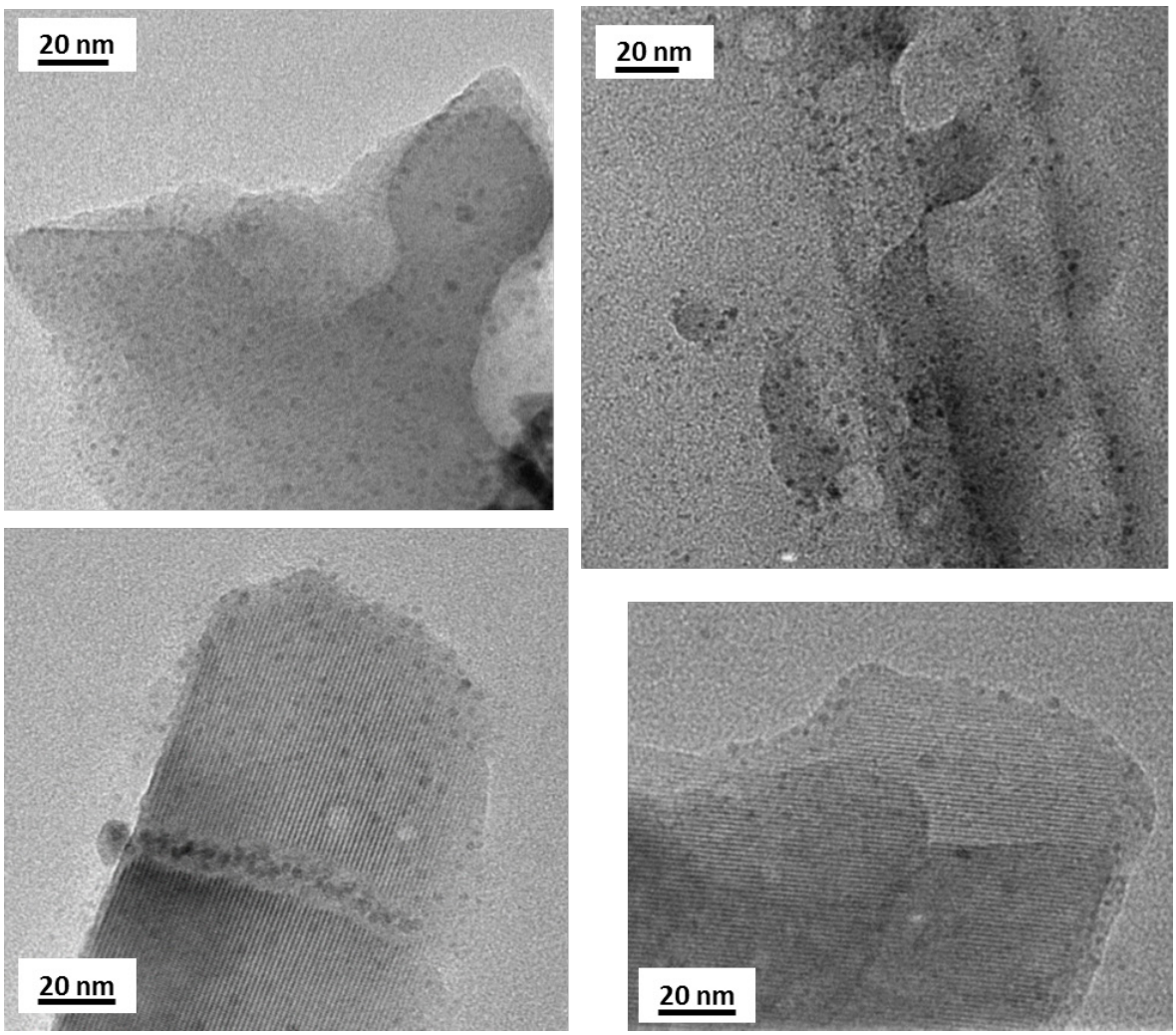

Figure 7-e: BF-TEM images of the AuPt/CuClP materials activated at 250 °C.

EXAFS analysis of these systems has proven to be problematic. Given the proximity of the Au and Pt L_{III} edges with the Au L_{III} absorption edge appearing within the Pt L_{III} EXAFS region, Au XANES and any, Au and Pt EXAFS analysis has not been acquired. Thus, only XANES data of the Pt L_{III} edge and Cu K edge could be attained. Nevertheless the Pt XANES spectra, depicted in Figure 7-f, demonstrates no observable changes to the Pt environment between the monometallic Pt/CuClP and the bimetallic AuPt/CuClP. Further, the Cu K edge spectra (Figure 7-g) suggests that through the incorporation of both Au and Pt within the M/CuClP system, the extrusion of Cu species can be limited with the XANES spectra indicating a predominance of higher oxidation Cu^{II} within the bimetallic system as opposed to its monometallic counterparts. Parallel with these preliminary structural investigations, the catalytic behaviour of the AuPt/CuClP materials activated at 250 °C have been assessed within two processes. Firstly, the aerobic oxidation of KA oil, analogous to that studied throughout these works. Secondly, the acetalisation of furfural (Scheme 7-a). The outcome of these investigations is shown in Table 7-a.

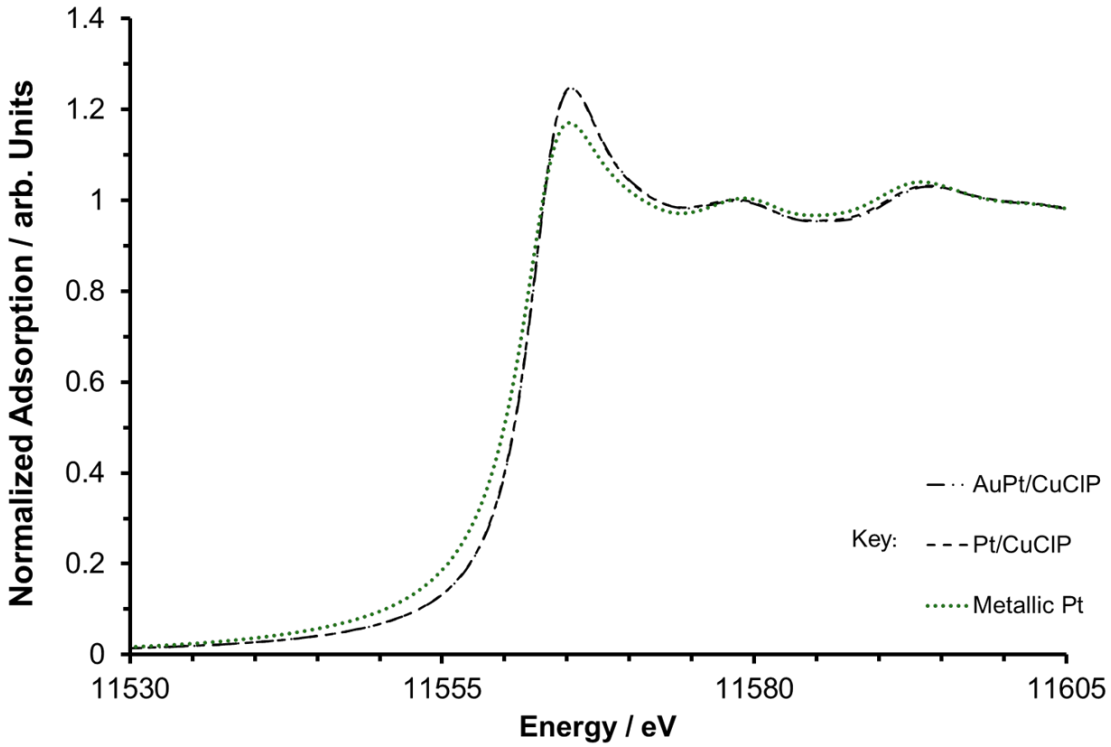

Figure 7-f: Stacked XANES data of the Pt L_{III} edge for the Pt/CuClP and AuPt/CuClP materials activated at 250 °C under reduction conditions with a metallic platinum reference in green.

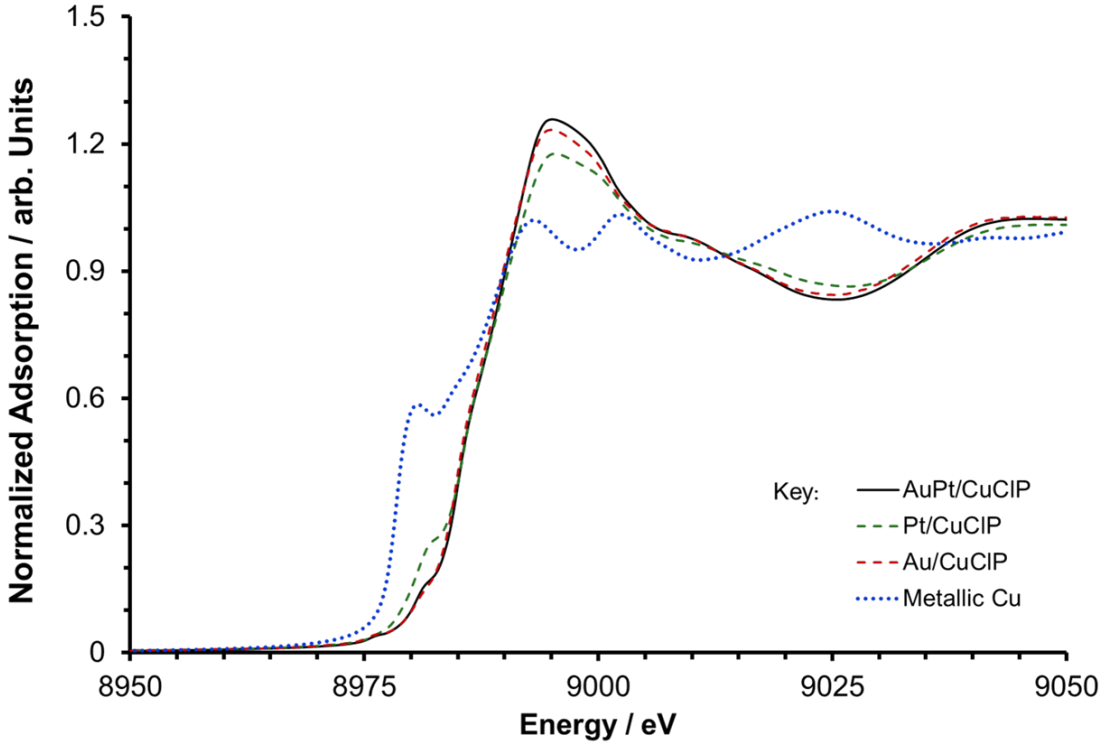

Figure 7-g: Stacked XANES data of the Cu K edge for the Au (red), Pt (green) and AuPt/CuClP (black) materials activated at 250 °C under reduction conditions with a metallic copper reference in blue.

While the justifications for catalytic investigations into the production of pure cyclohexanone from a KA oil feedstock have already been outlined in Section 1.3 and Chapter 4, the acetalisation of furfural might seem an unorthodox step forward. However, there is an ever growing need to diversify the current industrial capability to selectively transform biomass derived oxygenated compounds, such as furfural. However, most of the current research focus surrounds the production of furfural alcohol.[366,367] 2-furaldehyde dimethyl acetal on the other hand, is a highly sought after commodity chemical in itself. Such acetals have various applications in flavourings, perfumes, as fuel additives, pH sensitive linkages for drug delivery as well as other pharmaceutical applications.[368–370] 2-furaldehyde dimethyl acetal is not typically formed catalytically but as a side product of flash pyrolysis and due to its thermodynamic instability it will react to form other by-products.[370,371] Thus, establishing a means to produce this elusive compound catalytically would be significant. While acetal formation more generally is typically acid catalysed, herein the formation of 2-furaldehyde dimethyl acetal is achieved through coupling methanol to the biomass derived furfural and thus, an effective method of producing the short chained acetal has been established, as per Scheme 7-a.

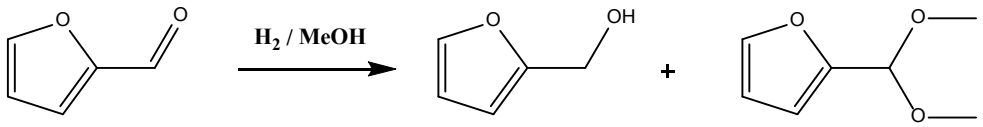

Scheme 7-a: The hydrogenation/acetalisation of furfural.

Catalyst	KA Oil Oxidation		Furfural Acetalisation		
	Conversion / mol%	Ketone Selectivity / mol%	Conversion / mol%	Alcohol Selectivity / mol%	Acetal Selectivity / mol%
CuClP	1	>99	17	0	>99
Pt/CuClP	79	>99	84	11	89
Au/CuClP	1	>99	88	0	>99
AuPt/CuClP	95	>99	93	1	99

Table 7-a: KA oil oxidation conditions: temperature: 210 °C, air flow: 25 mLmin^{-1}, substrate flow: 15 µLmin^{-1}, WHSV: 1.8 hr^{-1}, catalysts reduced at 250 °C. Acetalisation reaction conducted by Dr Martin J. Taylor and Dr Georgios Kyriakos analogously to previously published work.[367]

Table 7-a clearly depicts the catalytic enhancement available to these systems through the incorporation of an additional metal within both processes. The AuPt/CuClP materials demonstrate significantly superior levels of substrate conversion within both applications, leading to improved yields over both the monometallic variants. The remaining question is over the stability of these materials and whether this new multi-metallic system can follow

up the catalytic enhancements on offer with improved catalytic lifetimes over the monometallic Pt/CuClP system?

With preliminary structural investigations evidencing the extrusion of both metallic Au and Pt species, the precise nanoparticle morphology and composition has remained elusive. Thus, it is imperative for these new, multi-metallic systems that an understanding of the precise nature of the nanoparticle active site is established. This is required in order to ascertain the necessary structure-property correlations needed to fully understand the observed catalytic enhancements and the ensuing stability characteristics. One such technique, that would shine significant light upon the precise nature of the catalytic active site and nanoparticle environment within these systems, is the use μ-XRF/ptychography computed tomography, akin to XRF-CT (x-ray fluorescence computed tomography) work carried out by Price *et al.*[372] Price and co-workers demonstrated high resolution elemental maps of Mo and Pt nanoparticle species could be generated across a carbon support particle as demonstrated in Figure 7-h and Figure 7-i.

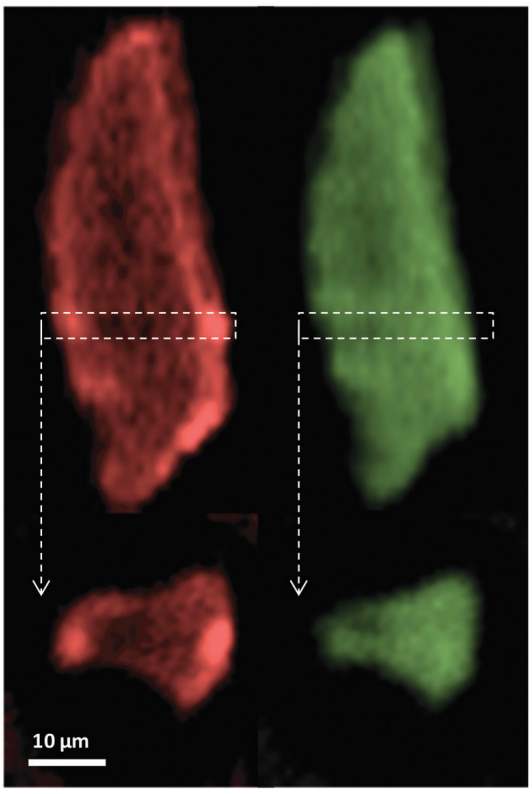

*Figure 7-h: Horizontal and vertical cross-sections from XRF tomography showing Pt (red) and Mo (green) distributions throughout the carbon support. Reproduced from S. W. T. Price, K. Ignatyev, K. Geraki, M. Basham, J. Filik, N. T. Vo, P. T. Witte, A. M. Beale, J. F. W. Mosselmans, Phys. Chem. Chem. Phys., 2015, **17**, 521–529 with permission from the PCCP Owner Societies.*[372]

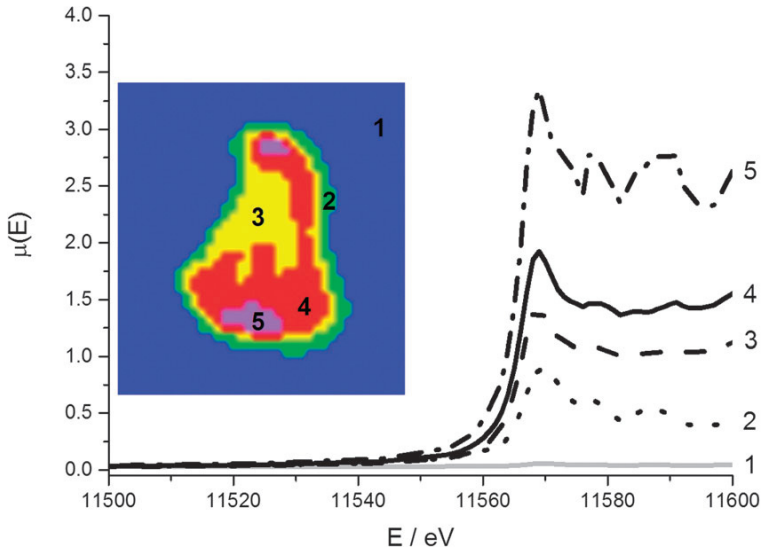

*Figure 7-i: Clustermap of reconstructed Pt XANES tomography data stack (inset) and associated XANES spectra. The clusters and corresponding spectra are matched (1 to 5). Reproduced from S. W. T. Price, K. Ignatyev, K. Geraki, M. Basham, J. Filik, N. T. Vo, P. T. Witte, A. M. Beale, J. F. W. Mosselmans, Phys. Chem. Chem. Phys., 2015, **17**, 521–529 with permission from the PCCP Owner Societies.*[372]

It is clear that activation procedures and interaction of the precursor species with the parent framework, prior to and during the extrusion process, influence the physico-chemical properties of the nanoparticles and the resulting catalytic outcomes. Therefore, use of μ-XRF/ptychography computed tomography as a characterisation tool could allow the 3D mapping of noble metal species throughout the crystalline host matrix. This could be done under different activation conditions, with a view to rationalizing changes in the local structural environment at the atomic level, through the utilisation of XANES mapping to investigate the oxidation states of the Pt and Au across the support particle. As previously stated in Chapters 4 and 5, there is a chemical distribution in the Au species present between the core and surface of the support, but not for the Pt. If this distribution is present in the bimetallic sample, it will reveal the nature of the interaction between the two metals (i.e. if oxidic Au is present alongside metallic Pt, then alloying is unlikely to have occurred). This combined approach will provide spatially resolved structural and elemental information, which is not easily measurable with other characterisation tools. μ-XRF/ptychography measurements on the precursor and fully reduced Pt/CuClP, Au/CuClP and AuPt/CuClP materials would map the distribution of metallic Pt and Au species. This would result in a vast broadening of our knowledge surrounding the structure-property correlations in play and the precise nature of the nanoparticle active sites within these materials.

References

1 J. M. Thomas and W. J. Thomas, *Introduction to the Principles of Heterogeneous Catalysis*, Academic Pres Inc. (London) Ltd, 1967.

2 M. W. Roberts, *Catal. Letters*, 2000, **67**, 1–4.

3 G. A. Somorjai and Y. Li, *Introduction to Surface Chemisrtry and Catalysis*, John Wiley & Sons, Inc., Second Edi., 2010.

4 L. B. Hunt, *Platin. Met. Rev.*, 1979, **23**, 29–31.

5 M. Bowker, *The Basis and Applications of Heterogeneous Catalysis*, Oxford University Press, 1998.

6 R. A. Sheldon and J. K. Kochi, *Metal-Catalyzed Oxidations of Organic Compounds*, Academic Pres Inc. (London) Ltd, 1981.

7 G. C. Bond, C. Louis and D. T. Thompson, *Catalysis by Gold*, Imperial College Press, 2006.

8 F. Zaera, *Chem. Soc. Rev.*, 2013, **42**, 2746–2762.

9 P. Sonström and M. Bäumer, *Phys. Chem. Chem. Phys.*, 2011, **13**, 19270–19284.

10 M. W. Roberts, *Catal. Letters*, 2000, **67**, 67–73.

11 M. W. Roberts, *Catal. Letters*, 2000, **67**, 5–13.

12 J. M. Thomas and W. J. Thomas, *Principles and Practice of Heterogeneous Catalysis*, Wiley-VCH Verlag GmbH & Co., Second., 2015.

13 M. Boudart, *Chem. Rev.*, 1995, **95**, 661–666.

14 R. A. Sheldon, *Catal. Today*, 2015, **247**, 4–13.

15 R. . Sheldon, I. W. C. . Arends and A. Dijksman, *Catal. Today*, 2000, **57**, 157–166.

16 D. J. Cole-Hamilton, *Science.*, 2003, **299**, 1702–1706.

17 A. Corma and H. Garcia, *Top. Catal.*, 2008, **48**, 8–31.

18 D. Astruc, F. Lu and J. R. Aranzaes, *Angew. Chemie - Int. Ed.*, 2005, **44**, 7852–7872.

19 A. T. Bell, *Science.*, 2003, **299**, 1688–1691.

20 R. A. Sheldon, *Chem. Soc. Rev.*, 2012, **41**, 1437–1451.

21 E. G. Rightor and C. L. Tway, *Catal. Today*, 2015, **258**, 226–229.

22 IEA, ICCA and DECHEMA, *Technology Roadmap:Energy and GHG Reductions in the Chemical Industry via Catalytic Processes*, 2013.

23 W. B. Fisher and J. F. Van Peppen, in *Kirk-Othmer Encyclopedia of Chemical Technology*, Catalysis, 2005, pp. 1–42.

24 J.-M. Brégeault, *Dalt. Trans.*, 2003, **17**, 3289–3302.

25 N. Z. Burns, P. S. Baran and R. W. Hoffmann, *Angew. Chemie - Int. Ed.*, 2009, **48**, 2854–2867.

26 A. Gavriilidis, A. Constantinou, K. Hellgardt, K. K. Hii, G. J. Hutchings, G. L. Brett, S. Kuhn and S. P. Marsden, *React. Chem. Eng.*, 2016, **1**, 595–612.

27 G. Franz and R. A. Sheldon, in *Ullman's Encyclopedia of Industrial Chemistry*, Oxidation, 2012, pp. 543–599.

28 T. Mallat and A. Baiker, *Chem. Rev.*, 2004, **104**, 3037–3058.

29 M. J. Kirschner, in *Ullmann's Encyclopedia of Industrial Chemistry*, Oxygen, 2012, pp. 617–635.

30 J. M. Campelo, D. Luna, R. Luque, J. M. Marinas and A. A. Romero, *ChemSusChem*, 2009, **2**, 18–45.

31 A. Roucoux, J. Schulz and H. Patin, *Chem. Rev.*, 2002, **102**, 3757–3778.

32 R. Ferrando, J. Jellinek and R. L. Johnston, *Chem. Rev.*, 2008, **108**, 845–910.

33 A. Chen and P. Holt-Hindle, *Chem. Rev.*, 2010, **110**, 3767–3804.

34 M. A. Neouze, *J. Mater. Sci.*, 2013, **48**, 7321–7349.

35 A. Moores and F. Goettmann, *New J. Chem.*, 2006, **30**, 1121–1132.

36 B. H. Kim, M. J. Hackett, J. Park and T. Hyeon, *Chem. Mater.*, 2014, **26**, 59–71.

37 P. K. Jain, X. Huang, I. H. El-Sayed and M. A. El-Sayed, *Acc. Chem. Res.*, 2008, **41**, 1578–1586.

38 H. Hu, J. H. Xin, H. Hu, X. Wang, D. Miao and Y. Liu, *J. Mater. Chem. A*, 2015, **3**, 11157–11182.

39 G. Hodes, *Adv. Mater.*, 2007, **19**, 639–655.

40 G. J. Hutchings and C. J. Kiely, *Acc. Chem. Res.*, 2013, **46**, 1759–1772.

41 M. Haruta, T. Kobayashi, H. Sano and N. Yamada, *Chem. Lett.*, 1987, **16**, 405–408.

42 B. Nkosi, N. J. Coville and G. J. Hutchings, *J. Chem. Soc. Chem. Commun.*, 1988, 71–72.

43 K. A. Willets and R. P. Van Duyne, *Annu. Rev. Phys. Chem.*, 2007, **58**, 267–297.

44 L. Nutzenadel, C., Zuttel, A., Chartouni, D., Schmid, G., Schlapbach, *Eur. Phys. J. D*, 2000, **8**, 245–250.

45 H. Tsunoyama and N. Ichikuni, *J. Am. Chem. Soc.*, 2009, **131**, 7086–7093.

46 H. Tsunoyama, H. Sakurai, Y. Negishi and T. Tsukuda, *J. Am. Chem. Soc.*, 2005, **127**, 9374–9375.

47 S. Nishimura and K. Ebitani, *ChemCatChem*, 2016, **8**, 2303–2316.

48 B. Roldan Cuenya and F. Behafarid, *Surf. Sci. Rep.*, 2015, **70**, 135–187.

49 S. Mostafa, F. Behafarid, J. R. Croy, L. K. Ono, L. Li, J. C. Yang, A. I. Frenkel and B. R. Cuenya, *J. Am. Chem. Soc.*, 2010, **132**, 15714–15719.

50 A. M. Henning, J. Watt, P. J. Miedziak, S. Cheong, M. Santonastaso, M. Song, Y. Takeda, A. I. Kirkland, S. H. Taylor and R. D. Tilley, *Angew. Chemie - Int. Ed.*, 2013, **52**, 1477–1480.

51 M. Crespo-Quesada, A. Yarulin, M. Jin, Y. Xia and L. Kiwi-Minsker, *J. Am. Chem. Soc.*, 2011, **133**, 12787–12794.

52 V. Komanicky, H. Lddir, K. C. Chang, A. Menzel, G. Karapetrov, D. Hennessy, P. Zapol and H. You, *J. Am. Chem. Soc.*, 2009, **131**, 5732–5733.

53 P. Mäki-Arvela and D. Y. Murzin, *Appl. Catal. A Gen.*, 2013, **451**, 251–281.

54 K. M. Bratlie, H. Lee, K. Komvopoulos, P. Yang and G. A. Somorjai, *Nano Lett.*, 2007, **7**, 3097–3101.

55 L. Jiao and J. R. Regalbuto, *J. Catal.*, 2008, **260**, 342–350.

56 L. Jiao and J. R. Regalbuto, *J. Catal.*, 2008, **260**, 329–341.

57 D. Widmann and R. J. Behm, *Acc. Chem. Res.*, 2014, **47**, 740–749.

58 I. X. Green, W. Tang, M. Neurock and J. T. Yates, *Angew. Chemie - Int. Ed.*, 2011, **50**, 10186–10189.

59 M. Farnesi Camellone and D. Marx, *J. Phys. Chem. C*, 2014, **118**, 20989–21000.

60 N. M. Schweitzer, J. A. Schaidle, O. K. Ezekoye, X. Pan, S. Linic and L. T. Thompson, *J. Am. Chem. Soc.*, 2011, **133**, 2378–2381.

61 Y. Lei, F. Mehmood, S. Lee, J. Greeley, B. Lee, S. Seifert, R. E. Winans, J. W. Elam, R. J. Meyer, P. C. Redfern, D. Teschner, R. Schlogl, M. J. Pellin, L. A. Curtiss and S. Vajda, *Science.*, 2010, **328**, 224–228.

62 L. Cheng, C. Yin, F. Mehmood, B. Liu, J. Greeley, S. Lee, B. Lee, S. Seifert, R. E. Winans, D. Teschner, R. Schlögl, S. Vajda and L. A. Curtiss, *ACS Catal.*, 2014, **4**, 32–39.

63 A. Berko, I. Ulrych and K. C. Prince, *J. Phys. Chem. B*, 1998, **102**, 3379–3386.

64 M. Bowker and E. Fourre, *Appl. Surf. Sci.*, 2008, **254**, 4225–4229.

65 M. Bowker, P. Stone, P. Morrall, R. Smith, R. Bennett, N. Perkins, R. Kvon, C. Pang, E. Fourre and M. Hall, *J. Catal.*, 2005, **234**, 172–181.

66 Z.-H. Qin, M. Lewandowski, Y.-N. Sun, S. Shaikhutdinov and H.-J. Freund, *J. Phys. Condens. Matter*, 2009, **21**, 134019.

67 J. B. Park, S. F. Conner and D. A. Chen, *J. Phys. Chem. C*, 2008, **112**, 5490–5500.

68 S. Bonanni, K. Aït-Mansour, H. Brune and W. Harbich, *ACS Catal.*, 2011, **1**, 385–389.

69 Y. N. Sun, L. Giordano, J. Goniakowski, M. Lewandowski, Z. H. Qin, C. Noguera, S. Shaikhutdinov, G. Pacchioni and H. J. Freund, *Angew. Chemie - Int. Ed.*, 2010, **49**, 4418–4421.

70 Y. Martynova, S. Shaikhutdinov and H. J. Freund, *ChemCatChem*, 2013, **5**, 2162–2166.

71 M. Lewandowski, Y. N. Sun, Z. H. Qin, S. Shaikhutdinov and H. J. Freund, *Appl. Catal. A Gen.*, 2011, **391**, 407–410.

72 M. Lewandowski, I. M. N. Groot, S. Shaikhutdinov and H. J. Freund, *Catal. Today*, 2012, **181**, 52–55.

73 Y. N. Sun, Z. H. Qin, M. Lewandowski, S. Kaya, S. Shaikhutdinov and H. J. Freund,

Catal. Letters, 2008, **126**, 31–35.

74 Y. N. Sun, Z. H. Qin, M. Lewandowski, E. Carrasco, M. Sterrer, S. Shaikhutdinov and H. J. Freund, *J. Catal.*, 2009, **266**, 359–368.

75 Z. Ma and S. Dai, *Nano Res.*, 2011, **4**, 3–32.

76 H. Ji, T. Mizugaki, K. Ebitani and K. Kaneda, *Tetrahedron Lett.*, 2002, **43**, 7179–7183.

77 B. M. Nagaraja, A. H. Padmasri, P. Seetharamulu, K. Hari Prasad Reddy, B. David Raju and K. S. Rama Rao, *J. Mol. Catal. A Chem.*, 2007, **278**, 29–37.

78 D. Ji, W. Zhu, Z. Wang and G. Wang, *Catal. Commun.*, 2007, **8**, 1891–1895.

79 Z. Ma, C. Liang, S. H. Overbury and S. Dai, *J. Catal.*, 2007, **252**, 119–126.

80 H. Yin, Z. Ma, S. H. Overbury and S. Dai, *J. Phys. Chem. C*, 2008, **112**, 8349–8358.

81 G. Decher, *Science.*, 1997, **277**, 1232–1237.

82 K. Ariga, J. P. Hill and Q. Ji, *Phys. Chem. Chem. Phys.*, 2007, **9**, 2319.

83 J. Schmitt, G. Decher, W. J. Dressick, S. L. Brandow, R. E. Geer, R. Shashidhar and J. M. Calvert, *Adv. Mater.*, 1997, **9**, 61–65.

84 S. H. Newland, W. Sinkler, T. Mezza, S. R. Bare, M. Carravetta, I. M. Haies, A. Levy, S. Keenan and R. Raja, *ACS Catal.*, 2015, **5**, 6587–6593.

85 J. M. Thomas, R. Raja and D. W. Lewis, *Angew. Chemie - Int. Ed.*, 2005, **44**, 6456–6482.

86 J. M. Thomas and R. Raja, *Top. Catal.*, 2006, **40**, 3–17.

87 N. Ren, Y. H. Yang, J. Shen, Y. H. Zhang, H. L. Xu, Z. Gao and Y. Tang, *J. Catal.*, 2007, **251**, 182–188.

88 M. Xiao, C. Zhao, H. Chen, B. Yang and J. Wang, *Adv. Funct. Mater.*, 2012, **22**, 4526–4532.

89 A. Dhakshinamoorthy, A. M. Asiri and H. Garcia, *ACS Catal.*, 2017, **7**, 2896–2919.

90 J. Zakzeski, A. Dbczak, P. C. A. Bruijnincx and B. M. Weckhuysen, *Appl. Catal. A Gen.*, 2011, **394**, 79–85.

91 D. Esken, S. Turner, O. I. Lebedev, G. Van Tendeloo and R. A. Fischer, *Chem.*

Mater., 2010, **22**, 6393–6401.

92 T. F. Degnan, *J. Catal.*, 2003, **216**, 32–46.

93 M. Alizadeh, F. Farzaneh and M. Ghandi, *J. Mol. Catal. A Chem.*, 2003, **194**, 283–287.

94 M. H. Peyrovi, V. Mahdavi, M. A. Salehi and R. Mahmoodian, *Catal. Commun.*, 2005, **6**, 476–479.

95 M. Salavati-Niasari, E. Zamani, M. R. Ganjali and P. Norouzi, *J. Mol. Catal. A Chem.*, 2007, **261**, 196–201.

96 V. Mahdavi, M. Mardani and M. Malekhosseini, *Catal. Commun.*, 2008, **9**, 2201–2204.

97 Y. Hong, X. Yan, X. Liao, R. Li, S. Xu, L. Xiao and J. Fan, *Chem. Commun.*, 2014, **50**, 9679–9682.

98 B. Zhan, M. A. White, T. Sham, J. A. Pincock, J. Doucet, K. V. R. Rao, K. N. Robertson, T. S. Cameron, M. Ii and C. Phen, *J. Am. Chem. Soc.*, 2003, **125**, 2195–2199.

99 J. Talebi, R. Halladj and S. Askari, *J. Mater. Sci.*, 2010, **45**, 3318–3324.

100 C. Gonzalez-Arellano, J. M. Campelo, D. J. MacQuarrie, J. M. Marinas, A. A. Romero and R. Luque, *ChemSusChem*, 2008, **1**, 746–750.

101 R. Li, X. Yan, X. Zhu, D. Shou, X. Zhou, Y. Dai and Y. Yang, *Catal. Today*, 2017, **298**, 269–275.

102 B. Karimi, Z. Naderi, M. Khorasani, H. M. Mirzaei and H. Vali, *ChemCatChem*, 2016, **8**, 906–910.

103 Z. Ma, H. Yang, Y. Qin, Y. Hao and G. Li, *J. Mol. Catal. A Chem.*, 2010, **331**, 78–85.

104 T. Mitsudome, A. Noujima, T. Mizugaki, K. Jitsukawa and K. Kaneda, *Adv. Synth. Catal.*, 2009, **351**, 1890–1896.

105 X. Jin, K. Taniguchi, K. Yamaguchi and N. Mizuno, *Chem. Sci.*, 2016, **7**, 5371–5383.

106 A. Jentys, *Phys. Chem. Chem. Phys.*, 1999, **1**, 4059–4063.

107 R. Reske, H. Mistry, F. Behafarid, B. Roldan Cuenya and P. Strasser, *J. Am.*

Chem. Soc., 2014, **136**, 6978–6986.

108 G. Mills, M. S. Gordon and H. Metiu, *J. Chem. Phys.*, 2003, **118**, 4198–4205.

109 M. Mavrikakis, P. Stoltze and J. K. Nørskov, *Catal. Letters*, 2000, **64**, 101–106.

110 J. Kim, E. Samano and B. E. Koel, *J. Phys. Chem. B*, 2006, **110**, 17512–17517.

111 B. . Hvolbæk, T. V. W. . Janssens, B. S. . Clausen, H. . Falsig, C. H. . Christensen and J. K. . Nørskov, *Nano Today*, 2007, **2**, 14–18.

112 N. Lopez, T. V. W. Janssens, B. S. Clausen, Y. Xu, M. Mavrikakis, T. Bligaard and J. K. Nørskov, *J. Catal.*, 2004, **223**, 232–235.

113 H. Mistry, F. Behafarid, E. Zhou, L. K. Ono, L. Zhang and B. Roldan Cuenya, *ACS Catal.*, 2014, **4**, 109–115.

114 H. Song, F. Kim, S. Connor, G. A. Somorjai and P. Yang, *J. Phys. Chem. B*, 2005, **109**, 188–193.

115 T. S. Ahmadi, Z. L. Wang, A. Henglein and M. A. El-Sayed, *Chem. Mater.*, 1996, **8**, 1161–1163.

116 T. S. Ahmadi, Z. L. Wang, T. C. Green, A. Henglein and M. A. El-Sayed, *Science.*, 1996, **272**, 1924–1925.

117 H. Iddir, V. Komanicky, S. Ogut, H. You and P. Zapol, *J. Phys. Chem. C*, 2007, **111**, 14782–14789.

118 S. Schauermann, N. Nilius, S. Shaikhutdinov and H. J. Freund, *Acc. Chem. Res.*, 2013, **46**, 1673–1681.

119 I. Lee, F. Delbecq, R. Morales, M. A. Albiter and F. Zaera, *Nat. Mater.*, 2009, **8**, 132–138.

120 M. Boudart, *Adv. Catal.*, 1969, **20**, 153–166.

121 S. E. Davis, M. S. Ide and R. J. Davis, *Green Chem.*, 2013, **15**, 17–45.

122 K. M. Bratlie, C. J. Kliewer and G. A. Somorjai, *J. Phys. Chem. B*, 2006, **110**, 17925–17930.

123 C. Tsung, J. N. Kuhn, W. Huang, C. Aliaga, L. I. Hung, G. A. Somorjai and P. Yang, *J. Am. Chem. Soc.*, 2009, **131**, 5816–5822.

124 J. N. Kuhn, W. Huang, C. Tsung, Y. Zhang and G. A. Somorjai, *J. Am. Chem. Soc.*,

2008, **130**, 14026–14027.

125 K. R. McCrea and G. A. Somorjai, *J. Mol. Catal. A Chem.*, 2000, **163**, 43–53.

126 G. Wang, Y. Morikawa, T. Matsumoto and J. Nakamura, *J. Phys. Chem. B*, 2006, **110**, 9–11.

127 L. R. Merte, M. Ahmadi, F. Behafarid, L. K. Ono, E. Lira, J. Matos, L. Li, J. C. Yang and B. R. Cuenya, *ACS Catal.*, 2013, **3**, 1460–1468.

128 E. Lira, L. R. Merte, F. Behafarid, L. K. Ono, L. Zhang and B. Roldan Cuenya, *ACS Catal.*, 2014, **4**, 1875–1884.

129 P. Panagiotopoulou and D. I. Kondarides, *J. Catal.*, 2004, **225**, 327–336.

130 F. H. Ribeiro, A. E. Schach Von Wittenau, C. H. Bartholomew and G. A. Somorjai, *Catal. Rev.*, 1997, **39**, 49–76.

131 G. C. Behera and K. M. Parida, *Appl. Catal. A Gen.*, 2012, **413**–**414**, 245–253.

132 W. B. Fisher and J. F. Van Peppen, in *Kirk-Othmer Encyclopedia of Chemical Technology*, Benzaldehyde, 2005, pp. 590–624.

133 F. Bruhne and E. Wright, in *Ullman's Encyclopedia of Industrial Chemistry*, Benzaldehyde, 2012, pp. 223–233.

134 K. G. Fahlbusch, F. J. Hammerschmidt, J. Panten, W. Pickenhagen, D. Schatkowski, K. Bauer, D. Garbe and H. Surburg, in *Ullman's Encyclopedia of Industrial Chemistry*, Flavours and Fragrances, 2012, pp. 74–192.

135 W. B. Fisher and J. F. Van Peppen, in *Kirk-Othmer Encyclopedia of Chemical Technology*, Vanillin, 2005, pp. 1–14.

136 V. Peneau, Q. He, G. Shaw, S. A. Kondrat, T. E. Davies, P. Miedziak, M. Forde, N. Dimitratos, C. J. Kiely and G. J. Hutchings, *Phys. Chem. Chem. Phys.*, 2013, **15**, 10636–10644.

137 M. Turner, V. B. Golovko, O. P. H. Vaughan, P. Abdulkin, A. Berenguer-Murcia, M. S. Tikhov, B. F. G. Johnson and R. M. Lambert, *Nature*, 2008, **454**, 981–983.

138 J. Pritchard, L. Kesavan, M. Piccinini, Q. He, R. Tiruvalam, N. Dimitratos, J. A. Lopez-Sanchez, A. F. Carley, J. K. Edwards, C. J. Kiely and G. J. Hutchings, *Langmuir*, 2010, **26**, 16568–16577.

139 N. Dimitratos, A. Villa, D. Wang, F. Porta, D. Su and L. Prati, *J. Catal.*, 2006, **244**,

113–121.

140 J. Zhu, J. L. Figueiredo and J. L. Faria, *Catal. Commun.*, 2008, **9**, 2395–2397.

141 V. R. Choudhary and D. K. Dumbre, *Top. Catal.*, 2009, **52**, 1677–1687.

142 A. Abad, A. Corma and H. García, *Chem. - A Eur. J.*, 2008, **14**, 212–222.

143 N. Zheng and G. D. Stucky, *Chem. Commun.*, 2007, **1**, 3862.

144 V. R. Choudhary and D. K. Dumbre, *Catal. Commun.*, 2011, **13**, 82–86.

145 W. Li, A. Wang, X. Liu and T. Zhang, *Appl. Catal. A Gen.*, 2012, **433**–**434**, 146–151.

146 C. Della Pina, E. Falletta and M. Rossi, *J. Catal.*, 2008, **260**, 384–386.

147 D. I. Enache, J. K. Edwards, P. Landon, B. Solsona-Espriu, A. F. Carley, A. A. Herzing, M. Watanabe, C. J. Kiely, D. W. Knight and G. J. Hutchings, *Science.*, 2006, **311**, 362–365.

148 K. Mori, T. Hara, T. Mizugaki, K. Ebitani and K. Kaneda, *J. Am. Chem. Soc.*, 2004, **126**, 10657–10666.

149 Q. He, P. J. Miedziak, L. Kesavan, N. Dimitratos, M. Sankar, J. A. Lopez-Sanchez, M. M. Forde, J. K. Edwards, D. W. Knight, S. H. Taylor, C. J. Kiely and G. J. Hutchings, *Faraday Discuss.*, 2013, **162**, 365.

150 H. Wang, W. Kong, W. Zhu, L. Wang, S. Yang and F. Liu, *Catal. Commun.*, 2014, **50**, 87–91.

151 Y. H. Ng, S. Ikeda, Y. Morita, T. Harada, K. Ikeue and M. Matsumura, *J. Phys. Chem. C*, 2009, **113**, 12799–12805.

152 V. R. Choudhary and D. K. Dumbre, *Catal. Commun.*, 2009, **10**, 1738–1742.

153 J. Ni, W.-J. Yu, L. He, H. Sun, Y. Cao, H.-Y. He and K.-N. Fan, *Green Chem.*, 2009, **11**, 756–759.

154 A. Mehri, H. Kochkar, G. Berhault, D. F. Cómbita Merchán and T. Blasco, *Mater. Chem. Phys.*, 2015, **149**, 59–68.

155 G. Zhan, Y. Hong, F. Lu, A. R. Ibrahim, M. Du, D. Sun, J. Huang, Q. Li and J. Li, *J. Mol. Catal. A Chem.*, 2013, **366**, 215–221.

156 J. C. Béziat, M. Besson and P. Gallezot, *Appl. Catal. A Gen.*, 1996, **135**, 9–13.

157 C. G. Jia, F. Y. Jing, W. D. Hu, M. Y. Huang and Y. Y. Jiang, *J. Mol. Catal.*, 1994, **91**, 139–147.

158 A. Abad, P. Concepción, A. Corma and H. García, *Angew. Chemie - Int. Ed.*, 2005, **44**, 4066–4069.

159 A. L. Tarasov, L. M. Kustov, A. A. Bogolyubov, A. S. Kiselyov and V. V. Semenov, *Appl. Catal. A Gen.*, 2009, **366**, 227–231.

160 A. L. Tarasov, L. M. Kustov, V. I. Isaeva, A. N. Kalenchuk, I. V. Mishin, G. I. Kapustin and V. I. Bogdan, *Kinet. Catal.*, 2011, **52**, 273–276.

161 W. B. Fisher and J. F. Van Peppen, in *Kirk-Othmer Encyclopedia of Chemical Technology*, Hydrocarbon Oxidation, 2005, pp. 1–31.

162 R. Raja, J. M. Thomas and V. Dreyer, *Catal. Letters*, 2006, **110**, 179–183.

163 H. Wu, L. Wang, J. Zhang, Z. Shen and J. Zhao, *Catal. Commun.*, 2011, **12**, 859–865.

164 S. Ordonez, L. Bello, H. Sastre, R. Rosal and F. V. Diez, *Appl. Catal. B Environ.*, 2002, **38**, 139–149.

165 S. A. C. Carabineiro, L. M. D. R. S. Martins, M. Avalos-Borja, J. G. Buijnsters, A. J. L. Pombeiro and J. L. Figueiredo, *Appl. Catal. A Gen.*, 2013, **467**, 279–290.

166 Y. Liu, H. Tsunoyama, T. Akita, S. Xie and T. Tsukuda, *ACS Catal.*, 2011, **1**, 2–6.

167 Z. Sun, G. Li, L. Liu and H. O. Liu, *Catal. Commun.*, 2012, **27**, 200–205.

168 R. Zhao, D. Ji, G. Lv, G. Qian, L. Yan, X. Wang and J. Suo, *Chem. Commun.*, 2004, 904–905.

169 K. Zhu, J. Hu and R. Richards, *Catal. Letters*, 2005, **100**, 195–199.

170 A. Alshammari, A. Koeckritz, V. N. Kalevaru, A. Bagabas and A. Martin, *ChemCatChem*, 2012, **4**, 1330–1336.

171 L. Kesavan, R. Tiruvalam, M. H. A. Rahim, M. I. bin Saiman, D. I. Enache, R. L. Jenkins, N. Dimitratos, J. A. Lopez-Sanchez, S. H. Taylor, D. W. Knight, C. J. Kiely and G. J. Hutchings, *Science.*, 2011, **331**, 195–199.

172 Y. T. Lai, T. C. Chen, Y. K. Lan, B. S. Chen, J. H. You, C. M. Yang, N. C. Lai, J. H. Wu and C. S. Chen, *ACS Catal.*, 2014, **4**, 3824–3836.

173 N. Radic, B. Grbic and A. Terlecki-Baricevic, *Appl. Catal. B Environ.*, 2004, **50**,

153–159.

174 M. I. Binsaiman, G. L. Brett, R. Tiruvalam, M. M. Forde, K. Sharples, A. Thetford, R. L. Jenkins, N. Dimitratos, J. A. Lopez-Sanchez, D. M. Murphy, D. Bethell, D. J. Willock, S. H. Taylor, D. W. Knight, C. J. Kiely and G. J. Hutchings, *Angew. Chemie - Int. Ed.*, 2012, **51**, 5981–5985.

175 W. B. Fisher and J. F. Van Peppen, in *Kirk-Othmer Encyclopedia of Chemical Technology*, Cyclohexanol and Cyclohexanone, 2005, pp. 1–7.

176 M. T. Musser, in *Ullmanns Encyclopedia of Industrial Chemistry*, Cyclohexanol and Cyclohexanone, 2000, pp. 49–60.

177 United States Patent Office, US4918239, 1990.

178 J. M. Thomas and R. Raja, *Proc. Natl. Acad. Sci. U. S. A.*, 2005, **102**, 13732–13736.

179 R. Mokaya and M. Poliakoff, *Nature*, 2005, **437**, 1243–1244.

180 United States Patent Office, US7579506, 2009.

181 United States Patent Office, US3305586, 1967.

182 United States Patent Office, US5395976, 1995.

183 Japanese Patent Office, WO2014/163080, 2014.

184 United States Patent Office, US3974221, 1976.

185 United States Patent Office, US3076810, 1963.

186 United States Patent Office, US2338445, 1944.

187 United States Patent Office, US3998884, 1976.

188 United States Patent Office, US2829166, 1958.

189 L. Wang, Z. Chen, M. Huang, Z. Yang, P. Sun, K. Wang and W. Zhang, *Catal. Letters*, 2016, **146**, 1283–1290.

190 European Patent Office, EP1350783, 2003.

191 United States Patent Office, US2218457, 1940.

192 United States Patent Office, US2970172, 1961.

193 United States Patent Office, US3149166, 1964.

194 E. R. Williams, R. M. Leithall, R. Raja and M. T. Weller, *Chem. Commun.*, 2013, **49**, 249–251.

195 M. T. Weller, *Inorganic Materials Chemistry*, Oxford University Press, 2009.

196 P. Atkins, T. Overton, J. Rourke, M. Weller and F. Armstrong, *Inorganic Chemistry*, Oxford University Press, Fourth., 2006.

197 M. Newville, *Fundamentals of XAFS*, Consortium for Advanced Radiation Sources, 2004.

198 M. Newville, *J. Synchrotron Radiat.*, 2001, **8**, 322–324.

199 B. Ravel and M. Newville, *J. Synchrotron Radiat.*, 2005, **12**, 537–541.

200 R. Brydson, *Aberration-Corrected Analytical Electron Microscopy*, John Wiley & Sons, Inc., 2011.

201 L. Ling and W.-X. Zhang, *RSC Adv.*, 2014, **4**, 33861–33865.

202 HyperSpy software package, *http://hyperspy.org*.

203 ImageJ software package, *https://imagej.nih.gov/ij/*.

204 J. M. Thomas, *Nature*, 1994, **368**, 289–290.

205 J. M. Thomas, R. Raja, G. Sankar and R. G. Bell, *Nature*, 1999, **398**, 227–230.

206 R. Raja, G. Sankar and J. M. Thomas, *J. Am. Chem. Soc.*, 1999, **121**, 11926–11927.

207 R. Raja, J. M. Thomas, M. Greenhill-Hooper and V. Doukova, *Chem. Commun.*, 2007, **19**, 1924–1926.

208 S. Neeraj, M. L. Noy and A. K. Cheetham, *Solid State Sci.*, 2002, **4**, 397–404.

209 a Choudhury, S. Neeraj, S. Natarajan and C. Rao, *Angew. Chemie - Int. Ed.*, 2000, **39**, 3091–3093.

210 A. Oki, M. Zeller, A. Reynolds, X. Qiu and A. D. Hunter, *J. Coord. Chem.*, 2007, **60**, 995–1004.

211 J. Mi, C. Wang, N. Chen, R. Li and Y. Pan, *J. Solid State Chem.*, 2010, **183**, 2763–2769.

212 K. Abu-Shandi, H. Winkler, B. Wu and C. Janiak, *CrystEngComm*, 2003, **5**, 180–189.

213 P. Bonnet, J. M. M. Millet, C. Leclercq and J. C. Vedrine, *J. Catal.*, 1996, **158**, 128–141.

214 J. A. Armstrong, E. R. Williams and M. T. Weller, *J. Am. Chem. Soc.*, 2011, **133**, 8252–8263.

215 Q. Huang, M. Ulutagay, P. A. Michener and S. J. Hwu, *J. Am. Chem. Soc.*, 1999, **121**, 10323–10326.

216 E. R. Williams, S. A. Morris and M. T. Weller, *Dalt. Trans.*, 2012, **41**, 10845–10853.

217 C. S. Hinde, S. Van Aswegen, G. Collins, J. D. Holmes, T. S. A. Hor and R. Raja, *Dalt. Trans.*, 2013, **42**, 12600–12605.

218 C. L. Bracey, P. R. Ellis and G. J. Hutchings, *Chem. Soc. Rev.*, 2009, **38**, 2231–2243.

219 J. Pritchard, M. Piccinini, R. Tiruvalam, Q. He, N. Dimitratos, J. A. Lopez-Sanchez, D. J. Morgan, A. F. Carley, J. K. Edwards, C. J. Kiely and G. J. Hutchings, *Catal. Sci. Technol.*, 2013, **3**, 308–317.

220 E. P. Clifford, P. G. Wenthold, R. Gareyev, W. C. Lineberger, C. H. Depuy, V. M. Bierbaum and G. B. Ellison, *J. Chem. Phys.*, 1998, **109**, 10293–10310.

221 I. V. Delidovich, O. P. Taran, L. G. Matvienko, A. N. Simonov, I. L. Simakova, A. N. Bobrovskaya and V. N. Parmon, *Catal. Letters*, 2010, **140**, 14–21.

222 W. Fang, J. Chen, Q. Zhang, W. Deng and Y. Wang, *Chem. - A Eur. J.*, 2011, **17**, 1247–1256.

223 A. Villa, C. E. Chan-Thaw, G. M. Veith, K. L. More, D. Ferri and L. Prati, *ChemCatChem*, 2011, **3**, 1612–1618.

224 J. Chen, Q. Zhang, Y. Wang and H. Wan, *Adv. Synth. Catal.*, 2008, **350**, 453–464.

225 M. Boronat, A. Corma, F. Illas, J. Radilla, T. Ródenas and M. J. Sabater, *J. Catal.*, 2011, **278**, 50–58.

226 M. Ilyas and M. Sadiq, *Chem. Eng. Technol.*, 2007, **30**, 1391–1397.

227 R. K. Grasselli, *Top. Catal.*, 2001, **15**, 93–101.

228 X. Huang, X. Wang, X. Wang, X. Wang, M. Tan, W. Ding and X. Lu, *J. Catal.*, 2013, **301**, 217–226.

229 W. Hou, N. A. Dehm and R. W. J. Scott, *J. Catal.*, 2008, **253**, 22–27.

230 D. V. Bavykin, A. A. Lapkin, S. T. Kolaczkowski and P. K. Plucinski, *Appl. Catal. A Gen.*, 2005, **288**, 175–184.

231 V. Mahdavi and M. Mardani, *J. Chem. Sci.*, 2012, **124**, 1107–1115.

232 M. P. Chaudhari and S. B. Sawant, *Chem. Eng. J.*, 2005, **106**, 111–118.

233 T. Wang, H. Shou, Y. Kou and H. Liu, *Green Chem.*, 2009, **11**, 562–568.

234 P. Fristrup, L. B. Johansen and C. H. Christensen, *Catal. Letters*, 2008, **120**, 184–190.

235 C. S. Hinde, D. Ansovini, P. P. Wells, G. Collins, S. Van Aswegen, J. D. Holmes, T. S. A. Hor and R. Raja, *ACS Catal.*, 2015, **5**, 3807–3816.

236 Z. Wang, X. Liu, D. W. Rooney and P. Hu, *Surf. Sci.*, 2015, **640**, 181–189.

237 V. Z. Fridman and A. A. Davydov, *J. Catal.*, 2000, **195**, 20–30.

238 V. Z. Fridman, A. A. Davydov and K. Titievsky, *J. Catal.*, 2004, **222**, 545–557.

239 M. Popova, Á. Szegedi, K. Lázár and A. Dimitrova, *Catal. Letters*, 2011, **141**, 1288–1296.

240 A. B. Hungria, R. Raja, R. D. Adams, B. Captain, J. M. Thomas, P. A. Midgley, V. Golovko and B. F. G. Johnson, *Angew. Chemie - Int. Ed.*, 2006, **45**, 4782–4785.

241 S. Hermans, R. Raja, J. M. Thomas, B. F. G. Johnson, G. Sankar and D. Gleeson, *Angew. Chemie - Int. Ed.*, 2001, **40**, 1211–1215.

242 G. Zhao, H. Hu, M. Deng, M. Ling and Y. Lu, *Green Chem.*, 2011, **13**, 55–58.

243 Z. Yang, J. Li, X. Yang, X. Xie and Y. Wu, *J. Mol. Catal. A Chem.*, 2005, **241**, 15–22.

244 D. V Cesar, C. A. Peréz, V. M. M. Salim and M. Schmal, *Appl. Catal. A Gen.*, 1999, **176**, 205–212.

245 N. P. Tangale, P. S. Niphadkar, S. S. Deshpande and P. N. Joshi, *Appl. Catal. A Gen.*, 2013, **467**, 421–429.

246 G. K. Reddy and P. K. Rao, *Catal. Letters*, 1997, **45**, 93–96.

247 G. R. Rao, S. K. Meher, B. G. Mishra and P. H. K. Charan, *Catal. Today*, 2012, **198**, 140–147.

248 F. M. T. Mendes and M. Schmal, *Appl. Catal. A Gen.*, 1997, **163**, 153–164.

249 X. Huang, X. Wang, M. Tan, X. Zou, W. Ding and X. Lu, *Appl. Catal. A Gen.*, 2013, **467**, 407–413.

250 S. Furukawa, A. Tamura, T. Shishido, K. Teramura and T. Tanaka, *Appl. Catal. B Environ.*, 2011, **110**, 216–220.

251 G. Bai, H. Wang, H. Ning, F. He and G. Chen, *React. Kinet. Catal. Lett.*, 2008, **94**, 375–383.

252 A. Romero, A. Santos, D. Escrig and E. Simón, *Appl. Catal. A Gen.*, 2011, **392**, 19–27.

253 B. M. Reddy, K. J. Ratnam and P. Saikia, *J. Mol. Catal. A Chem.*, 2006, **252**, 238–244.

254 V. Siva Kumar, S. Sreevardhan Reddy, A. H. Padmasri, B. David Raju, I. Ajitkumar Reddy and K. S. Rama Rao, *Catal. Commun.*, 2007, **8**, 899–905.

255 A. Valente, Z. Lin, P. Brandao, I. Portugal, M. Anderson and J. Rocha, *J. Catal.*, 2001, **200**, 99–105.

256 C. Li, Y. Wang, X. Guo, Z. Jiang, F. Jiang, W. Zhang, W. Zhang, H. Fu, H. Xu and G. Wu, *J. Phys. Chem. C*, 2014, **118**, 3140–3144.

257 H.-B. Ji, K. Ebitani, T. Mizugaki and K. Kaneda, *Catal. Commun.*, 2002, **3**, 511–517.

258 P. Sarmah, B. K. Das and P. Phukan, *Catal. Commun.*, 2010, **11**, 932–935.

259 S. K. Jana, Y. Kubota and T. Tatsumi, *J. Catal.*, 2008, **255**, 40–47.

260 K. Yamaguchi and N. Mizuno, *New J. Chem.*, 2002, **26**, 972–974.

261 V. Mahdavi and S. Soleimani, *Mater. Res. Bull.*, 2014, **51**, 153–160.

262 D. Santhanaraj, C. Suresh, P. Vijayan, N. Venkatathri and K. Shanthi, *React. Kinet. Mech. Catal.*, 2010, **99**, 439–446.

263 M. L. Parentis, N. A. Bonini and E. E. Gonzo, *React. Kinet. Catal. Lett.*, 2002, **76**, 243–248.

264 K. Li, D. Zhou, J. Deng, X. Lu and Q. Xia, *J. Mol. Catal. A Chem.*, 2014, **387**, 31–37.

265 N. Jappar, Q. Xia and T. Tatsumi, *J. Catal.*, 1998, **180**, 132–141.

266 A. Corma, P. Esteve and A. Martínez, *J. Catal.*, 1996, **161**, 11–19.

267 C. Holst, W. W. Schmahl and H. Fuess, *Zeitschrift fuer Krist.*, 1994, **209**, 322–327.

268 C. J. Powell, A. Jablonski, I. S. Tilinin, S. Tanuma and D. R. Penn, *J. Electron Spectros. Relat. Phenomena*, 1999, **98**–**99**, 1–15.

269 C. J. Powell and A. Jablonski, *Nucl. Instruments Methods Phys. Res. A*, 2009, **601**, 54–65.

270 J. S. Bradley, G. H. Via, L. Bonneviot and E. W. Hill, *Chem. Mater.*, 1996, **8**, 1895–1903.

271 J. T. Miller, A. J. Kropf, Y. Zha, J. R. Regalbuto, L. Delannoy, C. Louis, E. Bus and J. A. van Bokhoven, *J. Catal.*, 2006, **240**, 222–234.

272 S. Ajaikumar, J. Ahlkvist, W. Larsson, A. Shchukarev, A. R. Leino, K. Kordas and J. P. Mikkola, *Appl. Catal. A Gen.*, 2011, **392**, 11–18.

273 L. K. Ono, D. Sudfeld and B. Roldan Cuenya, *Surf. Sci.*, 2006, **600**, 5041–5050.

274 G. S. Pokrovski, B. R. Tagirov, J. Schott, E. F. Bazarkina, J. L. Hazemann and O. Proux, *Chem. Geol.*, 2009, **259**, 17–29.

275 F. Farges, J. A. Sharps and G. E. Brown, *Geochemica Cosmochim. Acta*, 1993, **57**, 1243–1252.

276 A. L. Patterson, *Phys. Rev.*, 1939, **56**, 978–982.

277 F. F. Y. Wang, *Acta Crystallogr. A*, 1970, **26**, 377–379.

278 J. H. Kang, L. D. Menard, R. G. Nuzzo and A. I. Frenkel, *J. Am. Chem. Soc.*, 2006, **128**, 12068–12069.

279 A. I. Frenkel, C. W. Hills and R. G. Nuzzo, *J. Phys. Chem. B*, 2001, **105**, 12689–12703.

280 M. K. Hargreaves, J. G. Pritchard and H. R. Dave, *Chem. Rev.*, 1970, **70**, 439–468.

281 X. Ji, Z. Zhong, S. Xue, S. Meng, W. He, R. Gao, Y. Li and Z. Li, *Chem. Pharm. Bull. (Tokyo).*, 2010, **58**, 1436–1441.

282 K. C. Nicolaou and C. J. N. Mathison, *Angew. Chemie - Int. Ed.*, 2005, **44**, 5992–5997.

283 Y. J. Bian, C. Y. Chen and Z. Z. Huang, *Chem. - A Eur. J.*, 2013, **19**, 1129–1133.

284 M. A. Ali, S. M. A. H. Siddiki, K. Kon, J. Hasegawa and K. Shimizu, *Chem. - A Eur. J.*, 2014, **20**, 14256–14260.

285 C. J. Perry and Z. Parveen, *J. Chem. Soc. Perkin Trans. 2*, 2001, **4**, 512–521.

286 N. B. Mehta, A. P. Phillips, F. Fu, Lui and R. E. Brooks, *J. Org. Chem.*, 1960, **25**, 1012–1015.

287 X. Yan, K. Fang, H. Liu and C. Xi, *Chem. Commun.*, 2013, **49**, 10650–10652.

288 K. M. Driller, H. Klein, R. Jackstell and M. Beller, *Angew. Chemie - Int. Ed.*, 2009, **48**, 6041–6044.

289 J. Zhang, M. Senthilkumar, S. C. Ghosh and S. H. Hong, *Angew. Chemie - Int. Ed.*, 2010, **49**, 6391–6395.

290 A. R. Doumaux and D. J. Trecker, *J. Org. Chem.*, 1970, **35**, 2121–2125.

291 A. R. Doumaux, J. E. McKeon and D. J. Trecker, *J. Am. Chem. Soc.*, 1969, **91**, 3992–3993.

292 S.-I. Murahshi, T. Saito, T. Naota, H. Kumobayashi and S. Akutagawab, *Tetrahedron Lett.*, 1991, **32**, 5991–5994.

293 S. Murahashi, T. Naota, T. Kuwabara, T. Saito, H. Kumobayashi and S. Akutagawalb, *J. Am. Chem. Soc.*, 1990, **112**, 7820–7822.

294 H. Takaya, K. Yoshida, K. Isozaki, H. Terai and S. I. Murahashi, *Angew. Chemie - Int. Ed.*, 2003, **42**, 3302–3304.

295 O. Alekseeva, M. Konstantinova, S. Rasumovskii and H. Timokhina, *Oxid. Commun.*, 2009, **32**, 537–545.

296 O. Alekseeva, M. Konstantinova and S. Rasumovskii, *Heteroat. Chem.*, 2008, **19**, 661–666.

297 A. A. Taherpour and H. R. Mansuri, *Turkish J. Chem.*, 2005, **29**, 317–320.

298 N. S. Kus and C. Kazaz, *Asian J. Chem.*, 2008, **20**, 1226–1230.

299 N. Toshima and T. Yonezawa, *New J. Chem.*, 1998, **22**, 1179–1201.

300 D. Wang and Y. Li, *Adv. Mater.*, 2011, **23**, 1044–1060.

301 R. G. Chaudhuri and S. Paria, *Chem. Rev.*, 2012, **112**, 2373–2433.

302 G. L. Brett, Q. He, C. Hammond, P. J. Miedziak, N. Dimitratos, M. Sankar, A. A.

Herzing, M. Conte, J. A. Lopez-Sanchez, C. J. Kiely, D. W. Knight, S. H. Taylor and G. J. Hutchings, *Angew. Chemie - Int. Ed.*, 2011, **50**, 10136–10139.

303 N. Dimitratos, J. A. Lopez-Sanchez, D. Morgan, A. F. Carley, R. Tiruvalam, C. J. Kiely, D. Bethell and G. J. Hutchings, *Phys. Chem. Chem. Phys.*, 2009, **11**, 5142–5153.

304 X. Liu, A. Wang, T. Zhang, D. S. Su and C. Y. Mou, *Catal. Today*, 2011, **160**, 103–108.

305 S. E. Allen, R. R. Walvoord, R. Padilla-Salinas and M. C. Kozlowski, *Chem. Rev.*, 2013, **113**, 6234–6458.

306 M. Haruta, *Nature*, 2005, **437**, 1098–1099.

307 Y. Zhang, X. Cui, F. Shi and Y. Deng, *Chem. Rev.*, 2012, **112**, 2467–2505.

308 T. Pasini, M. Piccinini, M. Blosi, R. Bonelli, S. Albonetti, N. Dimitratos, J. A. Lopez-Sanchez, M. Sankar, Q. He, C. J. Kiely, G. J. Hutchings and F. Cavani, *Green Chem.*, 2011, **13**, 2091.

309 E. Larios, Z. Molina, A. Maldonado and J. Tanori, *J. Dispers. Sci. Technol.*, 2012, **33**, 719–723.

310 A. Sandoval, C. Louis and R. Zanella, *Appl. Catal. B Environ.*, 2013, **140**–**141**, 363–377.

311 X. Li, S. S. S. Fang, J. Teo, Y. L. Foo, A. Borgna, M. Lin and Z. Zhong, *ACS Catal.*, 2012, **2**, 360–369.

312 J. A. Rodríguez, J. Evans, J. Graciani, J.-B. Park, P. Liu, J. Hrbek and J. F. Sanz, *J. Phys. Chem. C*, 2009, **113**, 7364–7370.

313 J. Yin, S. Shan, L. Yang, D. Mott, O. Malis, V. Petkov, F. Cai, M. Shan Ng, J. Luo, B. H. Chen, M. Engelhard and C. J. Zhong, *Chem. Mater.*, 2012, **24**, 4662–4674.

314 P. Kaminski and M. Ziolek, *Appl. Catal. B Environ.*, 2016, **187**, 328–341.

315 S. Asbrink and A. Waskowska, *J. Phys. Condens. Matter*, 1991, **3**, 8173–8180.

316 L. Delannoy, G. Thrimurthulu, P. S. Reddy, C. Méthivier, J. Nelayah, B. M. Reddy, C. Ricolleau and C. Louis, *Phys. Chem. Chem. Phys.*, 2014, 26514–26527.

317 R. J. Chimentão, F. Medina, J. L. G. Fierro, J. Llorca, J. E. Sueiras, Y. Cesteros and P. Salagre, *J. Mol. Catal. A Chem.*, 2007, **274**, 159–168.

318 N. Vilar-Vidal, M. C. Blanco, M. A. López-Quintela, J. Rivas and C. Serra, *J. Phys. Chem. C*, 2010, **114**, 15924–15930.

319 T. C. Ou, F. W. Chang and L. S. Roselin, *J. Mol. Catal. A Chem.*, 2008, **293**, 8–16.

320 E. K. Gibson, A. M. Beale, C. R. A. Catlow, A. Chutia, D. Gianolio, A. Gould, A. Kroner, K. M. H. Mohammed, M. Perdjon, S. M. Rogers and P. P. Wells, *Chem. Mater.*, 2015, **27**, 3714–3720.

321 P. Dash, T. Bond, C. Fowler, W. Hou, N. Coombs and R. W. J. Scott, *J. Phys. Chem. C*, 2009, **113**, 12719–12730.

322 J. C. Bauer, D. R. Mullins, Y. Oyola, S. H. Overbury and S. Dai, *Catal. Letters*, 2013, **143**, 926–935.

323 J. C. Bauer, D. Mullins, M. Li, Z. Wu, E. A. Payzant, S. H. Overbury and S. Dai, *Phys. Chem. Chem. Phys.*, 2011, **13**, 2571–2581.

324 S. Poulston, P. M. Parlett, P. Stone and M. Bowker, *Surf. Interface Anal.*, 1996, **24**, 811–820.

325 N. Pauly, S. Tougaard and F. Yubero, *Surf. Sci.*, 2014, **620**, 17–22.

326 J. Batista, A. Pintar, D. Mandrino, M. Jenko and V. Martin, *Appl. Catal. A Gen.*, 2001, **206**, 113–124.

327 C. Wu, M. Yin, S. O'Brien and J. T. Koberstein, *Chem. Mater.*, 2006, **18**, 6054–6058.

328 L. Liu, T. Matsushita, P. Concepción, A. Leyva-Pérez and A. Corma, *ACS Catal.*, 2016, **6**, 2211–2221.

329 C. Mondelli, D. Ferri, J. D. Grunwaldt, N. Ravasio and A. Baiker, *Catal. Today*, 2011, **178**, 124–131.

330 S. W. T. Price, J. D. Speed, P. Kannan and A. E. Russell, *J. Am. Chem. Soc.*, 2011, **133**, 19448–19458.

331 T. Magadzu, J. H. Yang, J. D. Henao, M. C. Kung, H. H. Kung and M. S. Scurrell, *J. Phys. Chem. C*, 2017, **121**, 8812–8823.

332 L. Wang, J. R. Gaudet, W. Li and D. Weng, *J. Catal.*, 2013, **306**, 68–77.

333 D.-W. Shin, C. Dong, M. Mattesini, A. Augustsson, S. Mao, C. L. Chang, C. Persson, R. Ahuja, J. Nordgren, S. X. Wang and J.-H. Guo, *Chem. Phys. Lett.*,

2006, **422**, 543–546.

334 C. H. Bartholomew, *Appl. Catal. A Gen.*, 2001, **212**, 17–60.

335 P. Gallezot, *Catal. Today*, 1997, **37**, 405–418.

336 J. L. Davis and M. A. Barteau, *Surf. Sci.*, 1988, **197**, 123–152.

337 M. Mavrikakis and M. A. Barteau, *J. Mol. Catal. A Chem.*, 1998, **131**, 135–147.

338 C. P. O'Brien, G. R. Jenness, H. Dong, D. G. Vlachos and I. C. Lee, *J. Catal.*, 2016, **337**, 122–132.

339 M. S. Ide, D. D. Falcone and R. J. Davis, *J. Catal.*, 2014, **311**, 295–305.

340 M. Cargnello, C. Gentilini, T. Montini, E. Fonda, S. Mehraeen, M. Chi, M. Herrera-Collado, N. D. Browning, S. Polizzi, L. Pasquato and P. Fornasiero, *Chem. Mater.*, 2010, **22**, 4335–4345.

341 M. Besson and P. Gallezot, *Catal. Today*, 2000, **57**, 127–141.

342 J. H. Vleeming, B. F. M. Kuster and G. B. Marin, *Ind. Eng. Chem. Res.*, 1997, **36**, 3541–3553.

343 M. Besson and P. Gallezot, *Catal. Today*, 2003, **81**, 547–559.

344 J. P. Wharry, M. J. Swenson and K. H. Yano, *J. Nucl. Mater.*, 2017, **486**, 11–20.

345 Y. Schuurman, B. F. M. Kuster, K. v d Wiele and G. B. Martin, *Appl. Catal. A Gen.*, 1992, **89**, 47–68.

346 I. Bakos, T. Mallat and A. Baiker, *Catal. Letters*, 1997, **43**, 201–207.

347 J. M. G. Carballo, E. Finocchio, S. García-Rodriguez, M. Ojeda, J. L. G. Fierro, G. Busca and S. Rojas, *Catal. Today*, 2013, **214**, 2–11.

348 D. Peña, A. Griboval-Constant, F. Diehl, V. Lecocq and A. Y. Khodakov, *ChemCatChem*, 2013, **5**, 728–731.

349 A. Carvalho, V. V. Ordomsky, Y. Luo, M. Marinova, A. R. Muniz, N. R. Marcilio and A. Y. Khodakov, *J. Catal.*, 2016, **344**, 669–679.

350 M. Raphulu, J. McPherson, G. Pattrick, T. Ntho, L. Mokoena, J. Moma and E. van der Lingen, *Gold Bull.*, 2009, **42**, 328–336.

351 F. A. De Bruijn, B. F. M. Kuster and G. B. Marin, *Appl. Catal. A Gen.*, 1996, **145**, 351–374.

352 S. Lee, J. Seo and W. Jung, *Nanoscale*, 2016, **8**, 10219–10228.

353 J. F. Blandez, I. Esteve-Adell, M. Alvaro and H. García, *Catal. Sci. Technol.*, 2015, **5**, 2167–2173.

354 P. Forzatti and L. Lietti, *Catal. Today*, 1999, **52**, 165–181.

355 J. A. Moulijn, A. E. Van Diepen and F. Kapteijn, *Appl. Catal. A Gen.*, 2001, **212**, 3–16.

356 J. García-Aguilar, I. Miguel-García, Berenguer-Murcia and D. Cazorla-Amorós, *ACS Appl. Mater. Interfaces*, 2014, **6**, 22506–22518.

357 R. D. Adams, M. Chen, G. Elpitiya, M. E. Potter and R. Raja, *ACS Catal.*, 2013, **3**, 3106–3110.

358 S. M. Rogers, C. R. A. Catlow, C. E. Chan-Thaw, A. Chutia, N. Jian, R. E. Palmer, M. Perdjon, A. Thetford, N. Dimitratos, A. Villa and P. P. Wells, *ACS Catal.*, 2017, **7**, 2266–2274.

359 J. Garcia-Aguilar, I. Miguel-Garcia, J. Juan-Juan, I. Such-Basanez, E. San Fabian, D. Cazorla-Amoros and Berenguer-Murcia, *J. Catal.*, 2016, **338**, 154–167.

360 J. Garcia-Aguilar, M. Navlani-Garcia, A. Berenguer-Murcia, K. Mori, Y. Kuwahara, H. Yamashita and D. Cazorla-Amoros, *Langmuir*, 2016, **32**, 12110–12118.

361 I. E. Beck, V. V. Kriventsov, D. P. Ivanov, V. I. Zaikovsky and V. I. Bukhtiyarov, *Nucl. Instruments Methods Phys. Res. Sect. A Accel. Spectrometers, Detect. Assoc. Equip.*, 2009, **603**, 108–110.

362 H. Imai, K. Izumi, M. Matsumoto, Y. Kubo, K. Kato and Y. Imai, *J. Am. Chem. Soc.*, 2009, **131**, 6293–6300.

363 E. M. C. Alayon, J. Singh, M. Nachtegaal, M. Harfouche and J. A. van Bokhoven, *J. Catal.*, 2009, **263**, 228–238.

364 C. Amuli, M. Elleb, J. Meullemeestre, M. Schwing and F. Vierling, *Inorg. Chem.*, 1986, **25**, 856–861.

365 W. L. Waltz, J. Lilie, A. Goursot and H. Chermette, *Inorg. Chem.*, 1989, **28**, 2247–2256.

366 A. Mandalika, L. Qin, T. K. Sato and T. Runge, *Green Chem.*, 2014, **16**, 2480–2489.

367 M. J. Taylor, L. J. Durndell, M. A. Isaacs, C. M. A. Parlett, K. Wilson, A. F. Lee and G. Kyriakou, *Appl. Catal. B Environ.*, 2016, **180**, 580–585.

368 I. Agirre, M. B. Güemez, A. Ugarte, J. Requies, V. L. Barrio, J. F. Cambra and P. L. Arias, *Fuel Process. Technol.*, 2013, **116**, 182–188.

369 E. R. Gillies, A. P. Goodwin and J. M. J. Fre, *Bioconjug. Chem.*, 2004, **3**, 1254–1263.

370 X. Hu, C. Lievens and C. Li, *ChemSusChem*, 2012, **5**, 1427–1434.

371 X. Hu, R. Gunawan, D. Mourant, C. Lievens, X. Li, S. Zhang, W. Chaiwat and C. Li, *Fuel*, 2012, **97**, 512–522.

372 S. W. T. Price, K. Ignatyev, K. Geraki, M. Basham, J. Filik, N. T. Vo, P. T. Witte, A. M. Beale and J. F. W. Mosselmans, *Phys. Chem. Chem. Phys.*, 2015, **17**, 521–529.